A N N U A L R E P O R T

2024

and list of publications

Bayerisches Forschungsinstitut
für Experimentelle Geochemie und Geophysik
Universität Bayreuth

Bayerisches Geoinstitut
Universität Bayreuth
95440 Bayreuth
Germany

Telephone: +49-(0)921-55-3700
Telefax: +49-(0)921-55-3769
e-mail: bayerisches.geoinstitut@uni-bayreuth.de
www: https://www.bgi.uni-bayreuth.de

Editorial compilation by: Florian Heidelbach and Petra Buchert
Section editors: Andreas Audétat, Tiziana Boffa Ballaran, Audrey Bouvier, Johannes Buchen, Dan Frost, Florian Heidelbach, Gregor Golabek, Tomoo Katsura, Hans Keppler, Nobuyoshi Miyajima, Gerd Steinle-Neumann, Tony Withers

Staff and guests of the Bayerisches Geoinstitut in **June 2024**:

Die Mitarbeiter und Gäste des Bayerischen Geoinstituts im **Juni 2024:**

first row, from left (1. Reihe, v. links) Dapeng Zhu, Anastasiia Minchenkova, Anaëlle Antunes, Amrita Chakraborti, Rebecka Matthäus, Dorothea Wiesner, Fariia Iasmin Akbar, Shan Zhou, Meredith Calogero, Xiaojun Hu, Cheng Qian

second row, from left (2. Reihe, v. links) Tomo Katsura, Andrea Piccolo, Danielle Silva Souza, Olga Gaspert, Petra Buchert, Janina Scharnagel, Stefan Übelhack, Pedro Valdivia Munoz, Jonathan Dolinschi, Edna Obengo

third row, from left (3. Reihe, v. links) Artem Chanyshev, Sven Linhardt, Kui Han, Melanie Pöppelbaum, Matej Hlede, Cristian Timoner Bosch, Heinz Fischer, Yuan Li, Chad Wittkop, Dan Frost, Dan Liu

fourth row from left (4. Reihe, v. links) Florian Heidelbach, Alena Aslandukova, Andrii Aslandukov, Gerald Bauer, Ilham Hamadi, Tatjana Weiler, Tony Withers, Caterina Melai, Yuqing Yin, Dmitry Bondar, Lin Wang

back rows, from left (hintere Reihen, v. links) Nobuyoshi Miyajima, Rémy Pierru, Biao Wang, Raphael Njul, Alexander Kurnosov, Gerd Steinle-Neumann, Erik Konrad, Marcel Thielmann, Audrey Bouvier, Hans Keppler, Arne Spang, Andreas Audétat, Yibo Qiao, Matteo Zippoli, Detlef Krauße, Fei Wang, Ibrahim Jemal, Jia Chang, Yunke Song

Absent (Es fehlten) Tiziana Boffa Ballaran, Johannes Buchen, Laura Czekay, Leonid Dubrovinsky, Gregor Golabek, Edith Kubik, Lianjie Man, Catherine McCammon, Sergey Ovsyannikov, Anke Potzel, Dave Rubie, Maximilian Schulze, Jinia Sikdar, Ulrike Trenz, Ran Zhao

Contents

Foreword

In 2024, the office and laboratory space of Bayerisches Geoinstitut was significantly expanded by the takeover of various rooms from the former chair of crystallography after the retirement of Professor Sander van Smaalen. This development will relieve some of the pressure on office and laboratory space we sometimes experienced in the past. At the same time, crystallography will remain an important and highly appreciated part of our research activities. Incidentally, in 2024 also a new, extremely strong laboratory X-ray source with a single crystal diffractometer was purchased and installed at the BGI. This instrument allows measurements and refinements of crystal structures under high pressure inside a diamond cell that normally would only be possible with synchrotron radiation. Some first examples are already shown on pages 146-148 of this annual report.

The Bavarian Academy of Sciences acts as an advisory board to the scientific activities of Bayerisches Geoinstitut since its foundation in 1986. In May 2024, BGI scientists therefore participated in the "Day of the Open Door" of the Academy in Munich. A total of more than 5000 people attended and an exploding volcano spitting out candy bars was a highlight in the children's program realised by BGI scientists.

The Bayerisches Geoinstitut attracts numerous Ph.D. students, postdocs, and short-time visitors from all over the world. However, most of them come from the developed countries of the "global North". We are therefore very pleased that in 2024, a proposal of Audrey Bouvier to DAAD (the German Academic Exchange Service) was approved, which will provide four fellowships to Ph.D. students specifically from developing countries in the coming years. Another welcome news in 2024 was that our young colleague Marcel Thielmann was offered a professorship in geophysics at the university in Bonn.

With the numerous research projects described in this Annual Report, it is difficult to single out some particularly noteworthy achievements. Nevertheless, I would like to highlight two contributions that may provide major scientific advances. The presence of traces of water has a major effect on the state of the Earth's mantle, as water drastically reduces melting temperatures and affects many other physical properties. The exchange of water between the surface and the mantle reservoir through volcanic degassing and water subduction contributed to slow changes in sea level in deep geologic time. While the storage mechanism and the actual concentrations of water in the upper mantle and the transition zone are reasonably well understood, there are still major uncertainties concerning water storage in the lower mantle, which by mass is the largest reservoir on our planet. Previous work, notably at Bayerisches Geoinstitut, has shown that of the three main minerals of the lower mantle, bridgmanite, ferrropericlase, and davemaoite, the first two only dissolve very small traces of water. Davemaoite, on the other hand, was so far poorly studied, because it is the least abundant mineral and because it is difficult to investigate, as it turns into an amorphous phase upon pressure release. On pages 97-

99, Lin Wang and colleagues use a combination of FTIR spectroscopy, nano-SIMS, and atomic probe tomography to investigate water solubility in davemaoite. They show convincingly that water is incorporated in this mineral mostly through the substitution of $Al^{3+} + H^{+}$ for Si^{4+}. Under plausible lower mantle conditions, the water solubility in davemaoite may be near 3000 ppm, such that this phase may be the main host of water in this part of the Earth.

A few decades ago, we had only a rather superficial understanding of the physical state of the other planets in the solar system. This has changed by numerous space missions that directly sampled planetary surfaces, in particular those of Mars. Most notably, the NASA InSight mission deployed a seismometer on the Martian surface that continuously records seismic activity and provides insights into the interior structure of the planet. These data have stimulated numerous experimental studies on the properties of plausible Martian mantle and core compositions under high pressure. The core of Mars may be rather rich in sulphur, and on pages 71-72, Lianjie Man and colleagues report the discovery of a new iron sulphide phase with composition $Fe_{4+x}S_3$ that may be stable in a solid inner Martian core.

On the behalf of my colleagues, I would like to thank the *Free State of Bavaria* as represented by the *Bavarian State Ministry of Science, Research and Art*, as well as the *Advisory Board for High-Pressure Research in Geoscience of the Bavarian Academy of Sciences* for their continuing support and strong commitment to the Bayerisches Geoinstitut. I would further like to thank the *President and Leadership of the University of Bayreuth* for their high regard of our institute. We also gratefully acknowledge generous support from external funding agencies, in particular the *Alexander von Humboldt Foundation*, the *European Union*, the *German Science Foundation,* and the *Federal Ministry of Education and Research*, which continue to contribute greatly to the further development and success of the Geoinstitut.

Bayreuth, March 2025 Hans Keppler

Vorwort

In 2024 konnte das Bayerische Geoinstitut nach der Emeritierung von Professor Sander van Smaalen etliche Büro- und Laborräume des früheren Lehrstuhls für Kristallographie übernehmen. Hierdurch konnten viele Engpässe der vergangenen Jahre überwunden werden. Gleichzeitig bleibt die Kristallographie ein wichtiger und hochgeschätzter Teil unserer Forschungsaktivitäten. Zufälligerweise wurde in 2024 auch ein neues Einkristall-Diffraktometer mit einer extrem starken Röntgenquelle beschafft und in Betrieb genommen. Mit diesem Instrument können Messungen und Strukturbestimmungen an Proben in Diamantstempel-Zellen unter hohem Druck durchgeführt werden, die sonst nur an Synchrotron-Einrichtungen möglich wären. Einige erste Beispiele werden bereits auf den Seiten 146-148 dieses Jahresberichts gezeigt.

Die Bayerische Akademie der Wissenschaften begleitet die wissenschaftlichen Aktivitäten am Bayerischen Geoinstitut seit seiner Gründung im Jahr 1986 in beratender Funktion. Im Mai 2024 waren daher Wissenschaftler des BGI am Tag der offenen Tür der Akademie in München beteiligt. Mehr als 5000 Besucher wurden gezählt und im Kinderprogramm war ein vom BGI konstruierter Vulkan, der Süßigkeiten in die Luft sprengte, eine besondere Attraktion.

Zahlreiche Doktoranden, Postdoktoranden und kurzzeitige Besucher kommen aus aller Welt an unser Institut. Die meisten stammen jedoch aus den Industrieländern des "globalen Nordens". Wir freuen uns daher sehr, dass in 2024 ein Projekt von Audrey Bouvier vom DAAD (Deutscher Akademischer Austauschdienst) genehmigt wurde, welches in den kommenden Jahren vier Stipendien für Doktoranden speziell aus Entwicklungsländern zur Verfügung stellen wird. Eine weitere erfreuliche Nachricht in 2024 war, dass unser junger Kollege Marcel Thielmann einen Ruf auf eine Professur in Geophysik an der Universität Bonn erhalten hat.

In Anbetracht der zahlreichen Projekte in diesem Jahresbericht ist es naturgemäß schwierig, besonders herausragende Beiträge zu identifizieren. Trotzdem möchte ich hier zwei Arbeiten hervorheben, die möglicherweise wichtige wissenschaftliche Fortschritte geliefert haben. Selbst Spuren von Wasser haben einen großen Einfluss auf den Zustand des Erdmantels, da Wasser die Schmelztemperaturen drastisch herabsetzt und auch viele andere physikalische Eigenschaften verändert. Der Austausch von Wasser zwischen der Erdoberfläche und dem Mantel durch vulkanische Entgasung und Subduktion verursachte langsame Veränderungen im Meeresspiegel in der geologischen Vergangenheit. Der Speichermechanismus und die tatsächlichen Konzentrationen von Wasser im oberen Mantel und der Übergangszone sind recht gut verstanden. Das gleiche gilt aber nicht für den unteren Mantel, der von der Masse her das größte Reservoir in der Erde darstellt. Frühere Arbeiten, insbesondere am Bayerischen Geoinstitut, haben gezeigt, dass von den drei Hauptmineralen des unteren Mantels (Bridgmanit, Ferroperiklas und Davemaoit) die ersten beiden nur geringe Spuren von Wasser aufnehmen können. Davemaoit ist jedoch nur wenig untersucht worden, weil es mengenmäßig das am

wenigsten häufige Mineral ist und es sich außerdem bei Druckentlastung in eine amorphe Phase umwandelt. Auf Seite 97-99 nutzen Lin Wang und Kollegen eine Kombination von FTIR, nano-SIMS und Atomsonden-Tomographie um den Einbau von Wasser in Davemaoit zu untersuchen. Sie zeigen eindeutig, dass Wasser in diesem Mineral primär durch die gekoppelte Substitution von $Al^{3+} + H^{+}$ für Si^{4+} eingebaut wird. Unter plausiblen Bedingungen für den unteren Mantel liegt die Wasser-Löslichkeit in Davemaoit um 3000 ppm, so dass diese Phase wohl der Hauptspeicher von Wasser in diesem Teil der Erde ist.

Bis vor wenigen Jahrzehnten hatten wir nur ein recht oberflächliches Verständnis von dem physikalischen Zustand anderer Planeten im Sonnensystem. Dies hat sich durch zahlreiche Raumfahrtmissionen geändert, die die Oberflächen anderer Planeten direkt beprobt haben. Die NASA InSight-Mission hat ein Seismometer direkt auf der Oberfläche von Mars installiert, welches kontinuierlich seismische Aktivität aufzeichnet und neue Einblicke in die innere Struktur des Planeten liefert. Diese Daten haben viele experimentelle Untersuchungen über die möglichen Eigenschaften von Materialien im Mantel und im Kern von Mars inspiriert. Der Kern von Mars ist möglicherweise reich an Schwefel und auf Seite 71-72 beschreiben Lianjie Man und Mitarbeiter die Entdeckung einer neuen Eisensulfid-Phase mit Zusammensetzung $Fe_{4+x}S_3$, die möglicherweise in einem festen Kern von Mars stabil sein könnte.

Meine Kollegen und ich möchten dem *Freistaat Bayern*, vertreten durch das *Bayerische Staatsministerium für Wissenschaft, Forschung und Kunst*, und dem *Beirat für Geowissenschaftliche Hochdruckforschung der Bayerischen Akademie der Wissenschaften* unseren Dank für ihre fortwährende Unterstützung des Bayerischen Geoinstituts aussprechen. Darüber hinaus möchten wir dem Präsidenten und der Hochschulleitung der Universität Bayreuth ausdrücklich für ihre zuverlässige und kontinuierliche Unterstützung unseres Instituts danken. Wir sind auch für die großzügige Förderung durch externe Geldgeber dankbar, insbesondere der *Alexander-von-Humboldt-Stiftung*, der *Europäischen Union* und der *Deutschen Forschungsgemeinschaft*, die ebenfalls wesentlich zur Entwicklung und zum Erfolg des Bayerischen Geoinstituts beigetragen haben.

Bayreuth, im März 2025 Hans Keppler

1. Advisory Board and Directorship

1.1 Advisory Board

The *Beirat für Geowissenschaftliche Hochdruckforschung der Bayerischen Akademie der Wissenschaften* advises on the organisation and scientific activities of the institute. Members of this board are:

Prof. Dr. Ulrich CHRISTENSEN	Emeritus, Max-Planck-Institut für Sonnensystem-forschung, Göttingen
Prof. Dr. Rudolf GROSS (Vice Chairman)	Walther-Meißner-Institut für Tieftemperatur-forschung (WMI), Garching
Prof. Dr. Francois HOLTZ	Institut für Mineralogie der Leibniz Universität Hannover
Prof. Dr. Klaus MEZGER	Institut für Geologie der Universität Bern
Prof. Dr. Herbert PALME	Emeritus, Institut für Mineralogie und Geochemie der Universität zu Köln – Senckenberg Forschungsinstitut und Naturmuseum Frankfurt/M.
Prof. Dr. Markus RIEDERER (Chairman)	Julius-von-Sachs-Institut für Biowissenschaften, Würzburg
Prof. Dr. Ekhard SALJE, FRS, FRSA († 24.02.2025)	Emeritus, Department of Earth Sciences, University of Cambridge
Prof. Dr. Christine THOMAS	Institut für Geophysik der Westfälischen Wilhelms-Universität Münster

1.2 Leadership

Prof. Dr. Hans KEPPLER (Director)
Prof. Dr. Dan FROST (Deputy Director)
Prof. Dr. Tomoo KATSURA
Prof. Dr. Audrey BOUVIER

2. Staff, Funding and Facilities

2.1 Staff

At the end of 2024 the following staff positions existed in the Institute:

- Scientific staff: **17**
- Technical staff: **14**
- Administrative staff: **2.5**
- Administrative officer: **1***

* The administrative officer is employed on 40 % of a full position provided by the central administration.

During 2024, 23 scientific positions (191.5 months) were funded by grants raised externally by staff members of the institute. In addition, 4 scientific positions (12.5 months) were funded by the resources of the BGI Visiting Scientists' Programme (see Sect. 8), which also supported short-term visits for discussing future projects or presenting research results (see Sect. 5). 9 student assistants (78 months) were funded by externally raised grants. 5 scientists and 6 PhD students (130 months) were supported by personal grants or stipends.
An additional position (72 months) for a tenure-track junior professorship was funded by BMBF and provided by courtesy of Bayreuth University.

2.2 Funding

In 2024, the following financial resources were available from the Free State of Bavaria:

- Visiting Scientists' Programme: 104.000 €
- Consumables: 793.000 €
- Investment funding 400.000 €

The total amount of national/international external funding *("Drittmittel"*) used for ongoing research projects in 2024 was 2.606.000 € (positions: 1.646.000 €; equipment, consumables and travel grants: 960.000 €).

	positions	**equipment, consumables, travel grants**	**total**
• AvH	43.000 €	5.000 €	48.000 €
• DFG	1.116.000 €	857.000 €	1.973.000 €
• BMBF	90.000 €	0 €	90.000 €
• EU	275.000 €	98.000 €	373.000 €
• Others	122.000 €	0 €	122.000 €
	1.646.000 €	**960.000 €**	**2.606.000 €**

(AvH = Alexander von Humboldt Foundation; DFG = German Science Foundation; EU = European Union; Others: DAAD, Chinese Scholarship Council, Japanese Society for the Promotion of Science, Swiss National Science Foundation)

In the following list, only the BGI components of the funding are listed in cases where joint projects involved other research institutions. Principal investigators and the duration of the grants are listed in brackets. Total project funding refers to the funding over the entire duration of this project.

Funding institution	Project, Funding			Total Project Funding
AvH	Project SEPARATION (E. Kubik – 3/23-2/25) "Segregation efficiency of planetary cores addressed through the isotopes of nickel"			
	Position:	24 months	70.000 €	
	Consumables:		19.200 €	89.200 €
DFG	AU 314/9-1 (A. Audétat – 6/24-6/27) "Das Verhalten volatiler Elemente und erzbildender Metalle während der Differentiation subduktionsgebundener Magmen unter hohen Drücken"			
	Positions:	E 13 (50 %), 36 months	115.200 €	
		student assistant	20.700 €	
	Consumables:		33.300 €	
	Overhead:		37.200 €	206.400 €
DFG	BO 2550/10-1 (T. Boffa Ballaran, B. Mihailova – 7/21-6/24) "Mehrskaliges Hochdruckverhalten der bleifreien ferroelektrischen Perowskitmischkristalle $(1-x)Na_{0.5}BiTiO_{3-x}BaTiO_3$"			
	Positions:	student assistant	15.000 €	
	Consumables:		6.900 €	
	Overhead:		4.800 €	26.700 €
DFG	DI 2751/2-1 (D. Di Genova – 10/21-9/24) "Rheology of nanocrystal-bearing natural silicate melts"			
	Positions:	E 13 (75 %), 36 months	160.900 €	
		student assistant	4.846 €	
	Equipment:		18.000 €	
	Overhead:		40.400 €	224.146 €
DFG	DU 393/13-2 (L.S. Dubrovinsky – 7/20-9/24) "Mantel-formende Materialien von Super-Erden bei statischen Drücken von über 500 GPa und hohen Temperaturen"			
	Positions:	E 13 (75 %), 36 months	158.600 €	
		student assistant	7.000 €	
	Equipment:		32.250 €	
	Overhead:		43.500 €	241.350 €

DFG	FR 1555/14-1 (D.J. Frost) – 6/24-7/27 "Fluid permeability and speciation in subduction zones" Positions: E 13, 36 months 232.900 € student assistant 18.026 € Consumables and travel funding: 21.609 € Publication costs: 2.250 € Overhead: 60.453 €	335.238 €
DFG	INST 91/467-1 FUGG (D. Frost – 2022-2024) Co-financing for a microfocus single-crystal X-ray diffractometer. Total DFG funding (50 % of total costs):	390.000 €
DFG	INST 91/503-1 FUGG (H. Keppler – 2024-2025) Co-financing of a Fourier-transform infrared spectrometer with microscope. Total funding:	197.500 €
DFG	KA3434/19-1 (T. Katsura – 02/21-08/25) "Evaluation of the aspect ratio of ferropericlase under lower-mantle conditions" Positions: E13, 24 months 152.200 € Consumables: 50.000 € Overhead: 44.400 €	246.600 €
DFG	KA 3434/20-1 (T. Katsura – 9/21-12/24) "Accurate determination of the melting relations of primitive peridotite under lower-mantle conditions up to 35 GPa using advanced multi-anvil techniques" Positions: E13, 24 months 154.100 € Consumables: 50.000 € Overhead: 44.900 €	249.000 €
DFG	KA 3434/24-1 (T. Katsura – 10/23-9/26) "H_2O solubilities in Al-free and Al-bearing high-pressure silica polymorphs as a function of pressure and temperature: H_2O storage in the lower mantle" Positions: E13, 36 months 246.800 € student assistant 5.000 € Consumables: 78.000 € Overhead: 72.600 €	402.400 €
DFG	KE 501/16-1 (H. Keppler – 4/21-10/24) "Cassiterite solubility, tin partitioning, and the origin of porphyry tin deposits" Total funding:	242.288 €
DFG	KE 501/18-1 (H. Keppler – 1/23-5/26) "Stability of organic molecules in subduction zone fluids" Total funding:	259.555 €

DFG	KE 501/19-1 (H. Keppler – 7/24-12/27) "Subduction fluids and the source of metals in porphyry deposits" Total funding:	259.603 €
DFG	KU 3447/1-2 (A. Kurnosov – 1/22-12/24) "Einkristall-Elastizität von Mars-Mineralen und ein flexibles CO_2 Laserheizsystem" Position: E 13, 36 months 237.100 € student assistant 10.000 € Consumables and travel funding: 23.550 € Overhead: 59.500 €	330.150 €
DFG	MC 3/20-2 (C.A. McCammon – 1/18-3/24) DFG FOR 2125 (CarboPaT) "Elastic properties of carbonates at high pressure and high temperature" Position: E 13 (67 %), 36 months: 132.800 € Equipment, consumables and travel funding: 27.750 € Overhead: 35.300 €	195.850 €
DFG	OV 110/3-3 (S.V. Ovsyannikov – 11/23-10/25) "High-pressure synthesis and properties of novel simple oxides with unusual stoichiometries" Position: E 13, 24 months: 159.900 € Consumables and travel funding: 36.000 € Overhead: 43.100 €	239.000 €
DFG	STE 1105/13-2 (G. Steinle-Neumann – 7/20-6/24) "Thermodynamic properties of silicate solids and liquids and iron to the TPa range from *ab initio* calculations" Positions: E 13 (75%), 36 months 158.600 € student assistant 7.000 € Consumables: 8.250 € Overhead: 38.200 €	212.050 €
DFG	STE 1105/15-1 (G. Steinle-Neumann – 7/23-6/26) "The role of light elements at the core-mantle boundary – partitioning, demixing and transport " Positions: E 13 (75%), 36 months 172.100 € student assistant 7.000 € Consumables: 10.250 € Overhead: 41.657 €	231.007 €
DFG	TH 2076/7-1 (M. Thielmann – 6/21-5/24) "Quantifizierung des Oberflächensignals durch Lithosphärenablösung in den Alpen" Positions: 244.700 € Consumables: 17.050 € Overhead: 57.600 €	319.350 €

DFG	TH 2076/8-1 (M. Thielmann – 11/21-10/24) "Identifizierung der Entstehungsprozesse tiefer Erdbeben" (Emmy-Noether-Programm) Positions: 670.913 € Consumables: 60.580 € Workshops: 5.000 € Overhead: 162.000 €	898.496 €
DFG	YU 358/1-1 (L. Yuan, G. Steinle-Neumann – 2/22-1/25) "Partitionierung flüchtiger Elemente im tiefen Magma Ozean der Erde" Positions: E 13, 36 months 232.900 € student assistant 10.000 € Consumables: 14.250 € Overhead: 56.600 €	313.750 €
EU	European Research Council (ERC) Advanced Grant No. 787 527 (T. Katsura – 10/18-9/24) "Chemistry and transport properties of bridgmanite controlling lower-mantle dynamics" ("UltraLVP") Positions (post docs): 860.144 € Travel funding: 187.380 € Equipment: 49.250 € Consumables: 997.722 € In-kind contributions: 24.000 € Overhead: 523.624 €	2.642.120 €
EU	European Research Council (ERC) Grant No. 949 417 (R. Hin – 1/21-12/25) "The chemical consequences of vapour loss during planetary accretion (VapLoss)" ("HORIZON 2020") Positions: 756.169 € Travel funding: 44.781 € Consumables: 129.403 € Equipment: 153.802 € Internally Goods and Services: 173.235 € Overhead: 314.348 €	1.571.738 €

2.3 Laboratory and office facilities

The institute occupies an area of

ca. 1589 m^2	laboratory space
ca. 505 m^2	infrastructural areas (machine shops, computer facilities, seminar room, library)
ca. 622 m^2	office space

in a building which was completed in 1994.

2.4 Experimental and analytical equipment

The following major equipment is available at the Bayerisches Geoinstitut:

I. High-pressure apparatus
- 15 MN/1500 tonne Kawai-type multianvil high-pressure apparatus (50 GPa, 3000 K)
- 6 x 8 MN/6x800 tonne independently acting-anvil press (40 GPa, 3000 K)
- 50 MN/5000 tonne multianvil press (25 GPa, 3000 K)
- 12 MN/1200 tonne multianvil press (25 GPa, 3000 K)
- 10 MN/1000 tonne multianvil press (25 GPa, 3000 K)
- 5 MN/500 tonne multianvil press (20 GPa, 3000 K)
- 5 MN/500 tonne press with a deformation DIA apparatus
- 5 piston-cylinder presses (5 GPa, 2100 K)
- Cold-seal pressure vessels (700 MPa, 1100 K, H2O), TZM vessels (300 MPa, 1400 K, Ar), rapid-quench cold-seal pressure vessels (400 MPa, 1200 K, H2O)
- Magma fragmentation device (0.1 GPa, 1400 K)
- Internally-heated autoclave (1 GPa, 1600 K)
- High-pressure gas loading apparatus for DAC

II. Structural and chemical analysis
- 1 X-ray powder micro-diffractometer
- 1 X-ray powder diffractometer with furnace and cryostat
- 2 automated single-crystal X-ray diffractometers
- High-brilliance X-ray system
- Single crystal X-ray diffraction diffractometer with rotating anode coupled with a Brillouin scattering system
- Single crystal X-ray diffractometer with high-brilliance source
- 1 Mössbauer spectrometer (1.5 - 1300 K)
- 3 Mössbauer microspectrometers
- 2 FTIR spectrometers with IR microscope

FEG transmission electron microscope (TEM), 200 kV analytical, with EDS
FEG scanning TEM, 80-200 kV analytical, with 4-SDDs EDS and post-column energy filter (EFTEM/EELS)
FEG scanning electron microscope (SEM) with BSE detector, EDS, EBSD and CL
Dual beam device, focused ion beam (FIB) and FEG SEM. In situ easy-lift manipulator, STEM, EDS and EBSD detectors, and beam deceleration option
3 Micro-Raman spectrometers with ultraviolet and visible lasers
Tandem-multipass Fabry-Perot interferometer for Brillouin scattering spectroscopy
Two electron microprobes; fully-automated with 14 resp. 12 crystals, 5 spectrometer configuration, EDX, capability for light elements, CL
193 nm Excimer laser-ablation quadrupole ICP-MS
Water content determination by Karl-Fischer titration
GC/MS-MS for organic analyses
Confocal 3D surface measurement system
1.4 Tesla sweepable ESR magnet
Isotope Cosmochemistry & Geochemistry Laboratory ISO 6 cleanrooms equipped with ISO 2-4 exhaust laminar flow cabinets for sample preparation
1-500 Hz 193 nm Excimer laser-ablation system
Triple quadrupole ICPMS for solution or in-situ LA-isotopic analysis
Multi-collector ICPMS/MS for solution or in-situ LA-isotopic analysis

III. *In situ* determination of properties

Diamond anvil cells for powder and single crystal X-ray diffraction, Mössbauer, IR, Raman, optical spectroscopy, NMR specroscopy, electrical resistivity measurements over 200 GPa
Facility for in situ hydrothermal studies in DAC
Externally heated DACs for in situ studies at pressures to 100 GPa and 1200 K
1-atm furnaces to 1950 K, gas mixing to 1600 K, zirconia fO2 probes
1-atm high-temperature creep apparatus
Megahertz ultrasonic interferometer
2 freezing-heating stages for fluid inclusion analysis (80-870 K; 300-1900 K)
Impedance/gain-phase analyser for electrical conductivity studies
Apparatus for in situ measurements of thermal diffusivity at high P and T
Laser-heating facility for DAC
Portable pulsed laser heating system for DAC

The Geoinstitut maintains a well equipped machine shop, an electronic workshop and sample preparation laboratories. It has access to supercomputing resources at the University and Leibniz computer centres.

3.1 Struktur und Dynamik der Erde und Planeten

In diesem Abschnitt werden in fünf Beiträgen Prozesse in der Erde und in Planeten von der Oberfläche bis zum Kern untersucht, im Sonnensystem und darüber hinaus. Die Beiträge beschäftigen sich mit dem Ursprung der Kruste von Asteroiden und den Auswirkungen von Impakt-Prozessen auf die thermische Entwicklung von Planetesimalen. Mit modernen Instrumenten wie dem James-Webb-Weltraumteleskop werden die frühen Stadien der Planetenentwicklung untersucht, während geophysikalische Simulationen Einblicke in tektonische Prozesse wie tiefe Erdbeben und die Dynamik von Subduktionszonen geben.

Im ersten Beitrag untersuchen Timoner und Kollegen zwei Anorthit-reiche Meteoriten. Im Allgemeinen geht man davon aus, dass sich die Anorthosite des Mondes durch Kristallisation in einem Magmaozean gebildet haben, wobei der Plagioklas aufschwamm, um die ursprüngliche Kruste zu bilden. Stattdessen deuten geochemische und Rb-Sr-Isotopendaten dieser Meteoriten darauf hin, dass diese Anorthosite wahrscheinlich aus geschichteten Intrusionen entstanden sind, die mit diogenitischen Kumulaten auf dem Asteroid Vesta verbunden sind. Die Ergebnisse geben neue Einblicke in die Prozesse der Planeten-differenzierung und Krustenbildung auf Asteroiden.

Im zweiten Beitrag untersuchen Obengo und Kollegen drei Angrite mit Hilfe von Elektronen-Rückstreubeugung (EBSD) und Raman-Spektroskopie, um Schockeffekte und ihre Auswirkungen auf die Interpretation chronologischer Daten zu bewerten. Sie stellen fest, dass die Schockdeformation und der Metasomatismus unterschiedlich stark ausgeprägt sind, was auf eine komplexe Einschlagsgeschichte und eine langanhaltende magmatische Aktivität auf dem Angrit-Mutterkörper hindeutet.

Im dritten Beitrag modellieren Zippoli und Mitarbeiter Kollisionen zwischen Planetesimalen, bei denen ein Planetesimal den größten Teil seines Mantels verliert, während sein Kern größtenteils intakt bleibt. Die Simulation der thermischen Entwicklung der eisenreichen Körper zeigt, dass die Abkühlungsraten gut mit denen von IIIAB-Eisenmeteoriten übereinstimmen.

Im vierten Beitrag vergleichen Golabek und Kollegen hochauflösende Beobachtungen durch das neue James-Webb-Weltraumteleskop (JWST) mit numerischen Modellen der Entwicklung des Magmaozeans auf dem gebundenen rotierenden Super-Merkur GJ 367 b. Dies erlaubt Einblicke in das sonst unzugängliche Magmaozean-Stadium junger terrestrischer Planeten.

Im letzten Beitrag untersuchen Weiler und Kollegen tiefe Erdbeben in der Hindukusch-Region, die mit der subduzierten unteren Kruste und der Ablösung der Erdplatte zusammenhängen. Zu diesem Zweck führen sie numerische 2D-Simulationen durch und stellen fest, dass die Subduktion der unteren Kruste die Ablösungstiefe der Platte stark beeinflusst.

3.2 Geochemie

Die Herkunft der flüchtigen Elemente auf der Erde ist ein wichtiges Problem in der Geochemie. Wie fast alle Gesteinskörper im Sonnensystem ist die Erde im Vergleich zum ursprünglichen Sonnennebel an flüchtigen Elementen verarmt. Wie im ersten Projekt dieses Abschnitts beschrieben, ist Fluor in der Erdkruste, im Erdmantel und in den Oberflächenreservoiren im Vergleich zu Chlor weniger verarmt, obwohl beide Elemente eine sehr ähnliche Flüchtigkeit aufweisen. Bisherige experimentelle Studien bei relativ niedrigem Druck haben ergeben, dass sich keines der beiden Elemente in nennenswertem Umfang im Erdkern angereichert haben dürfte. In diesem ersten Projekt wird jedoch mit Hilfe von molekular-dynamischen Simulationen gezeigt, dass Chlor möglicherweise in flüssiges Eisen übergeht und daher im Kern angereichert werden könnte, wenn der Druck des Metall-Silikat-Gleichgewichts über 80 GPa liegt. Dagegen verbleibt Fluor auch bei diesen Drücken im Silikat-Mantel. Die Fraktionierung von Fluor und Chlor in der Erde könnte daher ein Anzeichen für eine Gleichgewichts-Einstellung zwischen Kern und Mantel unter sehr hohem Druck sein, also in einem Magma-Ozean von über 1000 km Tiefe.

Die nächsten drei Beiträge befassen sich mit dem Verhalten von Schwefel und chalcophilen Elementen während der Akkretion und Kern-Mantel-Differenzierung der Erde. In der ersten Studie ermittelten Blanchard *et al.* mit Hilfe von Experimenten in einer laserbeheizten Diamant-Stempelzelle die Löslichkeit von Schwefel in einem Magma mit der Zusammensetzung und bei P-T-Bedingungen, die für einen tiefen Magmaozean relevant sind. Ziel dieser Experimente ist es, die Plausibilität der sog. "Hadean-Matte"-Hypothese zu prüfen. Diese Hypothese besagt, dass der kristallisierende Magmaozean gegen Ende der Akkretion der Erde eine Sättigung mit Eisensulfid erreichte, das sich als Flüssigkeit absetzte und in den Kern absank. Dabei sollen dem Magmaozean Elemente wie Platin und Gold entzogen worden sein, die sich in der Sulfidschmelze anreichern. Die Ergebnisse der Experimente deuten aber darauf hin, dass die Sulfidsättigung im tiefen Magmaozean nicht erreicht wurde, was die "Hadean-Matte"-Hypothese unwahrscheinlich macht. Eine ähnliche Frage wird in der folgenden Studie behandelt, in der Experimente mit laserbeheizten Diamant-Stempelzellen durchgeführt wurden, um die Auswirkungen von Schwefel auf die Verteilungskoeffizienten von Spurenelementen zwischen Metall- und Silikatschmelzen zu bestimmen. Es wird davon ausgegangen, dass Elemente wie Kadmium durch kernbildende schwefelhaltige Schmelzen aus dem Erdmantel extrahiert wurden. Vorläufige Ergebnisse zeigen jedoch, dass der Schwefelgehalt der Schmelze den Cadmiumgehalt bei niedrigen Drücken beeinflusst, während dieser Einfluss bei höheren Drücken zu verschwinden scheint. Im nächsten Projekt führten Liu und Li Stempel-Zylinder-Experimente durch, um die Verteilungskoeffizienten von Se und Te zwischen einer Sulfid- und einer Silikatschmelze zu bestimmen. Die relative Häufigkeit dieser Elemente und von S im Mantel ähnelt der in Chondriten. Sie könnten daher in der so genannten "late veneer" Phase der Akkretion auf die Erde gelangt sein, in der keine nachfolgende Kernbildung stattfand. Die Mantelgesteine, in denen S, Se und Te analysiert wurden, haben jedoch Schmelzvorgänge und metasomatische Vorgänge durchlaufen. Es stellt sich daher die Frage, ob diese Analysen die

tatsächlichen Werte des ursprünglichen Mantels widerspiegeln. Anhand der ermittelten Verteilungskoeffizienten ist es möglich, die Konzentrationen von S, Se und Te im Erdmantel auf der Grundlage ihrer Häufigkeit in aus dem Erdmantel stammenden Magmen zuverlässiger zu bestimmen. Die Ergebnisse zeigen, dass diese Elemente im Mantel nicht im chondritischen Verhältnis vorliegen, so dass sie wahrscheinlich nicht einfach als "late veneer" auf die Erde gelangt sind.

In der folgenden Studie von Pausch *et al.* wird die Stabilität der Wirtsphase für Phosphor im tiefen Erdmantel untersucht. Im oberen Erdmantel ist Phosphor teilweise im Apatit gebunden, der auch viele inkompatible Spurenelemente wie seltene Erden, Uran und Thorium enthalten kann. Apatit wandelt sich aber an der Basis des oberen Erdmantels in das Mineral Tuit um. Obwohl Apatit ein begrenztes thermisches Stabilitätsfeld hat, ist Tuit im unteren Mantel sogar bei Temperaturen oberhalb einer normalen Mantel-Geotherme stabil. Interessanterweise verliert Tuit jedoch bei niedrigeren Manteltemperaturen seine Rolle als Wirt für Spurenelemente, die dann stattdessen in das Kalziumsilikat-Perowskit-Mineral Davemaoit eingebaut werden.

Die nächsten beiden Beiträge befassen sich mit Experimenten über die Verteilung von dreiwertigem Eisen (Fe^{3+}) beim Aufschmelzen des Mantels. Mit solchen Daten kann die Ursprungskonzentration von Fe^{3+} im Mantel aus den Analysen von Magmen bestimmt werden. Die Experimente können auch zeigen, wie der Redoxzustand der Erde nach der Kristallisation eines primordialen Magmaozeans zustande kam. In der ersten dieser Studien werden partielle Schmelzexperimente unter den Bedingungen der Übergangszone der Erde (410-660 km Tiefe) durchgeführt, wobei verschiedene Puffer für die Sauerstoff-Fugazität verwendet werden. Ein interessantes Ergebnis ist, dass unter stärker oxidierten Bedingungen weniger kristalline Phasen mit der Schmelze koexistieren als unter reduzierten Bedingungen. Das zweite Projekt dieser Art wird bei niedrigerem Druck und unter den Bedingungen durchgeführt, unter denen Basalte im Mantel unter mittelozeanischen Rücken entstehen. Eines der Hauptziele dieser Studie ist die Herstellung von genau charakterisierten Proben von Basalt-Glas, die mit verschiedenen Techniken auf ihr Fe^{3+}/Fe^{2+}-Verhältnis untersucht werden können. Widersprüchliche Werte über das Fe^{3+}/Fe^{2+}-Verhältnis in der Literatur sind möglicherweise auf die Verwendung unterschiedlicher Techniken mit unterschiedlichen systematischen Fehlern zurückzuführen.

Die nächsten beiden Projekte sind eng miteinander verbunden und untersuchen Schmelzprozesse im tieferen Mantel und die anschließenden Schmelz-Gesteins-Reaktionen, die beim Aufstieg dieser Schmelzen durch den lithosphärischen Mantel stattfanden. Im Rahmen des ersten Projekts werden Schmelzexperimente durchgeführt, um den Ursprung der Komatiite zu verstehen. Dies sind Magnesium-reiche Magmen, die offenbar das Produkt eines sehr hohen partiellen Aufschmelzungsgrades sind. Die zweite Studie befasst sich damit, dass der tiefe subkratonische Lithosphären-Mantel in vielen Regionen reicher an Kieselsäure zu sein scheint als andere Mantelgesteine. Dies zeigt sich in einem höheren Anteil an Orthopyroxen im Vergleich zu Olivin. In dieser Studie wird die Hypothese getestet, dass dies auf die

Wechselwirkung mit aufsteigenden Komatiit-Magmen zurückzuführen ist. Vorläufige Experimente zeigen tatsächlich den gegenteiligen Effekt, da die Reaktion die Bildung von Olivin aus der Schmelze fördert. Dies könnte jedoch dazu geführt haben, dass die Komatiit-Magmen SiO_2-reicher wurden und damit eine Anreicherung von Kieselsäure in geringeren Tiefen verursachten.

Die nächsten fünf Beiträge betrachten alle die Bildung von magmatisch-hydrothermalen Erzlagerstätten. Hlede *et al.* untersuchten das Verhalten von Cu, Mo, Zn und W bei der Subduktion von Sedimenten. Dazu führten sie Experimente mit einer Piston-Cylinder-Apparatur durch, bei denen NaCl-haltige Fluide mit typischen subduzierten Sedimenten bei subsolidus Bedingungen equilibriert wurden. Das Fluid wurde hierbei im Porenraum von einer Lage von Diamantpulver in der Probenkapsel eingefangen. Aus LA-ICP-MS-Analysen des Fluids in dieser "Diamantenfalle" und entsprechenden Analysen von Mineralen im angrenzenden Gestein wurden Fluid-Mineral-Verteilungskoeffizienten berechnet. Es zeigt sich, dass Mo bei allen Salzgehalten bevorzugt ins Fluid übergeht, während dies für Cu und Zn nur bei hohen Salzgehalten beobachtet wird. Daraus wird gefolgert, dass die eigentliche Mo-Quelle in porphyrischen Erzlagerstätten subduzierte Schwarzschiefer sein könnten, da sie mehrere Größenordnungen mehr Mo enthalten als gewöhnliche Mantelgesteine. Die Studie von Keppler und Audétat befasst sich mit der Frage, ob die typische Assoziation von Sn-Lagerstätten mit reduzierten Magmen eine Folge der effizienteren Metallextraktion durch Fluide unter reduzierten Bedingungen sein könnte. Zu diesem Zweck wurden Experimente mit Hydrothermal-Autoklaven durchgeführt, um die Wirkung von fO_2 auf die Fluid-Schmelze-Verteilung von Sn zu untersuchen. Aufgrund der starken Legierung von Sn mit den üblicherweise als Kapsel-Material verwendeten Edelmetallen wurden die Verteilungskoeffizienten zwischen Flüssigkeit und Schmelze mittels LA-ICP-MS-Analyse von Flüssigkeitseinschlüssen in der abgeschreckten Silikatschmelze bestimmt. Hier kann man lokales Gleichgewicht zwischen dem Fluid und der unmittelbar benachbarten Schmelze annehmen, auch wenn Sn ständig durch Diffusion und Legierungs-Bildung mit dem Metall der Kapsel verloren geht. Die Ergebnisse zeigen, dass $D_{Sn}^{Fluid/Schmelze}$ mit zunehmendem fO_2 bis etwa zum Ni-NiO-Puffer zunimmt, oberhalb davon aber wieder abnimmt. $D_{Sn}^{Fluid/Schmelze}$ ist jedoch im Allgemeinen zu niedrig, um durch Entmischung von Fluid bei der fraktionierten Kristallisation Sn in der Silikatschmelze abzureichern. Entscheidend für die Bildung von Sn-Lagerstätten ist daher wahrscheinlich nicht eine besonders effiziente Metallextraktion durch die Fluide, sondern eher eine besonders effiziente Anreicherung von Sn in der Restschmelze bei der fraktionierten Kristallisation.

Die Studie von Qiao und Audétat untersucht, warum bestimmte Magmen porphyrische Kupfer-Lagerstätten bilden. Die Geochemie natürlicher Gesteine lässt vermuten, dass diese Magmen bei hohem Druck fraktioniert wurden. Es ist aber nicht klar, ob dies zu höheren Metallgehalten oder zu höheren Gehalten an S, Cl oder H_2O in den Restschmelzen führte. Um diese Frage zu beantworten, werden natürliche Inselbogen-Basalte, die mit geologisch realistischen Mengen

an Metallen und flüchtigen Bestandteilen dotiert sind, in Piston-Cylinder-Experimenten bei verschiedenen Drücken aufgeschmolzen und dann langsam abgekühlt. Bislang wurde nur die 10 kbar Serie abgeschlossen, die einen kontinuierlichen Anstieg von H_2O in der Restschmelze während der Magma-Differenzierung zeigt, während Cl und S aufgrund der Fluidentmischung oder der Bildung schwefelreicher akzessorischer Phasen zunächst zunehmen und dann abnehmen. Porphyrische Kupferlagerstätten sind auch Gegenstand der beiden folgenden Beiträge. Durch detaillierte geochemische und petrologische Untersuchungen von 13 mineralisierten Magmasystemen in der Sanjiang-Region im Südwesten Chinas fanden Chang *et al.* heraus, dass sich die Erz-bildenden Magmen in einer Tiefe von 10-20 km ansammelten und kristallisierten, bevor sie schließlich in 3-6 km Tiefe aufstiegen, wo sich die Erzlagerstätten bildeten. Anhand der Zusammensetzung der Schmelzeinschlüsse und mit Hilfe von Massenbilanzberechnungen lässt sich nachweisen, dass sich die meisten Erz-bildenden Fluide in Tiefen von 10-20 km entmischt haben. Das bedeutet, dass die mineralisierenden Fluide im Durchschnitt ~ 10 km vom Ort der Fluid-Freisetzung bis zum Ort der Erzausfällung zurückgelegt haben. Diese Entfernung ist wesentlich länger als erwartet, und es wird eine Erklärung dafür angeboten, wie so große Flüssigkeitsmengen durch porphyrische Intrusionen gelangen konnten, ohne große Spuren zu hinterlassen. Eine ähnliche Studie wurde von Audétat *et al.* im Central Mining District in New Mexico, USA, durchgeführt. Dort beträgt die Tiefe der letzten Magma-Kristallisation, die anhand von 13 porphyrischen Intrusionen bestimmt wurde, 10 bis 17 km, was zusammen mit einer Erzbildungstiefe von 4 bis 5 km zu einem durchschnittlichen Transportweg der mineralisierenden Fluide von ~ 9 km führt. Die Daten zeigen, dass unter dem Central Mining District ein großer Pluton in der oberen Kruste existiert, was das klassische Modell der Porphyr-Kupferbildung unterstützt. Gleichzeitig weisen hohe Sr/Y-Verhältnisse im Gesamtgestein auf eine Magmafraktionierung in mittleren bis unteren Krustenebenen hin. Folglich wird ein zweistufiges Evolutionsmodell vorgeschlagen, das eine erste Stufe der Magmafraktionierung in tiefen Krustenschichten umfasst, gefolgt von einer zweiten Stufe der Magmakristallisation in der oberen Kruste, ohne große Kristall-Fluid-Trennung, bevor einige der Magmen schließlich bis zur aktuellen Expositionstiefe aufstiegen, wo sie als Porphyr abgeschreckt wurden.

In der letzten Studie dieses Abschnitts werden radiogene Isotope verwendet, um die Ursprünge der Gesteine zu ermitteln, die von den Gletschern in Nordamerika während der letzten Eiszeit erodiert und dann abgelagert wurden. Durch die aufeinanderfolgenden Eiszeiten werden die Spuren früherer Vergletscherungsphasen allmählich verwischt, so dass es schwierig ist, die frühere Landschaft und die Bewegung der Gletscher zu rekonstruieren. Die von den Gletschern beim Schmelzen abgelagerten Sedimente können Hinweise auf die Gesteine liefern, die während der vergangenen Eiszeiten erodiert wurden. In dieser Studie werden radiogene Isotope als Fingerabdruck verwendet, um die Herkunft der verschiedenen Gesteine zurückzuverfolgen. Ein interessantes Ergebnis dieser Analyse ist, dass das alte Grundgebirge des kanadischen Schildes möglicherweise erst durch die erodierende Wirkung der Gletscher vor etwa einer Million Jahren an die Oberfläche gelangt ist.

3.3 Mineralogie, Kristallchemie und Phasenübergänge

Durch chemische Reaktionen und Phasenumwandlungen bestimmen Minerale die geophysikalische Struktur des Erdinneren und beeinflussen Prozesse, die tief im Inneren von Planeten ablaufen. Die chemischen und kristallographischen Eigenschaften von Mineralen können wiederum Aufschluss über die Bedingungen geben, unter denen sich ein Mineral gebildet hat und in manchen Fällen Möglichkeiten für technologische Anwendungen eröffnen. Die Beiträge in diesem Abschnitt untersuchen das Verhalten von Mineralen von den Eigenschaften auf atomarer Ebene bis hin zu Auswirkungen auf geochemische Kreisläufe.

Phasendiagramme sind von zentraler Bedeutung für die Untersuchung von Materialien bei hohen Drücken und extremen Temperaturen, sowohl für die Erforschung des Erdinneren als auch für technische Anwendungen. Um das Verhalten der seismischen Diskontinuität in einer Tiefe von 660 km im Erdmantel besser zu verstehen, untersuchten Chanyshev *et al.* das Phasendiagramm von $MgSiO_3$. Die Ergebnisse ihrer Experimente in Vielstempel-Pressen zeigen, dass die Phasengrenze zwischen den Mineralen Akimotoit und Bridgmanit bei Drücken liegt, die höher sind als an der 660-km-Diskontinuität. Jedoch könnte die Anwesenheit von Aluminium und Eisen die Phasengrenze in heißen Regionen des Erdmantels näher an die beobachtete Tiefe der 660-km-Diskontinuität heranschieben. Die maximale Menge an zweiwertigem Eisen (Fe^{2+}), die in Bridgmanit eingebaut werden kann, wird durch die Löslichkeit der Komponente $FeSiO_3$ bestimmt. Zippoli *et al.* untersuchten die Löslichkeit dieser Komponente in Bridgmanit, indem sie synthetische Olivin-Pulver mit unterschiedlichen Eisengehalten in einer Vielstempel-Presse in Bridgmanit und Ferroperiklas umwandelten. Die Ergebnisse deuten darauf hin, dass die Löslichkeit von Eisen in Bridgmanit höher sein könnte als bisher angenommen. Eisenoxide sind bekannt für ihre Vielfalt in Stöchiometrie, Kristallstrukturen und physikalische Eigenschaften. Li *et al.* synthetisierten Einkristalle der Verbindung Fe_5O_6 und erkundeten das Phasendiagramm dieser Verbindung bei hohen Drücken und geringen Temperaturen von bis zu 55 K mit Hilfe von Diamantstempelzellen. Auf der Grundlage ihrer Analyse von Röntgenbeugungsdaten identifizierten Li *et al.* vier verschiedene Modifikationen der Verbindung Fe_5O_6, von denen zwei Ladungsordnungs-Phänomene zeigen. Wasserhaltige Minerale, die sich in subduzierten Platten bilden, können H_2O bis in den unteren Erdmantel transportieren. Um die Phasenbeziehungen wasserhaltiger Minerale in Metasedimenten und Metabasalten bei Drücken und Temperaturen des unteren Erdmantels genauer zu bestimmen, untersuchten Song *et al.* das System Al_2O_3-SiO_2-H_2O mit Hilfe von Experimenten in Vielstempel-Pressen. Ausgehend von ihren experimentellen Ergebnissen konstruierten sie ein Reaktionsnetz, das sich zu deutlich höheren Drücken erstreckt als die Ergebnisse früherer Studien zu diesem System.

Die extremen Drücke und Temperaturen, die im Inneren von Planeten herrschen, können zur Bildung neuer Verbindungen führen, die bisher unbekannt waren. Dies gilt selbst für scheinbar einfache chemische Systeme mit nur wenigen verschiedenen Elementen. Die Chemie im

Inneren der Planeten Neptun und Uranus wird beispielsweise von den vier Elementen Kohlenstoff, Wasserstoff, Stickstoff und Sauerstoff dominiert. Mithilfe von Diamantstempelzellen, Laserheizung und Röntgenbeugung untersuchten Dubrovinsky *et al.* das ternäre System C-N-H und bestimmten die Kristallstrukturen zweier neuer Verbindungen, die auf Gerüsten von CN_4-Tetraedern basieren. Pantousas *et al.* entdeckten eine neue Phase im System H-C-O-Si-Ca, indem sie am Synchrotron ESRF die Vielkorn-Röntgenbeugungs-methode auf eine Probe in einer laserbeheizten Diamantstempelzelle anwandten. Sie beobachteten, dass das Mineral Davemaoit ($CaSiO_3$) in Gegenwart von H_2O mit Kohlenstoff zu einem neuen, wasserhaltigen Kalziumkarbonat reagieren kann. Diese Reaktion läuft bei Drücken und Temperaturen ab, die denen der Kern-Mantel-Grenze der Erde entsprechen. Mit ähnlichen Synchrotron-Röntgen-Methoden charakterisierten Man *et al.* eine neue Eisensulfidphase, $Fe_{4+x}S_3$, die im Kern des Planeten Mars stabil sein könnte. Einschlüsse von Kalzium-phosphatmineralen in natürlichen Diamanten könnten einen Einblick in das Vorkommen von seltenen Erden im Erdinneren geben. Die Phasenstabilität von Kalziumphosphatmineralen wie Merillit und Tuit bei hohem Druck könnte dazu beitragen, den Ursprung solcher Einschlüsse im oberen Erdmantel einzugrenzen. Novais-Rodrigues *et al.* führten Hochdruckexperimente in einer Vielstempel-Presse durch, um die Phasenbeziehungen komplexer Phosphate unter Hochdruckbedingungen zu untersuchen.

Geeignete Proben von Hochdruckmineralen werden benötigt, um ihre strukturellen und physikalischen Eigenschaften unter den Bedingungen des Erdinneren zu charakterisieren. Hamadi *et al.* berichten über die Synthese einer polykristallinen Probe von Al-haltigem Stishovit in einer Vielstempel-Presse, die in Zukunft zur Messung der physikalischen Eigenschaften bei hohen Drücken verwendet werden kann. Davemaoit, $CaSiO_3$ mit Perowskit-Struktur, ist ein potenzieller Kandidat für die Speicherung von Wasser im unteren Erdmantel. Darüber hinaus sind die elastischen Eigenschaften dieses Minerals für ein besseres Verständnis der seismischen Struktur des Erdmantels von Bedeutung. Da sich Davemaoite unter Umgebungsbedingungen zersetzt, synthetisierten Wang *et al.* dieses Mineral *in situ* in einer Diamantstempelzelle unter Verwendung eines kürzlich am BGI installierten CO_2-Laser-Heizsystems.

Die kristallchemischen Eigenschaften und das Verhalten von Mineralien auf atomarer Ebene können mit Hilfe der Transmissionselektronenmikroskopie (TEM) untersucht werden. Am BGI hat TEM zu vielen wichtigen Entdeckungen beigetragen und ist nach wie vor ein unverzichtbares Werkzeug, wie die letzten drei Beiträge in diesem Abschnitt zeigen. Die direkte Betrachtung atomarer Details mittels hochauflösender Raster-Transmissions-Elektronenmikroskopie (RTEM) ist eine der leistungsstärksten Methoden zum Nachweis von Kationenverteilungen und Strukturdefekten in kristallinen Materialien. Miyajima *et al.* verwendeten die RTEM in Verbindung mit einem ringförmigen Dunkelfeld-Detektor, um die Verteilung von dreiwertigen Eisenkationen (Fe^{3+}) sowie Aluminiumkationen in Bridgmanit abzubilden. Dreiwertiges Eisen bevorzugt die größeren Gitterplätze mit achtfacher Koordination. Mithilfe

von *ab initio*-Berechnungen untersuchten Yao *et al.* modulare Strukturmodelle für Verbindungen der Tetradymit-Reihe mit der Formel Bi_xTe_y und verglichen simulierte mit beobachteten RTEM-Bildern und Elektronenbeugungsmustern, um ihre Ergebnisse zu validieren. Auch geologische Prozesse auf sehr großen Skalen können Spuren in den Mikrostrukturen von Mineralien hinterlassen. Um den Zeitrahmen des Fluidaustauschs in Subduktionszonen abzuschätzen, simulierten Fukushima *et al.* das zeitabhängige Wachstum von Antiphasendomänen in Omphazit. Möglicherweise können Episoden der Fluidinfiltration, die weniger als 100.000 Jahre andauerten, durch die Analyse von Antiphasendomänen in natürlichem Omphazit nachgewiesen werden.

3.4 Physikalische Eigenschaften von Mineralen

Das dynamische Verhalten der Erde und anderer Planeten spiegelt die Materialeigenschaften der Minerale wider, aus denen sie besteht. Die Wärmeübertragung durch Konvektion steht in direktem Zusammenhang mit der Viskosität der Materialien des Erdinneren. Deformation als Reaktion auf Spannungen wird durch das Aggregatverhalten der Mineralien gesteuert und die Ausbreitung seismischer Wellen im Planeten hängt von den elastischen Eigenschaften der einzelnen Phasen ab. Da nun seismische Daten von Mars zur Verfügung stehen, müssen die elastischen Eigenschaften von Mineralen im Innern von Mars bestimmt werden. Der erste Beitrag in diesem Abschnitt nutzt die Brillouin-Spektroskopie zur Messung der elastischen Eigenschaften von Fe- und Ca-reichem majoritischem Granat, wie wir ihn im Marsmantel erwarten würden. Der höhere Fe^{3+}-Gehalt des Mars-Granats führt zu deutlich niedrigeren Wellengeschwindigkeiten im Vergleich zu irdischen Granaten, was für die Interpretation der von der InSight-Mission gesammelten Daten wichtig ist.

Wie die Erde hat auch der Mars einen metallischen Kern, der neben Fe und Ni auch ein leichteres Element enthalten muss. Es ist wahrscheinlich, dass eine beträchtliche Menge an Schwefel im äußeren, flüssigen Mars-Kern gelöst sein könnte. Nachdem bei der InSight-Mission die Flüssigkeitsdichte und die P-Wellen-Geschwindigkeit gemessen wurden, ist es nun wichtig, sowohl die Dichte als auch die P-Wellen-Geschwindigkeit von S-haltigen Fe-Schmelzen zu bestimmen. Der zweite Beitrag nutzt die Ultraschall-Interferometrie in Kombination mit Synchrotron-Röntgenmethoden, um sowohl die Dichte als auch die P-Wellen-Geschwindigkeit der Fe-S-Schmelzen unter Bedingungen zu messen, die denen des Mars-Kerns entsprechen. Hierbei wurde festgestellt, dass das Vorhandensein von Schwefel allein die InSight-Beobachtungen nicht ausreichend erklären kann.

Im unteren Erdmantel kann das Fe-haltige Al_2O_3 als Korund vorkommen. Die Zustandsgleichung von Korund wird im dritten Beitrag anhand von Synchrotron-Röntgen-messungen in einer Diamant-Stempelzelle untersucht. Der Zusatz von Fe erhöht das Volumen und die Kompressibilität dieser Phase. Im Gegensatz zu früheren Daten für das Endglied Al_2O_3

treten bei Drücken über 40 GPa im Fe-haltigen Material Komplikationen auf, die auf eine Änderung des Spinzustandes in Fe zurückzuführen sind. Eine weitere Hochdruckphase, die in einer basaltischen Zusammensetzung bei niedrigeren Manteldrücken besonders häufig vorkommt, ist $NaAlSiO_4$ mit der Calciumferritstruktur. Im nächsten Beitrag werden die elastischen Eigenschaften dieser "CF"-Phase durch *in situ*-Brillouin-Spektroskopie bei hohem Druck gemessen. Dies ist wichtig für die Interpretation seismischer Untersuchungen von tief subduziertem Krustenmaterial. Die Brillouin-Spektroskopie wird auch im folgenden Beitrag eingesetzt, um Messungen der elastischen Eigenschaften von Bridgmanit bei gleichzeitig hohem Druck und hoher Temperatur durchzuführen. Die neuen Messungen an polykristallinen Proben zeigen, dass Korngrenzeffekte in feinkörnigeren Proben zunehmend an Bedeutung gewinnen. Entsprechende Daten müssen daher von einer Vielzahl sorgfältig charakterisierter Proben aus Hochdruck-Syntheseexperimenten gesammelt werden.

Eine der wenigen direkt beobachtbaren Eigenschaften des tiefen Planeteninneren ist die elektrische Leitfähigkeit, die durch magnetotellurische Messungen ermittelt wird. Die Interpretation solcher Messungen setzt voraus, dass wir die Leitfähigkeiten von Hochdruck-mineralen kennen. Der folgende Beitrag berichtet über die Ergebnisse einer Reihe von systematischen Messungen der elektrischen Leitfähigkeit von Bridgmanit mit unterschiedlichem Fe-Gehalt, die einen deutlichen Anstieg der Leitfähigkeit mit zunehmendem Fe zeigen. Das Fe^{3+}/Fe^{2+}-Verhältnis scheint dagegen keinen starken Einfluss auf die Leitfähigkeit zu haben. Solche experimentell anspruchsvollen Leitfähigkeitsmessungen bei hohem Druck sind für die Bestimmung der Gesamtleitfähigkeit des unteren Erdmantels unerlässlich.

Der nächste Beitrag beschäftigt sich mit der Viskosität des unteren Erdmantels. Aufbauend auf sorgfältigen Experimenten, in denen die Abrundungsrate von verformten Ferroperiklas-Körnern quantifiziert wurde, wurde ein Modell erstellt, das die Abrundungsrate für unterschiedlich lang gestreckte Ferroperiklas-Körner beschreibt. Die Abrundungsrate ist so hoch, dass die Erholung von der Dehnung die Dehnungsrate im Mantel leicht übersteigt. Dies bedeutet, dass der weichere Ferroperiklas keine zusammenhängenden Bänder innerhalb des Mantels bilden kann. Die Rheologie wird daher von der festeren Bridgmanit-Phase gesteuert und muss viel höher sein, als bisher angenommen wurde. In einer weiteren Studie zur Verteilung von Spannung und Dehnung in polykristallinen Aggregaten werden im nächsten Beitrag Synchrotron-Messungen der dynamischen Dehnung in polykristallinem MgO als Reaktion auf die zyklische Belastung einer Diamant-Stempelzelle vorgestellt. Das Verständnis der Beziehung zwischen dynamischer differentieller Spannung und kristallographischer Orientierung wird zu einer vollständigeren Beschreibung der elastischen Eigenschaften polykristalliner Materialien führen. Der letzte Beitrag in diesem Abschnitt nutzt die Möglichkeiten des maschinellen Lernens, um die Zeit- und Längenskalen von Molekular-dynamik-Simulationen zu erweitern. Hiermit werden die Transporteigenschaften von Davemaoit im unteren Mantel bestimmt.

3.5 Fluide, Schmelzen und ihre Wechselwirkung mit Mineralen

Sowohl experimentelle Untersuchungen als auch Messungen an natürlichen Proben haben in den letzten Jahrzehnten gezeigt, dass der Erdmantel eine Menge an Wasser enthält, die ähnlich groß ist wie alle Ozeane an der Erdoberfläche zusammengenommen. In der fernen geologischen Vergangenheit bestimmte der Austausch zwischen diesen beiden Reservoiren die Höhe des Meeresspiegels. Darüber hinaus hat die Anwesenheit von Spuren von Wasser auch einen großen Effekt auf die physikalischen Eigenschaften des Mantels. Für den oberen Mantel und die Übergangszone ist die Speicherung von Wasser recht gut verstanden. Im Gegensatz dazu ist es nach wie vor umstritten, wieviel Wasser im unteren Mantel gespeichert sein könnte. Von den wichtigsten Mineralen des unteren Mantels – Bridgmanit, Ferroperiklas und Davemaoit – scheinen die ersten beiden kaum Wasser in ihre Struktur einzubauen. Davemaoit ($CaSiO_3$ mit Perowskit-Struktur) ist aber schwer zu untersuchen, da es sich bei Druckentlastung in eine amorphe Phase umwandelt. Dieses Mineral ist oft auch ignoriert worden, da es im unteren Mantel nur in geringen Anteilen vorkommt. Der erste Beitrag in diesem Abschnitt des Jahresberichts untersucht die Wasserlöslichkeit in Davemaoit mit einer Kombination aus Multi-Anvil-Experimenten, nano-SIMS, Atomsonden-Tomographie und Infrarot-Spektroskopie. Die Daten zeigen eindeutig, dass Davemaoit mehrere Tausend ppm von Wasser über die gekoppelte Substitution von $H^+ + Al^{3+}$ für Si^{4+} einbauen kann. Damit ist dieses Mineral wahrscheinlich der Hauptspeicher von Wasser im unteren Mantel. Obwohl die Löslichkeit von Wasser im unteren Mantel insgesamt gering ist, führt die große Masse dieses Reservoirs dazu, dass bis zu eine halbe Ozean-Masse an Wasser dort gespeichert sein könnte.

Zwei weitere Beiträge beschäftigen sich mit Berichten aus der Literatur über angebliche hohe Wasserlöslichkeiten in Mineralen des unteren Mantels. Stishovit (SiO_2 mit Rutil-Struktur) ist ein wichtiger Bestandteil in tief subduzierten Platten. Berichte über sehr hohe Wasserlöslichkeiten in diesem Mineral aus Experimenten mit Diamantzellen konnten in Multi-Anvil-Experimenten nicht bestätigt werden, so dass der Beitrag von Stishovit zum Wassertransport in den unteren Mantel wohl eher begrenzt ist. Auch frühere Berichte, wonach die Anwesenheit von Fluor die Wasserlöslichkeit in Bridgmanit erhöhen könnte, konnten nicht bestätigt werden. Ein weiterer Beitrag beschreibt neue Experimente zur Verteilung von Wasser zwischen Wadsleyit und Granat unter Wasser-untersättigten Bedingungen.

Wasserstoff liegt gegenwärtig in der Erde überwiegend in oxidierter Form vor, als molekulares H_2O oder als Hydroxylgruppen in Mineralen und Schmelzen. Während der Entstehung der Erde war dies aber möglicherweise anders. Der Magmenozean auf der frühen Erde war möglicherweise im Gleichgewicht mit einer H_2-reichen Atmosphäre und gelöstes H_2 in der Silikatschmelze hat eventuell die ursprüngliche Konzentration von Wasserstoff im Erdinnern bestimmt. Einige neuere Arbeiten haben auch vorgeschlagen, dass das Gleichgewicht mit einer H_2-reichen Atmosphäre entscheidend war für die Verteilung von flüchtigen Bestandteilen im

Erdinnern. Bisher basierten alle Daten zur Löslichkeit von H_2 in Silikatschmelzen auf Infrarot-Messungen an abgeschreckten Gläsern. Diese Messungen wurden quantifiziert mit Hilfe eines Infrarot-Extinktionskoeffizienten von H_2, der mit eher fragwürdigen Methoden an Quarzglas bestimmt worden war. In einem hier beschriebenen Projekt wurde daher dieser Extinktionskoeffizient für Silikatgläser neu kalibriert. Hierzu wurden zwei voneinander unabhängige Methoden benutzt, die sehr konsistente Resultate lieferten. Das Ergebnis unterscheidet sich von dem bisher akzeptierten Wert um eine Größenordnung. Frühere Untersuchungen haben daher wohl die Löslichkeit von H_2 in einem Magmenozean um einen Faktor von zehn überschätzt. In Anbetracht dieser neuen Kalibrierung erscheint es eher unwahrscheinlich, dass H_2 im Magmenozean einen größeren Beitrag zum ursprünglichen Inventar von flüchtigen Bestandteilen im Erdmantel oder im Erdkern geleistet hat.

Seismische Daten der InSight-Mission haben Hinweise auf eine etwa 150 km dicke Lage von Magma oberhalb des Kerns von Mars geliefert. In einem Beitrag werden mögliche Bedingungen für die Schmelzbildung in einem Fe-reichen Mars-Mantel sowie die Dichte und Viskosität der entsprechenden Schmelzen untersucht. Die bisher beobachteten Schmelztemperaturen sind aber mit der erwarteten Temperaturverteilung im Innern von Mars schwer vereinbar. Der folgende Beitrag beschäftigt sich ebenfalls mit den Eigenschaften von Schmelzen im tiefen Innern von Planeten. Die Struktur von wasserhaltigen Silikatschmelzen wurde unter hohem Druck mit einer Kombination von Neutronen- und Röntgenbeugung sowie mit molekular-dynamischen Simulationen untersucht. Die Daten zeigen eine Polymerisation der Schmelzen unter hohem Druck durch Ringschlüsse der Silikatgruppen sowie eine erhöhte Koordinationszahl von Wasserstoff mit entsprechend erhöhten O-H-Abständen.

Die nächsten sechs Berichte in diesem Abschnitt des Jahresberichts beschäftigen sich mit der Viskosität von Magmen und ihrer Auswirkung auf Vulkaneruptionen, insbesondere auch mit dem Einfluss von Nanolithen (Nanometer-große Kristalle, insbesondere von Eisenoxiden) auf Viskosität und Eruptionsverhalten. Die Bedeutung dieser Nanolithe, die sich sehr schnell während der Abkühlung, bei Druckabfall oder beim Entweichen flüchtiger Bestandteile bilden können, wurde erst vor kurzem erkannt. Sie können als feste Partikel in der Schmelze die Viskosität direkt beeinflussen oder auch indirekt durch die Veränderung der Zusammensetzung der verbliebenen Schmelze. Darüber hinaus sind sie mögliche Keime für die Bildung von Gasblasen und beeinflussen dadurch das Entgasungsverhalten.

Der letzte Beitrag in diesem Kapitel beschäftigt sich mit dem Verhalten von geschmolzenem Schwefel unter hohem Druck. Frühere Untersuchungen hatten plötzliche Veränderungen in den physikalischen Eigenschaften auf mögliche flüssig-flüssig-Phasenübergänge zurückgeführt. Messungen durch *in situ*-Ultraschall-Interferometrie bestätigen Anomalien in der Druckabhängigkeit der Schallgeschwindigkeiten, eindeutige Hinweise auf flüssig-flüssig-Phasenübergänge konnten aber nicht gefunden werden.

3.6 Rheologie

Das rheologische Verhalten von Gesteinen und Mineralen wird durch ihre Verformung als Reaktion auf angewandte mechanische Spannungen bestimmt. Je nach den physikalischen und chemischen Bedingungen im Erdinneren können die aktiven Verformungsmechanismen ein bruchhaftes bis duktiles makroskopisches Verhalten hervorrufen. Dies kann zu schnellen Bruchprozessen wie Erdbeben oder auch zu langsamen Bewegungen wie Platten-Verschiebungen oder Gebirgsbildung führen. Mit Hilfe von Verformungsexperimenten am BGI lassen sich die Verformungsmechanismen und letztlich die rheologischen Fließgesetze charakterisieren. Diese Daten werden durch numerische Modellierungen ergänzt, die eine Extrapolation im Parameterraum (z. B. Verformungsgeschwindigkeit) ermöglichen, der bei Experimenten begrenzt ist. Schließlich liefert auch die Untersuchung natürlich verformter Gesteine wichtige Anhaltspunkte.

Die ersten drei Beiträge befassen sich mit den möglichen Mechanismen für tiefe Erdbeben. In dem experimentellen Projekt von Silva Souza *et al.* werden erste Ergebnisse eines Versuchs vorgestellt, den Nukleations-Mechanismus von Erdbeben in Proben von Serpentinit bei hohem Druck und hoher Temperatur zu reproduzieren. Sie können zeigen, dass die Dehydratisierung von Serpentinit unter Spannung zur Bildung von Olivin auf ausgerichteten Störungsebenen führt. Dies deutet auf eine Kombination aus Dehydratisierungs-Versprödung und Phasen-umwandlung als Mechanismus für tiefe Erdbeben hin. Im Beitrag von Spang *et al.* wird die mögliche Rolle thermischer Überhitzung und des duktilen Bruchs als Nukleations-Mechanismus für Erdbeben in einem aus Olivin bestehenden Gestein modelliert. Sie zeigen, dass duktile Verformungsprozesse zu einer sehr hohen lokalen Spannungskonzentration und dadurch zur bruchhaften Deformation des Materials führen können. Dieser Mechanismus ist eine mögliche Erklärung für das Auftreten von Erdbeben in Regionen der Erde, in denen duktile Deformationsprozesse vorherrschen. Hamadi *et al.* untersuchten die Rolle der duktilen Verformung während der postseismischen Relaxation nach Erdbeben an der Grenzfläche von Subduktionszonen. Mit ihrem Modellierungsansatz können sie zeigen, dass es durch thermische Reduktion der Festigkeit zu einem Übergang von spröder zu duktiler Verformung kommt, der durch eine höhere Hintergrundtemperatur und einen höheren Festigkeitskontrast zwischen subduzierter Platte und Nebengestein verstärkt wird.

Der vierte Beitrag von Heidelbach *et al.* stellt eine experimentelle Verformungsstudie vor, bei der eine Reihe von Plagioklas-Klinopyroxen-Aggregaten unter axialer Kompression im duktilen Bereich verformt wurde, um den Einfluss auf die Texturentwicklung und die seismischen Eigenschaften zu untersuchen. Während die kristallographischen Texturen über die gesamte Serie hinweg recht ähnlich bleiben, ändern sich die seismischen Eigenschaften bei wechselnden Phasenanteilen. Damit kann die Interpretation seismischer Anisotropie in der unteren Erdkruste oder dem oberen Erdmantel verbessert werden. Das Projekt von Zhou *et al.* präsentiert experimentelle Daten über die Geschwindigkeit des Kornwachstums von

Bridgmanit in basaltischen Gesteinen unter Bedingungen des unteren Erdmantels, was einen wichtigen Faktor für das Deformationsverhalten subduzierter ozeanischer Platten darstellt. Ihre Ergebnisse zeigen, dass die Wachstumsrate von Bridgmanit in einer basaltischen Lithologie etwas geringer ist als in vergleichbarem peridotitischem Material. In einer mikrostrukturellen Studie an natürlich deformierten Gesteinen aus den Südalpen untersuchen Jemal und Miyajima die Reaktion von Albit zu Jadeit, die ein klassischer Indikator für Hochdruckbedingungen ist. Die Reaktion kann lokal aufgrund des Chemismus sowie der möglichen Erhaltung von prograden oder retrograden Reaktionstexturen erheblich variieren, was eine eindeutige Interpretation im Hinblick auf den p,T-Pfad erschwert.

3.7 Materialwissenschaften

Materialien können unter hohem Druck neuartige Eigenschaften annehmen. Technische Anwendungen werden jedoch oft durch die geringe Menge der unter hohem Druck synthetisierten Proben begrenzt. Nur wenn neuartige Materialien auch unter Normaldruck erhalten bleiben, sind praktische Anwendungen denkbar. Wie in den vergangenen Jahren werden die Beiträge in diesem Kapitel des Jahresberichts von verschiedenen Hochdruck-Reaktionsprodukten in der Diamant-Stempel-Zelle dominiert, die mit Röntgenbeugung an einer Synchrotronquelle charakterisiert wurden. Die Installation eines neuen Diffraktometers mit einer hochintensiven Röntgenquelle am BGI hat jedoch zwei Projekte ermöglicht, die außerhalb des typischen Spektrums der in den Vorjahren vorgestellten Arbeiten liegen.

Aufgrund des großen Energieunterschieds zwischen dem dreifach gebundenen Stickstoff-molekül und Stickstoffeinheiten mit Doppel- oder sogar Einfachbindungen sind Nitride mit hohem Stickstoffgehalt vielversprechend als Materialien mit hoher Energiedichte. Nach der Stabilisierung von CN_3^{5-} Anionen in Materialien auf Lanthanid-Basis, über die 2023 berichtet wurde, erweitert der erste Beitrag in diesem Kapitel diese Forschungsrichtung für Scandiumnitride. Hierbei wurden N_6^{6-} und N_8^{6-} sowie eine zweidimensionale Poly-Stickstoff-schicht bei sukzessivem höherem Druck in der Diamant-Stempel-Zelle erzeugt.

In ähnlicher Weise erweitert der zweite Beitrag in diesem Abschnitt ein im Jahresbericht 2023 vorgestelltes Projekt über Dysprosiumkarbide. Er befasst sich mit einer breiten Palette von Karbiden, die sich bei der Reaktion mit Seltenerdmetallen unter hohem Druck bilden und berichtet von der Synthese einer erstaunlichen Vielfalt gemeinsamer Strukturtypen mit unterschiedlichem Kohlenstoffgehalt. Im dritten Beitrag wird die Synthese von Rheniumkarbid Re_3C in der Diamant-Stempel-Zelle vorgestellt. Diese Phase wurde anhand von *ab initio*-Simulationen vorhergesagt und soll eine hohe Härte aufweisen. Der vierte Beitrag in diesem Kapitel befasst sich ebenfalls mit Karbiden: Statt Experimente im Megabar-Bereich, beschreibt er mögliche Synthesewege bei etwa 10 GPa in der Vielstempel-Presse zur Dotierung von Borkarbid mit Si, um dieses bereits superharte Material weiter zu härten.

In der Erde kommen Karbonate wie $CaCO_3$ (Calcit) vor allem in Sedimentgesteinen vor und sind unter hohem Druck mit planaren CO_3^{2-}-Einheiten bemerkenswert stabil. Im fünften Beitrag wird dagegen ein Karbonat mit CO_4^{4-}-Tetraedern als Bausteinen in der Diamant-Stempel-Zelle synthetisiert, sowie ein ähnlich strukturiertes Borat, beide mit Yttrium als Kation. Der sechste Beitrag in diesem Abschnitt untersucht das Verhalten organischer Verbindungen aus zwei oder mehr Benzolringen unter Druck. In der Studie zeigt Benzopyren eine Reihe von Phasenübergängen bei hohem Druck, bei denen die Grundeinheiten von fünf kondensierten Benzolringen neu angeordnet werden.

Die Installation eines Diffraktometers mit hochintensiver Röntgenquelle am BGI hat die beiden abschließenden Studien in diesem Abschnitt ermöglicht. In der ersten werden die Strukturen eines hybriden organisch-anorganischen Perowskits mit zwei Enantiomeren mit hervorragenden optoelektrischen Eigenschaften in der Diamant-Stempel-Zelle untersucht. Dies eröffnet in der Zukunft die Möglichkeit, diese Materialien auch bei hohem Druck zu untersuchen. In ähnlicher Weise ermöglichte der intensive Röntgenstrahl der neuen Quelle im letzten Beitrag dieses Kapitels die Strukturbestimmung zweier Fluoreszenz-Materialien, die möglicherweise als organische Leuchtdioden verwendet werden können.

3.8 Methodische Entwicklung

In diesem Jahr hat das Geochemielabor unter der Leitung von Prof. A. Bouvier erhebliche Fortschritte in der Isotopen- und Elementaranalyse gemacht. Durch den Einsatz eines neuen MC-ICP-MS/MS-Systems wurden Methoden wie die ^{176}Lu-^{180}Hf- und ^{149}Sm-^{150}Nd-Doppelmix-Spike-Kalibrierung entwickelt, um hochpräzise Sm-Nd- und Lu-Hf-Datierungen durchzuführen. Darüber hinaus entwickelte das Team von Prof. Bouvier eine hochpräzise Methode für die Zinn-Isotopenanalyse, mit der die Probleme der Isotopenfraktionierung während der Probenvorbereitung überwunden werden konnten. Außerdem synthetisierten sie einen Kassiterit-Standard für die *in situ*-Laserablations-Analyse. Ergänzend zu diesen Bemühungen stellten Zhang *et al.* einen verfeinerten Ansatz zur Messung hoch-siderophiler Elemente (HSE) in Meteoriten vor, der genauer ist als bestehende Neutronenaktivierungs-Methoden. Darüber hinaus etablierten Zhao *et al.* eine *in situ*-^{87}Rb-^{87}Sr-Datierungstechnik, die durch die geringere Zerstörung der Proben besonders vorteilhaft ist.

Im Bereich der experimentellen Geowissenschaften sind fünf bemerkenswerte Innovationen zu nennen. Erstens installierten Kurnosov *et al.* einen Bildplattendetektor in das kombinierte Röntgenbeugungs-Brillouin-System und verbesserten damit signifikant die Datenerfassung für elastische Eigenschaften von Mineralen unter Mantelbedingungen. Zweitens entwickelten Pöppelbaum *et al.* eine neuartige Methode zur *in situ*-Messung von Flüssigkeitsüberdruck und Permeabilität unter Hochtemperatur- und Hochdruckbedingungen mittels Röntgentomographie und -beugung. Drittens setzten Pierru *et al.* die ultraschnelle 3D-Mikrotomografie ein, um den

Liquidus komplexer Fe-Ni-Si-S-Systeme präzise abzubilden, was die Effizienz erheblich verbesserte. Viertens entwickelten Keppler und Di Genova eine neue Apparatur zur Untersuchung der Magma-Fragmentierung bei bisher unerreichten Temperaturen und Drücken. Minchenkova und Audétat untersuchten die Vertrauenswürdigkeit von synthetischen Flüssigkeitseinschlüssen in verschiedenen Wirtsmineralien um Druckkorrekturen von Stempelzylinder-Pressen zu bestimmen. Außerdem entwickelten sie eine neue Methode um die Temperaturverteilung innerhalb von Probenkapseln bei solchen Experimenten zu quantifizieren.

Im Bereich der geodynamischen Modellierung und Darstellung der Erde waren Mitglieder des Instituts an der Entwicklung von GeophysicalModelGenerator.jl beteiligt, einem Open-Source-Softwarepaket, das die Integration und Visualisierung verschiedener geowissenschaftlicher Datensätze erleichtert. Dieses Programmierwerkzeug unterstützt die Erstellung von verschiedenen Eingabe-Geometrien für die numerische Modellierung, gewährleistet die Kompatibilität mit unterschiedlichen Datenformaten und fördert die interdisziplinäre Zusammenarbeit, so dass es sich potentiell zu einem Standard in diesem Bereich entwickeln kann.

3. Research Projects

3.1 Earth and Planetary Structure and Dynamics

In this first section, five contributions investigate Earth and planetary processes from surface to core in the Solar System and beyond. They investigate the origins of asteroidal crusts and the effects of planetary impacts on the thermal evolution of planetesimals. Using advanced tools like the James Webb Space Telescope, researchers also delve into the early stages of planetary development, while geophysical simulations reveal insights into tectonic processes such as deep earthquakes and subduction dynamics.

In the first contribution, Timoner and colleagues study the first two anorthite-rich asteroidal meteorites. Lunar anorthosites are generally believed to have formed through density segregation in a lunar magma ocean, where plagioclase floated to form the primordial crust. Instead, geochemical and Rb-Sr isotopic data of these meteorites suggest that these anorthosites likely originated from layered intrusions associated with diogenitic cumulates on Vesta. The findings provide new insights into planetary differentiation and crust formation processes on asteroids.

In the second contribution, Obengo and colleagues investigate three pieces of angrite using Electron Backscatter Diffraction (EBSD) and Raman spectroscopy to evaluate shock effects and their impact on interpreting chronological records. They find varying levels of shock deformation and metasomatism, suggesting a complex impact history and prolonged magmatic activity on the angrite parent body.

In the third contribution, Zippoli and colleagues employ the outcomes of several sub-catastrophic collision models, where a planetesimal loses most of its mantle, while its core remains mostly intact, as input for thermal evolution simulation of the iron-rich remaining bodies. They find that the cooling rates of such bodies are in good agreement with those determined for IIIAB iron meteorites.

In the fourth contribution, Golabek and colleagues use the advent of high-resolution observations by the new James Webb Space Telescope (JWST) to compare global-scale numerical models of the magma ocean evolution on tidally locked super-Mercury GJ 367 b to JWST observations of this exoplanet, thus shedding light onto the otherwise inaccessible magma ocean stage of young terrestrial planets.

In the final contribution, Weiler and colleagues study deep earthquakes in the Hindu Kush region that are linked to the subducted lower crust and slab detachment. For this purpose, they perform data-driven 2D numerical simulations and find that the subduction of the lower crust strongly influences the detachment depth of the slab.

a. *Petrogenesis of asteroidal anorthosites (C. Timoner, D. Zhu, R. Zhao, A. Bouvier and B. Zhang/Houston)*

Two anorthite-rich meteorites were recently found, Northwest Africa (NWA) 15118 and Wan Zawatin (WZ) 001, questioning the formation mechanism of anorthosites on asteroids (10s to 100s km diameter). Anorthosites are fractionated magmatic rocks that generally require gravity and density gradients to segregate and float within a mafic magma. Anorthosites form the primordial crust of the Moon and were theorised to have formed during the cooling of the lunar magma ocean after the giant impact event or possibly later. NWA 15118 and WZ 001 have triple oxygen isotopic compositions that are compatible with the Howardite-Eucrite-Diogenite (HED) meteorites. The HEDs are a group of mafic and ultramafic rocks probably related to 4-Vesta, a ~ 525 km diameter and second largest asteroid in the belt, which is interpreted to be a preserved protoplanet. In a previous study, NWA 15118 has been interpreted to sample a lost primordial anorthositic crust on 4-Vesta, as this lithology is absent from remote sensing observations. The processes fractionating anorthosite in asteroid-sized objects early on in the solar system are unknown. The geochemical and geochronological features of these meteorites can, therefore, help us to understand planetary differentiation and crust formation in protoplanets.

We studied NWA 15118 and WZ 001 for *in situ* major and trace element compositions by EPMA and laser ablation (LA) TQ-ICP-MS and Rb-Sr radiogenic records using an ESL 193 nm Excimer LA system coupled with a Thermo Neoma MC-ICP-MS/MS. We set up a new methodology for *in situ* measurements of $^{87}Rb/^{86}Sr$ and $^{87}Sr/^{86}Sr$ ratios in feldspars (see further details in the report by Zhang *et al.*, this volume). Data reduction was performed with iolite-4 using NIST610 and AMNH #107160 labradorite as standards.

With 90 and 85 vol. % of plagioclase, NWA 15118 and WZ 001 are classified as an anorthosite and a leuconorite, respectively. The mineral major element compositions for the two meteorites

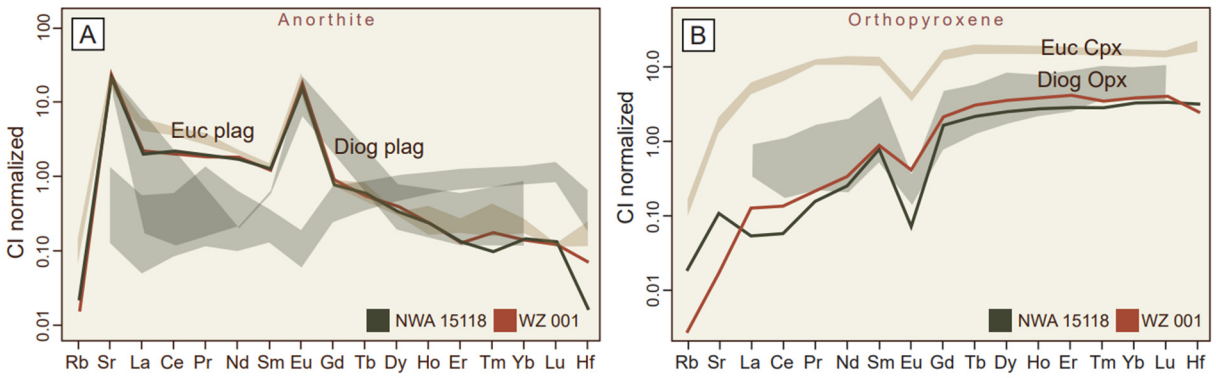

Fig. 3.1-1: Trace element patterns of anorthosites compared with eucrite and diogenite meteorites (A) Ca-rich plagioclase. (B) Orthopyroxene.

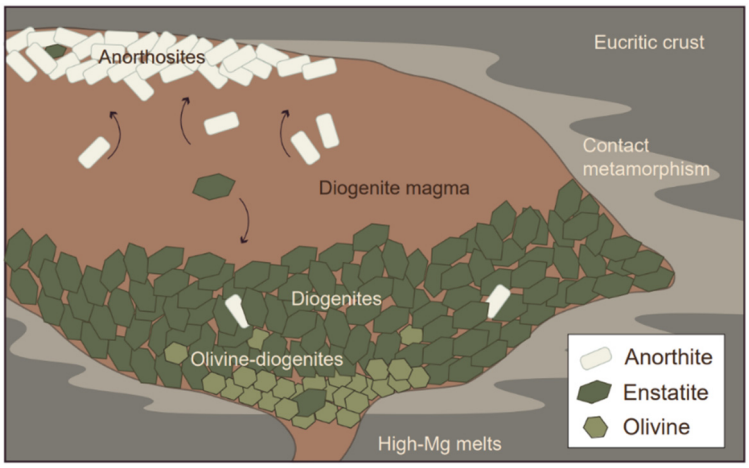

Fig. 3.1-2: Illustration of a post-eucritic diogenite intrusion with anorthosites fractionated at the top.

are identical, with $An_{95.5}$ and $En_{74.5}$ composition for plagioclase and orthopyroxene, respectively. No clinopyroxene is observed. The only accessory mineral found is low-Ti chromite. The high Mg#, chromite composition, and absence of clinopyroxene are characteristics of diogenites, suggesting a very close relationship compared to eucrites. Rb, Sr and REE (ppm) are nearly identical for both HED anorthosites. On average, the Eu/Eu* anomalies of anorthite and orthopyroxene are 17.6 and 0.18, respectively, while the $La/Yb_{(N)}$ values are 15.5 for anorthite and 0.02 for orthopyroxene (Fig. 3.1-1). The general depletion in REE in minerals again suggests a relation to diogenites. Extremely low Rb contents of 0.05 ppm in anorthite limit isotopic analyses. *In situ* Rb-Sr systematics of the anorthites and a shock vein of the two meteorites have a limited range of $^{87}Rb/^{86}SrF$ of 0.00 and 0.03. Nevertheless, the initial $^{87}Sr/^{86}Sr$ isotopic compositions of WZ 001 (0.69857±0.00048) and NWA 15118 (0.69887±0.00059) are both within an uncertainty of the value of the Basalt Achondrite Best Initial of the Solar System (0.69897) and lower than the $^{87}Sr/^{86}Sr_{(0)}$ of the Moon and Earth (0.69910). Sr model ages of NWA 15118 (0 to 32 Ma after CAIs) and WZ 001 (0 to 6 Ma after CAIs) suggest an early and syn- to post-eucritic origin after the strong devolatilisation of the HED parent body. We suggest that layered intrusions related to diogenitic cumulates best explain the petrogenesis of these anorthosites, where the negative Eu anomaly of unequilibrated diogenites could be explained by fractional crystallisation coeval to thin, anorthite-rich layers (Fig. 3.1-2).

b. *Shock effects and microstructural investigations in three angrite meteorites (E. Obengo, R. Zhao and A. Bouvier)*

Angrites are a relatively small group (including 53 individual specimens to date) of achondrites with mafic to ultramafic compositions. Besides D'Orbigny, all have been found in Antarctica and the Sahara desert over the last 20 years. The diverse lithologies of these meteorites broaden

our understanding of this group and the formation history of their parent body. These meteorites are some of the oldest igneous rocks formed in the solar system and offer valuable insights into early planetary evolution. The U-Pb-Pb crystallisation age of the D'Orbigny basaltic angrite has traditionally been used as an anchor for calculating model ages for short-lived radionuclide systems (*e.g.*, Al-Mg, Mn-Cr) measured in meteorites and evaluating the distribution of ^{26}Al (half-life ~ 0.7 Myr) within the protoplanetary disk. However, questions remain regarding the extent of magmatism and the impact history of the angrite parent body (APB).

Shock effects are structural and compositional changes in rocks that are induced by high-energy planetary impacts due to the propagation of shock waves. They provide valuable insights into the history of planetary collisions in the early solar system. Shock effects, brecciation, and mass-independent oxygen isotopic heterogeneities were recently reported in several angrites questioning the pristineness of the radiometric records of crystallisation and hence their interpretation.

In this study, we used Electron Backscatter Diffraction (EBSD) and Raman spectroscopy to investigate the microstructural characteristics of three angrites: NWA 8535, NWA 10463, and NWA 12004 (Fig. 3.1-3). We evaluate the magnitude of shock effects and their implications for the interpretation of the chronological records of these three individual meteorites and the formation history of the APB.

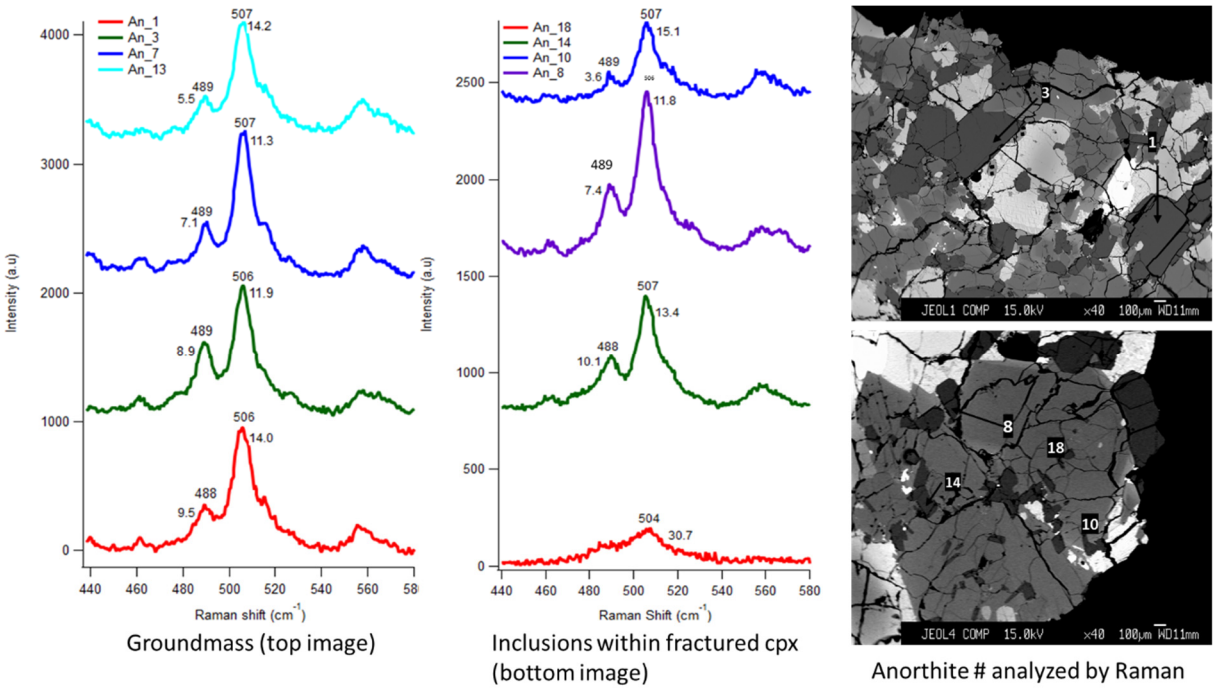

Fig. 3.1-3: Raman spectroscopy of individual anorthite grains in NWA 10463 found in the groundmass (left spectra, and top right image for location) and as inclusions within a fractured clinopyroxene (cpx) showing heterogeneous peak broadening at 488 and 507 cm^{-1} positions.

Our findings showed that (1) NWA 8535 had undergone negligible shock deformation, supporting prolonged magmatism until at least 4512 ± 18 Ma, driven by tectonic stresses and metasomatic activity in a shielded environment; (2) NWA 10463 displayed extensive shock effects, including shock deformation and brecciation, indicating a complex impact history and material redistribution through impact-induced endogenous mixing; and (3) NWA 12004 showed evidence of both shock deformation and impact-induced metasomatism. We identify that metasomatism, driven by fluid migration, played a significant role in mineralogical alterations after planetary impact.

Our findings and chronological records obtained for these meteorites support the hypothesis that the APB was large, potentially exceeding 300 km in radius, and capable of sustaining long-lasting magmatic and impact-driven processes. The use of EBSD and Raman spectroscopy provided key insights into the APB's evolutionary history, emphasising the role of both internal heat and external impacts in influencing its thermal evolution.

c. *Post-impact thermal evolution of iron-rich planetesimals (M. Zippoli, S. Raducan/Bern, M. Jutzi/Bern and G.J. Golabek)*

Metal-rich asteroids are widely believed to be the exposed cores of differentiated planetesimals, although the process that leads to their formation is still not well understood. One of the leading hypotheses that explains an asteroid's rich metal composition supposes that most of the primitive crust and mantle of the differentiated progenitor body was stripped off by hit-and-run collisions, leaving behind a bare core. However, these collisions are not able to strip off the entirety of the mantle without disrupting the metallic core. Sub-catastrophic impacts might be the missing link between the products of hit-and-run collisions and the metal-rich asteroids we observe today.

In this study, we use 1-D numerical simulations to explore sub-catastrophic collision scenarios by first investigating the post-impact thermal evolution of iron-rich planetesimals and ultimately assessing whether they meet the cooling regimes for the iron meteorite groups IIAB, IIIAB, and IVA, the most complete in terms of data availability. Metallographic cooling rates, determined from the Widmanstätten pattern of iron meteorites and Pd-Ag data, constrained start time and cooling rates.

We conducted 108 simulations in total, 36 for each of the IIAB, IIIAB, and IVA groups. For any of these categories, we applied 3 different 1-D input post-collision profiles based on different impact scenarios and considered model start times after CAIs in agreement with uncertainties. We also varied the number of nodal points over the profiles and space temperature to include cases with lower or higher resolution and colder or warmer external conditions, respectively. By conducting this parameter space survey, we constrained the thermal evolution of iron-rich planetesimals, and we were able to determine the fraction of the body's interior in line with both criteria.

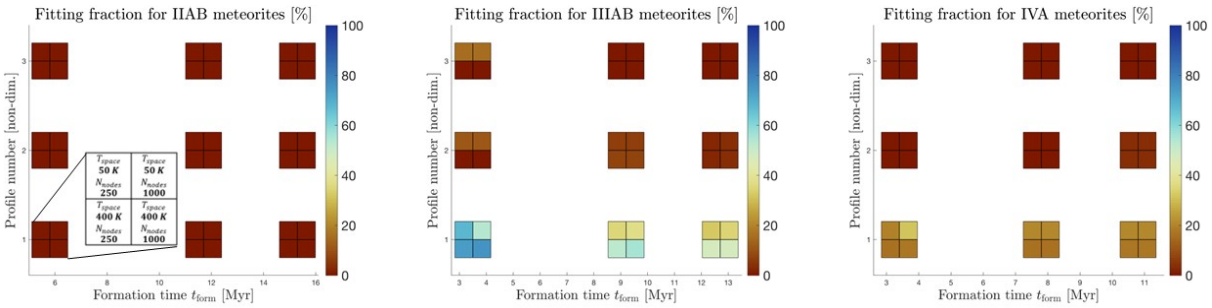

Fig. 3.1-4: Fitting fractions in percentages of grid points matching both metallographic cooling rates and cooling rates constrained by Pd-Ag data. Data shown for IIAB, IIIAB, and IVA irons. Each box contains 4 different simulations with parameter variations, as shown in the inset on the first figure.

Our results (Fig. 3.1-4) show that the profile featuring a mostly exposed iron core gives the best results. Moreover, the most suitable models are those for which an earlier start time after CAIs is applied. The combination of the two parameters gives the highest fitting fraction percentages. We obtained the best results for IIIAB meteorites, while IIAB and IVA irons have scarce if not null matching. This means that sub-catastrophic impact scenarios better resemble the cooling regime of the IIIAB parent body. The grid resolution did not affect our results. Future work will focus on testing the most promising results using 2D models.

d. *Magma oceanography of the dense, ultrashort-period sub-Earth GJ 367 b (G.J. Golabek, T. Lichtenberg/Groningen, L.M. Bartels/Groningen, T. Meier/Oxford, P.J. Tackley/Zurich and D. Bower/Zurich)*

The dawn of high-resolution observations with the James Webb Space Telescope (JWST) will enable spatially resolved observations of ultrashort-period rocky exoplanets. Some of these planets orbit so closely to their star that they lack an atmosphere, which gives direct access to their surfaces and opens a window to infer their geodynamics. The physical parameters of the ultrashort-period sub-Earth GJ 367 b have been observationally constrained to a planetary radius of about 0.72 to 0.75 Earth-radii and a mass between 0.48 and 0.55 Earth-masses, implying a density of 6200 to 8500 kg/m^3, which puts this planet in a Mercury-like interior regime with a thin mantle overlying a fractionally large core.

The dayside temperature ranges between 1500 to 1800 K, thus suggesting the presence of a permanent magma ocean or dayside magma pond on the surface, induced by stellar irradiation. The large uncertainty on the age of the stellar system, between 30 Myr and about 8 Gyr, however, introduces severe uncertainties related to the compositional and thermal evolution of the planetary mantle. We perform global 2D spherical annulus StagYY simulations of solid-state mantle convection and surface melting with the goal to constrain the geometric and compositional properties of the planet. The combination of JWST observations and numerical models offers a unique opportunity to constrain the compositional fractionation during magma

ocean epochs and provides avenues to constrain the delivery and loss cycle of atmophile elements on strongly irradiated exoplanets.

e. *Data-driven modelling: What affects the Hindu Kush's subduction and its earthquakes? (T. Weiler, A. Piccolo, A. Spang and M. Thielmann)*

The Hindu Kush region in the Western Himalayas is characterised by anomalously high seismic activity, which makes it one of the seismically most active regions worldwide. What makes this region even more interesting is the fact that a significant amount of the observed seismicity is not located at shallow depths but rather at depths exceeding 50 km, with large earthquakes (M>7) regularly occurring at depths of 200 km (Fig 3.1-5). These earthquakes cannot be explained by the same causes of surface near earthquakes. Instead, they are often linked to the subducted lower crust and slab detachment. To identify the mechanisms governing these events, the Hindu Kush thus represents an ideal natural laboratory.

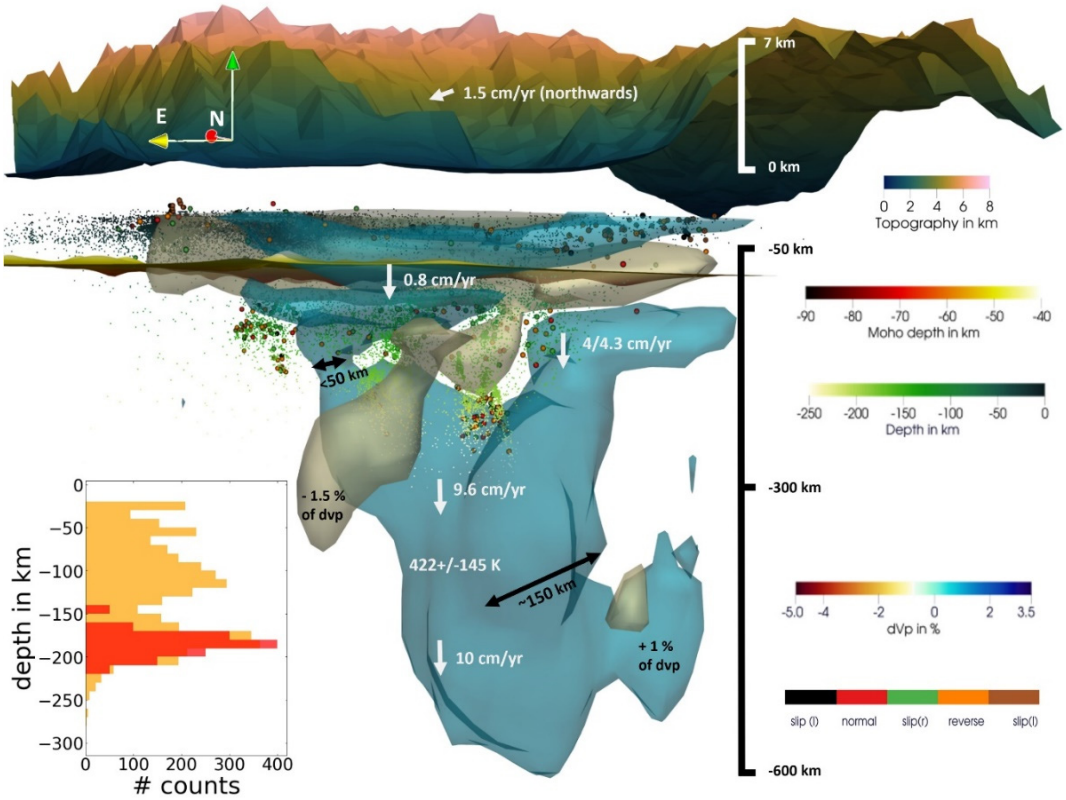

Fig. 3.1-5: Data collection for the Hindu Kush containing topography, Moho, earthquakes and tomography. The topography is 50 times exaggerated. The near horizontal layer shows Moho depth variations. Blue and white contours represent positive and negative velocity anomalies of the lithospheric mantle and the lower crust. Small dots show the earthquake hypocenters. Green, red, orange, brown, and black symbols: Faulting mechanism of the larger earthquakes. White arrows: Sinking velocity, black arrows: slab thickness. Left corner histogram: (yellow) earthquake depth distribution with earthquake gap, (red) modelled detachment depth results.

To constrain the conditions at which these large deep earthquakes occur, data-driven numerical models of the Hindu Kush are required to better understand its tectonic environment. Using these models, it becomes possible to quantify the effect of the different proposed rupture mechanisms.

Data-driven models require the collection and joint interpretation of available observational data. To obtain a data-based model of the Hindu-Kush, we first compiled a database of available open-source datasets. These datasets include data from the topography, Moho depth, earthquake locations and seismic tomographies. To merge these different datasets into one single joint dataset, we used the GeophysicalModelGenerator toolbox.

Based on these tectonic settings, 2D models with a non-linear visco-elasto-plastic rheology were set up to determine the deformation state and the controlling mechanism of the detachment process. This includes the effect of the subducted lower crust and the rheology properties of the eclogitised lower crust and lithospheric mantle. The viscosity ratio of the layers is the main factor which influences the subduction process. Since the lower crust is eclogitised, it is unclear which viscosity the lower crust has. Therefore, we varied the viscosity ratio between 0.1 and 10. Depending on the coupling between the layers, the lower crust can be subducted, and the detachment depth depends on the material properties of the subducted plate. Thus, it is likely that the subduction of the lower crust strongly influences the detachment depth.

the first results show that greater initial depths of the lower crust (d_{lc}) lead to lower detachment-depth to initial-depth ratios (d_{det}/d_{lc}) and shorter detachment times (t_{det}) ((Fig. 3.1-6). The break-off time increases linearly for the shallower lower crust (Fig. 3.1-6b). This trend becomes weaker for higher viscosity ratios (η_{lith}/η_{lc}). Low viscosity ratios exhibit an expanding depth ratio, while viscosity ratios higher than 2.8 exhibit an unclear depth ratio (Fig. 3.1-6a). This indicates a change in the deformation. The timing and detachment depth of the models are in line with observations of the formation of the Hindu Kush subduction and its deeper earthquake domain (Fig. 3.1-5), indicating an influence on the earthquake nest depth distribution.

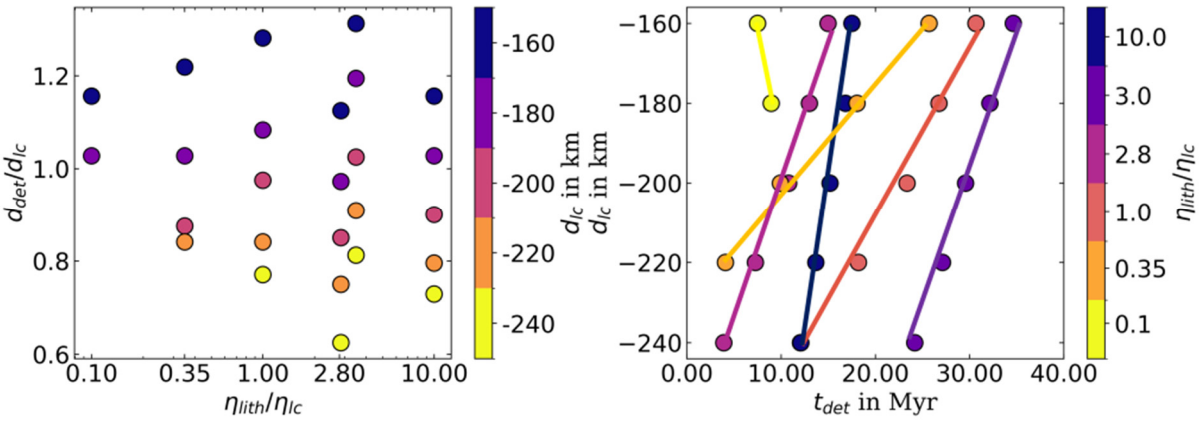

Fig. 3.1-6: Left: Relation of viscosity ratio of the lithosphere (η_{lith}) and lower crust (η_{lc}) to the ratio of the detachment depth (d_{det}) to initial setup depth (d_{lc}). Colours show the initial setup depth. Right: Detachment time (t_{det}) to the initial depth and viscosity ratio.

3.2 Geochemistry

An important question in geochemistry is how the Earth's inventory of volatile elements was established. The Earth, similar to almost all rocky bodies in the solar system, is depleted in volatile elements in comparison to the concentrations in the primordial solar nebula. This can be easily explained because volatile elements partition into the gas phase during high-temperature condensation or evaporation processes and, therefore, become depleted in the rocky bodies from which the Earth formed. However, as described in the first project in this section, the moderately volatile element fluorine appears to be over abundant in the Earth's crust, mantle and surface reservoirs, in comparison to chlorine, whereas both elements have very similar volatilities. Furthermore, existing experimental studies, performed only at relatively low pressures, have indicated that neither element should have partitioned significantly into the Earth's core. In this first project, however, computer simulations are used to show that chlorine may start to partition into liquid iron and hence could have been lost to the core, if pressures of metal silicate equilibration were over 80 GPa, whereas fluorine is found to remain in the silicate mantle at these pressures. This indicates that the fractionation of fluorine from chlorine in the Earth could be a signature of very high-pressure core mantle-equilibration in a magma ocean deeper than 1000 km.

The next three contributions deal with the behaviour of sulphur and chalcophile elements during the accretion and core-mantle differentiation of the Earth. In the first study, *Blanchard et al.* determined, by means of laser-heated diamond anvil cell experiments, the solubility of sulphur in a bulk silicate Earth magma composition at P-T conditions relevant for a deep magma ocean. The aim of these experiments is to test the feasibility of the "Hadean matte" hypothesis. This proposes that towards the end of Earth's accretion, the crystallising magma ocean reached saturation in iron sulphide, which separated as a liquid and segregated to the core. In doing so, it may have stripped the magma ocean of so-called highly siderophile elements, *i.e.*, elements, such as platinum and gold, that partition strongly into core-forming liquids. The results suggest that sulphide saturation may not have been reached in the deep magma ocean, casting some doubt on the validity of the Hadean matte hypothesis. A similar question is being addressed in the following study in which laser-heated diamond anvil cell experiments have been performed to determine the effect of sulphur on metal–silicate melt trace element partition coefficients. Elements such as cadmium are considered to have been extracted from the mantle by core-forming sulphur-rich Hadean matte melts. However, preliminary results show that while cadmium is influenced by the sulphur content of the melt at low pressures, this effect appears to disappear at higher pressures. In the next project *Liu and Li* performed piston-cylinder experiments to determine sulphide-silicate melt partition coefficients of Se and Te. These elements along with S are assumed to be in near-chondritic relative abundances in the mantle, indicating that they were added to the Earth in the so-called late veneer stage of accretion, where no subsequent core formation occurred. However, the mantle rocks analysed to make this assessment have undergone melting and metasomatic events, raising the question of whether these analyses reflect the true pristine mantle values. Using the obtained partition coefficients,

it is possible to assess the concentration levels in the mantle more reliably based on their values in mantle-derived magmas. The results show that the mantle abundances of these elements are not in chondritic relative proportions, indicating that they may not simply have been added in the late veneer.

The following study by *Pausch et al.* is an examination of the stability of the host phase for phosphorous in the deep mantle. In the shallow mantle, phosphorous is hosted by the calcium phosphate mineral apatite, which is also a host for many incompatible trace elements such as rare earths, uranium and thorium. It has been shown, however, that apatite transforms to a higher-pressure mineral called tuite towards the base of the upper mantle. Although apatite has a limited thermal stability field that prevents it from being stable at typical mantle temperatures, tuite is shown to be stable in the lower mantle at temperatures even above those of the average mantle. Interestingly, however, at lower mantle conditions, tuite loses its role as a host for trace elements, which instead partition into the calcium silicate perovskite mineral davemaoite.

The next two contributions address experiments performed to understand how ferric iron (Fe^{3+}) partitions during mantle melting. This is not only important for determining source concentrations of ferric iron from the analyses of magmas but also for understanding how the redox state of the Earth was initially established after the crystallisation of a primordial magma ocean. In the first of these studies, partial melting experiments are performed at conditions of the Earth's transition zone (410-660 km depth) using different buffering assemblages that influence the availability of oxygen to produce ferric iron from the normally more dominant ferrous iron (Fe^{2+}). An intriguing result is that as the ferric iron content increases, the phase assemblages approach those of the liquidus *i.e.*, where only a single mineral remains with the melt. While this might imply that ferric iron is depressing the melting temperature, it could also be an indication that more water is present under these more oxidising conditions. The second project of this type is performed at lower pressures and at the conditions where mid-ocean ridge basalts are produced in the mantle. One of the main aims in this study is to produce silicate glass samples that can be analysed for their ferric and ferrous iron contents using a range of different techniques. Such comparisons are vital, because currently there are differences reported in the literature for magma ferric iron contents that may simply be explained by the use of different techniques.

The next two projects are closely related and aimed at understanding Earth's deep melting processes and the ensuing melt-rock reactions that occurred as these melts ascended through the lithospheric mantle towards the surface. In the first of these, melting experiments are being performed to understand the origin of komatiites, which are magnesium-rich magmas that appear to be the products of very high degrees of partial melting. They are, therefore, products of a melting column that extended very deep into the mantle. The second study is aimed at addressing a perplexing characteristic of the deep subcratonic lithospheric mantle, which in many regions appears to be richer in silica than other mantle rocks. This is manifested in a higher proportion of orthopyroxene as compared to olivine. In this study, the hypothesis is

tested that this arises from melt-rock interaction as komatiite magmas pass through the lithospheric mantle. Preliminary experiments to reproduce this reaction, in fact, show the opposite effect, as the reaction induces olivine to form from the melt. However, this may have made the komatiite magmas more silica-rich, thus increasing their ability to cause silica enrichment at shallower depths.

The next five contributions are all related to the formation of magmatic-hydrothermal ore deposits. *Hlede et al.* investigated the behaviour of Cu, Mo, Zn, and W during the subduction of sediments. For this purpose, they conducted piston-cylinder diamond-trap experiments, in which varyingly NaCl-rich fluids were equilibrated with the global average of subducted sediments (GLOSS) at subsolidus conditions. From LA-ICP-MS analyses of the fluid in the diamond trap and corresponding analyses of minerals in the adjacent rock, fluid–mineral partition coefficients were calculated. It turns out that Mo has a relatively high bulk rock / fluid partition coefficient at all fluid salinities, whereas for Cu and Zn high bulk rock / fluid partition coefficients can be obtained only at high fluid salinities. It is concluded that the ultimate source of Mo in porphyry-type ore deposits may be subducted black shales, as they contain several orders of magnitude more Mo than common mantle rocks. The study of *Keppler and Audétat* focuses on whether the typical association of Sn deposits with reduced magmas could be a consequence of more efficient metal extraction by fluids at reduced conditions. For this purpose, cold-seal pressure vessel experiments were conducted to explore the effect of fO_2 on the fluid-melt partitioning of Sn. Due to severe alloying of Sn with commonly used noble-metals, fluid-melt partition coefficients were determined by means of LA-ICP-MS analysis of locally equilibrated fluid inclusions in the quenched silicate melt. The results suggest that $D_{Sn}^{fluid/melt}$ increases with increasing fO_2 until about the Ni-NiO buffer, above which point $D_{Sn}^{fluid/melt}$ decreases again. However, $D_{Sn}^{fluid/melt}$ is generally too low to result in Sn depletion in the silicate melt during fluid-saturated magma crystallisation. The latter observation suggests that Sn deposits do not form because of conditions that allow particularly efficient metal extraction by the fluids, but rather due to particularly efficient enrichment of Sn in the residual silicate melt during magmatic differentiation.

The aim of the study of *Qiao and Audétat* is to find out what rendered porphyry Cu-forming magmas so fertile. Based on the geochemistry of natural rocks it looks like these magmas fractionated at high pressure, but it is not clear whether this resulted in higher metal contents or higher abundances of S, Cl or H_2O in the residual melts. To answer this question, natural arc basalts doped with geologically realistic amounts of metals and volatiles are first melted and then slowly cooled in piston-cylinder experiments conducted at various confining pressures. So far, only the 10 kbar series has been completed, showing a continuous increase of H_2O in the residual melt during magma differentiation, whereas Cl and S first increase and then decrease due to fluid exsolution and the formation of sulphur-rich accessory phases, respectively. Porphyry copper deposits are also the subject of the following two contributions. By conducting detailed geochemical and petrological studies on 13 mineralised magma systems in the Sanjiang region in SW China, *Chang et al.* found that the ore-forming magmas accumulated and

crystallised at depths of 10-20 km before they finally ascended to 3-6 km depth, where the ore deposits formed. Based on the composition of melt inclusions and mass balance calculations it can be demonstrated that most of the ore-forming fluids exsolved at depths of 10-20 km. This means that the mineralising fluids travelled on average ~ 10 km from the site of fluid exsolution to the site of ore precipitation. This distance is considerably longer than expected, and an explanation is offered as to how such large volumes of fluid could have passed through porphyry intrusions, without leaving much trace. A similar study was conducted by *Audétat et al.* on the Central Mining District in New Mexico, USA. There, the last magma crystallisation depth, determined using 13 porphyry intrusions, is 10-17 km, which, together with an ore formation depth of 4-5 km, results in an average distance travelled by the mineralising fluids of ~ 9 km. The data demonstrate that a large, upper crustal pluton exists beneath the Central Mining District, which supports the classical model of porphyry copper formation. At the same time, high Sr/Y-ratios in the bulk rocks indicate magma fractionation at mid- to lower crustal levels. Consequently, a two-stage evolution model is proposed, which involves a first stage of magma fractionation at deep crustal levels, followed by a second stage of magma crystallisation at upper crustal levels, without much crystal-liquid separation, before some of the magmas finally ascended to the current exposure level, where they were quenched as porphyries.

The final study in this section uses radiogenic isotopes to trace the sources of rocks that were eroded and then deposited by glaciers that scoured North America during the last ice age. Successive ice age periods slowly erode the evidence of the earlier phases of glaciation, making it hard to reconstruct the previous landscape and the directions that glaciers travelled. Tills, which are sediments deposited by glaciers as they melt, can provide evidence of the rocks that were being eroded during past glacial events. In this study, radiogenic isotopes are used as a fingerprint to trace the providence of the different rocks that were being eroded at different time periods during the last ice age. One intriguing result of this analysis is that the ancient basement rocks of the Canadian shield may have only become exposed at the surface due to the action of glaciers approximately one million years ago.

a. *Earth's "missing" chlorine may be in the core (L. Yuan and G. Steinle-Neumann)*

Halogens, such as chlorine (Cl) and fluorine (F), play a critical role in various reservoirs of the Earth, including degrading stratospheric ozone, regulating ocean salinity and transporting ore-forming metals in geological fluids. Despite their importance, the proportions of halogens in the planet are poorly characterised due to uncertainty in the composition of the solid Earth. The abundance and distribution of halogens in the solid Earth are influenced by various processes, including the delivery, retention, and loss of volatiles during Earth's formation. In general, Earth's mantle displays a depletion pattern of volatile elements that aligns with their condensation temperatures. Consistent with low condensation temperatures, halogens are generally depleted in the mantle. However, in detail, although the abundance of F is consistent with the volatility trend, the abundances of heavier halogens such as Cl are significantly lower,

albeit with significant uncertainty and some controversy. Despite similar uncertainties in halogen abundances in the solar system, the relative concentration between F and Cl (F/Cl elemental ratio) in the silicate Earth remains greater than for primitive chondrites. This is commonly referred to as the "missing Cl problem". The superchondritic F/Cl ratio in the bulk silicate Earth raises questions about the behaviour of halogens during Earth's formation and possible processes that could have caused the preferential loss of Cl compared to F. Evaporation, for example, is an unlikely explanation, as it should have affected F and Cl in a similar way. This leaves preferential Cl sequestration into the core at high pressure (P) and temperature (T) as a possible explanation. However, experiments on partitioning between silicate and metallic liquid present a somewhat incomplete and contradictory picture.

We have investigated the partitioning behaviour of F and Cl between $MgSiO_3$ and Fe liquids using molecular dynamics simulations based on density functional theory (DFT). We calculate the Gibbs energy, G, of Cl and F incorporation into silicate and iron liquid at four P–T conditions along a model magma ocean adiabat, (10-130 GPa and 3000-5000 K), by considering the reaction $Mg_{15}Si_{15}O_{45}{\cdot}X + Fe_{75} \leftrightarrow Mg_{15}Si_{15}O_{45} + Fe_{75}{\cdot}X$, where X is the halogen under investigation. Based on the G of the components, we derive chemical potentials and equilibrium partition coefficients. Our calculations show that the Gibbs energy of the reaction, $\Delta_r G$, for Cl exchange is positive at low P–T, indicating lithophile behaviour. With increasing P–T, $\Delta_r G$ approaches zero and eventually becomes negative, indicating siderophile behaviour. By contrast, F exchange yields large positive $\Delta_r G$ values for all P–T conditions considered, indicating a strong lithophile character. From the chemical potentials, the halogen metal–silicate partition coefficients $D^{m/s}_{Cl/F}$ can be calculated. As shown in Figure 3.2-1, $\log_{10} D^{m/s}_{Cl}$ increases from approximately -2 at low P–T to approximately +2 at high P–T; for fluorine, there is no significant variation in $D^{m/s}_{F}$ with P–T, with $\log_{10} D^{m/s}_{F}$ in the rage -4 to -3. The partitioning of Cl between metal and silicate phases has been investigated by high P–T experiments, with strongly variable results (Fig. 3.2-1). Our predicted $D^{m/s}_{Cl}$ at 10 GPa and 3000 K falls within the range of existing experimental data (Fig. 3.2-1, inset). To the best of our knowledge, there have been no studies that explicitly determine the metal–silicate partition coefficients for fluorine. However, two crucial observations in experiments are consistent with our results: (1) negligible amounts of F partition into metal melt that coexists with silicate melt, *i.e.*, F is below the detection limit of an electron probe analysis; (2) there is a discernible trend that with increasing atomic radius, halogens exhibit higher compatibility with metal, indicating $D^{m/s}_{F} < D^{m/s}_{Cl}$.

The partition coefficients we have predicted offer insights solely into the relative concentrations of Cl and F in metals and silicates as they achieve equilibrium. To estimate the absolute amount of Cl and F in the core, and consequently in the bulk Earth, we need to know halogen concentrations in the magma ocean with which the core was equilibrated. Previous studies have estimated the Cl (F) budgets of the silicate Earth indirectly, using reference elements in the MORB or OIB mantle source and elemental ratios that undergo minimal fractionation during melting. Depending on the scaling approach, the estimated halogen budgets fall in the range from 17-30 µg/g for Cl and 25 µg/g for F on the conservative side, to 81 µg/g for Cl and 57 µg/g

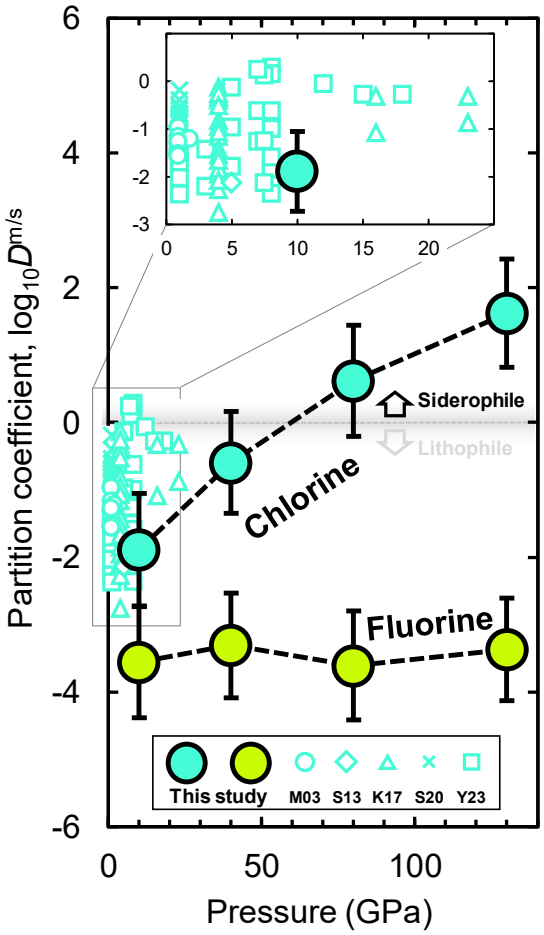

Fig 3.2-1: Metal–silicate partition coefficients $D_{Cl}^{m/s}$ and $D_{F}^{m/s}$ for Cl and F (on a log scale) as a function of pressure determined by equating the chemical potential in each phase. Inset: Zoomed low-pressure region showing our predicted $D_{Cl}^{m/s}$ in comparison with available experimental Cl partitioning data between metal (or S-bearing metal) and silicate: Mungall & Brenan (2003, Canadian Mineralogist, 41, 207-220) (M03: circles), Sharp & Draper (2013, Earth Planet Sci Lett, 369-370, 71-77) (S13: diamond), Steenstra *et al.* (2020, Geochim Cosmochim Acta, 273, 275-290) (S20: circles), Yang *et al.* (2023, Geochim Cosmochim Acta, 355, 62-74) (Y23: squares). To the best of our knowledge, there have been no studies that explicitly document the metal–silicate partition coefficients for F.

for F. To estimate the Cl (F) budgets of Earth's core to first order, we consider a single-stage core formation model with equilibrium conditions of 50 GPa and 4000 K. With $D_{Cl}^{m/s} \sim 0.5$ from our DFT predictions, equilibration between metal and silicate results in a Cl concentration of 9–44 µg/g (equivalent to 1.77-8.42 · 10^{19} kg) in the core (about 20 % of Earth's total Cl). For fluorine, our calculations indicate an F budget of 0.01-0.02 µg/g (1.59-3.62 · 10^{16} kg), < 0.1 % of Earth's total F content. Using multistage core formation models in multiple iterations aimed at matching the composition of the silicate Earth, we find about 40 % of Earth's total Cl content in the core, larger concentrations than from the single-stage model. The resulting F content of the core is comparable to the single-stage model.

b. *Sulphur solubility in a deep terrestrial magma ocean (I. Blanchard/Paris, E. Kubik and A. Minchenkova, in collaboration with L.M. Calvo and J. Siebert/Paris)*

Sulphur plays an important role in tracing Earth's formation processes due to its cosmochemical abundance and its siderophile and volatile properties. Understanding its partitioning behaviour during Earth's differentiation can help to solve the compositions of both the core and the primordial atmosphere. The mantle's budget of highly siderophile elements (HSE) is proposed to stem from HSE segregation into a sulphide matte, exsolved from the magma ocean towards the end of accretion. The corollary is that the magma ocean must have reached S saturation, enabling the segregation of a sulphide matte. The sulphur concentration at sulphide saturation (SCSS) in molten silicate has been the subject of numerous studies, focusing mainly on the effects of the silicate composition on SCSS. Recently, the effects of pressure (P) and temperature (T) have been studied, but either at limited P, T conditions or using basalt as the starting composition, which might not be relevant in the context of the Earth's formation.

We synthetised five samples using a laser heated diamond anvil cell (LH-DAC) at IPGP, Paris between 53 and 72 GPa and 3800 to 4050 K, replicating the high P, T conditions of the Earth's differentiation. The starting materials consisted of either a pyrolitic or a basaltic glass, both synthetised by aerodynamic levitation and subsequently polished and laser-cut into disks. Two disks were loaded in each experiment, with pure FeS interposed between them. The samples were recovered using a focused ion beam. Elemental measurements of the run products show that significant amounts of S can be stored in the deep magma ocean (~ 1 wt. %). We compiled our results with more than 200 data from existing literature to develop a thermodynamic parameterisation predicting the SCSS depending on pressure, temperature and silicate composition. This parameterisation was used in accretion and core formation models to

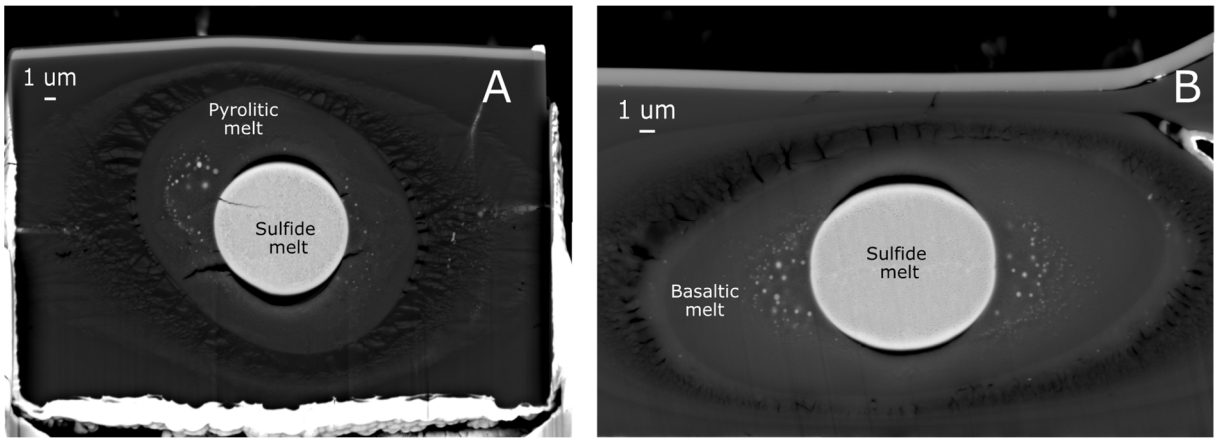

Fig. 3.2-2: Backscattered electron images of two typical recovered runs. A) Sample SCSS5 synthesised using pyrolitic glass as the starting material, and B) sample SCSS4 synthesised using basaltic glass as the starting material. Both runs were equilibrated at 53 GPa and 3800 K.

compare the SCSS with the predicted S abundance in the mantle from metal-silicate partitioning data in the case of the Earth. We show that the SCSS always exceeds the predicted S abundance present in the mantle as S partitions between mantle and core. We conclude that Earth's magma ocean likely never reached S saturation, thereby preventing the segregation of a sulphide-rich melt, also referred to as the "Hadean matte".

c. *Chalcophile element distribution during core formation: Testing the feasibility of a sulphide Hadean Matte (A. Minchenkova, E. Kubik, O.T. Lord/Bristol, E.M. Rogmann/Bristol and I. Blanchard/Paris)*

The Earth's unique features as a terrestrial planet—including dynamic geology, plate tectonics, and volatile-driven processes that support life—reflect a complex evolution shaped by its early formation processes. The element distribution within Earth's interior, notably the selective depletion of siderophile and chalcophile elements in the mantle, points to early accretion and differentiation events, especially through metal-silicate equilibration in a deep magma ocean. Sulphur, with its chalcophile nature, likely played a critical role by sequestering other elements into the core. This study investigates whether sulphur was incorporated into the core as a sulphur-bearing iron-rich liquid or as a separate sulphide liquid often referred to as the "Hadean sulphide matte". By examining the behaviour of key chalcophile elements such as Ag, Cd, Cr, and Mn under core-forming conditions, this research aims to clarify how the presence of sulphur affected the elemental composition of Earth's core and mantle, enhancing our understanding of early Earth processes and volatile element distribution.

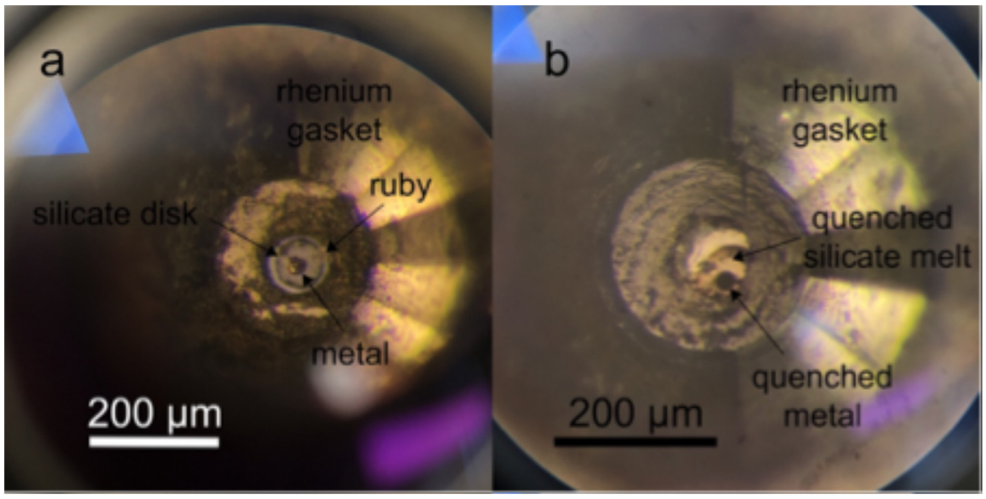

Fig. 3.2-3: Photomicrographs of a diamond anvil cell before and after laser heating. a) View of the starting materials before heating, loaded into a pre-indented and laser-drilled rhenium gasket. The experimental chamber is loaded with two silicate disks (one on each diamond), a small chunk of metal alloy and a ruby. b) View of the same diamond anvil cell after heating. The boundary between the hot spot and non-melted silicate is visible, as well as the spherical, quenched metal alloy.

Six high-temperature diamond anvil cell experiments were performed at the BGI and at the School of Earth Sciences, University of Bristol to simulate conditions at the base of a deep magma ocean. We loaded cells with pyrolitic silicate discs sandwiching a metal alloy (Fig. 3.2-3). We used three different metal alloys, composed of Fe, stoichiometric FeS or S-bearing Fe, each doped with chalcophile elements to examine their element distribution under core-forming pressures (50-60 GPa) and temperatures above the pyrolitic liquidus (*ca.* 3500-4000 K). Two 100 W Yb-doped fibre lasers were used to generate these extreme temperatures and to achieve super-liquidus conditions, followed by rapid cooling to quench the samples. Pressure was determined both before and after heating by measuring the shift of the R1 ruby fluorescence peak.

Preliminary and literature data suggest that Cd in the mantle likely exists in a 2+ valence state, supported by experimental data across a range of oxygen fugacity f(O_2) from ΔIW -3.5 to -1. Existing low-pressure literature data and preliminary diamond anvil cell measurements suggest that the partitioning of Cd is largely unaffected by variations in pressure or temperature, despite occasional temperature effects noted in other studies. The presence of sulphur, however, appears to enhance the siderophile nature of Cd, but only at pressures below 19 GPa. Above, we observed that Cd distribution in metal–silicate equilibria experiments remains similar regardless of sulphur concentration, implying that large sulphur additions to core-forming metal likely do not significantly impact Cd partitioning. Nevertheless, ongoing FIB work and EPMA analysis will reveal new data for Ag, Cd, Cr and Mn partitioning at core-forming conditions on Earth, and yield valuable insight into the scenarios capable of explaining the chalcophile signatures measured in the Earth's mantle.

d. *The partitioning of selenium and tellurium between sulphide liquid and silicate melt, and their abundances in the silicate Earth (Z. Liu and Y. Li)*

Near-chondritic relative abundances of sulphur (S), selenium (Se), and tellurium (Te) observed in mantle peridotites have been used to support the hypothesis of a carbonaceous chondrite-like late veneer added to the proto-Earth. However, the extent to which the observed S, Se, and Te compositions represent the signature of the silicate Earth remains a topic of debate. Some researchers argued that the variations in Se and Te found in mantle peridotites cannot be attributed solely to the melting process but rather reflect metasomatic overprinting by Se- and Te-rich sulphides and associated platinum-group minerals. If this is correct, then the near-chondritic S/Se and S/Te ratios observed in mantle peridotites would not represent a primitive signature of Earth's mantle. However, other authors argued that the correlations between Se, Te, and Al_2O_3 in mantle peridotites provide a reliable basis for estimating Se and Te abundances in the silicate Earth, irrespective of melting depletion or refertilisation. Mantle-derived melts, such as mid-ocean ridge basalts (MORBs), sourced from the depleted upper mantle, may help to clarify this debate by offering additional constraints on Se and Te abundances in the silicate Earth – provided the behaviour of Se and Te during MORB genesis and differentiation is well understood. Since Se and Te have a strong affinity for sulphides, and sulphide liquids are present during both MORB genesis and differentiation, the Se and Te concentrations and ratios

in MORBs are largely governed by sulphide liquid–silicate melt partitioning. However, accurate sulphide liquid–silicate melt partition coefficients of Se and Te ($D_{Se,Te}^{Sul/Sil}$) are currently limited.

We conducted laboratory experiments at 1 GPa, 1200-1600 °C, and oxygen fugacities (fO_2) of ~ FMQ-1.6 to FMQ+1.5 (FMQ refers to the fayalite–magnetite–quartz buffer) to examine the effect of temperature, fO_2, and sulphide and silicate melt composition on $D_{Se,Te}^{Sul/Sil}$. The results indicate that $D_{Se}^{Sul/Sil}$ range between 180-2200 and $D_{Te}^{Sul/Sil}$ between 1000-25400. Temperature has no clear effect on $D_{Se,Te}^{Sul/Sil}$ (Figs. 3.2-4 A and B). $D_{Se,Te}^{Sul/Sil}$ exhibits an inverted U-shaped dependence on the FeO_{tot} content of the silicate melt (Figs. 3.2-4 C and D). This inverted U-shaped dependence aligns with the U-shaped FeO_{tot}-dependence of the S or Se content in silicate melt at sulphide or selenide saturation. In addition, our $D_{Se,Te}^{Sul/Sil}$ values show no dependence on the Ni content of sulphide liquid or on experimental fO_2. The $D_{Se}^{Sul/Sil}$ / $D_{Te}^{Sul/Sil}$ ratio is always less than 0.4.

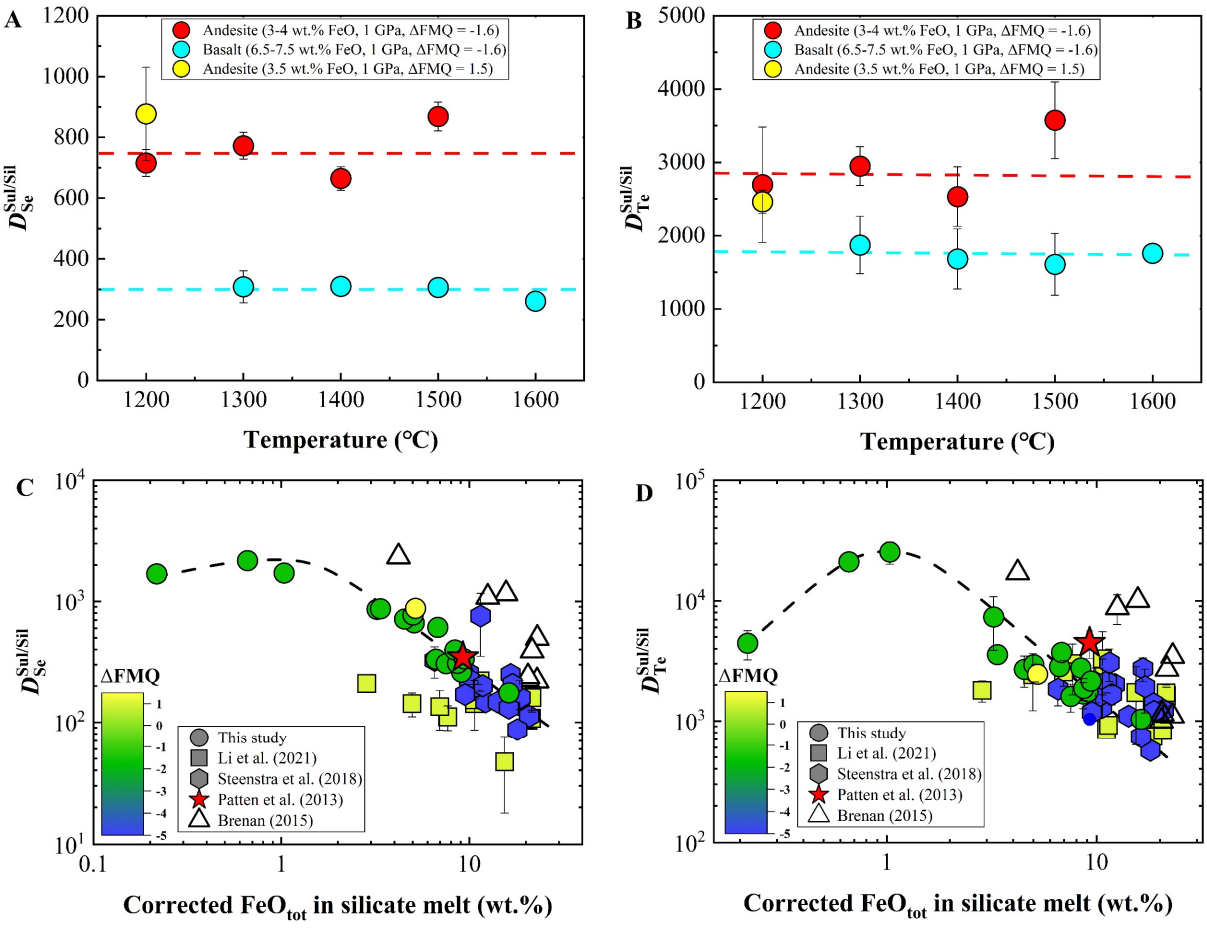

Fig. 3.2-4: Sulphide liquid–silicate melt partition coefficients of Se and Te ($D_{Se,Te}^{Sul/Sil}$). (A, B) The plot of $D_{Se,Te}^{Sul/Sil}$ from the experiments on basaltic and andesitic melts as a function of temperature, showing a negligible effect of temperature on $D_{Se,Te}^{Sul/Sil}$. (C, D) Plot of $D_{Se,Te}^{Sul/Sil}$ from all experiments (circles- this study, all other symbols from the literature) as a function of the FeO_{tot} content in silicate melt, corrected for an ideal activity of FeS in sulphide liquid.

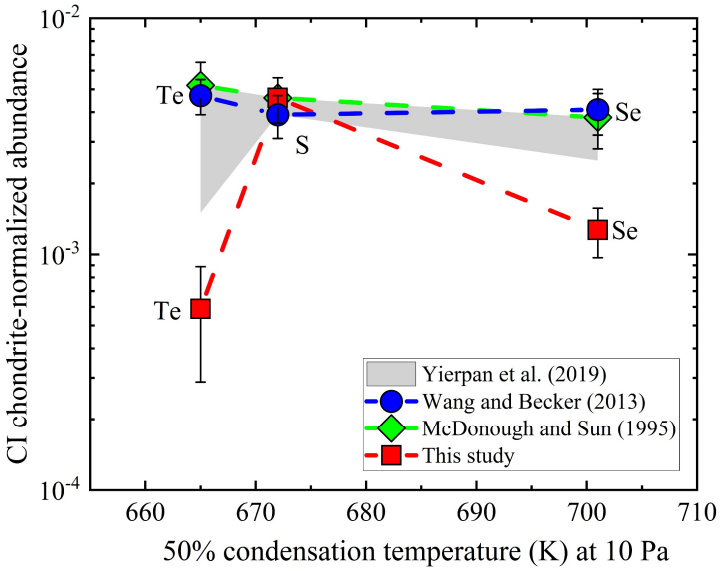

Fig. 3.2-5: A plot of the abundances of S, Se, and Te in the primitive mantle (PM) vs. their 50 % condensation temperature at 10 Pa. The red squares represent the Se and Te estimates in the PM from this study, and the others were taken from the literature. Our Se and Te abundances for the PM are lower than previous estimates and indicate superchondritic S/Se and S/Te ratios.

We parameterised $D_{Se,Te}^{Sul/Sil}$ as a function of the compositions of both silicate melt and sulphide liquid, enabling us to model the behaviour of Se and Te during magmatic differentiation and mantle partial melting. Our model effectively accounts for the Se, Te, and Cu systematics observed in MORBs and oxidised arc magmas. Using high-precision Se and Te data from MORBs collected along the Pacific–Antarctic ridge, we estimate the silicate Earth to contain ~ 25 ± 5 ng/g of Se and ~ 1.37 ± 0.7 ng/g of Te, which are significantly lower than previous estimates (Fig. 3.2-5). Therefore, the silicate Earth exhibits superchondritic S/Se and S/Te ratios, suggesting that the late veneer was likely not a major source of S, Se, and Te. Instead, it suggests that the abundances and isotopic compositions of S, Se, and Te in the silicate Earth were established during the main accretion phase. Future experiments should focus on determining the metal–silicate melt partitioning of Se and Te at the conditions of Earth's deep magma ocean. This research will help to ascertain whether the current estimates of Se and Te abundances in the silicate Earth can be explained solely by core formation.

e. *The potential role of tuite [γ-$Ca_3(PO_4)_2$]as a carrier of phosphorus and incompatible trace elements in the Earth's peridotitic lower mantle: An experimental study to 33 GPa and 2000 °C (T. Pausch, B. Joachim-Mrosko and J. Konzett/Innsbruck, F. Wang and T. Katsura)*

In the mantle wedge above the subducting oceanic lithosphere intense metasomatism takes place triggered by melts or fluids enriched in volatiles and incompatible trace elements that have formed by partial melting or dehydration reactions. One of the elements commonly

transferred from the subducting slab into the overlying mantle is phosphorus, as demonstrated by the frequent presence of apatite in metasomatically altered mantle wedge peridotites. Once stabilised, apatite also becomes an important host for volatiles and LIL elements including REE, Th and U, making apatite a major source of radioactive heat in the mantle. Through viscous coupling, the apatite-bearing mantle may be dragged down with the subducting slab, exposing apatite to increasingly higher pressures. Between approximately 8 and 9 GPa, corresponding to depths of ~ 250-280 km, apatite breaks down to form the Ca-phosphate tuite [γ-$Ca_3(PO_4)_2$]. Although tuite cannot host any significant proportion of volatiles, in contrast to apatite, it is an eminently suitable carrier for LIL elements. Recent experiments have shown that tuite is stable to at least 25 GPa, with an upper temperature stability limit between 1700 and 1750 °C in a CO_2-bearing model peridotite. Thus, tuite is potentially stable in the lower mantle and, together with apatite, forms part of a transport system operating in and near the subducting lithosphere, that transfers phosphorus and incompatible trace elements from the upper to the lower mantle. However, compared to a volatile-free system, the presence of CO_2 shifts the peridotite solidus to lower temperatures and stabilises carbonatitic melts. As these melts have a very high phosphorus solubility, the temperature stability of tuite is likely to be severely limited in their presence. In a volatile-poor or -free environment tuite is expected to be stable to much higher temperatures. This may extend its significance as a phosphorus and incompatible trace element carrier to mantle volumes characterised by temperatures close to or even above the average current mantle adiabat (ACMA). In any case, the significance of tuite for phosphorus and trace element storage is anticipated to undergo a notable transformation with increasing depth of subduction and temperature, particularly in the transition across the upper-to-lower mantle boundary. This is due to the disappearance of major phosphorus and/or LREE carriers, such as majoritic garnet and ringwoodite, and the emergence of new competitors for LILE-LREE-HFSE such as $CaSiO_3$ davemaoite. The present study was initiated for two purposes. Firstly, to explore the stability of tuite in a nominally dry peridotite at pressures significantly higher than the top of the lower mantle and at temperatures at or above the ACMA. Secondly, to examine the compositional evolution of tuite and its coexisting phases with a particular focus on the phosphorus contents of the silicates and the competition between tuite and davemaoite for incompatible trace elements.

High-pressure/-temperature experiments were conducted at 27 and 33 GPa in a temperature range of 1500-2000 °C using a 15-MN Osugi-type multianvil high-pressure apparatus. The 27 GPa experiments used a 7/3 mm assembly with a $LaCrO_3$ furnace, while the 33 GPa experiments used a 5.7/1.5 mm assembly with a rhenium furnace. The starting material was a model peridotite doped with 3 % β-$Ca_3(PO_4)_2$ and a trace element mixture consisting of Li, B, Be, all REE and selected LILE-HFSE.

Results show that tuite is stable at 27 and 33 GPa to at least 2000 °C, coexisting with bridgmanite + ferropericlase + davemaoite. This indicates that in a sufficiently phosphorus-rich bulk composition, tuite is not only stable within subduction zone pressure-temperature regimes but potentially also in ambient mantle to temperatures of at least 250 °C above the ACMA,

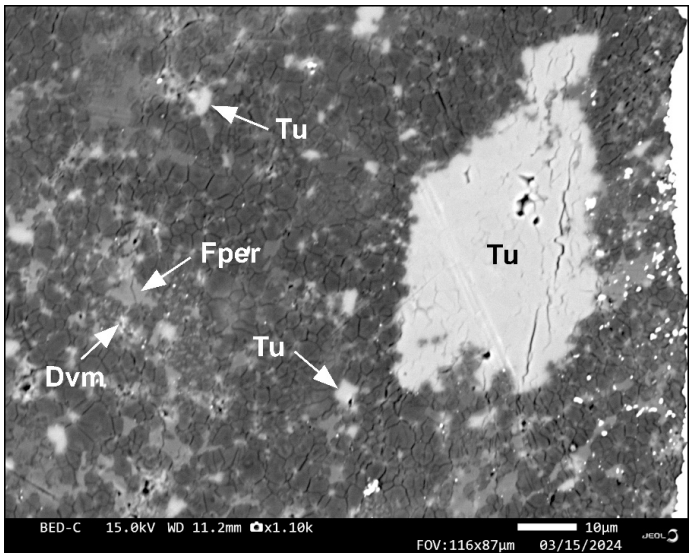

Fig. 3.2-6: Backscattered electron photomicrograph of part of an experimental charge from a run conducted at 33 GPa and 1800 °C, showing tuite (Tu) as single grains and as a large aggregate of grains, in a matrix consisting of bridgmanite (Brg), ferropericlase (Fper) and davemaoite (Dvm).

f. *Redox-controlled experiments to determine Fe^{3+} partitioning between majorite and melt in the transition zone (S. Ma/Cork, K. Kiseeva/New York and A.C. Withers)*

The oxidation state of the mantle is an important parameter that affects such major processes as magma genesis, mantle convection, and transport of material between the upper and the lower mantle. It is also linked to the formation of diamond and the deep carbon cycle. Despite its tremendous importance, the mantle oxidation state is not well-understood due to the lack of natural samples and consistent thermodynamic activity models, as well as analytical limitations. Very limited natural sample data for the mantle transition zone oxidation state exist, in the form of majoritic garnet inclusions in diamonds derived from depths between ~ 250 and 550 km.

Oxybarometers have been developed previously, based mainly on the ferric iron components in spinel and garnet, which can be used to examine oxygen fugacities of rocks from the cratonic lithosphere. At higher pressures, however, garnet becomes majoritic through the dissolution of pyroxene, which is currently not well accounted for in oxybarometers calibrations. A recent study has shown that majoritic garnets, both in experiments and in natural samples, contain elevated Fe^{3+} contents. Some models have proposed that this increase in Fe^{3+} still equates to relatively low oxygen fugacities, where iron metal can be present. However, other thermodynamic modelling has argued for relatively oxidised conditions in the transition zone attributed to interaction with oxidised fluids from subducted materials.

Further experimental data are therefore important for resolving differences in oxybarometers at transition zone pressures. Our experiments are designed to study mineral melt partitioning of

ferric iron at transition zone conditions. In this way, the redox state of potential metasomatic melts in the deep mantle can be understood. The high temperatures also ensure equilibrium assemblages for the calibration of activity-compositions relations for use in oxybarometer calculations. Majorite, olivine polymorphs and melt are produced from a fertile mantle composition at 15 GPa, which corresponds to the pressure near the top of the transition zone. The KLB-1 peridotite composition starting material is enriched in ^{57}Fe to increase the synchrotron Mössbauer spectroscopy (SMS) sensitivity. Samples were heated to 2200 °C, which is close to the liquidus of the KLB-1 peridotite. Various redox buffers or metals were added to either buffer or measure the equilibrium fO_2. These include Re-ReO_2, Mo-MoO_2, Ru-RuO_2, Fe and Ir. The Fe^{3+} in both majorite and melt and its partitioning between the phases are expected to vary over a range of fO_2 from -2 to +7 log units relative to the IW buffer. The investigation of the Fe^{3+} content of the run products will provide information that will supplement thermodynamic data, and will help us to constrain the fO_2 profile in the deep Earth, and understand the formation of ultra-deep diamond and the origin of kimberlitic melt.

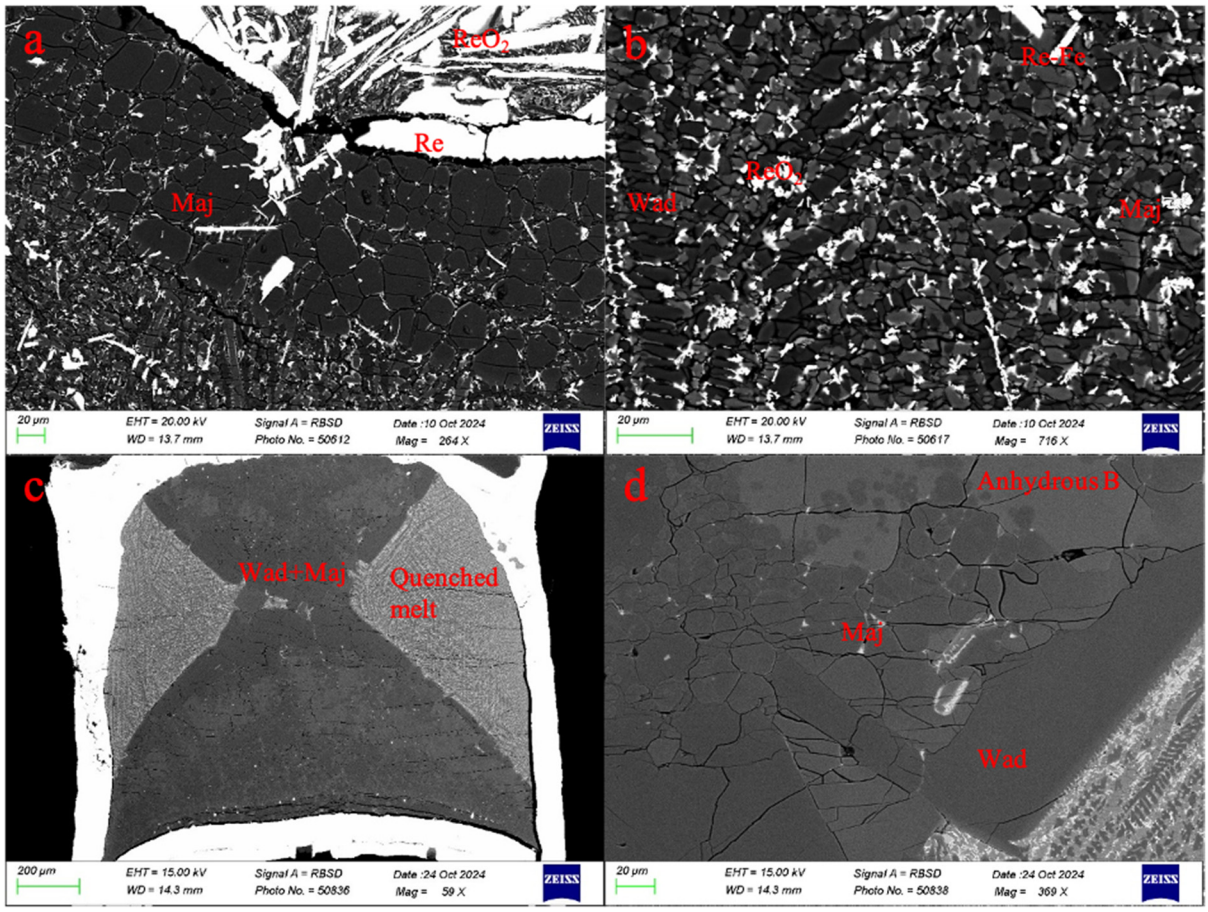

Fig 3.2-7: a) Re-ReO_2 buffered experiment with garnet and quenched melt; b: Re-ReO_2-buffered quenched melt consisting of micron-scale majorite and wadsleyite quench crystals; c: Experimental capsule of an Fe-saturated experiment; d: Fe-saturated experiment with a solid assemblage including wadsleyite, majorite and anhydrous phase B in contact with quenched melt.

Experiments were characterised using scanning electron microscopy (Fig 3.2-7). Majorite and wadsleyite are the major solid phases and form crystals between 10 and 50 μm in diameter. High-pressure MgO-rich melt has limited glass-forming ability, so small quench-crystals of majorite and wadsleyite, under 5 μm in diameter, are seen in the super-liquidus region of the capsules. The absence of Fe^{3+}-bearing minerals such as clinopyroxene will enable the measurement of Fe^{3+} content in the quenched melt and solid phases. Redox buffers were spread throughout the solid assemblage and melt regions of the experiments, thus ensuring that the experiments were buffered in fO_2. In the Re-ReO_2 buffered experiment, majorite is the only solid phase, while in a more reduced experiment containing metallic Fe, majorite, wadsleyite and anhydrous phase B were formed (Fig 3.2-7). In the next stage of this project, 100-130 microns thick double-polished sections cut from the experimental samples will be analysed using SMS at the European Synchrotron Radiation Facility.

g. *High-pressure and high-temperature experiments (1 GPa, 1350 °C) in the piston-cylinder in a multi-proxy approach to constrain the* fO_2 *of oceanic basalts (M. Motte/Nantes, E. Kubik, A. Bézos/Nantes, C. Guivel/Nantes and D. Zhu)*

Oxygen fugacity (fO_2) is an intensive thermodynamic parameter that characterises the oxidising potential of a system and defines the oxidation state and geochemical behaviour of multivalent elements it contains. Iron, as a major constituent in all Earth's geological reservoirs, is a key element to understand the formation and evolution of planetary interiors and atmospheres. Based on the geochemistry of major and trace multivalent elements (*e.g.*, Fe, V, Zn), experimental petrologists have developed a range of oxybarometers to determine fO_2 in igneous rocks. However, Fe- and V-based oxybarometers have produced conflicting results for subduction magmas, casting uncertainty on their accuracy and obscuring our understanding of the fO_2 in the subduction mantle wedge. This illustrates how challenging it is to calculate the fO_2 from the study of multivalent elements in magmatic samples. The goal of this project is to address two highly debated issues. The first one deals with analytical issues related to the determination of the $Fe^{2+}/\Sigma Fe$ ratio. The second one relates to the characterisation of the partition coefficient of Fe^{3+} during magmatic processes. The experimental study of MORB-like compositions equilibrated at different fO_2 conditions could provide the necessary material to: (1) perform a methodological comparison of $Fe^{2+}/\Sigma Fe$ measurement techniques (wet chemistry, Mössbauer and XANES), and (2) measure the Fe^{3+} mineral-melt partition coefficient values for the most relevant Fe^{3+}-bearing mineral phases (*e.g.*, clinopyroxene, spinel).

Synthetic powders reproducing primitive MORB compositions were prepared with mixtures of reagent grade oxides and carbonates and doped with a mixture of first-row transition elements (Sc, V, Ni, Cr, Co, Zn), which will help to determine equilibrium conditions and partition coefficients, as well as ^{57}Fe. For each experiment, FeO and Fe_2O_3 were added to the starting material to induce more reducing or more oxidising conditions, as well as 2 wt. % H_2O. To avoid excessive Fe loss during the experiments, 1 wt. % Fe^0 was added. The starting material

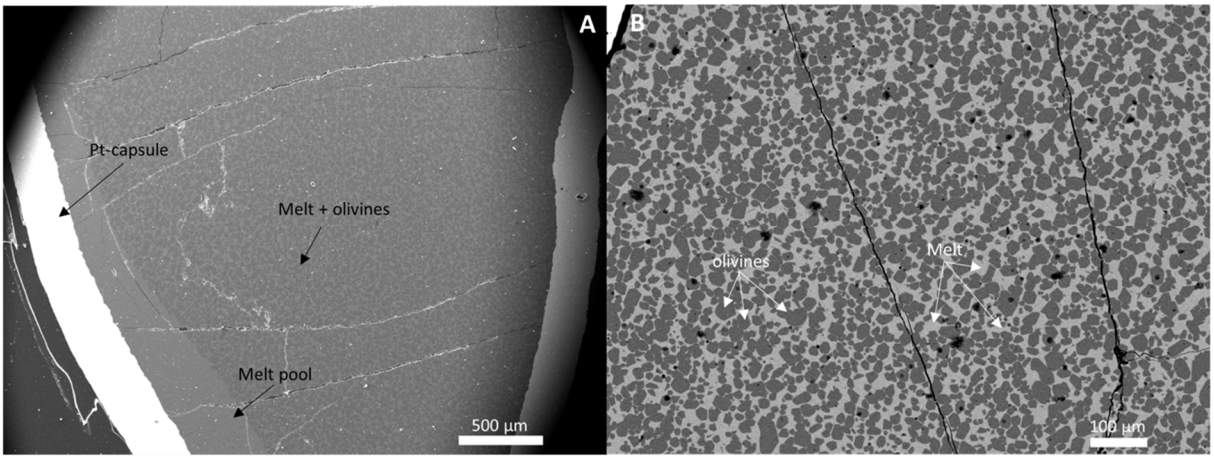

Fig. 3.2-8: Scanning Electron Microscopy images of a sample. A: image of the sample showing porphyric texture of melt and xenomorph olivines that represent ~ 50 % of the total volume. B: closeup of the sample showing melt (light grey) and olivines (dark grey).

was packed in Pt capsules, which were then sealed and placed in a talc-Pyrex assembly that comprised MgO spacers and a straight graphite furnace. Four high-pressure and high-temperature experiments were performed in an end-loaded piston cylinder apparatus housed at the BGI and using a ½" pressure vessel. The experiments were carried out at 1 GPa and 1350 °C for 24h, targeting clinopyroxene saturation. Each experiment was vertically cut, mounted in epoxy and polished for Scanning Electron Microscopy analyses (Fig. 3.2-8). The preliminary results indicate that olivine is the only phase at saturation. The textures of the experiments are highly porphyritic, featuring rounded-edges olivine crystals (50 % vol.) enclosed within a glassy matrix (Fig. 3.8-8B). The size of olivine crystals varies between ~ 10 and 30 µm, which allows LA-ICP-MS and Mössbauer/XANES spectroscopy analyses. Melt pools adjacent to the Pt-capsule walls are observed, associated with hotter regions due to thermal gradients in the experiments (Fig. 3.8-8A). The Fe contents measured in the melt and in the Pt-capsules were used to estimate the experimental fO_2 that varies between +0.1 and +2 unit log relative to the iron-wüstite buffer. These experiments, as well as other ones synthetised at the Laboratoire de Planétologie et Géosciences of Nantes (France), will be analysed by SEM, LA-ICP-MS, and nano-Mössbauer spectroscopy in order to perform the methodological comparison of $Fe^{2+}/\Sigma Fe$ measurement techniques.

h. *The melting behaviour of fertile and depleted peridotite at high pressures (C. Melai/Dublin, M.J. Walter and J. Yang/Washington, D.C., M. Rinaldi/Dublin, A.C. Withers and E. Tomlinson/Dublin)*

High-pressure and high-temperature melting experiments underpin our knowledge of mantle melting processes. This information is critical for elucidating the conditions of melting in modern mantle plumes, the generation of komatiites (particularly prevalent during the Archean), as well as impact melting and the dynamics of magma ocean processes in the early

Earth. Building upon a pioneering experimental study from the 1990s that mapped out the melting relations of a fertile peridotite (KR4003 from West Kettle River, British Columbia) to 7 GPa, this study significantly expands the previously investigated pressure range up to 12 GPa by means of multianvil experiments. Moreover, $^{176}Hf/^{177}Hf$ ratios of both cratonic peridotite and komatiite lavas require them to be derived from a depleted mantle source. Thus, we are also investigating the melting phase relations of a synthetic depleted peridotite over a pressure range from 4 to 12 GPa. The aim is to additionally investigate poorly constrained aspects of melting phase relations such as: i) the position of the transition of ortho- to clino-enstatite and its effect on the composition of orthopyroxene; ii) the depth over which peritectic orthopyroxene forms above the solidus; and iii) the stability and proportion of garnet in the residue across the melting range as well as the conditions at which garnet + olivine (rather than olivine + orthopyroxene) become the last phases present in the residue. This work allows the investigation of the influence of pressure on the melting behaviour of fertile and depleted peridotite and its potential role in komatiite melt formation.

This project faces significant technical challenges. Achieving the narrow temperature window between the solidus and liquidus necessary for successful experiments proves challenging, even with meticulous efforts to minimise thermal gradients within the multianvil assembly. Furthermore, employing graphite capsules, as utilised in previous work, is not feasible at high pressures due to the transformation of graphite to diamond. This transformation can lead to the loss of the melt into the porous space created during diamond formation, hindering proper retrieval and analysis. Additionally, with melt loss, equilibrium is not ensured in the experimental run, making the recovered samples unusable. In order to address this, test runs with an annealing time at subsolidus temperatures to allow the graphite to diamond transition in the capsule *before* the melting of the peridotite are being performed. Preliminary results show this may effectively solve the issue. For the successful runs, the chemical composition of the coexisting phases was analysed by means of an electron-probe microanalyser (EPMA) and phase proportions were calculated by least squares mass balance from the measured phase compositions at each pressure and temperature point.

i. *Experimental investigation of silica enrichment in Archean cratonic lithosphere (C. Melai/Dublin, A.C. Withers and E.L. Tomlinson/Dublin)*

A puzzling aspect of the Archean peridotite mantle is that it is often silica-rich, extending to lower MgO/SiO_2 ratios for a given magnesium number and with a high abundance of orthopyroxene. This silica enrichment cannot be explained by simple melting of fertile peridotite and requires interaction with Si-bearing fluid or melt. The observed narrow range of $\delta^{18}O$ in Archean cratonic peridotites aligns with ordinary upper mantle values that indicate a mantle origin of the reacting melt. A possible scenario for high-pressure silica enrichment would involve a peridotite reaction with ascending komatiite melt during craton formation. Aluminium-depleted komatiite is a plausible candidate as it has low Al_2O_3 and would therefore not stabilise additional garnet and, due to its ultramafic nature, would not suppress the molar

Mg/(Mg+Fe) ratio of the residue. Recently published thermodynamic modelling has shown that komatiite reaction can theoretically produce silica enrichment in the peridotite residue, with minimal effect on the concentrations of other elements.

In the present study, an experimental approach has been undertaken to test this hypothesis. A synthetic fertile peridotite, a depleted peridotite composition, and an Al-depleted komatiite starting material were produced by mixing reagent oxide powders. High-pressure multianvil experiments were performed to: (i) better understand the incongruent orthopyroxene forming reaction in non-pyrolytic compositions; (ii) provide insight into the effect of komatiite interaction on mineral and melt composition; (iii) provide insight into komatiite transport and the relative importance of diffuse porous and channelised melt flow during komatiite ascent. Experiments with mixed powders of komatiite and peridotite were conducted at 5 GPa at temperatures above the bulk solidus to investigate the melt productivity, and mineral/melt composition. The peridotite powders were also used to pre-synthesise cylindrical rods at 5 GPa and 1600 °C (Fig. 3.2-9) for reaction couple runs. In this set of experiments the rods were then prepared and utilised in a new run together with komatiite powder in a 70-30 ratio to investigate melt rock reaction and the porosity (*i.e.*, melt fraction) of the reactive boundary layers. Preliminary findings in the melt-rock reaction experiments with fertile peridotite at 1650 °C indicate that the phase assemblage at the boundary is composed of melt + olivine and pyroxene, while further into the peridotite rod garnet is observed together with olivine and pyroxene (Fig. 3.2-9B). The observed abundance of olivine in the melt zone and the high Mg# of that olivine suggests that olivine may be fractionated from the komatiite melt, which will have the effect of increasing the SiO_2/MgO ratio of the residual melt, increasing its ability to act as an agent of silica enrichment.

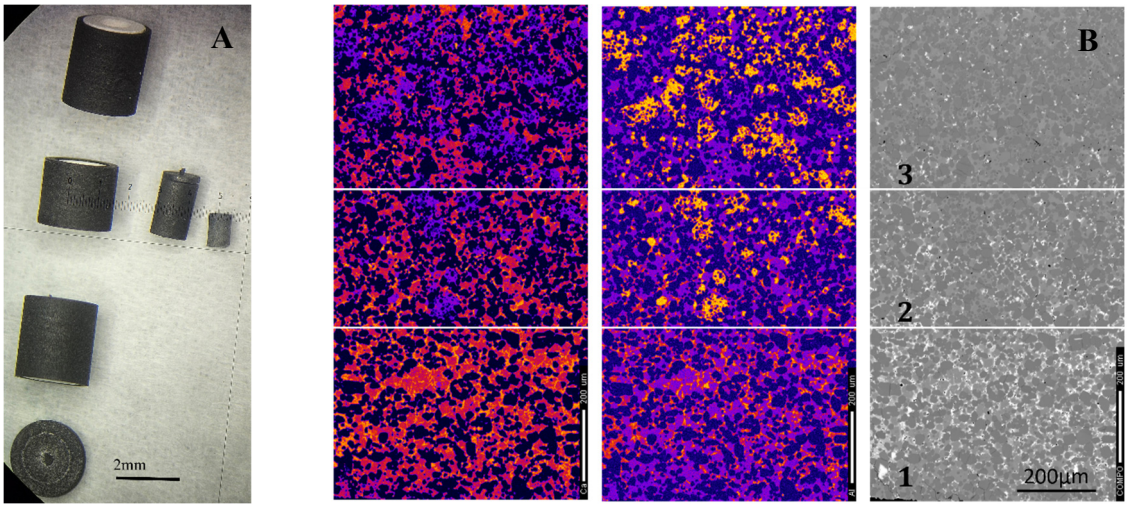

Fig. 3.2-9: (A) Graphite furnace part of an 18/11 assembly is presented together with the 2 mm long graphite capsule and the 1.8 mm cylinder synthesised at 5 GPa and 1600 °C; (B) Backscattered SEM image of sample S8030_F (right) together with Aluminium (Al) concentration map in the center to highlight the presence of the garnets, and to the left the Calcium (Ca) map, to highlight the melt. The sample is divided into 3 zones: (1) the bottom, the melt zone, (2) the reaction zone; and (3) unreacted peridotite.

j. *The contribution of subducted sediments to the formation of magmatic-hydrothermal deposits (M. Hlede, A. Audétat and H. Keppler)*

Porphyry copper and molybdenum deposits account for the majority of the world's copper and molybdenum reserves. Both metals are widely used in technology and industry: Copper is mainly used for electrical cables and in electronics because of its high heat and electric conductivity, while molybdenum has a wide range of applications in particular for alloys. However, the discovery rate of new porphyry deposits has plummeted since recent years, while the demand for these metals continues to grow. Because of this, predicting the possible location of yet undiscovered deposits is becoming a matter of increasing relevance. The correlation between porphyry copper deposits and subduction zones (active and ancient) is already well known. Moreover, most Climax-type porphyry molybdenum deposits are concentrated in a relatively small area in central North America, where the mantle likely was modified by fluids resulting from an ancient subducting zone. However, even though the magmatic system that leads to the formation of porphyry deposits is reasonably well understood, the primary source of the metals is debated. One possible source could be subducted sediments. In this study, we investigated the fluid/mineral partition coefficients of Cu, Zn, Mo and W under subduction zone conditions to determine whether the mobilisation of these metals from the subducted sediments due to dehydration of the slab is possible.

The experiments were performed using piston-cylinder presses at conditions corresponding to the dehydration of the slab. The solid starting material was a glass with a composition close to GLOSS (GLObal Subducting Sediment). A series of aqueous solutions was prepared by mixing distilled water with different amounts of NaCl (0, 5, 10, 15 wt. %) to check for the effect of Cl concentration on metal partitioning. To check for equilibrium, both forward and reversed experiments were performed. In the forward experiments, the solid sedimentary material was doped with the metals, while in the reversed experiments, the glass was left undoped, and the metals were added to the solutions. The Pt capsules were lined with copper foil to avoid diffusion of Cu from the starting material into the capsule walls. In the middle of the Pt capsules, we added a layer of diamond powder, which served as a high-porosity reservoir for the fluid to be trapped during the experiment. Above the diamond layer, we added some more solution and another layer of solid material. During the experiments, slow compression and decompression procedures were followed with the help of automated piston-cylinder presses to avoid fracturing of the capsules. Furthermore, a temperature cycling of ± 30 °C around the target temperature was implemented every 8 hrs to grow larger crystals by means of Ostwald ripening.

After the experiments, the samples were weighed to check for fluid loss and then kept in a freezer until the day of the analysis, when they were first cooled to liquid nitrogen temperature, allowed to heat back up to *ca.* -50 °C, opened with a razor blade, and then analysed in frozen state by laser ablation-ICP-MS. A typical cross-section of a capsule is shown in Figure 3.2-10a. Afterwards, SEM maps were acquired (Fig. 3.2-10b,c), followed by EMPA and LA-ICP-MS analysis of the minerals.

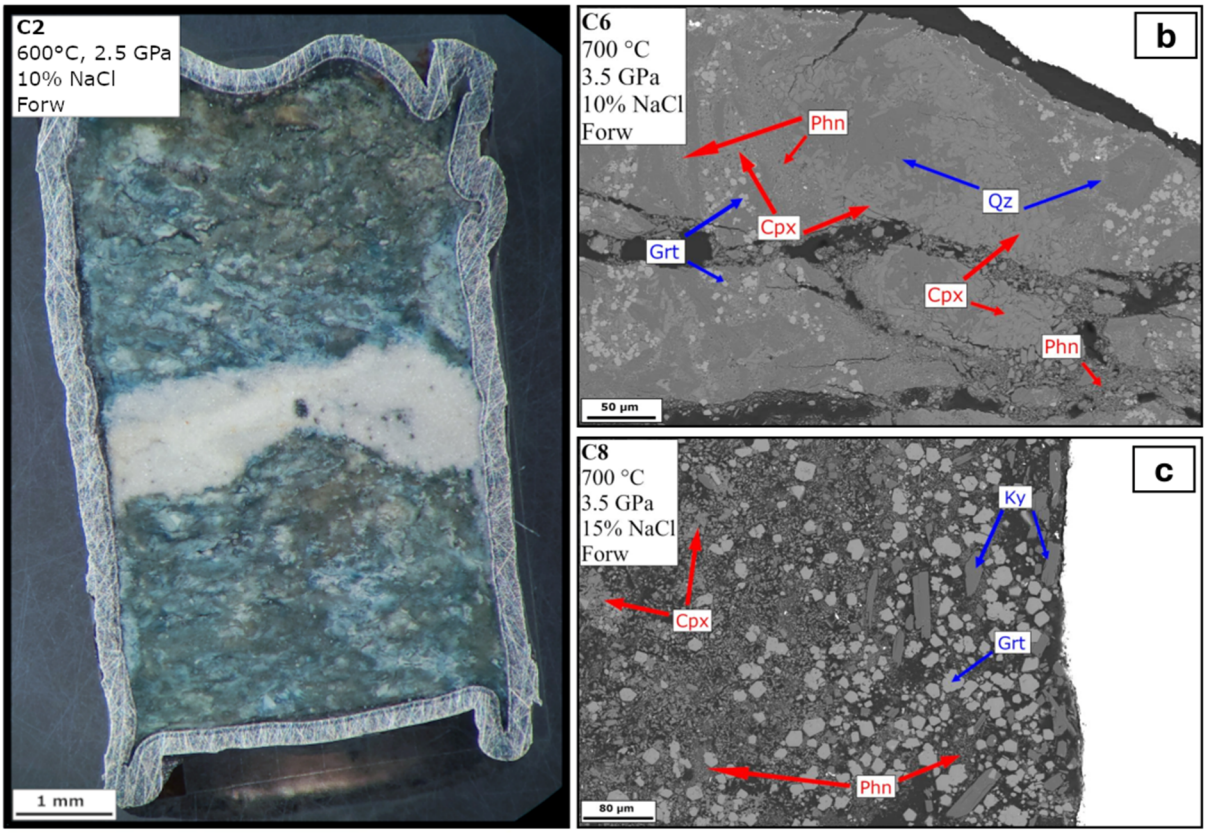

Fig. 3.2-10: a) Representative optical image of a sectioned sample. The white layer in the middle is the diamond trap. b, c) Representative backscattered electron images of other samples. Abbreviations: Qz – quartz, Phn – phengite, Cpx – clinopyroxene, Grt – garnet, Ky – kyanite.

The experiments were performed at two conditions: 600 °C, 2.5 GPa and 700 °C, 3.5 GPa. At the lower P-T conditions, a phase assemblage of quartz, clinopyroxene, chloritoid, phengite, zoisite, talc, rutile, and magnetite was observed, while at 700 °C and 3.5 GPa the assemblage changed to coesite, clinopyroxene, garnet, lawsonite, kyanite, phengite and rutile (Fig. 3.2-10b,c). The results show that at 0 wt. % NaCl in the fluid, neither Cu nor Zn partitions into the fluid phase (Fig. 3.2-11a,b), whereas at higher fluid salinities they do. In contrast to this, Mo and W show high partition coefficients at all conditions, with no obvious dependence on salinity (Fig. 3.2-11c,d). The only mineral that has the capacity of strongly concentrating Mo and W is rutile ($D^{\text{fluid/rutile}} \sim 0.01$). However, rutile is present only as very sparse, tiny crystals in a few runs, whereas it is completely absent in the other samples, implying that its effect on the bulk fluid/solid partitioning should be almost negligible. This suggests that the mobilisation of Mo from subducted sediments should be very efficient, particularly if compared to an eclogitic MORB assemblage, which contains far more rutile.

Molybdenum is known to be strongly enriched in some anoxic pelagic sediments, with concentration levels on the order of 100 ppm being commonly reached in black shales.

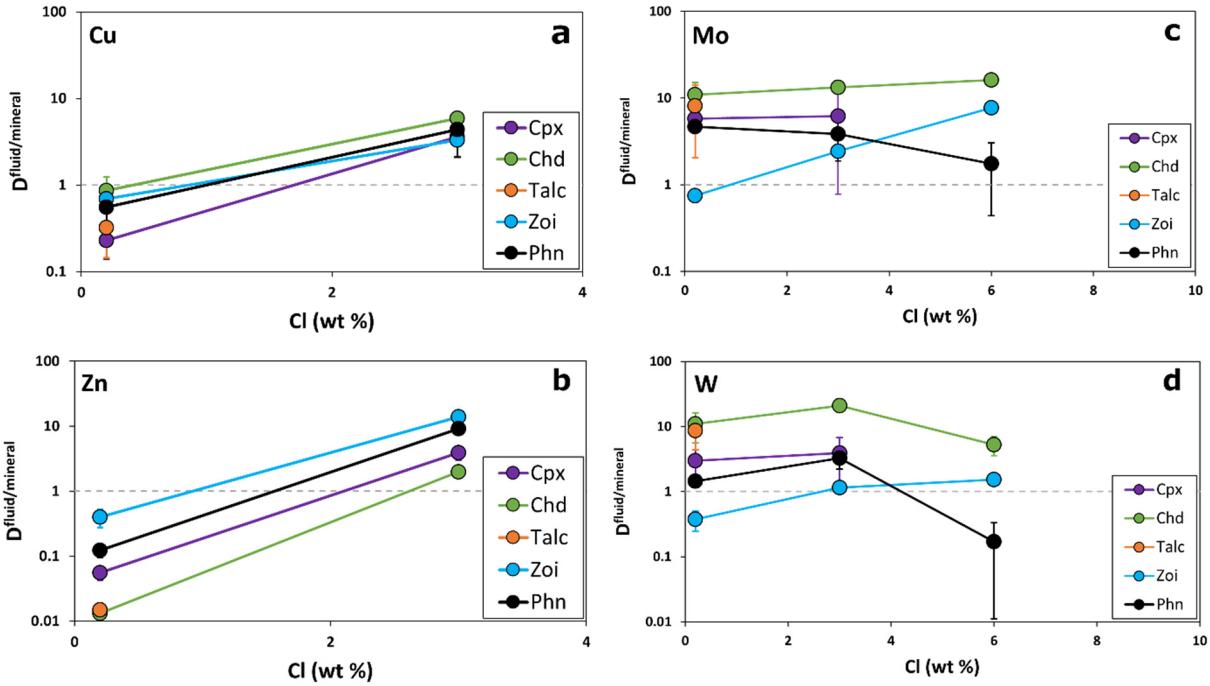

Fig. 3.2-11: Fluid/mineral partition coefficients at 600 °C, 2.5 GPa (forward experiments) for Cu (a), Zn (b), Mo (c), W (d) plotted as a function of fluid salinity. Error bars indicate one standard deviation uncertainties.

Therefore, subducted sediments likely represent a much richer source of Mo compared to both MORB (~ 300 ppb) and the depleted mantle (~ 30 ppb). Since porphyry molybdenum deposits are often concentrated in relatively small areas, their formation may ultimately be related to local subduction of black shales or other Mo-rich sediments.

k. *The redox dependence of the fluid/melt partitioning of tin (H. Keppler and A. Audétat)*

Tin is mined at least since the bronze age and is still an important raw material for electronic applications, such as lead-free solders. Almost all tin deposits of economic grade are ultimately related to highly fractionated and reduced S-type granites. While the relationship between hydrothermal tin mineralisation and granitic magmas is well established in the field, experimental studies for a long time had difficulties to simulate the extraction of tin from a magma into aqueous fluids. The reasons for this are inherent difficulties in experiments involving tin, which is readily absorbed by the noble metals that are conventionally used as sample containers in high-pressure experiments. The continuous loss of tin from the charge in such experiments makes the attainment of equilibrium difficult and previous studies likely reported erroneously low fluid/melt partition coefficients. Only recently, it was suggested that this problem could be solved by analysing fluid inclusions in quenched granitic glasses from high-pressure experiments. The tin concentrations inside these inclusions may be in local equilibrium with the tin concentrations in the quenched glass immediately next to the inclusion,

even if there is continuous tin loss from the charge to the capsule wall. In this study, we used this approach to investigate the effect of oxygen fugacity on the partitioning of tin between a coexisting aqueous fluid phase and a granitic magma, in order to better understand the reasons for the association of tin deposits with reduced magmas.

Experiments were carried out at 150 MPa and 800 ˚C in vertical rapid-quench cold seal pressure vessels. A synthetic, tin-doped and slightly peraluminous granitic glass was loaded together with aqueous solutions of various salinities (NaCl + KCl contents) into sealed Au capsules. For controlling oxygen fugacity, these capsules were usually sealed into an outer Au capsule containing both water and a solid buffer mixture. At the end of the experiment, samples were quenched to room temperature. The resulting glasses contained numerous fluid inclusions that were then analysed by laser ablation ICP-MS, together with the glass immediately adjacent to the inclusion. The ratio of the Sn concentration in the fluid to that of the surrounding glass yielded the fluid melt partition coefficient $D^{fluid/melt}$.

Experimental results are compiled in Figures 3.2-12 and 3.2-13. At all conditions studied, $D^{fluid/melt}$ increases linearly with salinity, implying the formation of some chloro-complex in the fluid, such as $SnCl^+$ or SnClOH. From the hematite-magnetite (Fe_3O_4-Fe_2O_3) buffer to near the Ni-NiO buffer, $D^{fluid/melt}$ increases (Fig. 3.2-12). This is expected, as the relatively fluid-insoluble Sn^{4+} is being replaced by the much more fluid-soluble Sn^{2+}. Very surprisingly, however, $D^{fluid/melt}$ decreases again at more reducing conditions, *i.e.*, from close to the Ni-NiO buffer to the Fe-FeO buffer (Fig. 3.2-13). A possible explanation for this unusual behaviour could be that with decreasing oxygen fugacity, the H_2O fluid is converted into an H_2O-H_2 mixture. The presence of non-polar H_2 likely decreases the dielectric constant and therefore the ability of the fluid to dissolve ionic or strongly polar species.

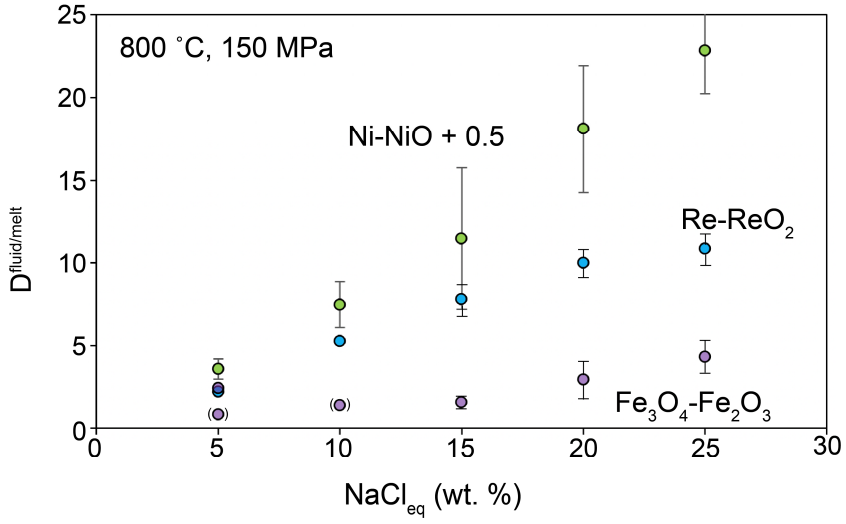

Fig. 3.2-12: Partitioning of tin between aqueous fluid and granitic melt under oxidising conditions at 800 ˚C and 150 MPa. Oxygen fugacities range from 0.5 to 1 log unit above the Ni-NiO buffer to the Fe_3O_4-Fe_2O_3 buffer. Data points in brackets imply that the Sn concentration in the fluid is below detection limit.

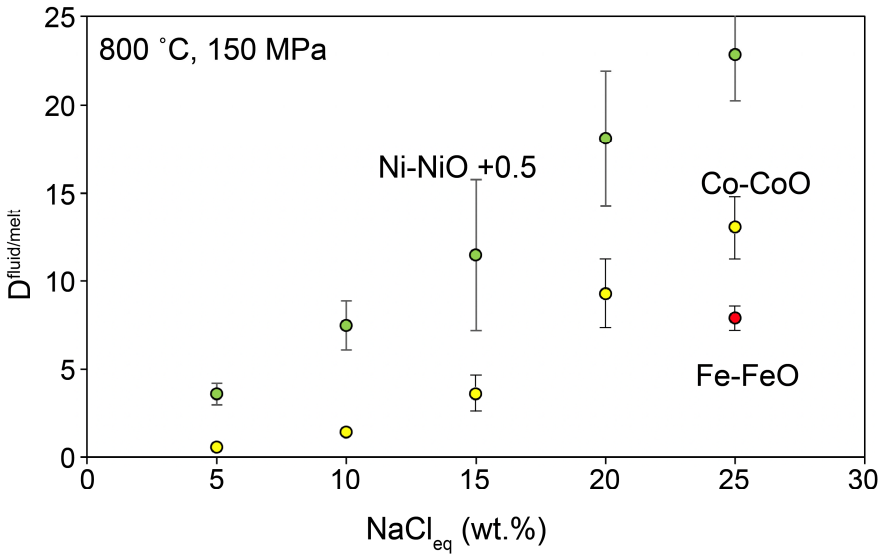

Fig. 3.2-13: Partitioning of tin between aqueous fluid and granitic melt under reducing conditions at 800 ˚C and 150 MPa. Oxygen fugacities range from 0.5 to 1 log unit above the Ni-NiO buffer to the FeO buffer.

Our data clearly show that under all realistic redox conditions, Sn preferentially partitions into fluids with elevated salinities. However, $D^{fluid/melt}$ is not particularly large, such that the extraction of tin into the fluid is only of limited efficiency. Upon vapour exsolution driven by fractional crystallisation, Sn continues to become enriched in the residual silicate melt during fractional crystallisation, in agreement with observations in natural systems. Consequently, the association of tin deposits with reduced magmas is not directly related to enhanced partitioning into fluid, but to the fact that Sn^{2+} prevailing at reducing conditions is much less compatible in crystallising minerals than Sn^{4+}. Detailed modelling using our data shows that a relatively efficient way to extract tin out of a magma into a fluid could be fluid exsolution following a rapid pressure loss induced by fracturing of the wall-rocks.

I. *Phase equilibria of a H_2O-CO_2-S-Cl-bearing arc basalt at 800-1200 °C and 1.0 GPa via slow-cooling experiments (Y. Qiao and A. Audétat)*

Porphyry copper deposits are genetically related to differentiated arc magmas that are characterised by high Sr/Y ratios, a feature that seems to result from magma fractionation at high pressure. However, significant debate persists regarding the question which specific property of these magmas rendered them so fertile. Potential candidates are: (1) higher Cu content, (2) higher S content, (3) higher Cl content, (4) higher H_2O content, or a combination of several of these factors.

We conducted a series of high-pressure fractional crystallisation experiments to determine how the concentrations of the above elements change during magma fractionation. However, this

type of experiment faces two major challenges: (1) sulphur, iron and chalcophile elements react with commonly used noble metal capsules, and (2) the mineral grains and melt pools produced in traditional crystallisation experiments are too small to measure their trace element contents and H_2O and CO_2 contents by LA-ICP-MS and FTIR, respectively. In this study we used zircon liners to effectively prevent the loss of Fe, S, and chalcophile elements to noble metal capsules. Furthermore, to produce larger crystals and melt pools, we employed cooling rates that exponentially decreased from 13 °C/hour at 1100 °C to 0,45 °C/hour at 800 °C.

The starting material for all experiments was a natural basaltic trachyandesite that was doped with volatiles and trace elements at geologically realistic concentrations, resulting in the following starting composition: 50.0 wt. % SiO_2, 18.8 wt. % Al_2O_3, 1.7 wt. % FeO_{tot}, 9.4 wt. % CaO, 6.4 wt. % MgO, 3.1 wt. % Na_2O, 1.2 wt. % K_2O, 3.5 wt. % H_2O, 4800 ppm CO_2, 2200 ppm S, 1000 ppm Cl, and 200 ppm Cu. Sulphur was added in the form of anhydrite, which buffered the oxygen fugacity at $\log_{10}fO_2$ = FMQ+2.0 (±0.5). The experiments were conducted at a constant pressure of 1.0 GPa, with slow cooling to target temperatures of 1200 °C, 1100 °C, 1050 °C, 1000 °C, 950 °C, 850 °C, and 800 °C. Figure 3.2-14 shows a quantitative SEM-EDS map obtained for the 800 °C experiment.

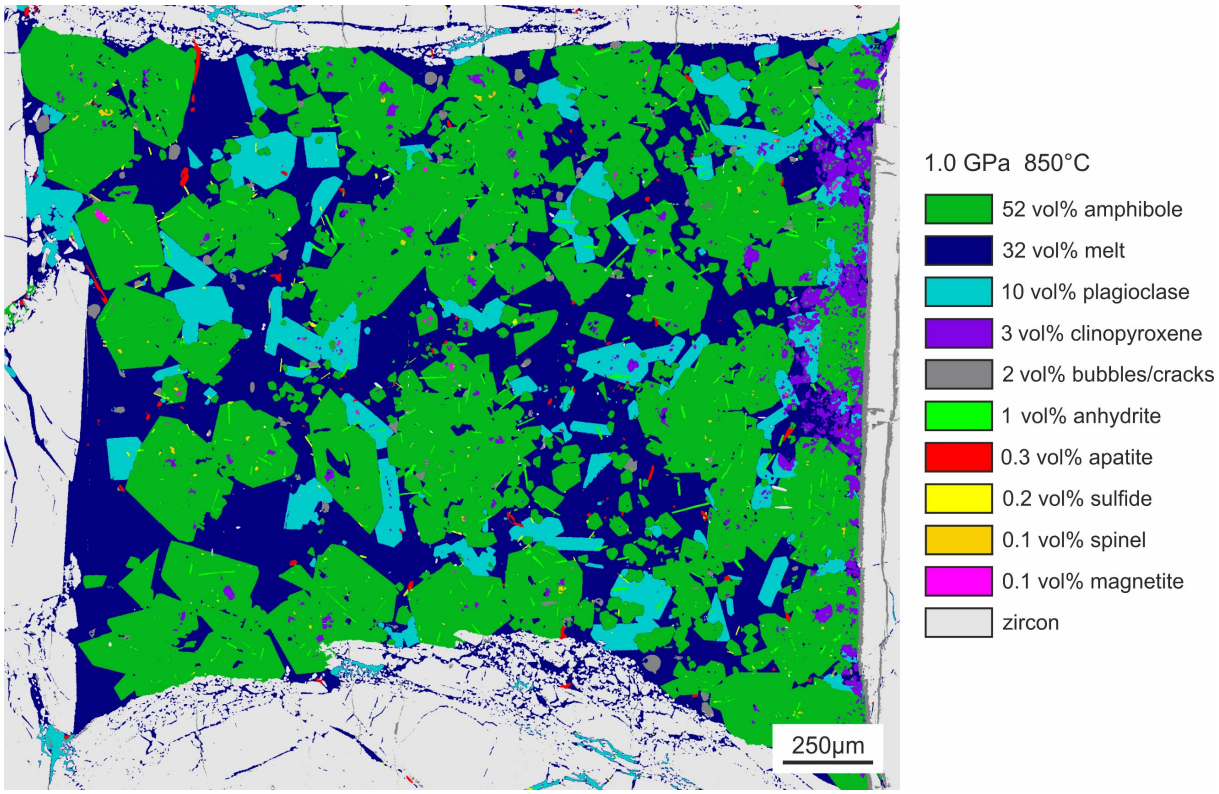

Fig. 3.2-14: SEM-EDS map of experiment YQ024 (850 °C, 1.0 GPa). Abbreviations: cpx – clinopyroxene; amp – amphibole; pl – plagioclase; anh – anhydrite; mag – magnetite; zrn – zircon; ap – apatite. Numbers next to the phases represent their modal abundance, normalised to 100 vol. % excluding zircon.

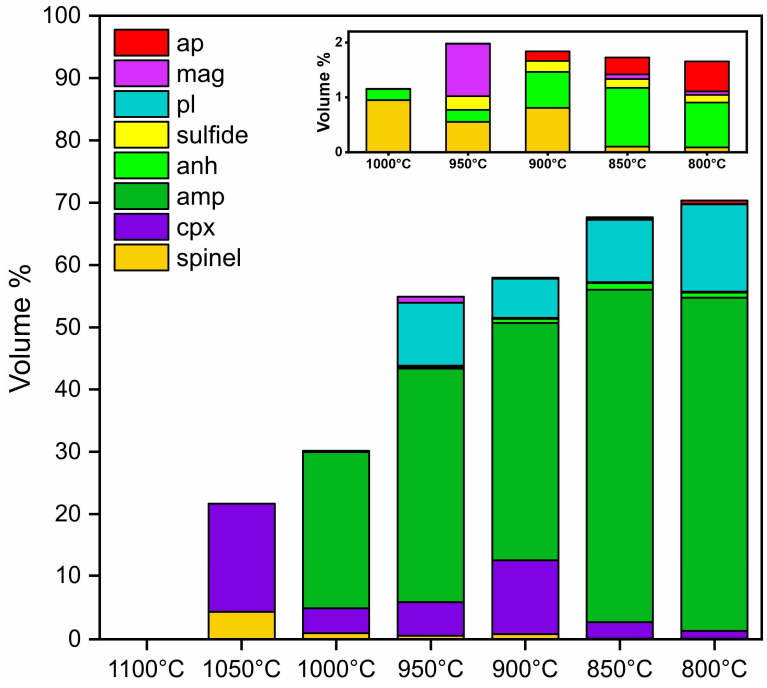

Fig. 3.2-15: Modal phase proportions in the 1.0 GPa series experiments. The inset at the upper right shows a magnified view of the abundances of the accessory phases.

The phase proportions obtained at different target temperatures are summarised in Figure 3.2-15. Spinel was the first mineral phase to appear at 1100 °C, followed by clinopyroxene at 1050 °C. Amphibole and anhydrite appeared at 1000 °C, along with trace amounts of sulphides. At 950 °C, plagioclase and magnetite started to crystallise, accompanied by minor apatite. By that stage, all mineral phases had formed. During further cooling, mostly amphibole, plagioclase and apatite crystallised.

Using electron probe microanalysis (EPMA) and Fourier-transform infrared spectroscopy (FTIR), we determined the H_2O, Cl, and S contents of the quenched silicate melts (Fig. 3.2-16). The H_2O content of the silicate melt continuously increased. The Cl content increased with increasing crystallinity until the silicate melt reached ~ 68 wt. % SiO_2 at 850 °C, after which point it started to decrease. The S content increased until a melt SiO_2 content of ~ 55 wt. % at 1050 °C, after which point anhydrite and sulphide started to crystallise. The CO_2 and trace element abundances have not been measured yet.

Theoretical H_2O concentrations calculated based on the assumption that no H_2O fractionated into the crystallising minerals nor into the fluid phase are consistent with the values measured by FTIR, indicating that no significant H_2O exsolution occurred. In contrast, at melt SiO_2 contents greater than ~ 64 wt. % the theoretical Cl concentrations are significantly higher than the actual concentrations measured by EPMA. This suggests that above ~ 64 wt. % SiO_2 in the silicate melt, Cl started to fractionate efficiently into the exsolving fluid phase, which still seems to have been dominated by CO_2 at that stage.

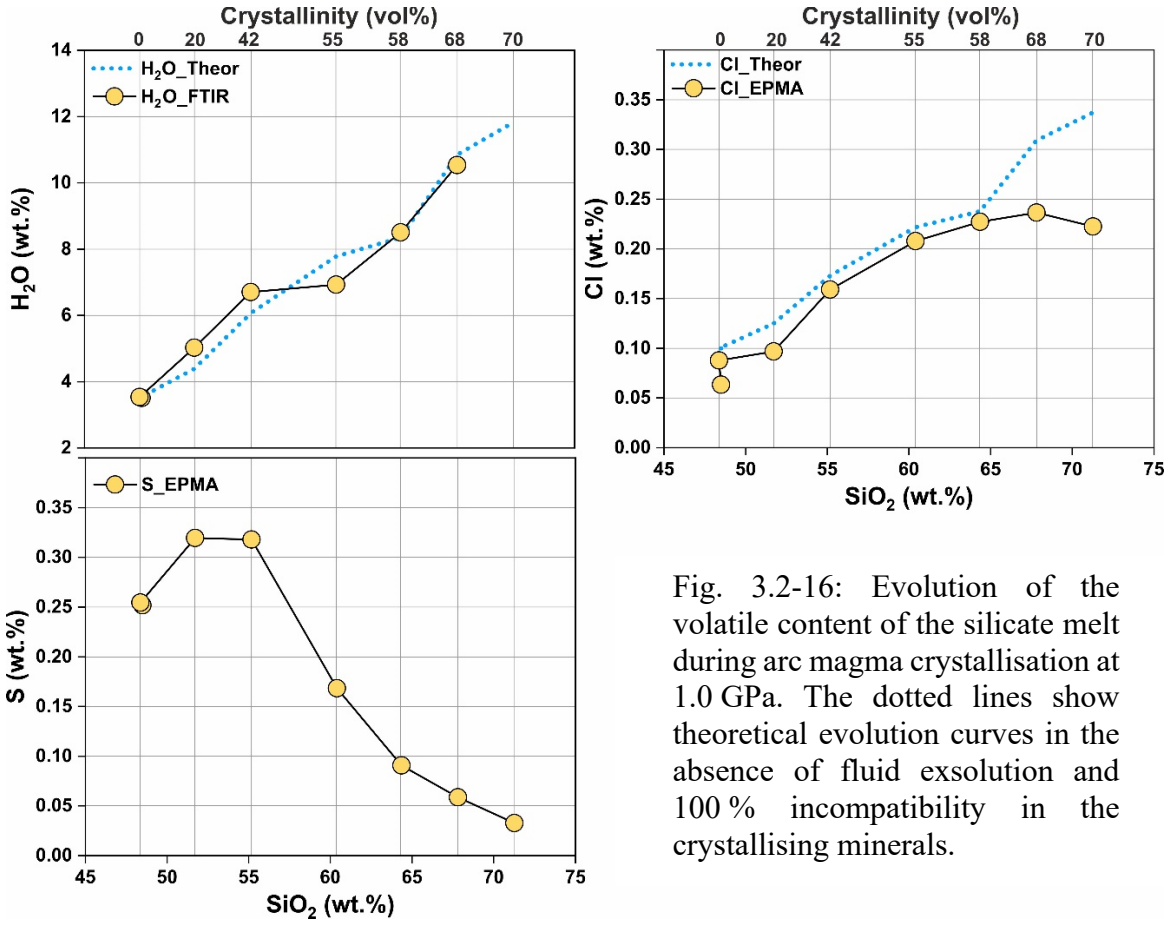

Fig. 3.2-16: Evolution of the volatile content of the silicate melt during arc magma crystallisation at 1.0 GPa. The dotted lines show theoretical evolution curves in the absence of fluid exsolution and 100 % incompatibility in the crystallising minerals.

m. *Depth and mode of porphyry Cu (Au, Mo)-forming fluid exsolution in the Sanjiang region, China (J. Chang, A. Audétat and T. Pettke/Bern)*

Porphyry-type Cu (Au, Mo) deposits are among the economically most important ore resources. Geochemical evidence suggests that the mineralising, intermediate to felsic magmas were produced by high-pressure differentiation of mafic arc magmas in the lower crust, but where and how these fertile magmas exsolved the ore-forming fluids is still a matter of debate. In the traditional model, the fertile magmas accumulated at upper crustal depths of perhaps 4–10 km to form large magma reservoirs, from where, upon further magma crystallisation, porphyry magmas and fluids were expulsed that ultimately formed the ore deposits. In contrast, some recent models suggest that the fertile magmas started to exsolve fluids already at lower crustal levels and during their ascent to the current exposure level, with no need to produce magma reservoirs on the way.

Melt inclusions, which are tiny droplets of silicate melt trapped in growing minerals, provide a unique approach to quantify magmatic volatile and metal contents before and after fluid exsolution, and, together with the mineral composition, preserve information about the pressure of magma crystallisation. We conducted a combined melt inclusion and geobarometric study on 36 samples collected from six mineralised magmatic systems in the Sanjiang metallogenic belt in southwestern China, which allows us to explicitly resolve the aforementioned question.

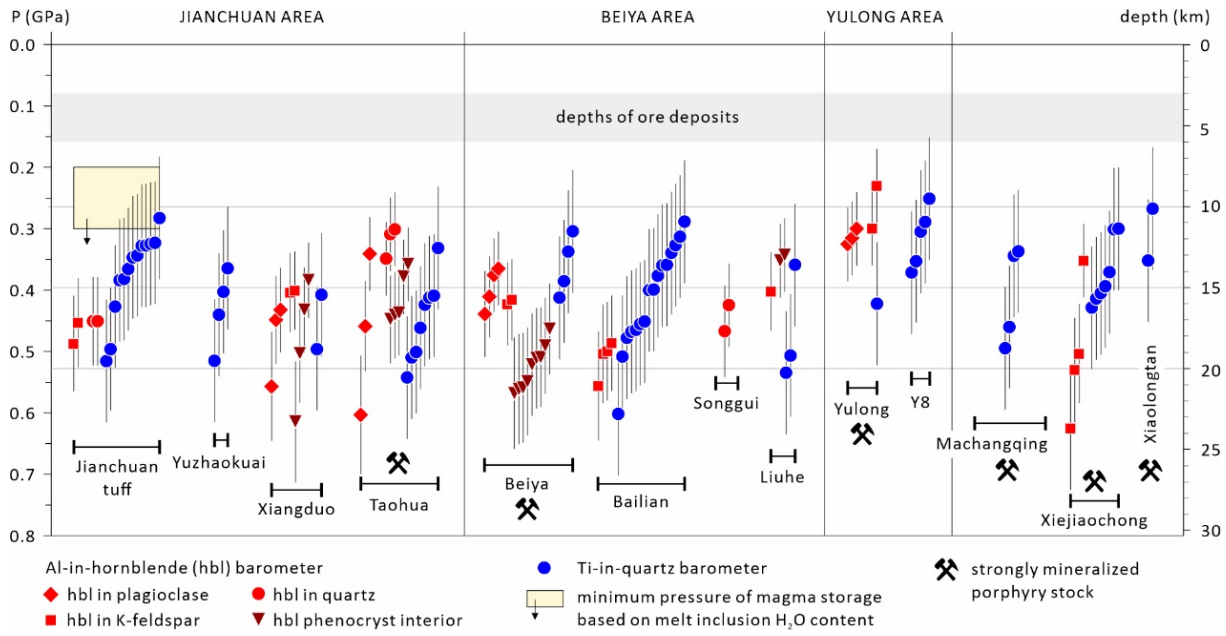

Fig. 3.2-17: Pressures at which the phenocrysts of 14 felsic magmas in the Sanjiang region crystallised before final magma ascent to the level of the ore deposits. The corresponding depths were calculated based on a crustal density of 2.7 g/cm^3.

Melt inclusions trapped in phenocrysts of mineralising, felsic magmas record a strong depletion in Cl, S, and metals compared to melt inclusions in phenocrysts of cogenetic, less-evolved magmas. Petrographic, apatite volatile content, and mass balance evidence suggests that this depletion was caused by the exsolution of aqueous fluids, which extracted 63-97 % of the Cl, S, and metals from the felsic magmas. Three independent geobarometers reveal that all the major phenocrysts in the felsic magmas crystallised within the pressure range of 0.3–0.5 GPa, some potentially even up to 0.6 GPa (Fig. 3.2-17). Hence, the ore-forming fluids exsolved from magmas that crystallised at mid- to upper crustal depths of ~ 10-20 km, rather than from magmas crystallising entirely within the upper crust or from magmas directly ascending from the lower crust. Since the ore deposits occur at the top of volumetrically small porphyry stocks located at crustal depths of ~ 3-6 km, large volumes of fluids had to percolate ~ 10 km upward to the ore deposit level, likely first by means of bubbles suspended in the ascending porphyry magmas, which then evolved to an interconnected fluid network for subsequent fluid transport.

n. *Depth of magma crystallisation and fluid exsolution beneath the porphyry-skarn Cu deposits at Santa Rita and Hanover-Fierro, New Mexico, USA (A. Audétat, J. Chang and S.P. Gaynor/Denver)*

The depth at which porphyry-Cu forming magmas fractionate and exsolve mineralising fluids is actively debated. In the classical model, major magma fractionation occurs in large, upper crustal magma chambers, and concomitant fluid exsolution leads to forceful expulsion of

residual magmas in the form of porphyry dikes, stocks, and breccia pipes, which subsequently serve as pathways for the mineralising fluids. In contrast, some recent studies highlighting the role of high-pressure magma fractionation in the formation of porphyry-Cu deposits essentially deny the existence of upper crustal magma chambers at the time of mineralisation. To address this issue, we conducted a detailed geochemical and thermobarometric investigation on 13 porphyritic intrusive rocks related to porphyry-skarn Cu mineralisation at Santa Rita and Hanover-Fierro, New Mexico, USA, representing two pre-mineralisation magmas (60-61 Ma), seven syn-mineralisation magmas (58-60 Ma), and four late- to post-mineralisation magmas (57-58 Ma).

For each sample, the pressure of the last magma crystallisation before the final magma ascent to the current exposure level was reconstructed based on Al-in-hornblende barometry of small hornblende inclusions trapped within quartz phenocrysts, as well as based on titanium-in-quartz (TitaniQ) barometry of the quartz phenocrysts themselves. Since quartz is one of the last-crystallising minerals and no significant phenocryst growth can have occurred in the dikes after the final magma ascent, the quartz phenocrysts and their hornblende inclusions should faithfully record the depth of last magma crystallisation prior to their final ascent. When present, hornblende inclusions in other minerals and hornblende phenocrysts were analysed as well. Both barometers return consistent pressures of 2.5-4.5 kbar for the entire suite of pre- to post-mineralisation magmas, corresponding to depths of 10-17 km (Fig. 3.2-18).

The volume of the mineralising porphyry dikes and stocks emplaced at the current exposure level (4-5 km paleodepth) is far too small to have provided all the fluid and metals that were required to form the ore deposits at Santa Rita and Hanover-Fierro. Therefore, the majority of the ore-forming fluids must have originated from the magmas crystallising at 10-17 km depth. This implies that most of the mineralising fluids travelled in average 9 km from their source to the eventual site of ore precipitation. The relatively unaltered nature and low veining degree of the deeper parts of mineralised porphyry dikes and -stocks suggests that fluid transport through these intrusive bodies occurred mostly at near-solidus conditions by means of fluid percolation along grain boundaries.

In summary, our thermobarometric results suggest that (i) a large, mid- to upper crustal pluton existed beneath the Santa Rita and Hanover-Fierro deposits, (ii) that considerable magma crystallisation occurred at this depth level, and (iii) that this pluton was the main source of the ore-forming fluids. However, the investigated rocks have relatively high Sr/Y ratios, indicating substantial magma fractionation at lower crustal levels. As a result, our preferred model is a combination of the two endmember models introduced at the beginning, with most magma fractionation having occurred in the lower crust, and residual melts then having ascended and accumulated at 10-17 km depth, where they continued to crystallise without much crystal–liquid separation, before some of the magmas raised to shallow levels and were quenched to porphyries.

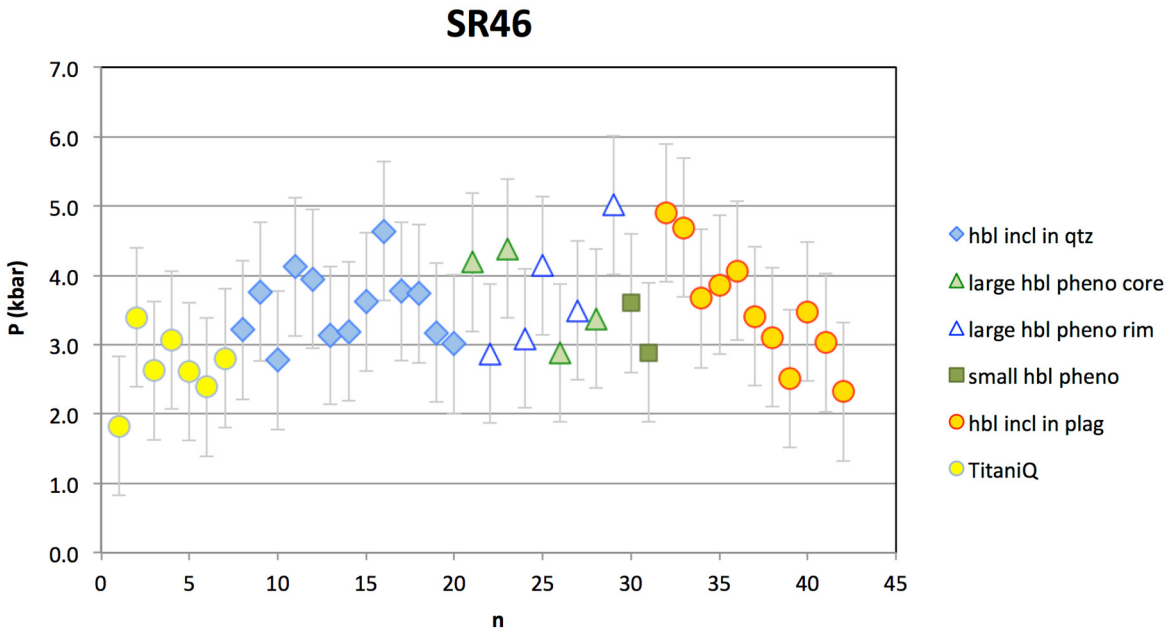

Fig. 3.2-18: Titanium-in-quartz (TitaniQ) and Al-in-hornblende pressures obtained for one of the 13 investigated porphyries. hbl - hornblende; incl – inclusion; qtz – quartz; pheno – phenocryst; plag – plagioclase.

o. *Constraints on sediment sources and glacial processes from the geochemistry and radiogenic (Sr, Nd, and Hf) isotopic compositions of Pleistocene glacial till sediments from Indiana and Missouri (C. Wittkop/Mankato, A. Bouvier and X.-J. Hu)*

Glacial tills are unsorted and unstratified sediments that are directly deposited by the action of a glacier. They consist of a mixture of a variety of materials, including clay, silt, sand, gravel, and boulders, that have been picked up and carried by moving ice. Their composition and age help us to track changes in Earth's climate over geological time. We prepared 8 North American glacial till samples for trace element and Sr-Nd-Hf isotope analysis at the BGI isotope geochemistry laboratory. The till samples included a set from Missouri (MO) USA that are the oldest known Pleistocene tills in North America, dating to approximately 2.4 Ma. A second set of samples from Indiana (IN) USA includes Middle Pleistocene tills that likely range in age from ~ 0.8 to ~ 0.15 Ma. Prior to dissolution, ~ 200 mg samples were leached using a two-step procedure for carbonate and Fe-oxide dissolution in sodium acetate (50 °C for 48 h) and hydroxylamine hydrochloride in acetic acid (room temperature for 48 h), respectively. At this stage, 3 samples with higher ZrO_2 contents (from XRF) were split with half of the mass placed in individual Parr vessels to dissolve refractory phases such as zircons. After dissolution in HF-HNO_3, $HClO_4$ and HCl, a 10 % aliquot was set aside for ICP-MS trace element analysis, and the remainder was processed for Sr and Nd, and Hf extraction using a 4-step ion exchange column protocol. Isotope ratio analyses of Sr, Nd, and Hf of till samples, standards and bulk-rock reference materials were performed using a Thermo Neoma MS/MS Multi-Collector (MC) ICP-MS equipped with an ESI Apex Omega high-sensitivity desolvating nebuliser at the BGI.

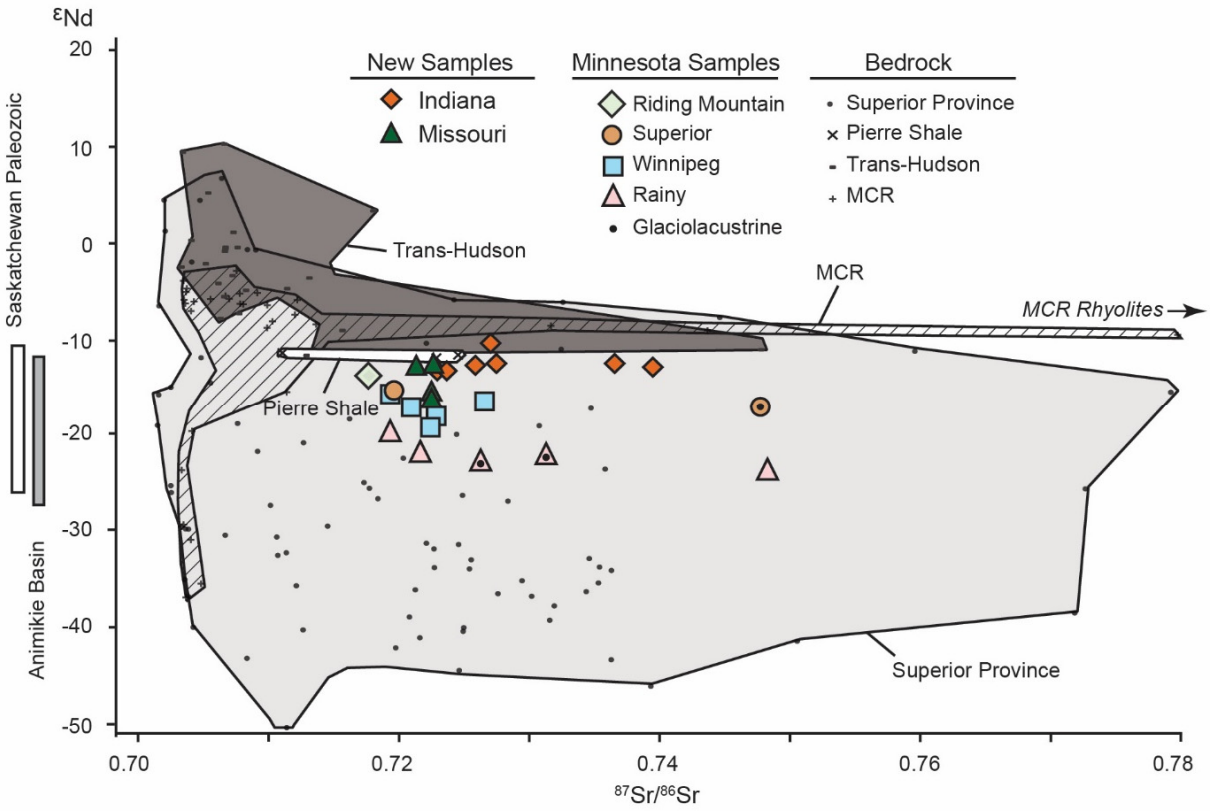

Fig. 3.2-19: εNd-Sr isotopic data for regional bedrock sources compared with glacial samples with new samples from MO and IN compared with previous till samples from MN and bedrocks (MCR = Midcontinent Rift). Bedrock whole rock data are from the GEOROC database, excluding komatiites. The $^{143}Nd/^{144}Nd$ isotope ratios are expressed in the ε-notation, which is a deviation from CHUR in parts per 10000 (Chondritic Uniform Reservoir with a value of 0.512630).

Figure 3.2-19 compares the Sr and Nd isotopic compositions of the MO and IN samples against a previously analysed sample set from Minnesota USA (MN). The MN samples represent the youngest (~ 20-40 Ka) and most lithologically diverse materials. In Sr-Nd isotope space, each of the regions plots in distinct zones consistent with their provenance. Samples from MO represent Cenozoic and Mesozoic sediments from the Midcontinent; IN samples appear to be influenced by Proterozoic intrusive rocks of the Sudbury and Grenville provinces of Canada. Initial interpretation of till sample isotope composition versus a compilation of North American sediments appears to support a relatively late (Mid-Pleistocene or later) unroofing of the Canadian Shield, with secondary influences from source rock provenance (IN) and basement uplift in the Rocky Mountain region (MO). The Hf-Nd isotope relationships indicate that the IN and MO samples are, for the most part, representative of the rocks they are eroded from, with minimal influence of sediment reworking.

3.3 Mineralogy, Crystal Chemistry and Phase Transformations

Through their chemical reactions and phase transformations, minerals shape the geophysical structure of the Earth's interior and modulate the processes that operate in planetary interiors. The chemical and crystallographic characteristics of minerals, in turn, may retain a record of the conditions under which a mineral formed and, in some cases, open up possibilities for technological applications. The contributions in this section explore the behaviour of minerals from properties on the atomic scale to the impact on geochemical cycles.

Phase diagrams are central to the study of materials at high pressures and extreme temperatures, both in the context of deep-Earth research and to tune material properties for technological applications. To better understand the behaviour of the discontinuity in seismic wave speeds at depths around 660 km in the Earth's mantle, Chanyshev *et al.* performed experiments on the composition $MgSiO_3$. The results of their multianvil press experiments show that the phase boundary between the minerals akimotoite and bridgmanite is located at pressures that correspond to depths significantly above the 660-km discontinuity. The effects of aluminium and iron, however, may shift the phase boundary closer to the observed depth of the 660-km discontinuity in hot regions of the mantle. The maximum amount of ferrous iron (Fe^{2+}) that may be incorporated into bridgmanite is limited by the solubility of the component $FeSiO_3$. Zippoli *et al.* studied the solubility of this component in bridgmanite by transforming synthetic olivine compositions with different iron contents to mixtures of bridgmanite and ferropericlase in a multianvil press. The results indicate that the solubility of ferrous iron in bridgmanite might be higher than previously reported. Iron oxides are known for their diversity in terms of stoichiometries, crystal structures, and physical properties. Li *et al.* synthesised single crystals of Fe_5O_6 and mapped the phase diagram of this compound to high pressures and to temperatures as low as 55 K using diamond anvil cells. Based on their analysis of X-ray diffraction patterns, Li *et al.* identified four different polymorphs of Fe_5O_6 two of which show charge-ordering phenomena. Hydrous minerals that form in subducted slabs may transport H_2O all the way into the lower mantle. To better constrain the phase relations of hydrous minerals in metasediments and metabasalts at pressures and temperatures of the lower mantle, Song *et al.* studied the system Al_2O_3-SiO_2-H_2O by means of multianvil press experiments. Based on their experimental results, they constructed a reaction grid that extends to significantly higher pressures than the results of previous studies on this system.

The extreme pressures and temperatures that prevail in planetary interiors may result in the formation of compounds that are otherwise unknown. This holds true even for seemingly simple chemical systems with only a few different elements. The chemistry of the interiors of the planets Neptune and Uranus, for example, is dominated by the four elements carbon, hydrogen, nitrogen, and oxygen. Using diamond anvil cells in combination with laser heating and X-ray diffraction, Dubrovinsky *et al.* studied the ternary C-N-H system and reported the crystal structures of two new compounds that are based on networks of CN_4 tetrahedra. Pantousas *et*

al. discovered a new phase in the system H-C-O-Si-Ca by applying multi-grain X-ray diffraction to a sample in a laser-heated diamond anvil cell at the ESRF synchrotron facility. They found that the mineral davemaoite, $CaSiO_3$, may react with carbon to produce a new, hydrous calcium carbonate compound under hydrous conditions and at the pressures and temperatures that correspond to those at the core–mantle boundary in the Earth. By using similar techniques based on brilliant synchrotron X-ray radiation, Man *et al.* characterised a new iron sulphide phase, $Fe_{4+x}S_3$, on the iron-rich side of the Fe-S system that they found when simulating conditions of the Martian core. Inclusions of calcium phosphate minerals in natural diamonds might provide a glimpse into the budget of rare earth elements in the Earth's interior. The phase stability of calcium phosphate minerals such as merillite and tuite at high pressure may help to constrain the origin of such inclusion in the upper mantle. Novais-Rodrigues *et al.*, carried out high-pressure experiments in a multianvil apparatus to investigate the phase relations of complex phosphates at high-pressure conditions.

High-quality samples of high-pressure minerals are needed to characterise their structural and physical properties under conditions of the Earth's interior. The coupled substitution of $Si^{4+} = Al^{3+} + H^+$ in the rutile-structured SiO_2 phase stishovite, for example, may control the solubility of hydrogen in stishovite, which may act as a host for H_2O in basaltic compositions under conditions of the Earth's lower mantle. Hamadi *et al.* report the synthesis of a polycrystalline sample of Al-bearing stishovite in a multianvil apparatus that may be used to characterise bulk physical properties at high pressures in the future. Davemaoite, perovskite-structured $CaSiO_3$, is a potential candidate for storing H_2O in pyrolitic compositions at the Earth's lower mantle. Beyond that, the elastic properties of this presumably abundant mantle mineral are important for better understanding the seismic structure of the Earth's mantle. Because the mineral is unquenchable to ambient conditions, Wang *et al.*, synthesised davemaoite *in situ* in a diamond anvil cell by using a recently installed CO_2 laser-heating system at BGI.

At the microscale, the crystal-chemical properties and behaviour of minerals may be examined by transmission electron microscopy (TEM). At BGI, TEM has contributed to many important discoveries and remains an indispensable tool, as demonstrated by the last three contributions to this section. The direct view of atomic columns in high-resolution scanning transmission electron microscopy (STEM) is one of the most powerful tools to detect cation distributions and structural defects in crystalline materials. Miyajima *et al.* applied high-angle annular dark-field STEM to image the distribution of ferric iron (Fe^{3+}) and aluminium cations in bridgmanite and found that ferric iron prefers the larger crystallographic site with eight-fold coordination. Using *ab initio* computations, Yao *et al.* explored modular structure models for compounds of the tetradymite series with compositions of Bi_xTe_y and compared simulated to observed STEM images and electron diffraction patterns to validate their results. Even large-scale geological processes may leave an imprint on the domain structure of minerals. To evaluate the timescale of fluid exchange in subduction zones, Fukushima *et al.* simulated the time-dependent growth of antiphase domains in omphacite and suggested that episodes of fluid infiltration that last for less than 100 kyr may be resolved by analysing antiphase domains in natural omphacite.

a. *Phase relations in the $MgSiO_3$ system in plume zones near the 660-km seismic discontinuity (A. Chanyshev, N. Purevjav/Seoul, D. Bondar, H. Tang/Changchun, H. Fei/Hangzhou, L. Wang, F. Wang, E.J. Kim/Gongju, D. Liu/Wuhan, T. Ishii/Misasa, S. Bhat/Hamburg, R. Farla/Hamburg and T. Katsura)*

The 660-km seismic discontinuity (D660) is a global feature of the Earth's mantle and provides insights into mantle structure and dynamics. D660 is usually attributed to the dissociation of ringwoodite to bridgmanite and periclase. Many seismic studies have shown that D660 is elevated in hot plume zones and depressed in cold subduction regions. This elevated D660 in hot plume zones was previously interpreted by the negative Clapeyron slope (dP/dT) of the ringwoodite dissociation, but our recent experimental study revealed that this dissociation boundary in the Mg_2SiO_4 composition has an almost neutral Clapeyron slope. Therefore, an alternative explanation of the D660 elevation in plume zones is needed.

A possible interpretation is the majorite-bridgmanite transition. Previous experimental and computational studies have shown that this transition in the $MgSiO_3$ system occurs at slightly lower pressure than the ringwoodite dissociation at plume conditions (2200-2400 K) near the D660 (≈ 23.4 GPa). We re-investigated the $MgSiO_3$ system at 2200-2350 K and 17.4-20.3 GPa using an advanced multianvil technique with *in situ* X-ray diffraction. A key point of our technique is the determination of the phase transition boundary by balancing the phase transition's forward and reverse reactions *in situ*.

We found that in the studied temperature range with increasing pressure, $MgSiO_3$ transforms first from garnet to akimotoite at 17.4-18.7 GPa and then from akimotoite to bridgmanite at 20.2-20.3 GPa. The determined akimotoite-bridgmanite boundary agrees with our previous experimental results at 1250-2040 K (Fig. 3.3-1). The akimotoite-bridgmanite boundary at

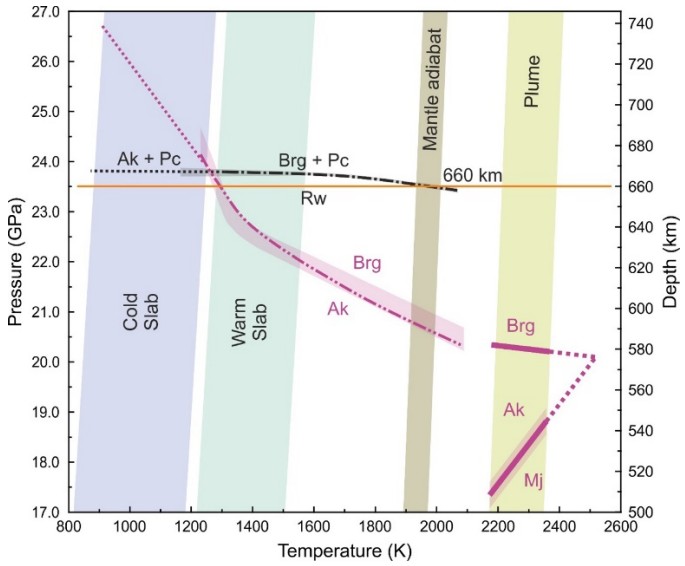

Fig. 3.3-1: Combination of the present results (bold solid violet curves) with our previous data (dot-dashed black and violet curves).

2200-2350 K has an almost neutral slope of -0.6 MPa/K, and the garnet-akimotoite boundary has a positive steep slope of 8.8 MPa/K. The triple akimotoite-bridgmanite-garnet point is located at around 20.1 GPa and 2520 K by linear extrapolation of the determined boundaries.

The elevated D660 in plume zones cannot be explained by the akimotoite-bridgmanite transition in $MgSiO_3$. However, bridgmanite in the lower mantle at plume conditions contains significant amounts of Al and Fe, and the akimotoite-bridgmanite transition in an Al,Fe-rich system occurs at higher pressures than in the pure $MgSiO_3$ system. We, therefore, propose that the elevated D660 beneath plume zones is caused by the Al,Fe-rich akimotoite-bridgmanite transition.

The Clapeyron slope of the phase transition boundary of major mantle minerals affects mantle convection. If the dP/dT of a phase transition is positive or negative, the phase transition enhances or impedes mantle convection, respectively. The determined akimotoite-bridgmanite boundary at 2200-2400 K has an almost neutral slope, meaning that this transition has no effect on mantle convection beneath plume zones.

b. *Maximum iron content of $(Fe^{2+},Mg)SiO_3$ bridgmanite (M. Zippoli, A. Chanyshev and T. Katsura)*

Understanding the mineralogy and chemistry of Earth's lower mantle is crucial for insights into its evolution and dynamics. $(Mg,Fe^{2+})SiO_3$ bridgmanite (Bdm), the most abundant mineral in the lower mantle, plays a key role in shaping the stability of mineral assemblages in this region. In the existing literature, there is a clear discrepancy between older studies and more recent ones, where older studies report lower contents in the maximum solubility of ferrous iron in Bdm (φ_{Fe}^{Bdm}) compared to recent studies.

In this study, phase relations in the $MgSiO_3$-$FeSiO_3$ system have been investigated at 24 GPa and 2000 K with the multianvil apparatus (MAP) technique, focusing primarily on the maximum solubility of ferrous iron in bridgmanite. Experimental runs of 24 hours were conducted with synthesised olivine compositions of varying iron content (Fo70, Fo60, Fo50, Fo40) in iron capsules. Phase assemblages of Bdm + ferropericlase (Fper) and Bdm + Fper + stishovite (Sti) were identified using micro-focused X-ray diffraction (MF-XRD) and scanning electron microscopy (SEM) equipped with energy dispersive spectroscopy (EDS) (Fig. 3.3-2). Metallic iron was observed in the run products, suggesting potential challenges in controlling oxygen fugacity.

Our results show that φ_{Fe}^{Bdm} is 17 mol. % at 24 GPa and 2000 K. However, data for Fper were scattered, possibly due to oxygen fugacity issues or the capsule material used. Consequently, the iron partition coefficient values deviate from those reported in the literature, and we could not verify the reason for this discrepancy. A shorter 1-hour experiment revealed an assemblage of ringwoodite (Rwd) + Fper + Sti with metallic iron but no Bdm, indicating the pressure may

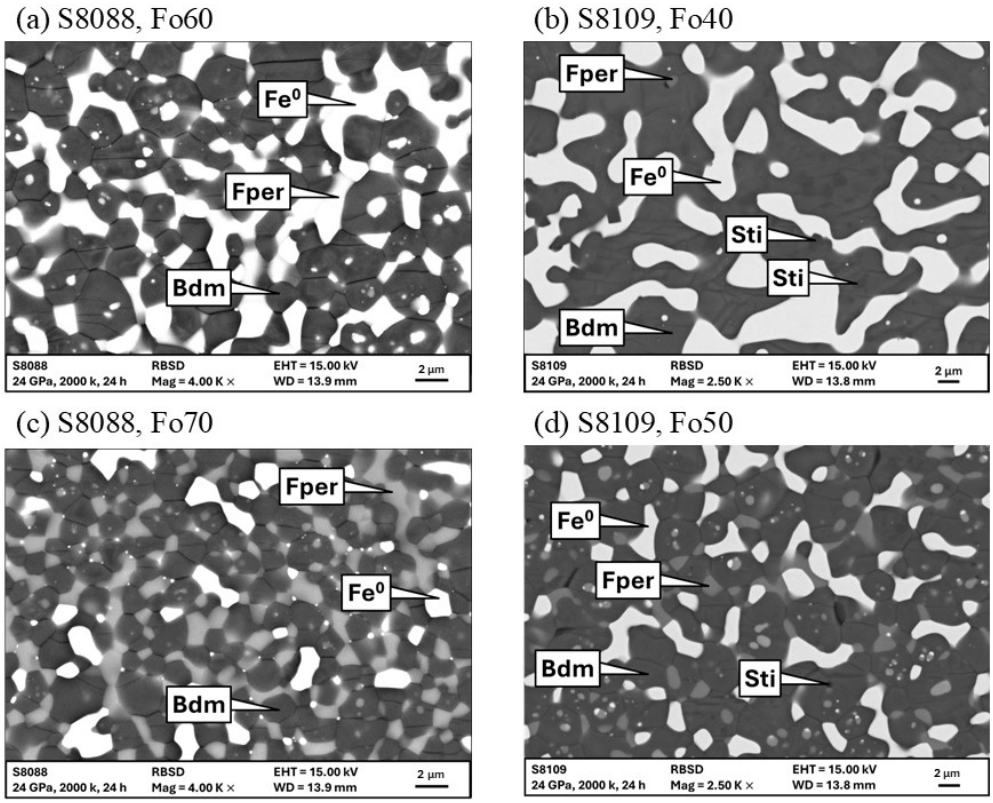

Fig. 3.3-2: SEM images obtained with a Robinson Backscattered electron Detector (RBSD) of the recovered samples S8088 (a,c) and S8109 (b,d). Bdm – bridgmanite, Fper – ferropericlase, Sti – stishovite, Fe^0 – metallic iron.

have been lower than intended. Our findings support recent studies suggesting higher Fe^{2+} solubility in Bdm compared to earlier MAP studies. Further research is necessary to resolve discrepancies in Fper data and to understand the complex phase relations in the MgO-FeO-SiO_2 system.

c. *High-pressure low-temperature phase diagram of Fe_5O_6 (X. Li/Grenoble, D. Vasiukov/Lund, L. Man, H. Tang, C. Qian, T. Boffa Ballaran, F.I. Akbar, E. Kolesnikov/Münster, K. Glazyrin/Hamburg, S. Yaroslavtsev/Grenoble, G. Aprilis/Grenoble, D. Bessas/Grenoble, A. Chumakov/Grenoble, L.S. Dubrovinsky, C. Sanchez-Valle/Münster and I. Kupenko/Grenoble)*

Understanding unusual transformations in iron oxides, accompanied by peculiar changes in atomic and electronic structures, is essential not only for geoscience but also for condensed matter physics and applied technologies. Here, we investigated the high-pressure low-temperature phase diagram of a novel mixed-valent iron oxide with an unconventional Fe_5O_6 stoichiometry utilising single-crystal X-ray diffraction. We find one charge-disordered and two charge-ordered phases in our experiments (Fig. 3.3-3a). We reveal that, similar to the situation in Fe_4O_5, pressure can tune the charge-ordering pattern and affect the ordering temperature of Fe_5O_6.

High-quality single crystals of Fe_5O_6 were synthesised at 13-15 GPa and 1200-1400 °C using multianvil presses at BGI. The crystals were prepared from stoichiometric mixtures of Fe_2O_3 and Fe. Under ambient conditions, Fe_5O_6 adopts an orthorhombic *Cmcm* structure, where iron cations occupy linear chains of octahedral (Fe1 and Fe2) and trigonal prismatic (Fe3) sites (Fig. 3.3-3b). Bond-valence-sum (BVS) analysis of the Fe-O bond lengths in this structure yields BVS values of 2.59(8), 2.48(6), and 1.94(5) for the Fe1, Fe2, and Fe3 atoms, respectively. These results indicate that the larger trigonal prismatic Fe3 sites are occupied by Fe^{2+} ions, while the two inequivalent octahedral sites are filled with a mixture of Fe^{2+} and Fe^{3+} ions.

During the experiments, we performed high-pressure and low-temperature X-ray diffraction of Fe_5O_6 in diamond anvil cells and a cryostat up to 60 GPa and down to 55 K using the facilities of the P02.2 beamline. Upon compression at room temperature, we identified two phase transitions. Fe_5O_6 undergoes the first phase transition at ~ 4 GPa from the original orthorhombic *Cmcm* phase (a = 2.877 Å, b = 9.917 Å, c = 15.340 Å, V = 437.75 Å^3) to a monoclinic $P2_1/c$ (a = 5.146 Å, b = 15.242 Å, c = 5.690 Å, β = 106.00°, V = 428.9630 Å^3; Figs 3.3-3b and 3.3-3c). After the phase transition, a well-ordered array of superlattice reflections appears in the diffraction patterns. Fe-Fe distances in octahedral chains in this phase display a pronounced separation into pairs, resulting in the formation of dimers. The second phase transition happens at ~ 20 GPa from $P2_1/c$ to $C2/m$ space group with five distinct sites for Fe ions (Fig. 3.3-3e) and with the lattice parameters: a = 9.581 Å, b = 2.796 Å, c = 15.380 Å, β = 106.55°, V = 394.8344 Å^3. The superlattice reflections disappear in the $C2/m$ phase, indicating that it is a charge-disordered phase. This phase can be preserved up to at least 60 GPa (the highest pressure in this study).

Upon cooling down, Fe_5O_6 undergoes another phase transition from the orthorhombic *Cmcm* to the monoclinic $P2_1/m$ at 275 K and ambient pressure (Figs 3.3-3a and 3.3-3d). Unlike the $P2_1/c$ phase, the $P2_1/m$ phase adopts dimers in both octahedral and prismatic chains. The formation

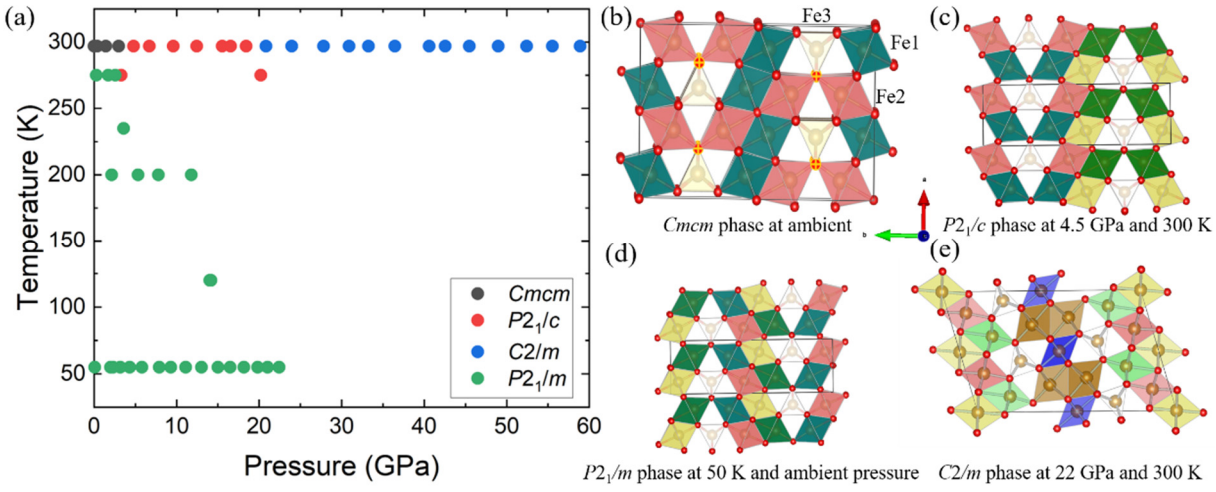

Fig. 3.3-3: (a) The high-pressure low-temperature phase diagram of Fe_5O_6. (b-e) Crystal structures of various phases of Fe_5O_6 found at the indicated pressures and temperatures.

of dimers in the prismatic chains may be related to the electron hopping between different Fe sites. Our experiment reveals that pressure can tune the charge-ordering patterns and affect the ordering temperature.

d. *Phase relations in the system Al_2O_3-SiO_2-H_2O at pressures up to 33 GPa (Y. Song, X. Guo/Guiyang, A. Chanyshev, F. Wang and T. Katsura)*

The lower mantle serves as a significant potential water reservoir on Earth, playing a crucial role in the deep-water cycle and geochemical evolution. Subduction is a key process in the hydration of the lower mantle over geological timescales. Subduction zones act as conduits, transporting water-rich slabs into the Earth's interior. As these slabs descend, hydrated minerals release water, some of which reaches the transition zone and even deeper regions of the mantle. This mechanism ensures a continuous supply of hydrous components to the lower mantle.

However, the major lower-mantle minerals, such as bridgmanite and ferropericlase, can incorporate only limited amounts of water. Consequently, water is predominantly transported into the lower mantle as hydrous minerals within the pelitic and basaltic layers of subducted slabs. Understanding the phase relations of H_2O-bearing minerals in silicic and mafic systems is therefore essential for deciphering water transport into the lower mantle via subduction. The Al_2O_3-SiO_2-H_2O system is a simplified model that simulates the pelitic and basaltic compositions. Consequently, its phase relations have to be reliably determined under lower-mantle conditions. Previous studies investigated this system up to 26 GPa, which is just the topmost part of the lower mantle. Therefore, the investigation of phase relations in this system in a wider pressure range is desired. We are experimentally investigating the phase relations to higher pressures. This contribution reports the phase relations in this system at pressures from 23 to 33 GPa.

Experiments were conducted using multianvil presses. Mixtures of Al_2O_3, $Al(OH)_3$, and SiO_2 powders with 6 different ratios have been prepared for starting materials. They were sealed in a Pt capsule, compressed to a desired pressure and heated to a desired temperature for a certain time. Run products have been analysed using a microfocused X-ray diffractometer and a scanning electron microscope. Phase relations have been constructed by analysing the experimental data based on Schreinemaker's analysis.

The current results are shown in Figure 3.3-4. Observed phases are stishovite, corundum, δ-AlOOH, phase egg ($AlSiO_3(OH)$), phase D ($Al_2SiO_4(OH)_2$), and liquid. Water is stored in δ-AlOOH, phase egg ($AlSiO_3(OH)$), and phase D under subsolidus conditions. The stability limits of these minerals are shown by the blue, green, and red lines, respectively, in Figure 3.3-4. δ-AlOOH is stable at relatively low temperatures. The stability limit is located at 1400 °C at 15 GPa, and shifts to a higher temperature of 1600 °C with increasing pressure to 35 GPa. δ-AlOOH contains a small amount of SiO_2 and decomposes to corundum and liquid together with either phase D or phase egg at pressures above and below 23 GPa, respectively. Compared to the previous study, the stability limit of δ-AlOOH is located at lower temperatures by 100 ~

200 K. The stability field of phase egg is much wider than suggested by the previous study. This phase is stable at pressures up to approximately 30 GPa at temperatures lower than 1500 °C. The high-pressure stability limit of phase egg is located at 30-31 GPa and constrained by the reaction phase egg = δ-AlOOH + stishovite + corundum at temperatures up to 1500 °C. The high-temperature stability limit is located at 1900-2100 °C and is constrained by the reaction phase egg = stishovite + corundum + liquid at pressures up to 25 GPa. Between these two limits, the stability is constrained by the reaction egg = phase D + stishovite + corundum. This reaction has a steep, negative slope. Phase D is stable at 21 GPa and 800 °C, with the pressure stability limit increasing with temperature and reaching 24 GPa at 2000 °C. Beyond this point, the temperature stability limit increases rapidly with increasing pressure. At 33 GPa, phase D can be stable at 2300 °C but decomposes at 2500 °C.

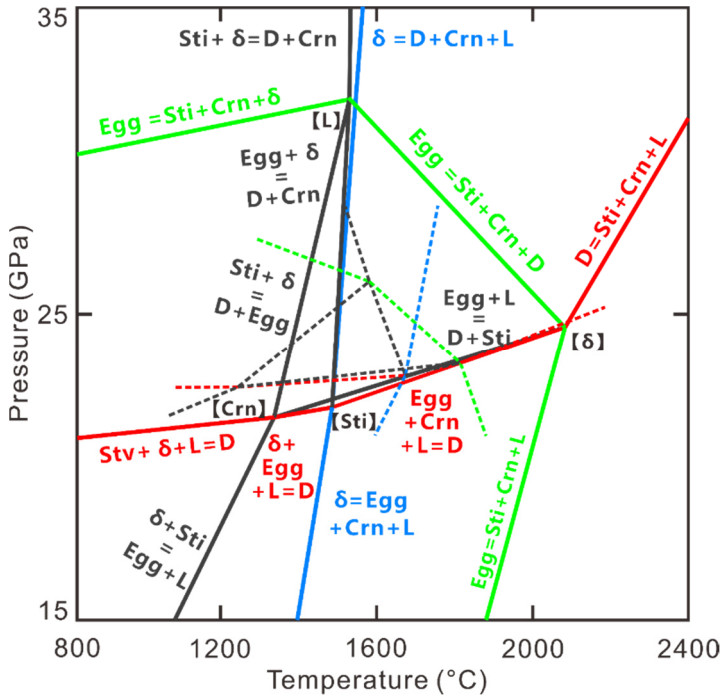

Fig. 3.3-4: Schreinemaker's bundle in the system Al_2O_3-SiO_2-H_2O at pressures from 15 to 35 GPa. Abbreviations are as follows. Sti: stishovite; Crn: corundum; δ: δ-AlOOH; Egg: phase egg; D: phase D. The solid lines indicate the univariant reactions with four phases estimated in this study. The dashed lines indicate those proposed in a previous study. The blue, green, and red lines indicate the critical reactions that define the stability limits of δ-AlOOH, phase egg, and phase D, respectively. Mineral abbreviations in square brackets indicate invariant points of five-phase coexistence where the mineral in brackets is absent.

These results suggest that the pelitic and basaltic layers of subducted slabs are likely capable of transporting water into the deep lower mantle. Furthermore, the pelitic and basaltic systems can contain water at temperatures higher than the normal mantle geotherm. Therefore, water can reach and stay as hydrous minerals in the deep lower mantle.

e. *Carbon-nitrogen compounds at interiors of the giant planets (L.S. Dubrovinsky, W. Zhou, Y. Yin, A. Aslandukova and N.A. Dubrovinskaia)*

The chemistry between the elements carbon, hydrogen, nitrogen, and oxygen is quintessential to a vast array of research fields. These elements play a fundamental role as key ingredients of life, our quest to produce ever more performing technological materials, and our understanding of extraterrestrial bodies. Indeed, the ice giants Uranus and Neptune consist mainly of these four elements. In their interiors, high-pressure (HP) and high-temperature (HT) conditions prevail. Under these conditions, CH_4, NH_3, and H_2O molecules are expected to be broken apart and assembled in fully extended covalent network structures with properties anticipated to explain many of the peculiarities of such extraterrestrial bodies. Before this complex quaternary system can be investigated, it is crucial to improve our understanding of the simpler binary and ternary systems, essential to benchmark theoretical calculations and guide future experiments.

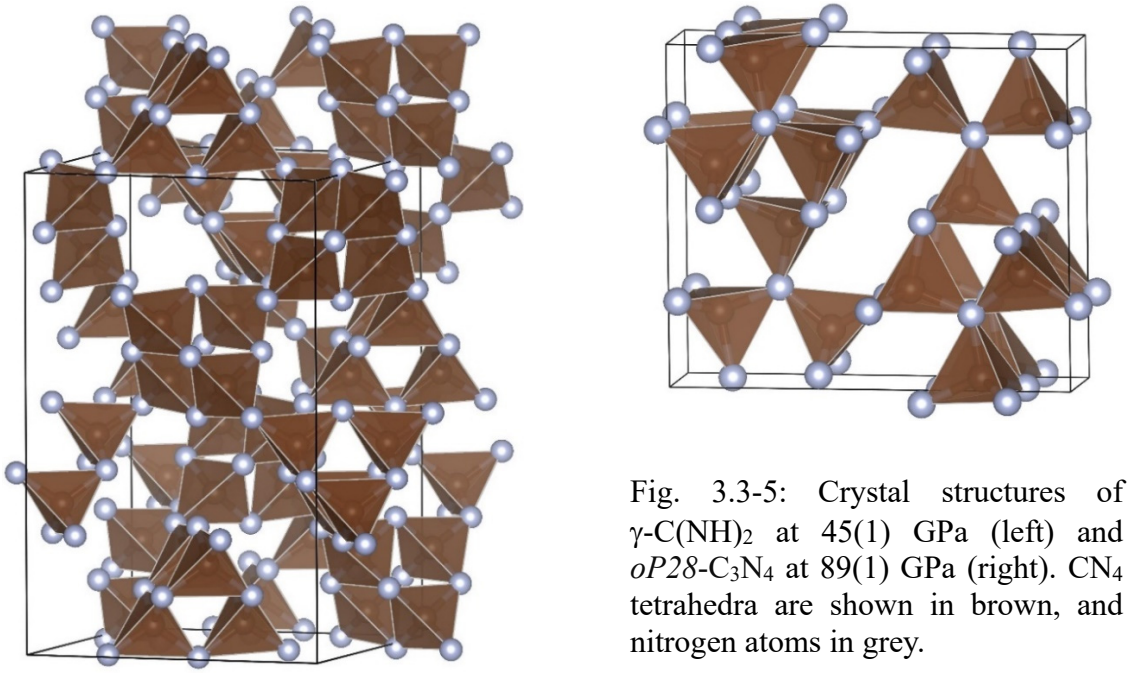

Fig. 3.3-5: Crystal structures of γ-$C(NH)_2$ at 45(1) GPa (left) and *oP28*-C_3N_4 at 89(1) GPa (right). CN_4 tetrahedra are shown in brown, and nitrogen atoms in grey.

Exploring the carbon-hydrogen system, predictions indicate that at high temperatures and pressures, the lifetimes of C–C and C–H molecular bonds become very short. As a result, hydrocarbon molecules exist only briefly, making it more accurate to think of the system as a mixture of carbon and hydrogen atoms rather than stable molecules. Under the extreme conditions found in icy planets, carbon and hydrogen separate, leading hydrocarbons to transform into diamond and a hydrogen-rich phase. In the context of icy planets, diamonds engendered from such transformations boast a density surpassing that of the surrounding ices. The gravitational forces at play propel these diamonds to greater depths within the planet, imparting an additional heat source that can significantly influence the evolution and internal dynamics of these celestial bodies. However, interiors of icy planets are chemically more complicated, and the effects of other elements, particularly nitrogen, in addition to carbon and hydrogen, should be considered.

It is established by now, due to the work of several groups, including ours, that at pressures up to approximately 45 GPa and high temperatures, compounds consisting of C-N-H bonded atoms transform into dense phases built from sp^3-hybridised carbon and sp^2-hybridised nitrogen (such as dwur-$C_2N_2(NH)$, α and β $C(NH)_2$). At pressures above approximately 70 GPa and temperatures above 1500 K, carbon and nitrogen form different dense CN, C_3N_4, and CN_2 compounds. To apply these results to the analysis of the phase composition of planetary interiors containing C, N, and H, the next step would be to check if C-N-H compounds could be synthesised from hydrocarbons and nitrogen, and if these C-N-H compounds exist at pressures above approximately 70 GPa.

Here, we conducted experiments on a mixture of the hydrocarbon naphthalene ($C_{10}H_8$) and nitrogen at approximately 45 GPa, and the hydrocarbon anthracene ($C_{14}H_{10}$) and cyanuric triazide (CTA, C_3N_{12}) up to ~ 90 GPa. Based on single-crystal X-ray data analysis, we demonstrated the formation of carbon nitride imide dwur-$C_2N_2(NH)$ and the new phase γ-$C(NH)_2$ at a pressure of 45 GPa (Fig. 3.3-5) as well as a novel orthorhombic carbon nitride *oP28*-C_3N_4 at 89 GPa (Fig. 3.3-5). For all compounds, the positions of carbon and nitrogen atoms were determined and refined, and the amount of hydrogen was inferred based on the analysis of C-N, C-C, and C-N bonds. The study shows that at pressures above ~ 40 GPa, sp^3-hybridised carbon chemically binds with nitrogen, forming CN_4 tetrahedra. At pressures above ~ 70 GPa, even in a hydrogen-rich environment, carbon and nitrogen surprisingly form only binary compounds. This indicates that in the presence of nitrogen, the formation of planets with pure diamond cores is unlikely.

f. *Fate of $CaSiO_3$ in the hydrous lower mantle (A. Pantousas, K. Skrzyńska, A. Pakhomova/ Grenoble and L.S. Dubrovinsky)*

Calcium perovskite, $CaSiO_3$ (Ca-Pv) is the third most abundant mineral of the lower mantle constituting from 6 to 12 wt. %. Recent advances in the deep-water cycle demonstrate that water can be delivered to the deepest portions of the lower mantle, affecting its properties and mineralogy. Even though Ca-Pv has been intensively investigated over the last decades, our knowledge on the fate of Ca-Pv in the presence of water is very limited, also due to the methodological limitations. In continuation of our previous experiments on interactions of Ca-Pv and H_2O at conditions of the lower mantle, we propose to perform *in situ* powder and single-crystal multi-grain X-ray diffraction (XRD) at pressures of 30-120 GPa and temperatures 1500-2900 K and verify the role of the oxygen fugacity in the reactions with B-doped diamond in the Ca-Si-O-C-H system.

The lower mantle represents the largest fraction of the Earth, taking more than 55 % of its volume. The dominant minerals of the lower mantle are (Mg,Fe)O ferropericlase, $(Mg,Fe)SiO_3$ bridgmanite, and calcium perovskite, $CaSiO_3$ (Ca-Pv). In order to understand the geophysical and geochemical behaviour of the lower mantle, these minerals have been studied over the last

decades for their elastic and rheological properties, decomposition reactions, chemistry-structure correlations, *etc*. New interest in these materials is stimulated by the recent discoveries on the deep-water cycle and water storage capacity of the lower mantle. Thus, a number of hydrous phases were reported to be stable up to lower mantle conditions. Other phases appear to be stable up to the deepest portions of the lower mantle or even at the core–mantle boundary. Until now, there is only one published study dedicated to the $CaSiO_3$-H_2O chemical interaction at high pressure and high temperature. Upon laser heating at 30-60 GPa up to 1600 K, no phase change has been observed using powder X-ray diffraction. However, the usage of multi-grain single-crystal XRD in the course of our latest experiment at the beamline ID27 (ES-1442) of the ESRF, allowed us to observe the formation of a new hydrous phase of $Ca(CO_3)(H_2O)$ at 33 GPa (Fig. 3.3-6), formed as a result of laser heating of calcium silicate hydrate (CHS, Ca:Si 1:1, 20 wt. % H_2O) and B-doped diamond. This constitutes the first observation of a hydrous mineral of calcium at the conditions of the lower mantle. Interestingly, this phase was observed only at one pressure point while, at higher pressures up to 120 GPa, we observed crystallisation of Ca-Pv solely. Our working proposition is that the oxidation environment in the system plays an important role in the reactions that are taking place. Thus, depending on the temperature, laser heating may or may not induce the decomposition of H_2O into H_2 and O_2 and thus affect the oxygen fugacity. To verify this theory and to complement the existing data, we perform a series of experiments including laser-heating experiments of CHS (1:1) and B-doped diamond following the same procedure as in the previous experiments in the pressure range 80-120 GPa and also laser-heating experiments on the Ca-Si-O-H system with different precursors providing an excess of O_2, specifically CaO_2 + SiO_2 + H_2O or $CaSiO_3$+H_2O_2 (~ 30 wt. % solution in water).

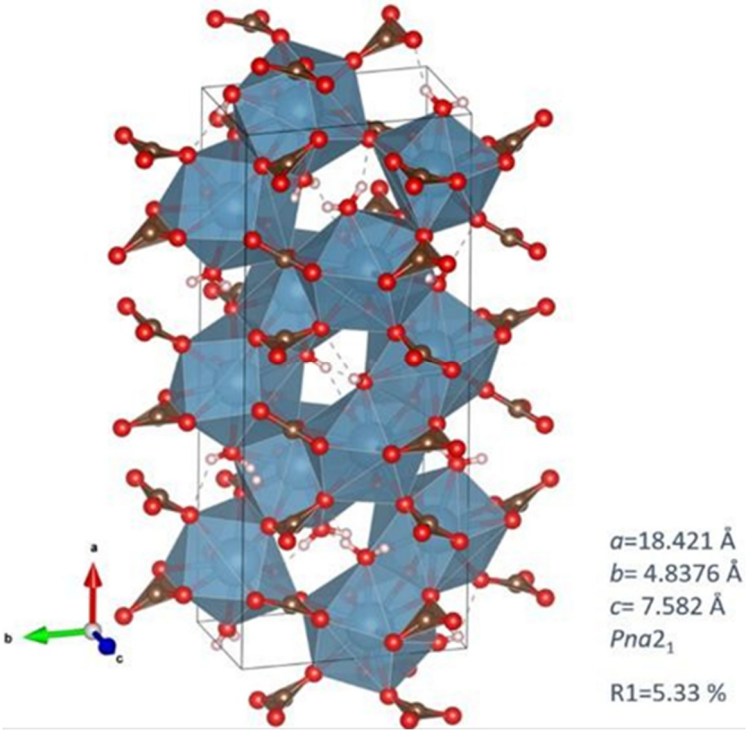

Fig. 3.3-6: The crystal structure (CCDC Deposition Number 2379889) of $Ca(CO_3)(H_2O)$ at 33 GPa as determined by single-crystal XRD at the beamline ID27 (ES-1442) of the ESRF. Ca: blue, O: red, C: brown, H: white

For some experiments, powder of CHS (1:1) is used as a precursor, while for other experiments a stochiometric mixture of Ca and Si oxides is prepared and loaded along with liquid water (or peroxide solution). DACs, equipped with Boehler-Almax diamonds with culets of 250 μm, are used for experiments up to 80 GPa. To maintain high temperatures, the double-sided YAG laser-heating system available at ID27 is used along a B-doped diamond as a coupler. Firstly, each DAC is compressed to the pressure of interest and powder or/and single-crystal XRD are collected prior to heating. The laser power is gradually increased, and powder XRD data (without rotation of the DAC) are collected during the heating. As soon as new reflections appear in the diffraction pattern (indicating that a chemical reaction is initiated and new compound(s) are formed), the sample is quenched. Single-crystal XRD data are collected at the heated spot and around it, mapping the heated area.

The resulting new crystal structures will allow us to extrapolate a chemical pathway of reactions that occur at the temperature and pressure conditions of the Earth's mantle, as well as the behaviour of various elements in the presence of water. This will help us to better understand the deep-water cycle and the water storage capabilities of the mantle.

g. *The discovery of $Fe_{4+x}S_3$ and its stability under Martian inner core conditions (L. Man, T. Boffa Ballaran, W. Zhou, A. Néri, A. Kurnosov, L.S. Dubrovinsky and D.J. Frost, in collaboration with X. Li/Grenoble, J. Chantel/Lille, I. Kupenko/Grenoble, G. Aprilis/Grenoble, O. Namur/Leuven, M. Hanfland/Grenoble, N. Guignot and L. Henry/Saint-Aubin)*

Seismic, geodetic, and cosmochemical evidence point to Mars having a sulphur-rich liquid core. Due to the similarity between estimates of the core's sulphur content and the iron-iron sulphide eutectic composition at core conditions, it has been concluded that temperatures are too high for Mars to have an inner core. Recent low-density estimates for the core, however, appear consistent with sulphur contents that are higher than the eutectic composition, leading to the possibility that an inner core could form from a high-pressure iron sulphide phase. Below pressures of around 14 GPa, the Fe-FeS system is a simple binary eutectic system, and FeS V is the only sulphide phase stable as a liquidus phase on the S-rich side. Beyond 14 GPa, however, the melting phase diagram of the Fe-FeS system becomes more complex, and a range of intermediate iron sulphide phases emerge, including $Fe_{3+x}S_2$, Fe_3S, Fe_2S, $Fe_{12}S_7$, and Fe_5S_2, each appearing under specific combinations of pressure, temperature, and composition. Understanding the crystal structures and densities of these high-pressure sulphide phases is critical for understanding the status and evolution of the Martian core.

In this study, we conducted a series of high-pressure and high-temperature experiments, employing multiple *in situ* and *ex situ* characterisation techniques to investigate the crystal chemistry and melting phase relations in the Fe-FeS system. Using high-pressure single-crystal X-ray diffraction (SC-XRD) following *in situ* synthesis via laser heating in a diamond anvil cell at 15-20 GPa, we identified a new Fe-sulphide structure, which, based on its distribution of crystallographic sites, is best described as $Fe_{4+x}S_3$. This structure, with space group *Pnma*, consists of four edge-sharing Fe-S square pyramids and one partially occupied interstitial Fe

site (Fig. 3.3-7), which allows the stoichiometry to vary from x = 0 to 1. Phases previously synthesised under similar conditions, such as Fe_3S_2 and $Fe_{3+x}S_2$ (with undetermined crystal structures), are likely to share this same structure. *In situ* high-pressure and high-temperature powder X-ray diffraction measurements at a synchrotron multianvil beamline confirmed that $Fe_{4+x}S_3$ is the thermodynamically stable phase in the Fe-FeS system. Although a Martian inner core has not yet been detected, our modelled melting phase relations for the Fe-FeS system indicate that an $Fe_{4+x}S_3$ inner core could crystallise if temperatures at Mars's centre drop below 1960(±105) K. This temperature remains within the estimated range of current conditions for the Martian core.

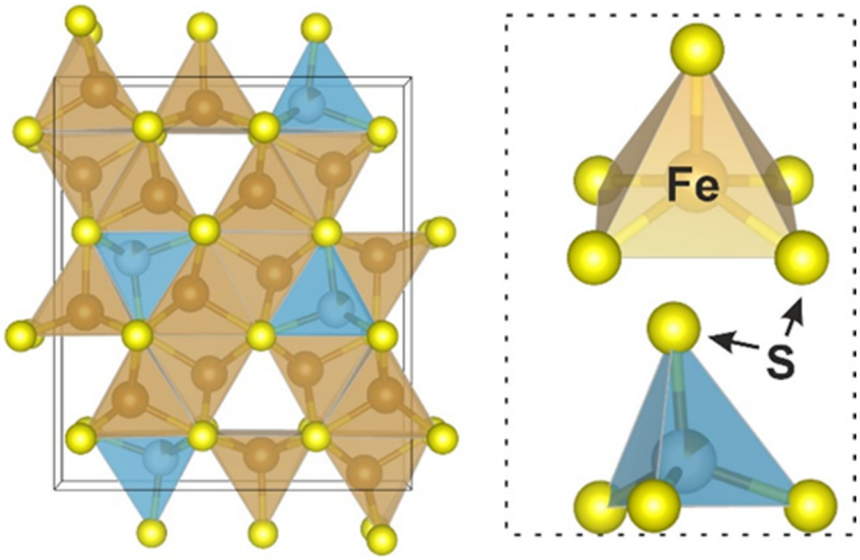

Fig. 3.3-7: The structural model of $Fe_{4+x}S_3$ as determined by SC-XRD (left). The building blocks of $Fe_{4+x}S_3$ consist of four Fe-S pyramids and one semi-occupied Fe-S tetrahedron (right).

h. *The high-pressure conversion of merrillite to tuite in the upper mantle (E. Novais-Rodrigues and F. Nestola/Padova, T. Boffa Ballaran and A.C. Withers)*

Merrillite [$Ca_9NaMg(PO_4)_7$] is commonly present as an accessory phosphate in meteorites and lunar rocks. Its first terrestrial occurrence was reported recently in 2022 in a super-deep diamond from the lower mantle, where it was interpreted to have formed by retrograde reaction from the higher-pressure phase tuite [γ-$Ca_3(PO_4)_2$]. Merrillite and tuite can potentially serve as significant reservoirs for rare earth elements (REE) and large-ion lithophile elements (LILE) in the deep Earth. The phase relations in the Na_3PO_4-$Mg_3(PO_4)_2$-$Ca_3(PO_4)_2$ system need to be better constrained at upper-mantle pressures if we are to understand the significance of the occurrence of merrillite in super-deep diamonds. Previous experimental studies indicate that apatite [$Ca_5(PO_4)_3$(Cl, F, OH)] decomposes into tuite at mantle depths greater than 200-250 km in both basaltic and peridotitic compositions, with tuite remaining stable down to at least 700 km. Whitlockite [$Ca_9Mg(PO_4)_6(PO_3OH)$], which is structurally similar to merrillite, also

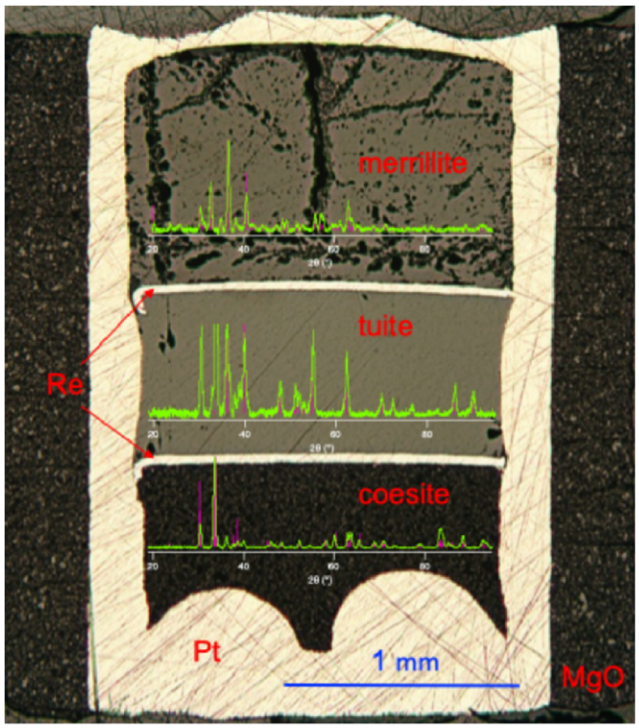

Fig. 3.3-8: Photograph of a capsule from an experiment at 3.5 GPa and 1000 °C. Overlain on the photograph are µ-XRD diffractograms collected from the three sample chambers. The vertical bars mark the peak positions calculated for reference structures for the labelled phases. Some low-angle peaks from the coesite pressure marker are present in the pattern for $Ca_3(PO_4)_2$ tuite in the centre chamber.

transforms into tuite under high-pressure conditions. The phase boundary between anhydrous, whitlockite-structured $Ca_3(PO_4)_2$ and tuite has been investigated and modelled using thermodynamic data. No comparable analysis has yet been conducted for the merrillite-tuite system.

To investigate the phase boundary between merrillite and tuite, high-pressure experiments were performed using a multianvil apparatus. Polycrystalline powders of merrillite were synthesised using a high-temperature solid-state reaction. The starting materials – $CaCO_3$, Na_2CO_3, $(NH_4)_2HPO_4$, and $4MgCO_3{\cdot}Mg(OH)_2{\cdot}5H_2O$ – were mixed and ground in an agate mortar for one hour. The mixture was pelletised under a pressure of 7 kg/cm^2, placed in a platinum crucible, and annealed at 1200 °C for 13 hours under atmospheric conditions. X-ray diffraction confirmed the reaction product as merrillite. The merrillite powder was loaded into Pt capsules. In most experiments, additional layers of $Ca_3(PO_4)_2$ and a pressure marker (either Fe_2SiO_4, $CaGeO_3$ or SiO_2) were added to the sample capsule and separated from each other by Re foil. Experiments were conducted in an 18/11 assembly, using graphite and $LaCrO_3$ furnaces. Post-experiment analysis was conducted using micro-X-ray diffraction (µ-XRD) and scanning electron microscopy (SEM) equipped with an energy-dispersive spectroscopy (EDS) detector for phase characterisation.

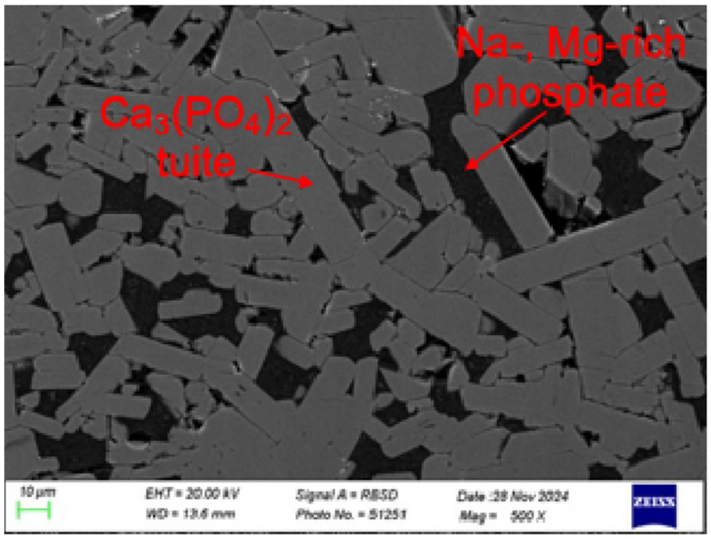

Fig. 3.3-9: SEM backscattered electron image of run products from the merrillite chamber of a capsule from an experiment at 5 GPa and 1300 °C. Tuite with a composition close to $Ca_3(PO_4)_2$ coexists with an Na-, Mg-rich phosphate phase.

At 1000 °C and pressures of 3-4.5 GPa, merrillite was detected, while $Ca_3(PO_4)_2$ in separate chambers of the capsules was present as tuite (Fig. 3.3-8). In experiments at 5 GPa, at 1000 °C, 1300 °C, and 1400 °C, µ-XRD patterns are consistent with the complete conversion of merrillite to tuite. However, SEM analysis of the experiments at 1300 °C and 1400 °C revealed two phosphate phases: 100-µm euhedral crystals of a Ca-rich tuite, together with an interstitial phase containing Ca but enriched in Na and Mg (Fig. 3.3-9). In a higher-pressure experiment (15 GPa, 400 °C), only tuite was identified, with Na and Mg incorporated into its structure. These preliminary observations suggest that at 5 GPa and 1000-1400 °C, Ca-rich tuite coexists with either Na- and Mg-enriched merrillite, or with another Na- and Mg-rich phosphate phase, whileat higher pressures, tuite can contain at least as much Na and Mg as merrillite. Merrillite is stabilised relative to tuite by the addition of a $NaMgPO_4$ component. Further experiments are required to constrain the pressure of the merrillite-tuite transition at higher temperature and to characterise Na and Mg solubility in each phase.

i. *Sintered polycrystals of Al-bearing stishovite: Synthesis and characterisation (M.I. Hamadi, J. Buchen, T. Withers and T. Boffa Ballaran)*

Stishovite, a high-pressure SiO_2 mineral, contributes with more than 10 vol. % to the mineral assemblage of metabasaltic rocks at pressures and temperatures of the Earth's lower mantle and may act as a host for H_2O in the lower mantle. A possible mechanism to incorporate H_2O into stishovite is through the coupled substitution reaction $Si^{4+} = Al^{3+} + H^+$. For this mechanism, the H_2O and Al_2O_3 contents are coupled to each other. However, stishovite may contain up to 2.5 wt. % Al_2O_3 even in a dry system, and hydrous Al-bearing stishovite usually shows molar ratios of Al/H > 1. The incorporation of alumina affects the stability field, density, compressibility,

and other physical properties of stishovite. It remains unclear, however, whether these changes result from the incorporation of either alumina or hydrogen or from the coupled substitution involving both. Since the majority of Al-bearing stishovite studied so far either contain water or have not been analysed for their water content, to understand the effect of Al substitution alone, synthesis of well-characterised dry Al-bearing stishovite samples is needed.

In this study, we synthesised polycrystalline Al-bearing stishovite at 16 GPa and 1600 °C using an almost dry glass sample as the starting material. The SiO_2–Al_2O_3 glass was prepared with a composition close to the eutectic point in the SiO_2–Al_2O_3 system at ambient pressure. The H_2O content of the glass was determined by Fourier-transform infrared spectroscopy to be below 100 ppm by weight. A cylinder was drilled from the bulk glass and loaded into a rhenium capsule, which was then placed inside a standard 10/5 assembly for the subsequent multianvil press experiment. We found that annealing the glass at 16 GPa and 1600 °C for 60 min yielded an assemblage of stishovite and kyanite. The run product was characterised by electron probe microanalysis (EPMA), scanning electron microscopy (SEM), and powder X-ray diffraction.

The results of the characterisation suggest that Al-bearing stishovite with 0.95 ± 0.24 wt. % Al_2O_3 formed together with kyanite (Al_2SiO_5) as a secondary phase (Fig. 3.3-10a). The Al-bearing stishovite synthesised in our experiment displays a significant variation of the Al_2O_3 concentration (Fig. 3.3-10b). On average, however, the synthesised stishovite contains significantly less Al_2O_3 when compared to hydrous Al-bearing stishovite samples. The average Al_2O_3 concentration of our sample is consistent with the previously reported range of Al_2O_3 concentrations for anhydrous Al-bearing stishovite. Further experiments are needed to optimise the synthesis procedure and to synthesise more homogenous Al-bearing stishovite samples. Such samples may then be characterised in terms of their H_2O content and be used in follow-up experiments to determine their physical properties.

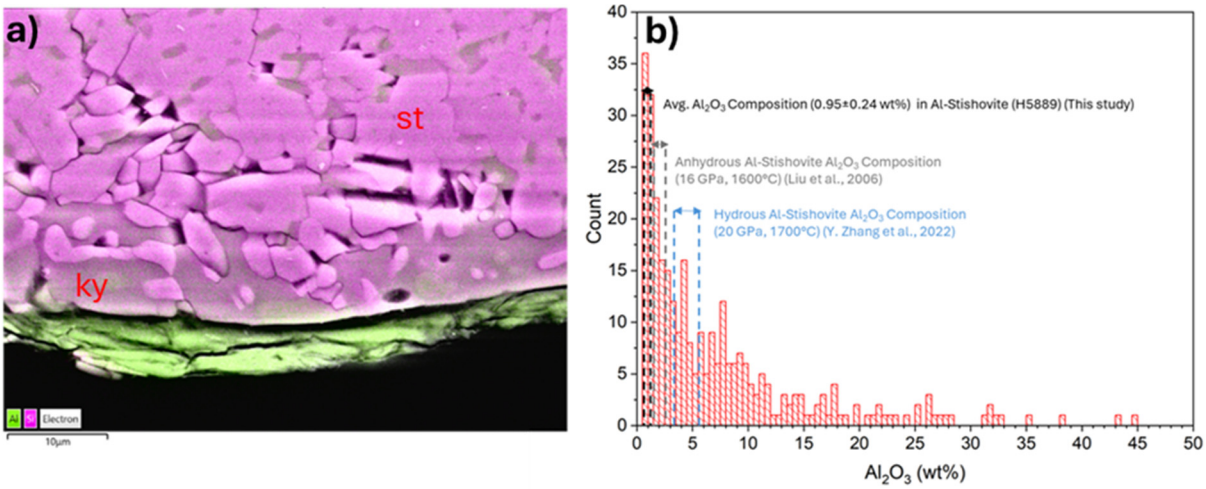

Fig. 3.3-10: (a) Compositional map of the run product (H5889). st = stishovite, ky = kyanite. (b) Histogram of Al_2O_3 contents of the sample H5889 as determined by EPMA. The dashed lines highlight the range of Al_2O_3 contents in stishovite from the previous studies.

j. *Synthesis of $CaSiO_3$ perovskite using CO_2-laser heating. (B. Wang/Oxford, A. Kurnosov, E. Ledoux/Oxford, K. Marquardt/Oxford, T. Boffa Ballaran and H. Marquardt/Oxford)*

$CaSiO_3$ perovskite (CaPv) is the third most abundant mineral obtained in phase equilibria experiments at conditions of the Earth's lower mantle. Studying its elastic properties and phase stability under mantle high-pressure and high-temperature conditions is, therefore, crucial for interpreting seismic observations and refining geodynamic models. However, CaPv is not thermodynamically stable under ambient conditions, making it impossible to retrieve samples from high-pressure laboratory experiments. Not being able to study this mineral at ambient conditions makes it challenging to interpret experimental data obtained at high pressures and temperatures. In previous studies, CaPv has been synthesised and kept in a Multi-Anvil Press (MAP) or a Diamond Anvil Cell (DAC) for *in situ* characterisations. In MAP experiments, pressures are limited to 25 GPa. However, CaPv is expected to be stable up to the lowermost mantle, where pressure will be above 100 GPa. In previous DAC experiments, $CaSiO_3$ has been powdered and mixed with laser absorbers, such as platinum, for synthesis during heating with a Nd: YAG laser.

This study explored the possibility of synthesising CaPv with a well-defined shape in a DAC using CO_2-laser heating. A CO_2 laser operates by exciting CO_2 gas molecules, causing them to emit infrared light at a wavelength of 10.6 μm. CO_2 laser radiation is particularly effective for heating because this wavelength is readily absorbed by many materials. In contrast, Nd:YAG laser operates at a much shorter wavelength (1 μm) in the near-infrared region. This shorter wavelength is less efficiently absorbed by many transparent materials, requiring an additional laser absorber to facilitate heating. The difference in absorption characteristics between these two lasers means that CO_2 lasers generally provide more uniform heating with smaller temperature gradients in synthesising CaPv from transparent $CaSiO_3$ glass.

Pure $CaSiO_3$ glass was initially polished to a thickness of 15 μm and subsequently cut into circular disks with a diameter of 60 μm using a focused ion beam. These disks were then loaded into a DAC equipped with 350 μm culet diamonds. Helium was used as the pressure-transmitting medium (PTM) to ensure quasi-hydrostatic conditions which would be important for measuring the elastic properties of this material once synthetised, and ruby served as pressure calibrant (Fig. 3.3-11a). Before laser heating, the pressure in the DAC was increased to 15 GPa. The sample was then heated to 1500 K for approximately 30 minutes. Initially, the $CaSiO_3$ glass was transparent and positioned near the centre of the cell. After laser heating, cracks developed during crystallisation, causing the sample to become less transparent and shift toward the edge of the cell (Fig. 3.3-11b). X-ray diffraction patterns of the sample were collected post-heating using the newly installed Rigaku X-ray diffractometer at BGI (Fig. 3.3-11c). The results confirmed the formation of a polycrystalline material having the perovskite structure. The successfully synthesised $CaSiO_3$ perovskite (CaPv) sample in a helium PTM will be used in further X-ray diffraction experiments at a synchrotron facility.

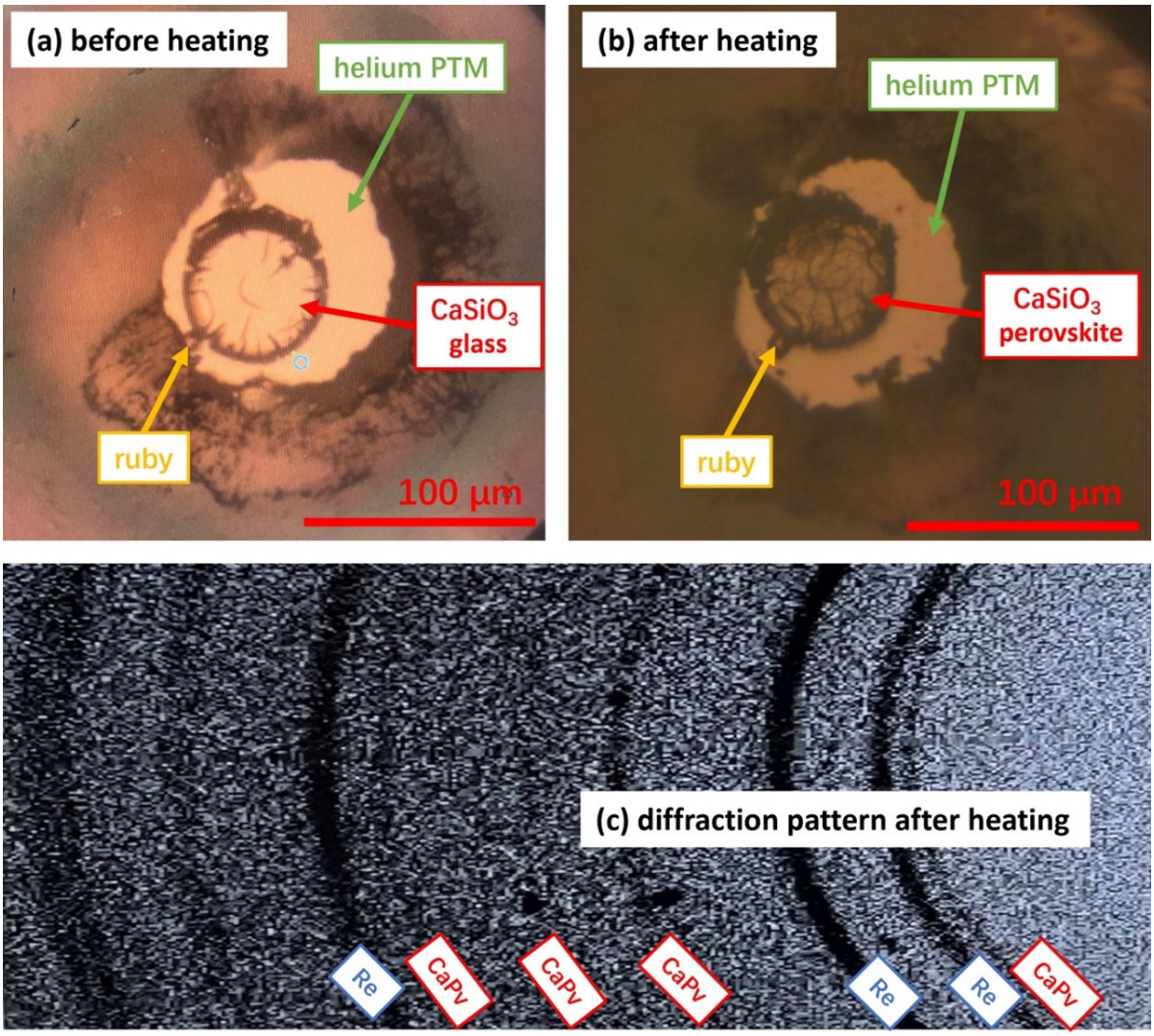

Fig. 3.3-11: (a) $CaSiO_3$ glass before laser heating; (b) $CaSiO_3$ perovskite after laser heating; (c) *in situ* X-ray diffraction pattern of $CaSiO_3$ perovskite using the Rigaku diffractometer at BGI. Helium was used as a pressure-transmitting medium (PTM), and ruby was used for pressure determination.

k. *Direct view of ferric iron distribution in an iron and aluminium-bearing bridgmanite by high-resolution scanning transmission electron microscopy (N. Miyajima, L. Wang and T. Katsura)*

Substitution mechanisms of trivalent cations in bridgmanite can control its physical properties in the Earth's lower mantle. Among them, the behaviour of iron has long been in the spotlight because ferric iron can substitute into both cation sites, the 8-fold coordinated A-site and the 6-fold coordinated B-site, and its electron spin state changes at high pressure. For a basic understanding of the behaviour, we want to know which cation sites iron occupies in the ABO_3 orthorhombic perovskite structure. High-resolution scanning transmission electron microscopy (STEM) with a high-angle annular dark-field (HAADF) detector potentially provides a direct view of individual cation columns in the 2-dimensional projected image showing different

electron scattering cross-sections of thermal diffuse scattering in the target materials at high-angle electron scattering process. This TEM technique is simply called "Z-number contrast imaging of atomic columns in HAADF-STEM". HAADF-STEM imaging has recently been used in high-pressure mineralogy to find relatively high Z-number domains and grains in bulk rock at low magnification (up to several 100k times). The application of "Z-number contrast imaging of atomic columns" at high magnification (more than 1M times), however, is still largely limited to conventional rock-forming silicate minerals in the upper mantle because of the fragile characteristics of the high-pressure minerals under electron-beam irradiation. Despite the limitation, we try to directly observe ferric iron in a synthetic bridgmanite (Bdm) having a $MgSiO_3$ orthorhombic silicate perovskite structure. It is worth noting that conventional high-resolution TEM imaging has been successfully applied to the $MgSiO_3$-endmember orthorhombic silicate perovskite since 1980 (Hassan *et al.*, Mineral. Mag., 60, 799, 1980).

The studied (Fe,Al)-bearing bridgmanite with the mineral formula of $Mg_{0.62}Ca_{0.004}Fe^{3+}_{0.32}Fe^{2+}_{0.05}Si_{0.66}Al_{0.35}O_{2.99}$ was synthesised at 33 GPa and 2300 K for 24 hrs by using a 15-MN ultrahigh-pressure multianvil press (IRIS-15) equipped with the Osugi-type guide-block system. The thin-foil sample for STEM observation was prepared in a dual-beam focussed ion milling machine. HAADF-STEM imaging was performed with a non-Cs-corrected STEM (no spherical aberration corrector in the convergent lens system) operated at 200 kV. The chemical composition and ferric iron content were characterised by energy-dispersive X-ray spectroscopy and electron energy loss spectroscopy, respectively, in the same STEM instrument.

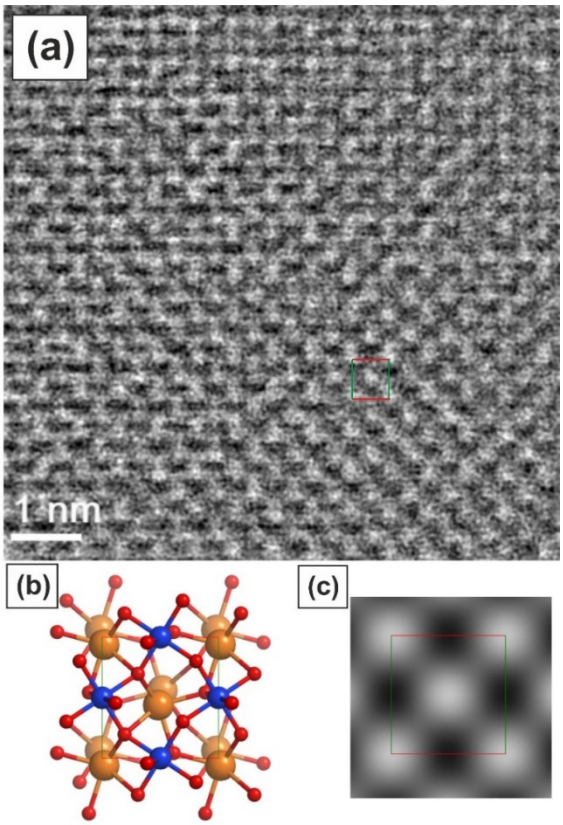

Fig. 3.3-12: (a) High-angle annual dark-field (HAADF) scanning transmission electron microscopy (STEM) image of (Fe,Al)-bearing bridgmanite viewed along the [001] axis and recorded at an acceleration voltage of 200 kV. (b) Structural drawing of bridgmanite viewed along the ***c***-axis. Blue: Si, Al in the 6-fold coordinated B-site; Orange: Mg, Fe in the 8-fold coordinated A-site. (c) The corresponding simulated HAADF-STEM image. The rectangles indicate the orthorhombic unit cell with horizontal ***a***-axis of ~ 0.48 nm length (red) and vertical ***b***-axis of ~ 0.50 nm (green).

For the STEM observation, a particular Bdm grain was oriented with the [001] zone axis parallel to the electron beam. The HAADF-STEM images were recorded on trial at several different magnifications and scanning rates. The original images were often very noisy due to the weak HAADF signal, and the amorphous material formed on the surface of the Bdm under electron radiation. Noisy contrast in the HAADF images was compensated by a noise filtering technique. The filtered HAADF image (Fig. 3.3-12a) displays bright ball-shaped contrasts that correspond to one of the cation columns in the Bdm structure (Fig. 3.3-12b). Comparison between theexperimental contrast with a simulated HAADF-STEM image based on structural data of a (Fe,Al)-bearing Bdm (Nakatsuka *et al.*, Sci. Rep., 11, 22839, 2021) (Fig. 3.3-12c) suggests that the distribution of the bright contrasts is consistent with ferric iron in the 8-fold coordinated A-site. This is the first direct view of the ferric iron distribution in an aluminium-iron bearing Bdm using HAADF-STEM imaging.

l. Ab initio *calculations and crystal structure simulations for mixed layer compounds from the tetradymite series (J. Yao, C.L. Ciobanu, N.J. Cook and K. Ehrig/Adelaide, G.B. Dima/Boulder and G. Steinle-Neumann)*

The tetradymite series with general composition $Bi_x(Te,Se,S)_y$ comprises phases with crystal structures derived from the tetradymite archetype (Bi_2Te_2S), and several named minerals and unnamed phases in the tetradymite group are reported from natural assemblages, particularly from gold deposits – yet remarkably few have been subject to crystal structure determination.

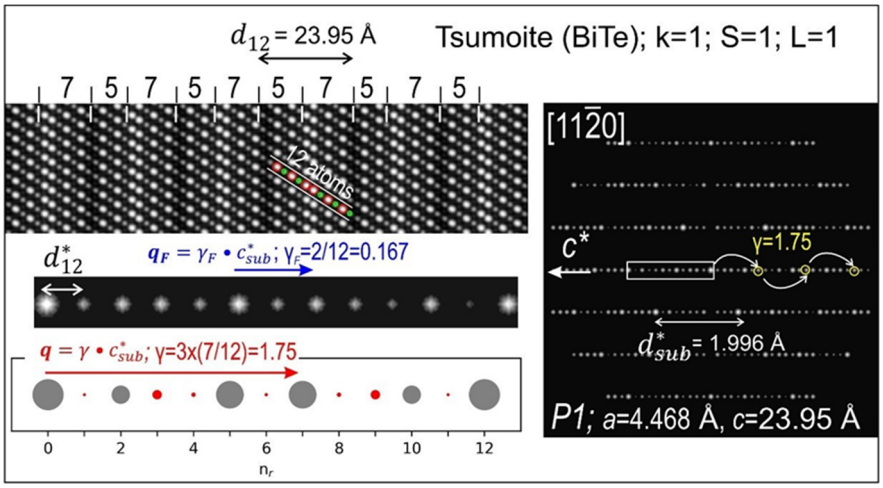

Fig. 3.3-13: Computed scanning transmission electron microscopy image (left) and electron diffraction (ED) patterns (right) obtained on zone axis for the relaxed structures corresponding to the double module phase Tsumonite ($Bi_2Te_3 \cdot Bi_4Te_3$, *i.e.*, BiTe). The two stripes under each image show the interval cropped from ED patterns (area rectangle) and computed intensity variation for reflections across this interval. They describe the number of reflections and two modulation vectors ($\mathbf{q}_F$ and $\mathbf{q}$) in the structure for the distribution of reflections and their intensity, respectively. Modulation lengths (γ_F and γ) are related to characteristics of the structural units and their combination (k, S and L). The atom sequence representing the structure is marked by overlays on the image.

For the sake of simplicity, we chose Te as the only chalcogen and explored structures in the system Bi_xTe_y. One modular model for the structure description is based on a series with formula $S(Bi_{2k}Te_3)\cdot L[Bi_{2(k+1)}Te_3]$, where for given k, short (S) and long (L) modules are combined. The modules have a fixed number of Te atoms and allow for the description of the incremental enrichment with Bi (7, 9, 11 atom units) relative to the 5-atom archetype, Bi_2Te_3. Here we investigate seven members in the tetradymite series with compositions ranging from Bi_2Te_3 to Bi_8Te_3. We perform structure optimisation with *ab initio* simulations and find that simulated electron diffraction patterns and reflection modulations from these structures (example shown in Fig. 3.3-13) are in good agreement with obtained scanning transmission electron microscopy data. Combined with the fact that the *ab initio* simulations predict energetic stability of all investigated compounds relative to the endmembers Bi and Bi_2Te_3, the results suggest that the underlying modular description of structures in the tetradymite group is valid. Based on this insight, we further predict that Bi-rich compositions beyond a stoichiometry of $Bi_{14}Te_3$ are likely disordered alloys of bismuth.

m. *Phase-field approach to investigate cation ordering in omphacite (R. Fukushima and T. Tsujimori/Sendai, N. Miyajima)*

Solute-bearing aqueous fluids in subduction zones, which are generated by the dehydration of subducted slabs, facilitate volatile and metal transportation. The behaviour of the slab-derived fluids also controls rheological properties of rocks, thereby affecting the deformation mechanism and seismicity around the slab–mantle wedge interface. Estimating timescales of dehydration reactions and fluid–rock interaction is thus of importance to comprehensively understand the kinetics of fluid-involved subduction-zone processes. However, natural records in exhumed high-pressure oceanic crusts, or low-temperature eclogite, indicate that fluids repeatedly infiltrated in a span of $< 10^5$ years, which is generally too short to be resolved with conventional geochronology.

Here, we focused on ordering transformation kinetics of omphacite, an essential mineral found in eclogite, as a dynamic recorder of the dehydration history. It has been known that omphacite first nucleates as a metastable disordered phase regardless of temperature. Through macroscopic phase-field simulation, we explored the growth of antiphase domains (APDs) in metastable disordered omphacite, discussing the feasibility of constraining metamorphic reaction kinetics based on the size and morphology of omphacite APDs in eclogitic oceanic crust (Fukushima *et al.*, Phys. Earth Planet. Inter., 354, 107227, 2024).

Our simulation corroborated that omphacite nucleating later during prograde metamorphism can exhibit an incompletely ordered state with sparsely distributed ordered domains, as observed in omphacite from Syros, Greece (Fig. 3.3-14). The order parameter abruptly changes after the incubation time (Fig. 3.3-14a), the duration of which strongly depends on the initial cation configuration in the metastable disordered omphacite. Considering that such an incompletely ordered omphacite can be formed in 1 million years after its nucleation, there is no surprise if the abrupt ordering occurs within $< 10^5$ years.

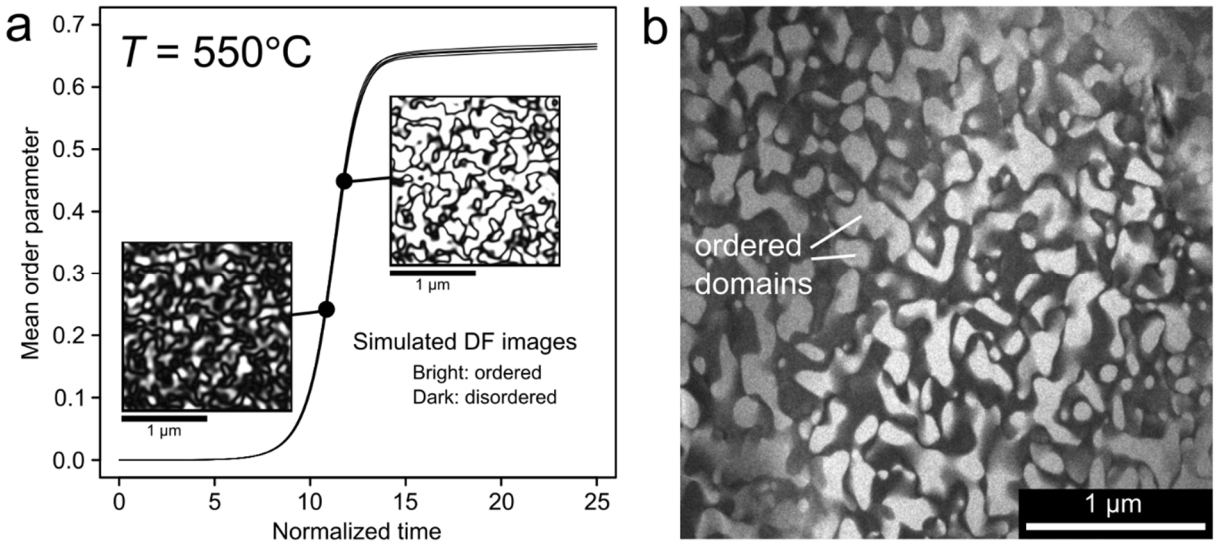

Fig. 3.3-14: Equiaxed APDs in omphacite in simulation and observation. (a) Simulated time evolution of the spatially averaged order parameter at 550 °C. Representative dark-field images generated by our simulation are presented as insets. (b) Real dark-field TEM image of an omphacite grain from a low-temperature eclogite from Syros, Greece (with a diffraction vector $\boldsymbol{g}$ = 050).

The initial cation configuration (*i.e.*, degree of short-range order and/or spatial heterogeneity in ordering) in the metastable disordered omphacite is enigmatic. It may be diverse depending on the pressure–temperature conditions and the kind of its precursor phase, such as blueschist-facies hydrous minerals (*e.g.*, chlorite, glaucophane, epidote/lawsonite) and non-crystalline phases (*e.g.*, fluid, Si–Al amorphous phase). Further nanoscale analysis of APDs in omphacite would enlarge our views on short-span events during oceanic crust dehydration as well as contribute to the understanding of the physics of mineral nucleation.

3.4 Physical Properties of Minerals

The dynamic behaviour of the Earth and of other planets is a reflection of the material properties of the constituent minerals. The transfer of heat by convection is directly related to the viscosity of the interior materials, the deformation of materials in response to stress is controlled by the aggregate behaviour of the minerals, and the transfer of seismic waves through planetary interiors is dependent upon the elastic properties of the constituent phases. Now that seismic data are being collected on Mars, it has become important to determine the elastic properties of minerals with compositions appropriate for the Martian interior. The first contribution in this section uses Brillouin spectroscopy to measure the elastic properties of Fe- and Ca-majoritic garnet, such as we would expect in the Martian mantle. The higher Fe^{3+} content of the Martian-composition garnet results in significantly lower wave speeds than for terrestrial garnets, which is important for interpreting data collected by the InSight space mission.

Mars, like Earth, has a metallic core that, in addition to Fe and Ni, must contain some lighter elements. It is likely that a significant amount of S could be dissolved in the outer, liquid Martian core. Now that the liquid density and P-wave velocity have been measured in the InSight mission, it becomes essential to constrain both the density and P-wave velocity of S-bearing Fe liquids. The second contribution uses ultrasonic interferometry combined with synchrotron X-ray methods to produce enough data to able to model both the density and the P-wave velocity of the Fe-S liquids at conditions appropriate for the Martian core, from which it is determined that the presence of sulphur alone cannot account for the InSight observations.

In the Earth's lower mantle, Fe-bearing Al_2O_3 may be present as a corundum. The equation of state of corundum is investigated in the third contribution, using synchrotron X-ray measurements in a diamond anvil cell. The addition of Fe increases the volume and compressibility of this phase. In contrast to previous data for endmember Al_2O_3, complications arise at pressures above 40 GPa in the Fe-bearing material owing to the spin crossover transition in Fe. Another high-pressure phase that is particularly abundant in a basaltic composition at lower mantle pressures is calcium-ferrite structured $NaAlSiO_4$. In the next contribution, the elastic properties of this "CF" phase are measured by high-pressure *in situ* Brillouin spectroscopy. This is important for the interpretation of seismic studies of deeply subducted crustal material. Brillouin spectroscopy is also used in the following contribution to make challenging measurements of the elastic properties of bridgmanite at simultaneous high pressure and temperature. The new measurements of polycrystalline samples show that grain-boundary effects become increasingly important in finer-grained samples, highlighting the need for collecting data from a variety of carefully characterised high-quality materials from high-pressure synthesis experiments.

One of the few directly observable properties of deep planetary interiors is the electrical conductivity, as provided by magnetotelluric measurements. Interpretation of such measurements requires that we know the conductivities of high-pressure minerals. The next contribution reports the results of a series of systematic measurements of the electrical

conductivity of bridgmanite with varying Fe content, showing a clear increase in conductivity with increasing Fe. The Fe^{3+}/Fe^{2+} ratio, on the other hand, does not seem to have a strong influence on conductivity. Experimentally challenging high-pressure conductivity measurements such as these are essential for constraining the bulk conductivity of the Earth's lower mantle.

The next contribution seeks to constrain the viscosity of the lower mantle. Building upon careful experiments in which the rounding rate of deformed ferropericlase grains was quantified, a model was created to describe the rounding rate for variably elongated ferropericlase grains. Rounding rates are sufficiently high that recovery from elongation easily exceeds the rate of strain in the mantle. This means that the softer ferropericlase cannot form interconnected bands within the mantle. Therefore, the rheology is controlled by the stronger bridgmanite phase and must be much higher than has been previously hypothesised. In another study of how stress and strain are partitioned in polycrystalline aggregates, the next contribution presents synchrotron measurements of dynamic strain in polycrystalline MgO in response to cyclic loading of a diamond anvil cell. Understanding how dynamic differential stress is related to crystallographic orientation will lead to a more complete description of the bulk elastic properties of polycrystalline materials. The final contribution in this section harnesses the power of modern machine learning techniques to extend the time and length scales of molecular dynamics simulations, which finds an application in determining the transport properties of the lower mantle phase davemaoite.

a. *Elastic measurement of a majoritic garnet with Martian composition (A. Antunes, A. Kurnosov, G. Criniti and T. Boffa Ballaran)*

Thanks to the InSight lander mission, valuable seismic data from Mars were acquired and permitted scientists to better constrain the seismic profile of this planet. We are therefore in the position to test possible mineral-physics models to try to constrain the mineralogy and temperature of the interior of Mars. To this end, however, accurate elasticity data for plausible minerals present in the Martian mantle are needed. From high-pressure experiments with bulk compositions derived from SNC meteorites, the assemblage which is likely to be stable in the deeper regions of the Martian mantle is made of Fe-rich ringwoodite and of an Fe,Ca-rich majoritic garnet. Since the elastic behaviour of Fe-rich majoritic garnets have never been studied so far, we present here a room temperature and high-pressure study of this mineral performed using Brillouin scattering and X-ray diffraction up to 12.71 GPa.

The Fe-rich majoritic garnet was synthesised at 19 GPa and 1800 °C in a multianvil apparatus and the compositions of several crystals recovered from the synthesis run were measured using the electron probe micro-analyser (EPMA), resulting in the chemical formula $(Na_{0.02}Ca_{0.17}Fe_{0.71}Mg_{2.1})(Fe_{0.13}Al_{0.99}Si_{0.44}Mg_{0.44})(SiO_4)_3$. High-quality crystals, all of which have cubic symmetry, have been selected for the Brillouin scattering study, and have been

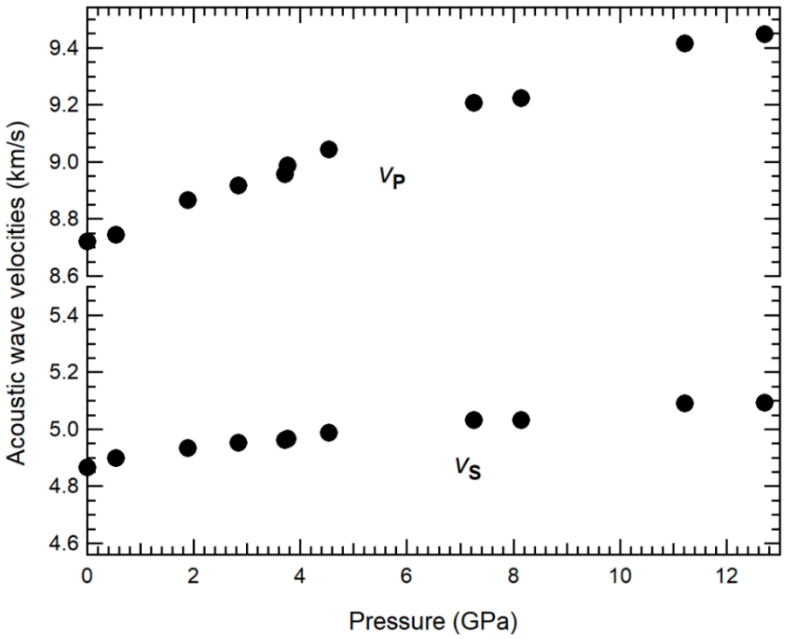

Fig. 3.4-1: Variation of the acoustic wave velocities of Fe-bearing majoritic garnet measured at room temperature up to 12 GPa.

double-sided polished down to 15 µm. The Brillouin scattering measurements performed in several orientations reveal that the anisotropy of this mineral is practically negligible, therefore the average of all collected acoustic longitudinal V_P, and shear, V_S, wave velocities at a given pressure were used as the measure of the aggregate velocities of the majoritic garnet (Fig. 3.4-1). Density was obtained at each pressure by measuring the unit-cell lattice cell parameters using X-ray single crystal diffraction. By coupling the density and the speed waves velocities, the evolution with pressure of the elastic moduli of the majoritic garnet were derived. This Fe-rich majoritic garnet is softer than the alumino-silicate garnets like grossular, almandine, pyrope and Fe-free majorite. This is likely due to the substitution of Al^{3+} by Fe^{3+} on the octahedral site of the garnet structure.

b. *The influence of sulphur on the elastic properties of the Martian core (L. Man, A. Néri, T. Boffa Ballaran and D.J. Frost, in collaboration with J. Chantel/Lille, R. Farla/Hamburg, N. Guignot/Saint-Aubin and Y. Wang/Chicago)*

Recent geophysical observations, particularly seismic data from the InSight mission, have revealed the size of the Martian core and provided direct constraints on the P-wave velocity at the top part of the liquid core. Geophysical models based on seismic observations indicate that the density of the Martian core is significantly lower than that of pure liquid Fe under the same pressure and temperature conditions. However, the constrained P-wave velocity at the top of the Martian core remains comparable to that of pure liquid Fe. If the effects of light elements, including sulphur, on the density and P-wave velocity of liquid iron under high pressures and

temperatures are systematically constrained by experimental and theoretical studies, seismic observations of the Martian core can provide strong evidence for the core's composition, and for Mars' early differentiation and evolution processes.

In this study, we have used ultrasonic interferometry and several *in situ* X-ray methods, independently and simultaneously, to determine the elastic properties of pure Fe and Fe-S liquids under high pressures and temperatures, including density and P-wave velocity (V_P). By combining experimental constraints on solid phase density and melting curves, along with endmember thermodynamic data at ambient pressure and melting curves from the literature, we have developed a new self-consistent thermodynamic model for the Fe-FeS system that is applicable to the conditions of the Martian core. Models that are fit in this way to the widest possible number of experimental constraints are essential due to the large uncertainties inherent in liquid property measurements.

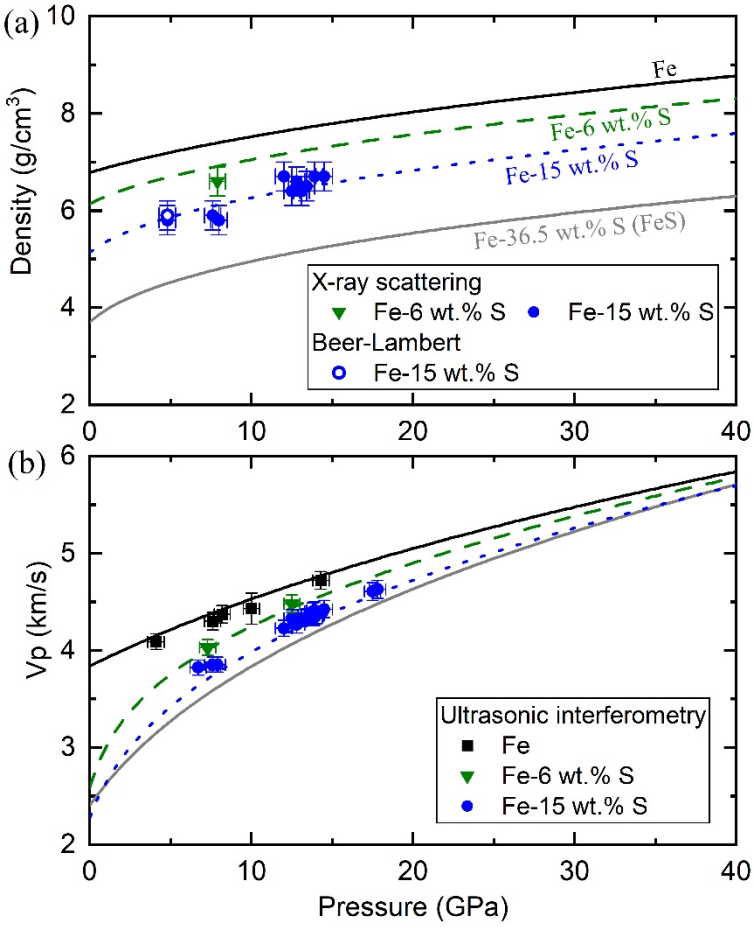

Fig. 3.4-2: Densities (a) and P-wave velocities (b) of liquid Fe-FeS solutions. The black squares, green inverted triangles, and blue circles indicate experimental data from this study for Fe (1873-2273 K), Fe-6 wt. % S (1690-1873 K), and Fe-15 wt. % S (1473-2073 K), respectively. The curves in the figure are derived from the thermodynamic model determined in this study, calculated at 2150 K for Fe (black solid curves) and 1750 K for Fe-6 wt. % S (green dashed curves), Fe-15 wt. % S (blue dotted curves), and FeS (grey solid curves).

Our results indicate that sulphur lowers both the density and P-wave velocity of liquid Fe under Martian core conditions (Fig. 3.4-2). To account for the observed density deficit in the Martian core, at least 20 wt. % sulphur would be required. However, such high sulphur concentrations would lower the P-wave velocity of liquid Fe, most significantly at the top of the Martian core, which conflicts with seismic observations from the InSight mission. This indicates that significant proportions of other light elements, most likely carbon or hydrogen, are required alongside sulphur to explain the large density deficit while maintaining the apparent high longitudinal wave velocity in the Martian core.

c. *Thermal equation of state of Fe-bearing Al_2O_3 (C. Qian, T. Boffa Ballaran and D.J. Frost, in collaboration with Y.G. Liu/Hebei, X. Li, K. Skrzyńska, S. Gallego-Parra, A.D. Rosa, G. Garbarino and I. Kupenko/Grenoble, H.P. Song and X. Wu/Wuhan)*

In the Earth's mantle, aluminium oxide (Al_2O_3) is an important constituent and it might even be present as a separate phase according to petrological studies of diamond inclusions in mantle xenoliths. Although the properties of aluminium oxides are well known, the effect of cation substitution into the corundum structure is still not properly constrained. In particular, since iron is the most abundant transition-metal element in the Earth's mantle, we can expect such substitution to play an important role in determining the physical properties of this phase in the Earth's interior.

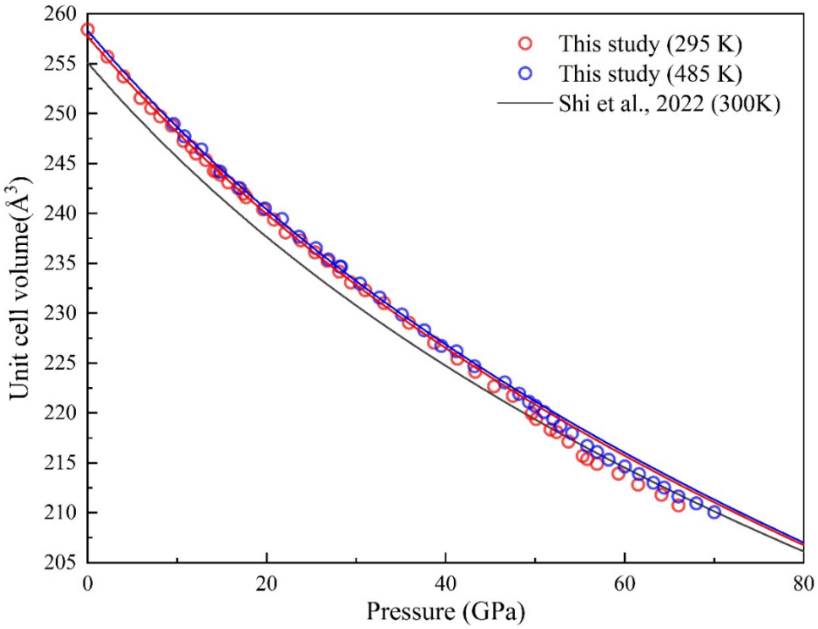

Fig. 3.4-3: Pressure-volume relationship of Fe-bearing Al_2O_3 at high *P-T*. Open circles: experimental measurements at slightly different temperatures as indicated in the legend; curves: fitting results from our data using third-order Birch-Murnaghan equation of state before the Fe spin crossover. The black line indicates the experimental fitting result from Shi *et al*., (2022, J. Geophys. Res.-Solid Earth, 127, 4) for pure corundum.

High-quality single crystals of Fe-bearing Al_2O_3 were synthesised at ~ 24 GPa and 1800 °C using the 1200-ton multianvil press at BGI. The recovered sample consisted of black single crystals with grain sizes ranging between 20 and 80 μm. Under ambient conditions, Al_2O_3 adopts a trigonal *R*-3*c* structure, and energy dispersive spectroscopy analysis indicated that the atomic percentage of iron (Fe/Fe+Al) is approximately 10 %.

High-pressure and high-temperature single-crystal X-ray diffraction of Fe-bearing Al_2O_3 using a diamond anvil cell were performed at the beamline ID15B of the European Synchrotron Radiation facility up to 70 GPa and 885 K. At room temperature (Fig. 3.4-3), we observed a smooth and progressive deviation of the unit-cell volume from the extrapolation of the equations of state determined using the data only up to ~ 40 GPa. We attributed such changes to a spin crossover occurring in the Fe atoms at high pressure. The phenomenon of spin crossover was also observed at a similar pressure at 485 K (Fig. 3-4.3). The *P-V-T* curve of Fe-bearing Al_2O_3 up to 40 GPa (before the spin crossover) was fitted to a third-order Birch-Murnaghan equation of state to derive thermoelastic parameters. By comparison with data for pure endmember corundum (Fig. 3.4-3), it is clear that the incorporation of Fe increases the volume and compressibility of Al_2O_3.

d. *Elasticity of $NaAlSiO_4$ calcium-ferrite type phase at high pressures (M. Hlede, A. Kurnosov, G. Criniti, T. Ishii/Misasa and T. Boffa Ballaran)*

In order to correctly interpret Earth's seismic velocity profiles in terms of temperature and chemical composition of the mantle, a mineral physics model taking into account all the relevant phases that may be present at depth is required. It was found in recent years that around 25 vol. % of MORB material at lower mantle conditions is expected to be composed of an orthorhombic, calcium-ferrite type phase (CF) with chemical formula $X^{+}(Y^{3+}Z^{4+})O_4$ with orthorhombic *Pnma* space group. Here, our goal is to investigate the elastic properties of the $NaAlSiO_4$ CF-endmember by determining its elastic stiffness parameters and aggregate elastic properties.

Two crystals of $NaAlSiO_4$ CF were oriented along the (111) and (551) planes, double-sided polished to a thickness of 10 μm and two platelets were cut out using an FBI (focused ion beam) machine. They were loaded into a BX90 piston-cylinder-type diamond anvil cell (DAC) with He gas as pressure-transmitting medium and a ruby chip for pressure calibration. Brillouin spectra were collected at different χ angles, at different pressures up to 9.6 GPa. Density was obtained at each pressure point by measuring the unit-cell lattice parameters using the Huber single-crystal diffractometer coupled with the Brillouin scattering set up. After the collection, the data were processed using the AniSound_pro function implemented in the Origin Pro software and used to calculate the full elastic tensor from which the bulk (K) and shear (G) moduli, the aggregate compressional (V_P) and shear (V_S) wave velocities.

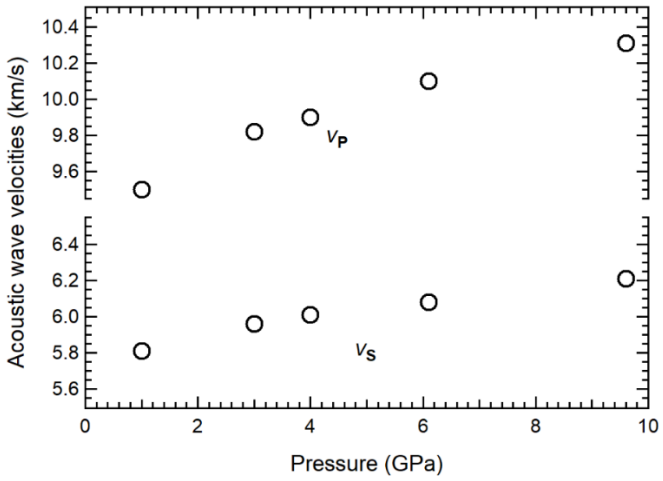

Fig. 3.4-4: Aggregate acoustic velocities measured at different pressures and at room temperature for the $NaAlSiO_4$ CF-type phase.

Both elastic moduli and acoustic wave velocities (Fig. 3.4-4) were found to increase with pressure. The axial compressibility, β, calculated from the elastic tensors obtained at different pressures is very anisotropic, with the *c*-axis being the stiffer direction, whereas the *a*- and *b*-axes having similar compression ($\beta_b \geq \beta a$). Moreover, the *a*- and *b*- axes become less compressible with increasing pressure, whereas the *c*-axis shows little change and stays virtually the same throughout the pressure range investigated.

Further measurements are needed to better constrain the elastic properties of the Na endmember at the conditions of Earth's lower mantle in which this phase is stable.

e. *Elasticity of polycrystalline $MgSiO_3$ bridgmanite to lower mantle conditions (C. Qian, A. Kurnosov, L. Man, T. Boffa Ballaran and D.J. Frost)*

It is widely accepted that bridgmanite is the primary constituent of the Earth's lower mantle, therefore knowledge of its elastic properties at lower mantle conditions are necessary for constraining the structure of the Earth's deep interior. Bridgmanite single-crystal acoustic velocities have been measured at BGI up to 80 GPa at room temperature, providing a reliable high-pressure reference for the seismic signature of this important mineral at high pressures. However, high-temperature conditions are essential for accurately constraining the mineralogy and chemical composition of the lower mantle. For orthorhombic crystals such as bridgmanite, determining the nine independent elastic stiffness components (C_{ij}) becomes especially challenging under simultaneous high-pressure and high-temperature conditions. Polycrystalline materials are instead easier to measure, since velocities are equal in all directions if the grains are randomly oriented. However, the grain size of polycrystalline samples significantly influences the acoustic velocity and there is a large discrepancy in the literature between results obtained using powdered or single-crystal samples. In order to identify the causes of this discrepancy in terms of grain size, sample preparation, and pressure medium used, we have undertaken a series of Brillouin and X-ray diffraction measurements on polycrystalline $MgSiO_3$ bridgmanite samples.

The polycrystalline $MgSiO_3$ bridgmanite samples were synthesised using a 1200-ton multianvil (MA) press at BGI at 24 GPa and at different temperature conditions to control the grain growth of the bridgmanite crystals. Two samples were selected: one with a grain size of approximately 500 nm synthesised at 1800 K, and another with a grain size of approximately 5 µm synthesised at 1500 K. The samples were polished into thin platelets (~ 15 µm thick) and further cut into circular disks using the focused ion beam (FIB). High-pressure X-ray diffraction and Brillouin spectroscopy measurements were conducted so far up to 35 GPa at room temperature using a diamond anvil cell (DAC).

The preliminary results show that both samples exhibit pressure-volume relationships consistent with previous studies conducted on single-crystals. However, the wave velocities (V_S and V_P) of these two polycrystalline samples are consistently lower than those obtained from the full elastic tensors of bridgmanite obtained in a previous single crystal study (Fig. 3.4-5), with the sample having the smaller grain size (500 nm) exhibiting even lower velocities compared to the sample with larger grain size (5 µm). Note that V_P is visible only at the lower pressure point (*i.e.*, 5 GPa). At higher pressure the signal from bridgmanite is always covered by the large V_S signal from the diamonds. The lower wave velocities obtained in this study confirm that grain-boundary effects become more pronounced in finer-grained samples. Furthermore, the diffraction data indicate that the synthesis process may have induced some preferred orientation in the polycrystalline sample with smaller grain size.

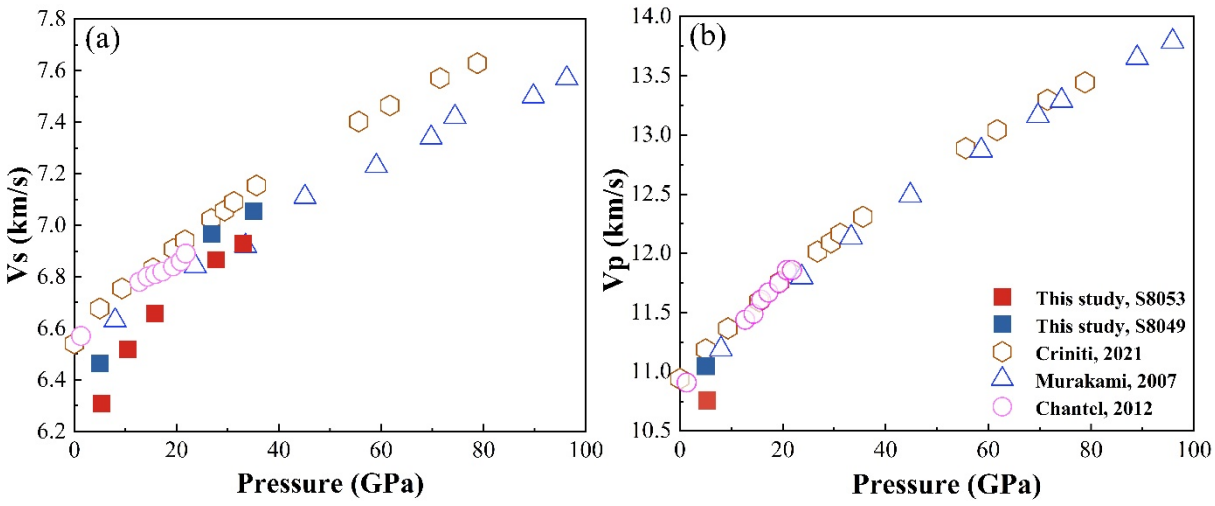

Fig. 3-4.5: Shear wave velocity (a) and longitudinal wave velocity (b) of a polycrystalline sample of $MgSiO_3$ bridgmanite as a function of pressure at 300 K. The red and blue squares indicate data from this study, with the red square indicating samples with a grain size of about 500 nm and the blue square indicating those with a grain size of approximately 5 µm. For comparison, pink hexagons indicate single crystal DAC data from Criniti *et al.*, (2021, J. Geophys. Res.-Solid Earth, 126, 5), the yellow circles indicate polycrystalline DAC data from Murakami *et al.*, (2007, Earth Planet. Sci. Lett., 256, 1-2), and the grey triangles indicates hot pressed polycrystalline multianvil data from Chantel *et al.*, (2012, Geophys. Res. Lett., 39, 19).

f. *The effect of iron content on the electrical conductivity of Al,Fe-bearing bridgmanite (K. Han, H. Fei, F. Wang, L. Man, A.C. Withers and T. Katsura)*

Geophysical observations reveal the presence of lateral variation in electrical conductivity in the uppermost part of the lower mantle, where conductive anomalies can be one order of magnitude higher than the ambient mantle. Also, the electrical conductivity increases considerably from the overlaying transition zone to the uppermost lower mantle underneath North America. The interpretation of such conductivity profiles could provide constraints on the composition and structure of the lower mantle.

Bridgmanite is the most abundant mineral in the lower mantle. The chemical composition of bridgmanite could be heterogeneous, owing to the subduction of oceanic plates and plumes that rise from from the core-mantle boundary. In a pyrolitic mantle composition, bridgmanite generally contains 10 wt. % of FeO/Fe_2O_3 at the uppermost lower mantle, while in a basaltic composition, the total iron content could be as high as 25 wt. %. However, the correlation between iron content and electrical conductivity remains poorly understood.

Here we report measurements of electrical conductivity to determine the dependence upon iron content at 27 GPa and temperatures up to 2000 K performed using a multianvil apparatus. A series of Al, Fe-bearing bridgmanites with varying iron contents were pre-synthesised at 1700 °C and pressures of 24 or 27 GPa. Fourier-transform infrared spectroscopy and Mössbauer spectroscopy were employed to quantify the H_2O content and Fe^{3+}/Fe^{2+} ratio in the synthesised

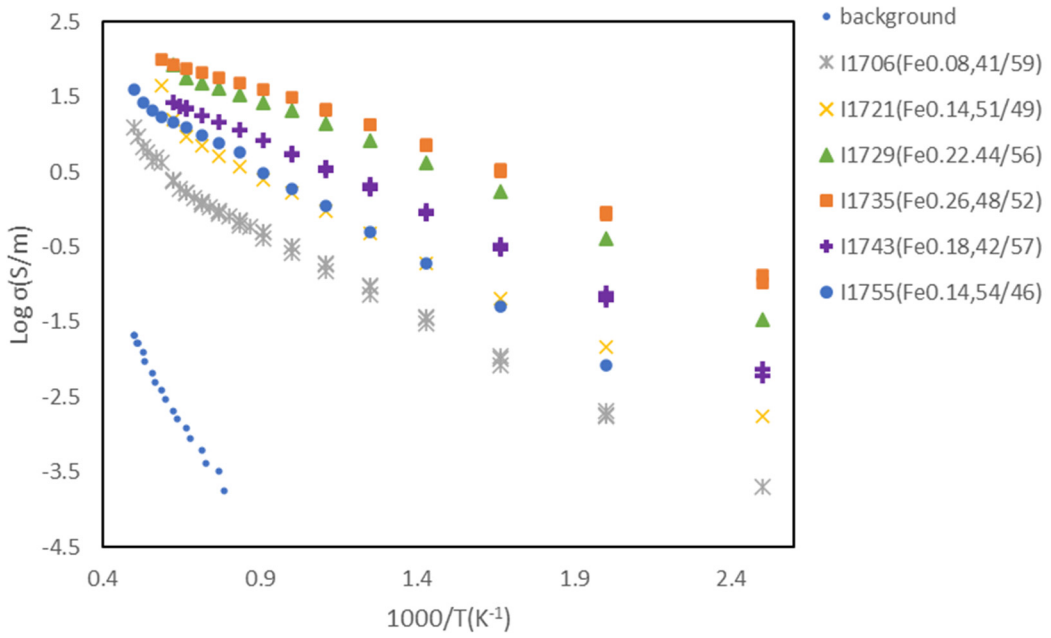

Fig. 3.4-6: The logarithmic conductivity of Al,Fe-bearing bridgmanite as a function of reciprocal temperature. The bracketed text in the legend shows the total iron content and the Fe^{2+}/Fe^{3+} ratio.

samples, respectively. The electrical conductivity of Al, Fe-bearing bridgmanites was measured at 27 GPa and varying temperatures (Fig. 3.4-6), using a Solartron 1260 Impedance Analyser. The voltage amplitude was 0.5 V with a frequency range from 0.1 to 10^7 Hz. The electrical conductivity of bridgmanite increases with increasing total iron content. However, the ferric and ferrous ion ratio (Fe^{2+}/Fe^{3+}) appears to exert a limited effect on the electrical conductivity. The conduction is controlled by different mechanisms in the low- and high-temperature ranges. Small polaron hopping conduction dominates at temperatures below 1600 K, while oxygen vacancies control the conduction at higher temperatures. A complementary model for the electrical conductivity of bridgmanite will enable us to interpret the chemical composition of the Earth's lower mantle from geomagnetic observations.

g. *Bridgmanite-ferropericlase interface energy controls viscosity of the lower mantle (A. Chakraborti, H. Fei, Y. Nishihara/Matsuyama, M. Thielmann, F. Heidelbach, N. Tsujino/Sayo, A. Chanyshev, L. Man, J. Dolinschi, W. Wu/Matsuyama, Y. Higo/Sayo and T. Katsura)*

The viscosity of the Earth's lower mantle controls the upwelling of hot plumes, the subduction of cold slabs, as well as material- and heat-exchanges through 60 % of the Earth's volume. The lower-mantle viscosity is that of a predominantly two-phase system consisting of the minerals bridgmanite and ferropericlase . Estimations of the lower mantle viscosity vary by as much as 5 orders of magnitude depending on whether the lower-mantle rheology is bridgmanite-controlled or ferropericlase-controlled. The stronger bridgmanite could control the bulk viscosity through its higher volume fraction, while the weaker ferropericlase could form interconnected layers through grain elongation, significantly reducing the bulk viscosity. Here we show experimentally that the increased surface energy of irregularly bonded structures prevents ferropericlase grains from elongating significantly and thus from developing interconnected layers. We calculated the rounding rate of deformed ferropericlase grains (Fig. 3.4-7) in a two-phase bridgmanite-ferropericlase system at relevant pressure and temperature

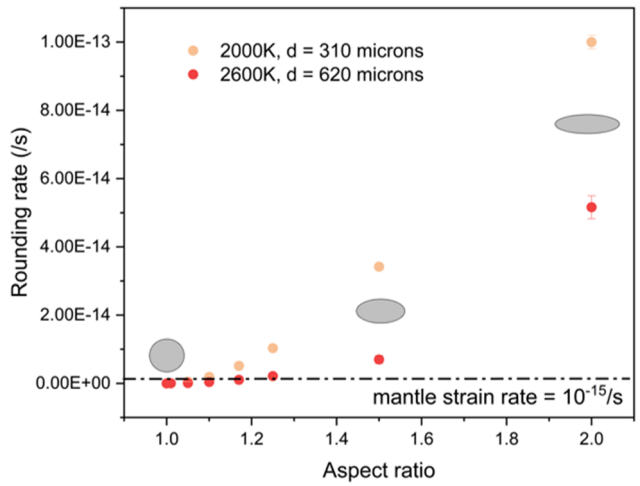

Fig. 3.4-7: Change in rounding rate with aspect ratio of ferropericlase clusters calculated at 2000 K for grain sizes of 320 µm and at 2600 K for grain sizes of 620 µm. These conditions correspond to the top and the bottom of the lower mantle, respectively. The dashed line corresponds to the reference mantle strain rate. The rounding rate overcomes the mantle strain rate when the elongated clusters have an aspect ratio above 1.16.

conditions and found that the rounding rate is significantly higher than the rate of elongation by mantle flow. Our results thus demonstrate that the viscosity of the lower mantle is close to that of bridgmanite, and orders of magnitude higher than previously hypothesised.

h. *Stress and strain partitioning in polycrystalline MgO at seismic frequencies and at high pressures (J. Buchen, B. Wang, N. Satta and V. Trautner/Oxford, G. Criniti, A.S.J. Méndez/Hamburg, H.-P. Liermann/Hamburg and H. Marquardt/Oxford)*

The partitioning of stress and strain between the grains that form a polycrystalline aggregate affects the elastic behaviour and properties of the aggregate. In a similar manner, the elastic properties of rocks in the Earth's mantle depend on how stress and strain are partitioned between the grains of rock-forming minerals, which typically have contrasting and anisotropic elastic properties. When calculating the seismic wave speeds of mantle rocks from the elastic properties of the rock-forming minerals, the elastic moduli of the rock are typically approximated by the Voigt bound, the Reuss bound, or by their arithmetic mean. The Voigt and Reuss bounds assume that either strain or stress, respectively, are uniform throughout the rock. Because the elastic properties of neighbouring grains may differ substantially, however, neither stress nor strain are expected to be uniform throughout the rock. The actual elastic response of the rock may therefore not correspond to either of the bounds and may vary with temperature and with the frequency of elastic waves.

We probed the elastic response of polycrystalline MgO to cyclic strain oscillations with frequencies between 10 and 100 mHz and at pressures between 40 and 70 GPa using a dynamic diamond anvil cell (DAC) in combination with time-resolved X-ray diffraction in radial diffraction geometry. MgO powder was loaded into X-ray transparent gaskets without any pressure-transmitting medium and compressed in a DAC. The DAC was then coupled to a piezoelectric actuator. By applying an oscillating voltage to the piezoelectric actuator, we subjected the powder inside the DAC to loading cycles with varying amplitudes and frequencies. During the sequence of loading cycles, X-ray diffraction patterns were recorded at a rate of 1 pattern/second and in radial diffraction geometry to capture the behaviour of lattice planes with different orientations relative to the compression axis of the DAC. All experiments were carried out at the Extreme Conditions Beamline (P02.2) at the synchrotron radiation source PETRA III in Hamburg.

The sequences of recorded diffraction patterns were analysed by extracting *d*-spacings from the 200 and 220 reflections of MgO both as a function of time and of the angle between the diffraction vector and compression axis of the DAC. As a result, we obtained the variations of volume strain and lattice strain with time, which we then separated into static and oscillating dynamic contributions. Using the elastic properties of MgO as reported in the literature, we translated the dynamic parts of volume and lattice strain into oscillations of pressure and differential stress, respectively. As an example, Figure 3.4-8 shows the dynamic lattice strains

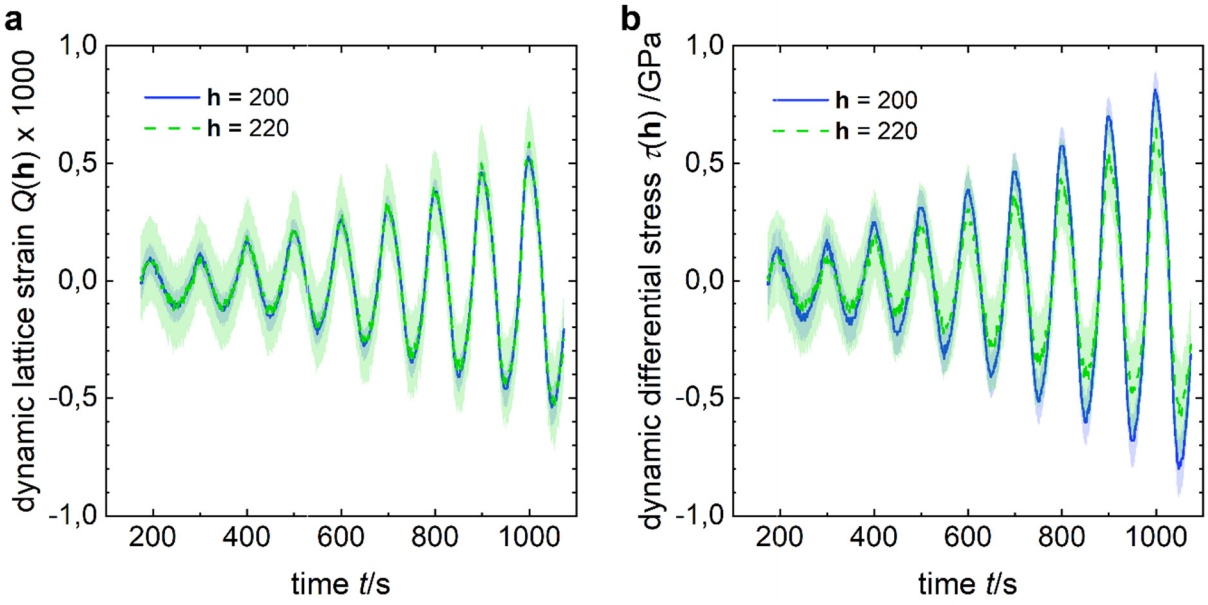

Fig. 3.4-8: Dynamic components of the lattice strain (**a**) and differential stress (**b**) in polycrystalline MgO during cyclic loading at pressures between 40 and 45 GPa as derived from the 200 and 220 reflections. The period of the loading cycles is 100 s.

(Fig. 3.4-8a) and dynamic differential stresses (Fig. 3.4-8b) derived from the 200 and 220 reflections of MgO for one of the cyclic loading experiments. The dynamic lattice strains for both reflections are essentially identical and indicate that the dynamic elastic response is close to the Voigt bound. Despite some overlap of the uncertainties on the dynamic differential stresses derived from both reflections, the dynamic differential stress for the reflection 200 oscillates with systematically higher amplitudes than the dynamic differential stress for the reflection 220. The systematic difference in the amplitudes shows that the dynamic differential stresses are not partitioned equally between different crystallographic directions. A more detailed analysis of dynamic stresses and strains may provide a more quantitative description of stress and strain partitioning between grains and can help to improve models for the elastic properties of polycrystalline materials and rocks.

i. *Properties of $CaSiO_3$ davemaoite studied by machine learning molecular dynamics simulations (M. Schulze and G. Steinle-Neumann)*

$CaSiO_3$ perovskite, or davemaoite, is generally considered to be the third most abundant mineral in the Earth's lower mantle. Detailed knowledge of the physical and chemical properties of davemaoite is therefore crucial to understanding the physical state of the deep Earth. Experimental investigations are challenging due to the high temperatures and pressures of the davemaoite stability field and the fact that it cannot be preserved upon quenching to ambient conditions. Complementary to experiments, davemaoite has been the subject of numerous

computational studies, utilising both static density functional theory (DFT) calculations and DFT driven molecular dynamics (MD) simulations. The advantage of the latter approach is that anharmonic contributions to the atomic vibrations and temperature effects can be treated explicitly. Conventional DFT-MD simulations are, however, usually limited to system sizes of a few hundred atoms and simulation times in the picosecond range. This often prevents a reliable assessment of uncertainties arising from finite size effects, or the evaluation of the statistical significance of results. Furthermore, certain properties, such as mass diffusion, often occur on such large time scales that they cannot be studied at all using the DFT-MD approach.

To overcome these limitations in time and length scales, MD simulations in which the potential energy surface of an atomic system are predicted by machine learning potentials offer an attractive alternative to conventional DFT-MD simulations. This makes it possible to perform simulations of thousands of atoms that last up to several nanoseconds while maintaining the quality of DFT calculations. Here, we follow this route to study the physical and chemical properties of davemaoite by constructing high-dimensional neural network potentials (HDNNP) within the Behler-Parinello framework. In the Behler-Parinello approach the potential energy E of the system is represented as the sum of individual local atomic energies E_i, $E = \sum_i^N E_i$, where N is the total number of atoms. HDNNPs establish a functional relationship between E_i and the corresponding atomic environment by employing so-called many-body atom-centered symmetry functions. These symmetry functions are translational, permutational, and rotational invariant, ensuring that each unique atomic environment corresponds to exactly one unique value for E_i.

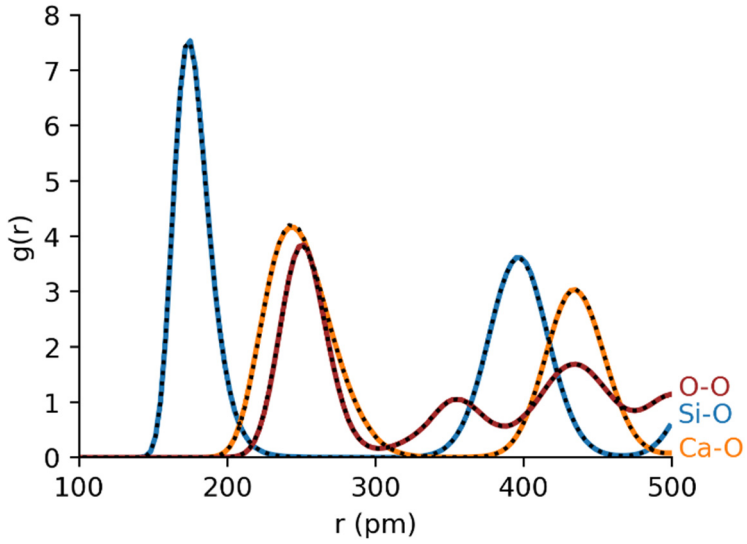

Fig. 3.4-9: Partial distribution functions *g(r)* for the element pairs Si-O, Ca-O, and O-O in $CaSiO_3$ davemaoite. The coloured solid curves represent *g(r)* obtained from DFT-MD simulations conducted at 2000 K and ~ 24 GPa. The black dotted curves show the respective *g(r)* obtained from a molecular dynamics simulation driven by the HDNNP currently under development.

To generate the training set for the HDNNP consisting of energies and forces, we use DFT as the reference method. Calculations are performed with the Vienna *Ab Initio* Simulation Package (VASP, version 6.4.3). The PBE generalised gradient approximation and the projector augmented plane wave (PAW) method are used. The Brillouin zone is sampled using a 2 × 2 × 2 k-point mesh and a basis set energy cutoff of 850 eV. PAW potentials with 10, 4, and 6 valence electrons and core radii of 1.22, 1.01, and 0.80 Å are used for Ca, Si, and O, respectively. The HDNNP is constructed using the N2P2 package. The training set includes ideal crystal structures as well as structures with defects. The final MD simulations utilising the HDNNP are carried out with the LAMMPS code (version 2, August 2023), compiled with the HD-NNP package.

Tests of the currently developed HDNNP show excellent agreement with the results of DFT-MD simulations, as can be seen in a comparison of the partial distribution functions *g(r)* (Fig. 3.4-9). The training of the HDNNP is continued so that it can be used over the entire temperature and pressure range of the lower mantle, with the goal of applying the final HDNNP for the investigation of the transport properties of davemaoite.

3.5 Fluids, melts and their interaction with minerals

Both experimental studies and measurements on natural samples in recent decades have firmly established that Earth's mantle contains a reservoir of water that is comparable to all oceans on the surface combined. In deep geologic time, the exchange of water between these two reservoirs controls slow variations of global sea level. The presence of water also has a major effect on the physical properties of the mantle itself. While for the upper mantle and the transition zone, water storage is reasonably well understood, there are still major controversies concerning the behaviour of water in the lower mantle. Among the main minerals of the lower mantle – bridgmanite, ferropericlase, and davemaoite – the first two do not seem to accept much water in their structure. Davemaoite ($CaSiO_3$ with perovskite structure), however, is difficult to study because it turns into an amorphous phase upon pressure release. Moreover, since it is the least abundant phase in the lower mantle, it was often ignored in considerations of water storage. The first contribution in this section of the annual report re-visits water solubility in davemaoite by a combination of multianvil experiments with nano-SIMS, atomic probe tomography and infrared spectroscopy. The data show convincingly that aluminous davemaoite may incorporate thousands of ppm of water by the coupled substitution of $H^+ + Al^{3+}$ for Si^{4+}. This implies that this mineral is actually the main host of water in the lower mantle. While the bulk solubility of water in the lower mantle remains low due to the high mass of this reservoir, it may potentially hold up to 0.5 ocean masses of water.

Two more studies in this section look at claims of high water solubilities in lower-mantle minerals. Stishovite (SiO_2 with rutile structure) is not a mineral of the normal lower mantle, but it may be abundant in slabs that have been deeply subducted. Claims of very high water solubilities from studies in diamond anvil cells could not be reproduced in multianvil experiments, implying a more limited capacity of stishovite to transport water into the lower mantle. Similarly, previous claims that the presence of fluorine enhances water solubility in bridgmanite could not be confirmed. Another contribution describes new experiments of the partitioning of water between wadsleyite and garnet under water-undersaturated conditions.

In the modern Earth, hydrogen is mostly contained in oxidised form, as molecular H_2O or as hydroxyl groups in minerals and melts. However, during the formation of the Earth, this may have been different. The magma ocean on the early Earth may have been in equilibrium with an H_2-rich atmosphere and the dissolution of H_2 in the silicate melt may have controlled the initial concentration of hydrogen in Earth's interior. Indeed, some recent studies have emphasised that equilibration with an H_2-rich atmosphere may have been the essential step controlling the volatile distribution in Earth's interior. Unfortunately, available measurements of H_2 solubility in silicate melt are mostly based on infrared measurements of quenched glasses using an infrared extinction coefficient for silica glass that was obtained through some rather questionable experimental procedure. Therefore, in one project described here, the infrared extinction coefficient of H_2 in silicate glass was re-calibrated. This was done with two completely independent methods, which yielded highly consistent data. The result differs from

the previously accepted value by one order of magnitude and implies that previously, the solubility of H_2 in a magma ocean was over-estimated by a factor of ten. In the light of this new calibration, it appears rather unlikely that the dissolution of H_2 in the magma ocean made a major contribution to the initial volatile budget of Earth's mantle and core.

The InSight mission on Mars has generated seismic data that may indicate the presence of a magma layer (~ 150 km) on top of the Martian core. In one contribution, possible conditions for partial melting in the Fe-rich Martian mantle are explored, and the density and viscosity of the resulting melts are measured. So far, however, the inferred melting temperatures are difficult to reconcile with the estimated temperature distribution in the interior of Mars. The structure and properties of silicate melts in deep planetary interiors are also the subject of the following contribution, which looks at hydrous silicate melts under high pressure by a combination of neutron and X-ray diffraction as well as molecular dynamics simulations. The data indicate polymerisation of the silicate melt at higher pressures due to ring-closing, together with an increased coordination number of hydrogen leading to higher O-H distances.

The next six contributions in this section of the annual report investigate the viscosity of magmas relevant to volcanic eruptions and, in particular, the possible effects of nanolites (nanometer-size crystals, mostly of Fe-oxides) on viscosity and eruption behaviour. The importance of these nanolites that may form very rapidly during cooling or decompression and volatile loss was only recently recognised. They may directly affect viscosity as solid particles inside the melt, or indirectly by changing the composition of the residual melt. Moreover, they may act as nucleation sites for gas bubbles and therefore change degassing behaviour.

The last section in this chapter looks at the behaviour of molten sulphur under high pressure. Previous studies have attributed abrupt changes in properties to a possible liquid-liquid phase transition. Measurements by *in situ* ultrasonic interferometry confirm anomalies in the pressure dependence of ultrasonic velocities, however, definitive evidence for a liquid-liquid phase transition could not be detected.

a. *Davemaoite as the lower mantle water reservoir (L. Wang, Y. Yang/Guangzhou, T. Long/Beijing, J. Wang/Washington, D.C., T. Withers, H. Keppler and T. Katsura)*

The Earth's lower mantle contains more than 70 % of the mass of the entire mantle, and accordingly, even a small amount of water in its constituent minerals could represent a significant reservoir. The majority of the lower mantle is composed of bridgmanite, ferropericlase, and davemaoite. Previous studies have shown that bridgmanite and ferropericlase are largely anhydrous, raising questions about where water could be stored in this region. Davemaoite, although less abundant, plays an important role due to its capacity to incorporate incompatible trace elements and potentially water. Elevated water contents in ocean island basalts (OIB) would be consistent with some water being stored in davemaoite.

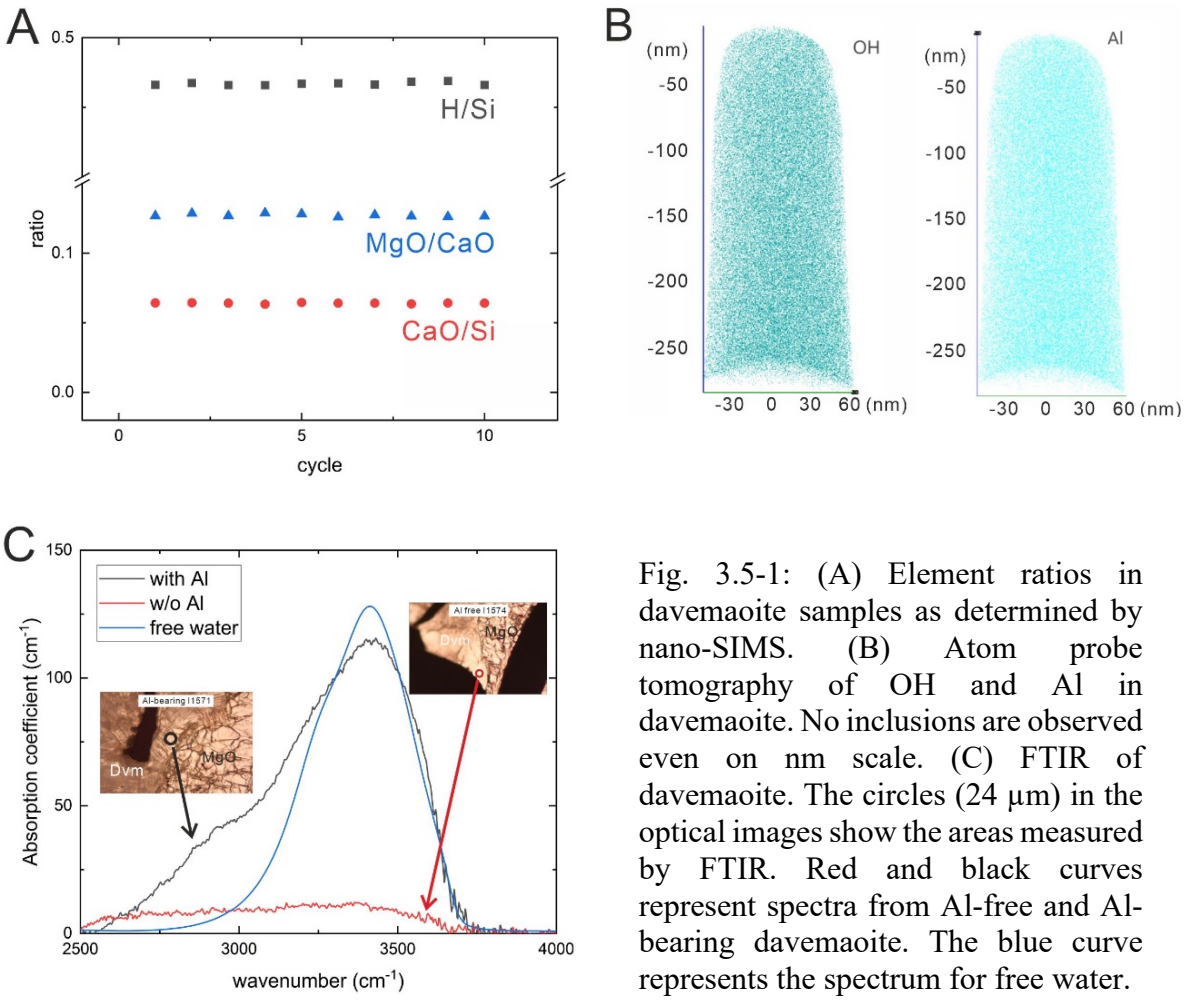

Fig. 3.5-1: (A) Element ratios in davemaoite samples as determined by nano-SIMS. (B) Atom probe tomography of OH and Al in davemaoite. No inclusions are observed even on nm scale. (C) FTIR of davemaoite. The circles (24 µm) in the optical images show the areas measured by FTIR. Red and black curves represent spectra from Al-free and Al-bearing davemaoite. The blue curve represents the spectrum for free water.

In this study, we systematically investigated the water storage ability of both pure ($CaSiO_3$) and Al-bearing davemaoite at 27 GPa and 1700 - 2000 K. The recovered samples were carefully investigated by nano-SIMS, atom probe tomography and FTIR. Although davemaoite transformed into an amorphous phase upon quenching from high pressure and high temperature to ambient conditions, the H depth profile in nano-SIMS (Fig. 3.5-1A), atom probe tomography (Fig. 3.5-1B) and FTIR spectra (Fig. 3.5-1C) suggest that the water is homogeneously distributed in the davemaoite and no hydrous inclusions are present even on the nm scale.

The water contents in davemaoite were quantified by nano-SIMS. Our results demonstrate that davemaoite without aluminium can store approximately 300 ppm by weight of water, whereas aluminium-bearing davemaoite may contain up to 5000 ppm. Temperature is found to increase the water content (Fig. 3.5-2A), which is also coupled coupled to Al content (Fig. 3.5-2B). The Al/H ratio of 1 observed in the Al-bearing sample indicates that H is mainly incorporated into Al-bearing davemaoite by a charge-coupled mechanism with $Al^{3+} + H^{+}$ substituting for Si^{4+} or $2Ca^{2+}$. The Al/H ratio of 1 also confirms that the measured water resides in the crystal structure and is not due to any contamination.

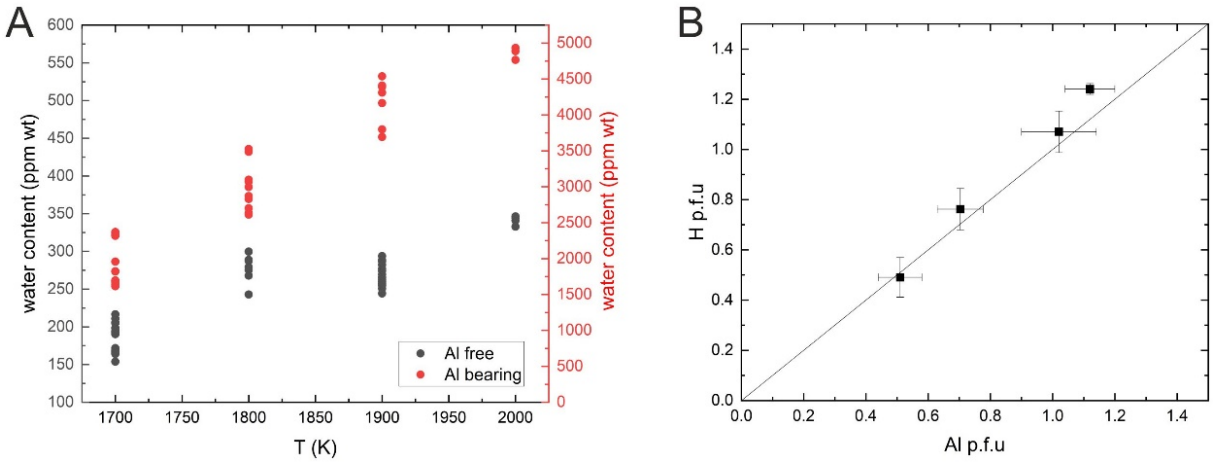

Fig. 3.5-2: Water contents in davemaoite as determined by nano-SIMS versus temperature (A) and Al content (B). In diagram (A), note the different scales on the left and on the right, for Al-free and Al-bearing davemaoite, respectively.

Given the anhydrous nature of bridgmanite and ferropericlase, these findings suggest that davemaoite is the primary water reservoir in the lower mantle. The Al content in davemaoite in a pyrolite assemblage is 0.03-0.05 atoms p.f.u. at 27 GPa and geotherm temperature. At least 3000 ppm water can be stored in such davemaoite. This corresponds to a 0.5 ocean mass of H_2O, which is within the limits of 0.1-2 ocean mass of H_2O stored in the mantle based on geochemical arguments.

b. *Water solubility in stishovite in the deep mantle (F. Wang, A. Chanyshev, L. Man, Y. Song, L. Wang, T. Ishii/Misasa, R. Farla/Hamburg, N. Tsujino/Sayo and T. Katsura)*

Stishovite, a nominally anhydrous mineral, is a major phase in the subducted oceanic crust, comprising about 20 % of its minerals. While earlier quenching experiments suggested low water solubility in stishovite (0.1 wt. % in pure SiO_2), recent studies appeared to indicate higher water contents (up to 10 wt. %) under lower mantle conditions. This discrepancy highlights the need for further investigation into the water solubility in stishovite.

To address this, we conducted high-pressure and high-temperature experiments using a multianvil apparatus with *in situ* X-ray diffraction at pressures up to 40 GPa and temperatures up to 1300 K. Silica gel containing approximately 10 wt. % of water was used as the starting material. Hydrous stishovite was synthesised at the target pressure and temperature, and X-ray diffraction data were collected at high pressure but after quenching to room temperature. The derived unit cell parameters were compared to those of dry stishovite and calculated using a well-established equation of state at the same condition. The slightly larger volume of hydrous stishovite indicates hydration. However, the volumes observed in our study are much smaller than those obtained in previous diamond anvil cell experiments, suggesting low water contents.

Our findings suggest that water solubility in stishovite at lower mantle conditions is significantly lower than previously estimated by diamond anvil cell experiments, but aligns more closely with values determined by quenching experiments. This indicates that although hydrous stishovite may still contribute to transporting water into the deep mantle, even after dense hydrous magnesium silicates become unstable, the amount of water that may be transported is limited.

c. *Fluorine and water incorporation in bridgmanite and stishovite (C. Qian and D.J. Frost, in collaboration with X. Li/Grenoble, Y.G. Liu/Hebei, X. Wu/Wuhan and T. Yoshino/Misasa)*

Bridgmanite is the dominant mineral in the lower mantle. Investigating the amount of water that can be accommodated as hydroxyl in the bridgmanite lattice is important for the water storage capacity of the lower mantle. Unlike minerals of the transition zone and upper mantle, it is possible that bridgmanite is at or near H_2O saturation in the lower mantle, because some previous estimates of its maximum H_2O content are close to those expected for the subducting lithosphere or the mantle as a whole. Previous studies disagree, however, on the amount of H_2O that can be stored in bridgmanite, with estimates ranging from tens to thousands of ppm. Studies that have proposed very high levels of bridgmanite H_2O accommodation have mainly used Fourier-transform infrared spectroscopy (FTIR) to determine these concentrations. However, it is possible that these studies have overestimated the H_2O concentrations by not effectively distinguishing between bridgmanite and hydrous inclusions within bridgmanite in the FTIR spectra. Therefore, the maximum H_2O concentration in bridgmanite remains somewhat controversial.

Recently, Yoshino and Jaseem (2018, EPSL 504:106-114) demonstrated that bridgmanite may contain up to 13000 ppm of fluorine and that the presence of F apparently raises the maximum H_2O concentration in bridgmanite from approximately 2000 ppm up to 6000 ppm. However, in these previous experiments, only the $MgSiO_3$ bridgmanite end-member was investigated, whereas bridgmanite formed in subducted oceanic crust will contain significant concentrations of Al and Fe that might also affect the accommodation of volatiles in this mineral. Therefore, we have studied the incorporation of H_2O and F in a bridgmanite composition that would be more typical of that formed from subducted oceanic crust in the lower mantle. We produced $(Fe,Mg)(Al,Si)O_3$ bridgmanite coexisting with a water-bearing silicate melt using a series of simplified basaltic compositions with varying H/F ratios.

The samples were equilibrated at 25 GPa and 1800 °C for 4 hours using a multianvil press. Recovered samples were polished for analysis with the electron microprobe and then prepared for further analysis using secondary ion mass spectrometry (SIMS). The samples contained Fe-Al-bearing bridgmanite coexisting with stishovite and a hydrous silicate melt. SIMS measurements were employed to determine the concentration of F and H in bridgmanite, and to explore the partitioning between bridgmanite and stishovite. The results show that the

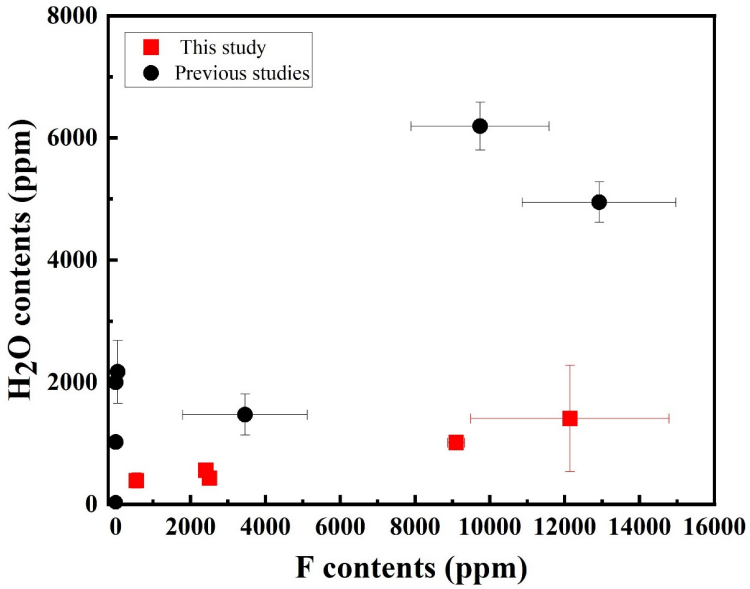

Fig. 3.5-3: H_2O concentrations in bridgmanite as a function of the F content, for experiments performed in this study and compared to previous studies (Yoshino and Jaseem 2018, EPSL 504:106-114).

concentration of F in bridgmanite is between 553 to 12138 ppm, and the concentration of H_2O in bridgmanite is between 390 to 1407 ppm. Our results indicate much lower bridgmanite H_2O contents than those reported in the previous study of Yoshino and Jaseem (2018), over the same range of F contents (Fig. 3.5-3). Moreover, when bridgmanite and stishovite coexist, F tends to partition into bridgmanite, while H_2O partitions preferentially into Al-rich stishovite. The contents of F and H_2O in bridgmanite appear correlated but this correlation is much weaker than that reported in previous studies. For F concentrations typical of subducted basalt, *i.e.*, < 300 ppm, the effect on the bridgmanite H_2O content will be near negligible.

d. *Water partitioning between wadsleyite and garnet under water-undersaturated conditions (M. Sakurai and N. Tsujino/Misasa, A.C. Withers, T. Boffa Ballaran and T. Katsura)*

Most experimental studies on water solubility in mantle minerals, as well as on water partitioning between these minerals, have been conducted under water-saturated conditions or at high water fugacity. However, it is unlikely that the whole mantle is saturated with water. To understand the actual water distribution between mantle minerals, experiments under water-undersaturated conditions are required.

In this study, to determine water partitioning between wadsleyite and garnet under water-undersaturated conditions, large single crystals of both minerals were synthesised using a solvent ($K_2Mg(CO_3)_2$) in a single run. The chemical composition of the silicate starting material corresponded to a 1:1 molar ratio of forsterite to enstatite in an iron-free system, with an

appropriate amount of Al_2O_3 added. Annealing experiments were carried out to investigate the effects of water fugacity on water partitioning between wadsleyite and garnet under the conditions corresponding to the Earth's mantle transition zone. These experiments were performed using a Kawai-type multianvil apparatus at 16 GPa and 1873K. The solvent was packed to fill 1/15 to 1/6 of the Pt capsule. The remaining capsule volume was filled with the silicate starting material. To introduce variations in the water fugacity, the samples were subjected to three types of treatment before sealing the capsules by welding: (1) Dried in a vacuum oven at 200 °C for over 24 hours (to remove water from the hydrated solvent). (2) Dried in an oven at 110 °C for over 40 hours (to remove surface-adsorbed water). (3) No special treatment.

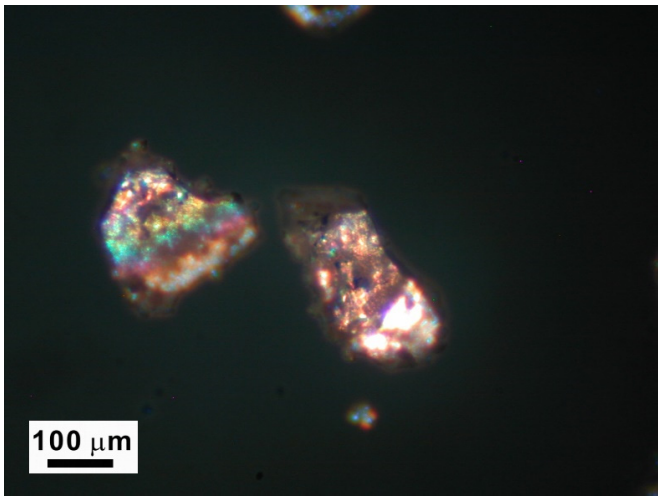

Fig. 3.5-4: Polarized-light optical microscopic images of wadsleyite crystals under crossed nicols.

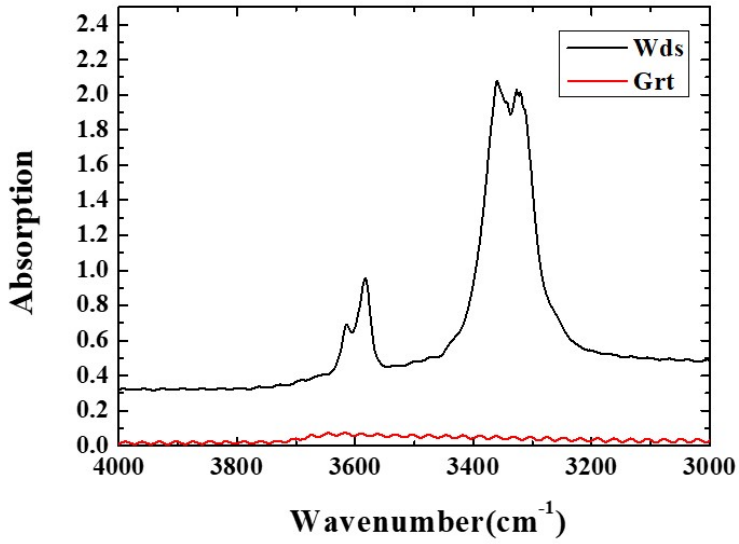

Fig. 3.5-5: Typical polarised absorption spectra of wadsleyite (black) and coexisting garnet (red).

Single crystals of both wadsleyite and garnet were successfully synthesised under all conditions, with sizes up to 300 and 500 μm, respectively (Fig. 3.5-4). The run products were analysed by X-ray diffraction and by polarised infrared absorption spectroscopy of oriented sections (Fig. 3.5-5). For the samples with the relatively water-rich starting conditions (type 3), wadsleyite contains about 1500 ppm by weight of water, and garnet about 200 ppm, implying preferential partitioning of water into wadsleyite. The water partitioning in the samples of type 1 and type 2 still needs to be quantified.

e. *The extinction coefficient of H_2 in silicate glasses and the fate of hydrogen in a magma ocean (H. Keppler)*

Molecular hydrogen (H_2) was the main component of the solar nebula during the formation of the solar system. The magma ocean on Earth and Moon may have equilibrated with a hydrogen-rich atmosphere. For this reason, the solubility of H_2 in silicate melts has received considerable attention in recent years, as the dissolution of H_2 in the magma ocean may have contributed to or even dominated the initial hydrogen reservoir in the mantle. Hydrogen partitioning between metal and the magma ocean may even have produced a major hydrogen reservoir in Earth's core.

Previous studies of hydrogen solubility in silicate melts, however, were mainly based on the quantification of dissolved H_2 concentrations in quenched glasses by infrared spectroscopy using the infrared extinction coefficient for H_2 reported by Shelby *et al.* (1994, J Non-Cryst. Solids 179: 138). This method of quantifying dissolved H_2, however, is rather questionable for two reasons: (i) The extinction coefficient of Shelby *et al.* (1994) was calibrated for pure silica glass and may not be applicable to glasses with the composition of natural magmas. Infrared extinction coefficients are generally matrix-dependent. For H_2, this matrix-dependence may be particularly strong, as the H_2 molecule has no permanent dipole moment and the infrared activity is only activated by interactions with the matrix, which induces a minor dipole moment. (ii) The coefficient of Shelby *et al.* (1994) was determined by a simple gravimetric method, which attributed the weight loss of H_2-loaded silica glass upon heating exclusively to the loss of H_2. This is obviously a rather questionable assumption.

We calibrated the infrared extinction coefficient for H_2-loaded haplogranitic glasses using two independent methods: (i) We used Karl Fischer Titration to determine the total H content in the glasses and subtracted the H_2O content obtained by infrared spectroscopy from the total H content to obtain the concentration of hydrogen present as H_2. (ii) We treated the H_2-bearing glasses at high pressure in a pure O_2 atmosphere, such that any H_2 present was oxidised to H_2O. The corresponding increase in H_2O concentration was again determined by infrared spectroscopy. The two different calibrations yielded highly consistent results. The regression line shown in Figure 3.5-6 corresponds to a linear molar absorption coefficient for the 4100 cm^{-1} band of H_2 of 2.12 liter $mol^{-1}cm^{-1}$. Notably, this is about one order of magnitude larger than

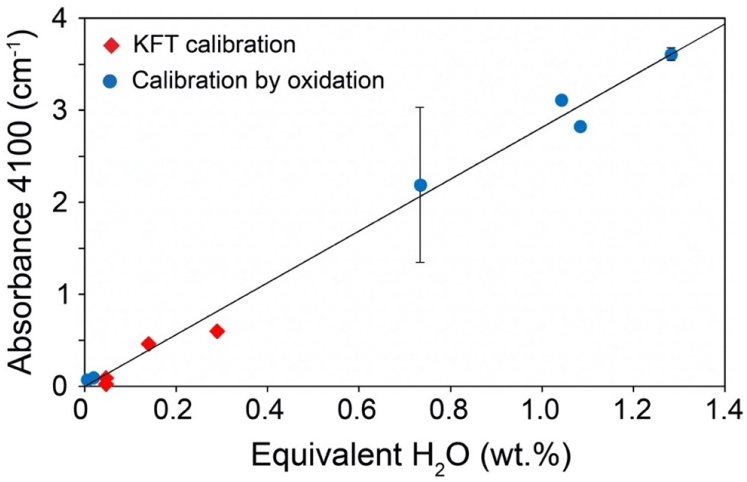

Fig. 3.5-6: Calibration of the 4100 cm^{-1} infrared band of H_2 in haplogranitic glass by Karl Fischer titration (KFT) and by oxidation with O_2. The sample with the large error bar was initially inhomogeneous. Where no error bar is shown, the uncertainty is smaller than the size of the symbol. "Equivalent H_2O" is the concentration of H_2O (in wt. %) corresponding to the equal molar concentration (in mol/liter) of H_2 in the glass.

the value reported by Shelby (1994) for H_2 in silica glass (0.26 liter $mol^{-1}cm^{-1}$). A consequence of this re-calibration is that previous measurements of H_2 solubility in silicate melts likely overestimated H_2 concentrations by one order of magnitude.

If previous measurements of H_2 solubility in basaltic melt are evaluated using the new infrared extinction coefficient, predicted H_2 solubilities are so low that likely, under all plausible conditions, the amount of H_2 in a magma ocean will be far subordinate as compared to that of H_2O. The low H_2 solubility in the melt also makes strong sequestration of H_2 into the Earth's core rather unlikely, even if H is partitioned very strongly in favour of the metal phase in equilibrium with silicate melt. This is because, during accretion, the cores of impacting planetesimals may break up and become emulsified in the magma ocean. Even if H then strongly partitions into the metal, the amount of H that could be sequestrated will be limited by the low initial H_2 concentration in the silicate melt.

f. *Melting of the Martian mantle: Physical properties of mafic-ultramafic melts (R. Pierru, L. Man, L. Henry and N. Guignot/Paris, R. Farla/Hamburg, D. Antonangeli/Paris and D.J. Frost)*

Very recently, seismic data from the NASA InSight mission has provided crucial new information and constraints on the internal structure and thermal evolution of Mars. The collected results allowed for a single-station seismic analysis of the Martian interior, placing constraints on discontinuities within the crust and the depth of the crust-mantle boundary. A major mid-mantle discontinuity and the core-mantle boundary were detected. One of the most

intriguing discoveries of the InSight mission was the identification of a thick layer of basal magma (~ 150 km) on top of the Martian core, which is distinct from the core-mantle boundary structure of Earth. However, the ability to fully exploit the seismic records from the SEIS seismometer to produce accurate compositional, structural, and dynamical models of Mars depends critically on knowledge of the physical properties of the relevant minerals, liquids, and mineralogical assemblages under appropriate conditions.

Partial melting in the Martian mantle could still occur today in the upper mantle and close to the core-mantle boundary, but certainly at limited degrees of partial melting and only in specific regions. However, the mantle of Mars is considered to be cold, characterised by low potential temperatures and a significantly thick lithosphere. Current solidus models can hardly explain the occurrence of mantle melting beneath Tharsis in the context of a cold, mixed mantle, let alone a basal magma ocean. Furthermore, the composition of the melt controls the viscosity and buoyancy of the liquid, and thus the ability of liquids to reach the surface or stagnate in the source.

Crystallisation, fractionation, and possibly overturn of a magma ocean in Mars could have led to the formation of a compositionally distinct layer at the bottom of the mantle. The physicochemical properties of a magma ocean determine its evolution and have a profound impact on the structure and composition of the modern mantle. However, current models used to understand mantle thermal evolution, crustal extraction and volcanic evolution rely on very limited knowledge of the state of the Martian mantle, the melting process and the physical properties of Martian magmas. Notably, the fact that the Martian mantle appears to be richer in iron than Earth's mantle will not only affect the stable mineralogy, but will also have a direct impact on mantle melting temperatures, the chemistry of the magmas and also the physical properties, such as density and viscosity, of melts produced at different pressures.

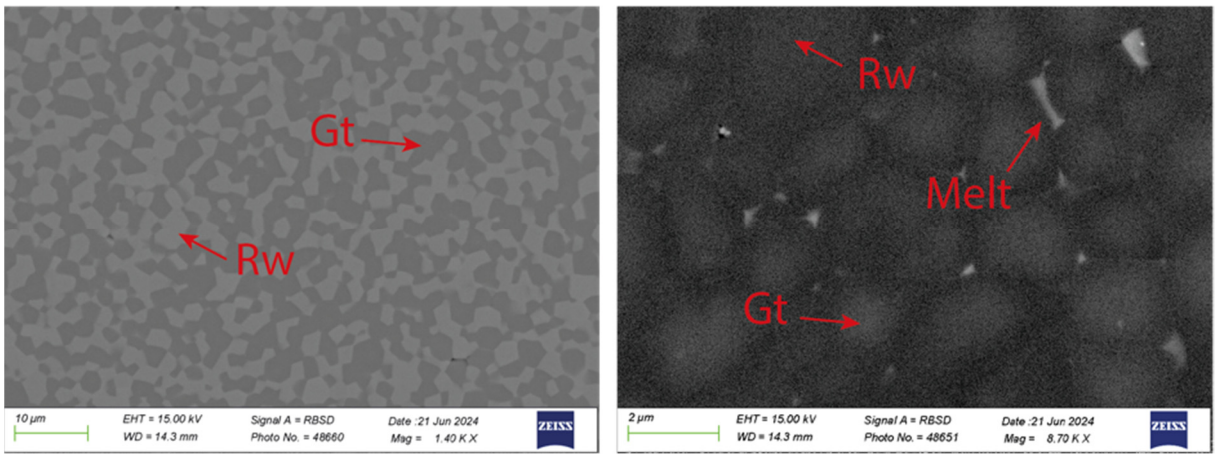

Fig. 3.5-7: Backscattered electron microscopic images of synthesised and partially molten samples at subsolidus and solidus conditions, respectively (≈18 GPa). Rw: Ringwoodite; Gt: Garnet.

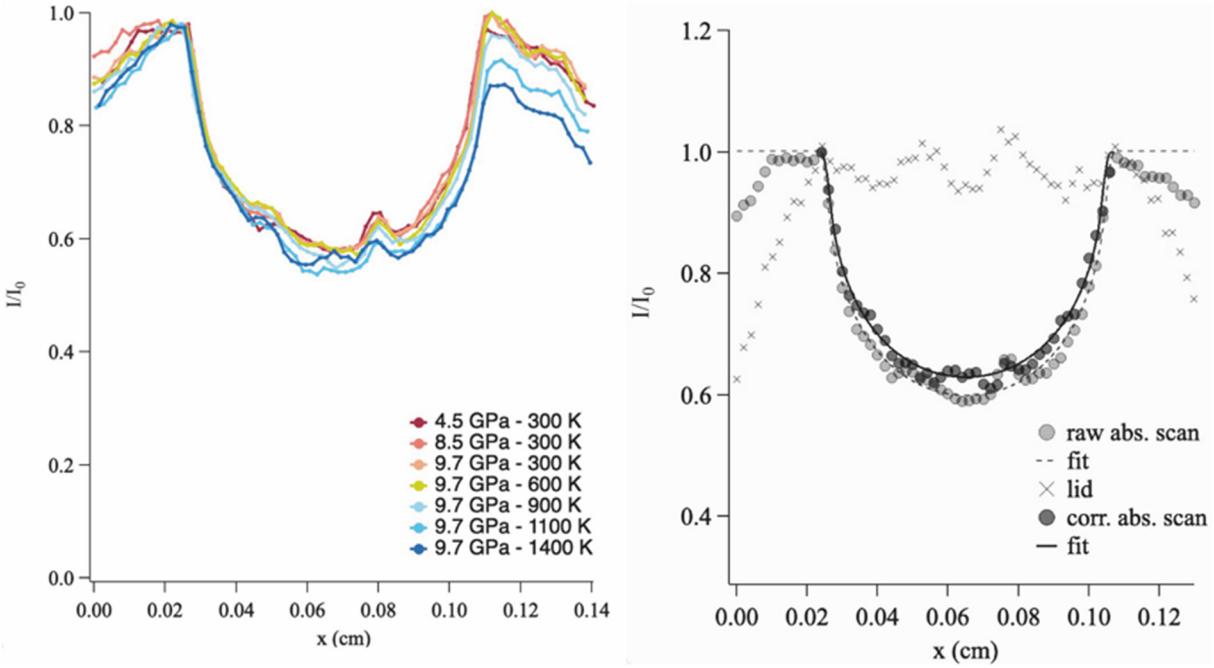

Fig. 3.5-8: Example of density measurement of a Martian-type glass realised at Psiché, Soleil (Paris) using a multianvil apparatus. (Left) X-ray absorption at different pressure and temperature. (Right) Data corrected using the absorption scan of a diamond lid at the top of the diamond capsule.

To address these questions, Martian mantle-like compositions have been synthesised using gas mixing furnaces to control the redox state of the materials. We performed high-pressure iterative melting experiments in the range 15-22 GPa in the multianvil apparatus to understand the temperatures required to melt the deep Martian mantle (Fig. 3.5-7). Current estimates for the temperature at the base of the Martian mantle appear to be far too low to cause significant mantle melting, even of iron-rich compositions at this depth. For this reason, the effects of iron-content contents have been examined under the further constraint that the oxygen fugacity of the magma would be buffered by the proximity of the likely sulphur-bearing Martian core.

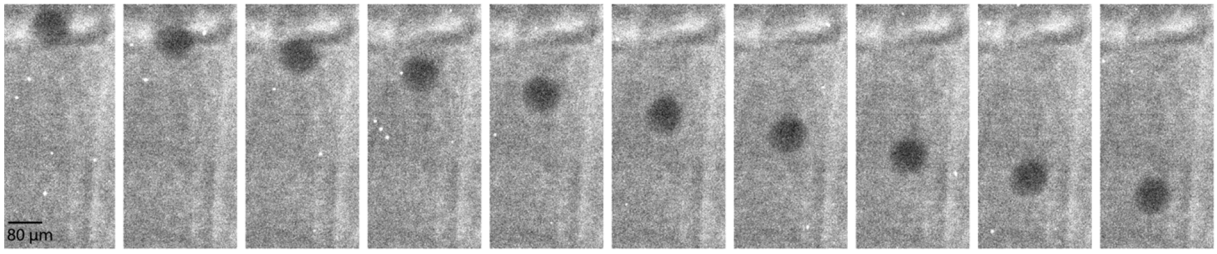

Fig. 3.5-9: X-ray radiographic image of a falling sphere (Re) at 7 GPa in a melt of Martian-type composition, realised at beamline P61b, DESY (Hamburg).

These in-house melting experiments have been extended by performing complementary *in situ* experiments to measure the density (X-ray absorption using the Beer-Lambert law) and the viscosity (falling sphere) of Martian-type glasses and melts from the deep mantle. With high pressure density measurements (Fig. 3.5-8), we aim to determine whether the different melts generated at great depths in the Martian mantle, according to the chemistry and the melt fraction, may migrate upward or sink on a relatively short geological time scale or whether they may remain trapped at given depths due to neutral buoyancy. Viscosity influences the extent of chemical equilibrium between silicates and metallic liquids forming the core and the physics of crystal settling in a convecting magma. The viscosity of a magma ocean also controls crystal growth rates and convection dynamics. The low viscosity of Martian melts measured (Fig. 3.5-9) has implications for magmatic processes in planetary interiors, like the differentiation, the crystallisation mechanisms but also the lifetime of a magma ocean.

g. *Pressure-induced elongation of hydrogen-oxygen bond in sodium silicate melts (T. Ohashi, T. Sakamaki and A. Suzuki/Sendai, K.-I. Funakoshi and T. Hattori/Tokai, L. Yuan and G. Steinle-Neumann)*

Based on geophysical observations from seismology and magnetotellurics, magma is suggested to be present locally in the Earth's deep interior: In the mantle wedge, above subducting slabs, at the lithosphere-asthenosphere boundary, above the 410-km and below the 660-km seismic discontinuities, and above the core-mantle boundary. Due to faster transport and increased reactivity, even a small amount of melt can significantly affect the chemical evolution of the Earth. Despite the importance of exploring macroscopic properties and structures of silicate melts at high pressure and high temperature, they are not well understood, as *in situ* experiments on melts at high pressure are difficult.

Sodium is a network-modifier cation, which significantly lowers the liquidus temperature and the degree of polymerisation in silicate melts: Along the Na_2O-SiO_2 join, $Na_6Si_8O_{19}$ (N3S8) has a relatively low liquidus temperature. Melting is further promoted by volatiles, with water being the most abundant component. Here we report data from *in situ* X-ray and neutron diffraction experiments together with results from *ab initio* molecular dynamics (MD) simulations to determine the structure of dry and hydrous/deuterated $Na_6Si_8O_{19}$ glasses and melts at high pressure and temperature, with compositions N3S8-D9 (9 wt. % D_2O), N3S8-D10, and N3S8-D12 in the experiments, and N3S8-H8 (8 wt. % H_2O) and N3S8-H14 in the computations.

From the experimental X-ray and neutron structure factors, total pair distribution functions are computed via Fourier transformation, and peaks can be assigned to atomic pair correlations, *i.e.*, D-O, Si-O, Na-O, O-O and Si-Si with increasing mean-interatomic distances $r_{\alpha\beta}$ (Fig. 3.5-10 shows r_{DO}, r_{SiO}, r_{OO}, and r_{SiSi}). With pressure, the distance between D and O monotonically increases due to an increase in D-O coordination number, *i.e.*, the formation of -O-D-O- bridges

at the expense of -O-D deuteroxyls with the proportion of molecular D_2O remaining constant, as seen in the *ab initio* MD results. The -O-D-O- bridges formed on compression can hold hydrogen more rigidly in the melt structure than -O-D and D_2O species, and a larger number of -O-D-O- bridges contributes to an increase in solubility and ideality of mixing in the silicate-water system, supporting the general notion that water solubility in silicate melts increases with pressure. Similarly, the distance between Si and O for the dry and hydrous N3S8 melts generally increase with compression, likely due to a gradual decrease in the Si-O-Si angle and weakening of the Si-O bond. The r_{SiO} values determined from the X-ray structure factor are virtually independent of water content, showing that SiO_4 tetrahedra are not modified by H_2O. Effective r_{SiO} obtained from neutron diffraction for deuterated compositions are larger than for the dry glass due to the influence of D-D correlations at $r \sim 1.6$ Å, also accounting for the difference of ~ 0.01 Å in r_{SiO} for the hydrous melts between X-ray and neutron diffraction experiments.

To further elucidate the pressure dependence of chemical speciation, we consider the molar fractions of Si-O-Si, Si-O^- + Na^+, Si-O-H, and Na-O-H species in our MD simulations (Fig. 3.5-11) to explore the depolymerisation of the Si-O-Si bridges according to the mechanism Si-O-Si + $Na_2O \rightarrow 2\cdot$(Si-O^- + Na^+). With increasing water content, the relative abundance of Si-O-Si speciation decreases, while that of Si-O^- + Na^+ and Si-O-H increases, with Na_2O being

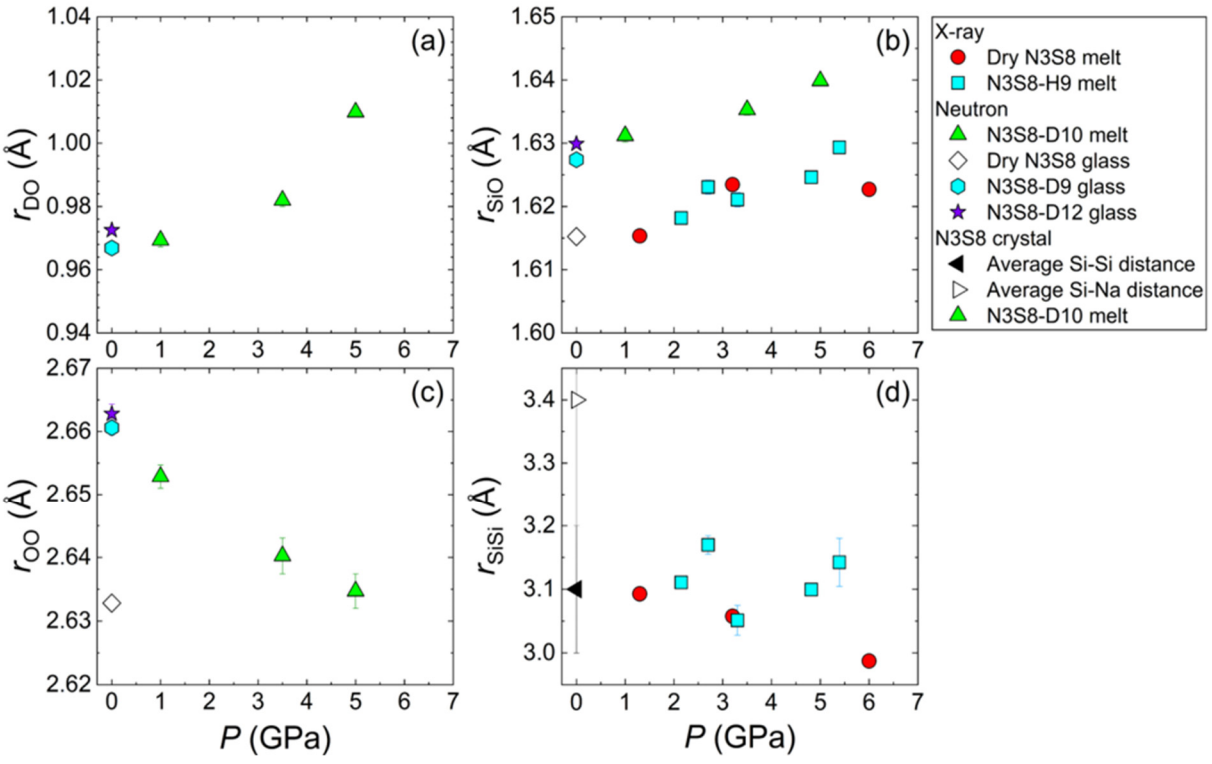

Fig. 3.5-10: Pressure dependence of interatomic distances r_{DO} (a), r_{SiO} (b), r_{OO} (c), and r_{SiSi} (d) for dry and hydrous $Na_6Si_8O_{19}$ melts and glasses inferred from the total pair distribution functions $g^X(r)$ and $g^N(r)$ via Fourier transformation of the neutron and X-ray structure factors, respectively. In (d), Si-Si and Na-Si distances and their distribution for $Na_6Si_8O_{19}$ crystal are included.

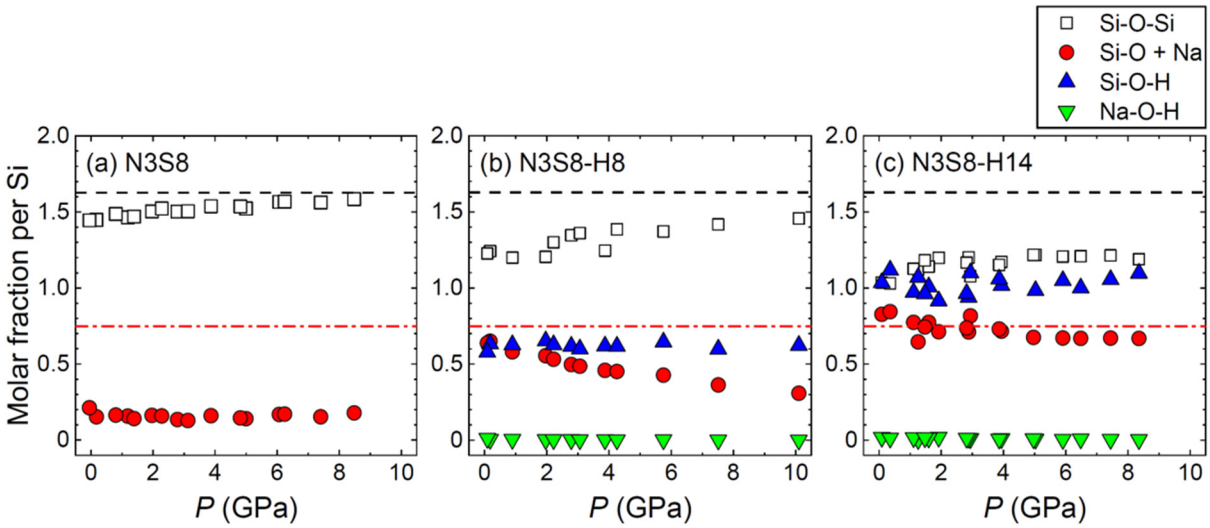

Fig. 3.5-11: Pressure dependence of cation-oxygen-cation speciation in molar fractions for dry N3S8 (a), hydrous N3S8-H8 (8 wt. % H_2O) (b), and N3S8-H14 (14 wt. % H_2O) (c) from molecular dynamics simulations at 3000 K. The black dashed lines show the maximum proportion of Si-O-Si species in anhydrous N3S8, the red dash-dotted lines indicate the molar fraction of $Si\text{-}O^- + Na^+$ species when all Na_2O are dissociated to terminate Si-O-Si bridges without involving H_2O.

fully dissociated in N3S8-H14. The population of Si-O-Si in dry N3S8 increases with pressure, while the population of $Si\text{-}O^- + Na^+$ remains constant. This suggests that polymerisation is mainly caused by ring closure, which scavenges the Na^+ cation from its network-modifying role by a "zipper" mechanism, $2\cdot(^{[4]}Si\text{-}O^- + Na^+) \rightarrow {}^{[4]}Si\text{-}(O\text{-}^{[5]}Si\text{-}O)^{2-} + 2\cdot Na^+$, with one O shared by a four-fold and five-fold coordinated Si; charge balance for Na^+ is maintained by a negatively charged O atom in the SiO_5 polyhedron. This "zipper" mechanism suggests that in hydrous melts compression changes the structural role of Na^+ from a network modifier to a charge-balancing cation, with the dissociation of Na_2O induced by H_2O. The latter reaction also increases the H-O coordination number, probably enhancing water solubility with pressure. The virtual absence of Na-O-H complexes is consistent with previous NMR results on hydrous sodium silicate glasses.

h. *Investigating melt structure and viscosity of Agnano–Monte Spina (Campi Flegrei caldera) trachyte and Pollena (Vesuvius) phonotephrite (S. Abeykoon/Camerino, D. Di Genova, S. Dominijanni and E.C. Bamber/Rome, D. Bondar and P. Valdivia Munoz, M. Carroll and F. Arzilli/Camerino)*

Volcanic eruptions are among the most hazardous natural phenomena, profoundly impacting the socio-economic and environmental landscape. This study focuses on two historically significant volcanic events in southern Italy: The Agnano–Monte Spina (AMS) eruption within

the Campi Flegrei caldera and the Pollena eruption of Mount Vesuvius. Here, we investigate the melt viscosity and short-range structure of the liquid phase of erupted magmas. We aim to better understand the relationship between physicochemical properties of magma and the structure of volcanic melts.

Both events, categorised as highly explosive eruptions (sub-Plinian and Plinian), have left vast impacts on society. The Agnano-Monte Spina eruption, which occurred approximately 4,100 years ago, stands out as the largest event during the most recent period of activity in the Campi Flegrei caldera, an area now densely populated. This eruption serves as a critical reference point for future volcanic activity, especially as current monitoring systems indicate greater activity in the region. Similarly, the 472 AD Polena eruption of Vesuvius, classified as sub-Plinian, serves as a reference eruption for future volcanic activity and risk mitigation strategies. Together with the Plinian Agnano-Monte Spina eruption, it represents one of the most intense volcanic scenarios expected for Vesuvius. These two eruptions not only provide valuable insights into explosive volcanic behaviour but also highlight the need for continued research and preparedness in regions of high volcanic risk.

High-pressure and high-temperature experiments (using the piston-cylinder apparatus and TZM cold seal pressure vessels) were conducted to synthesise Agnano-Monte Spina trachyte and Pollena phonotephrite with varying water contents (0.5-5.0 wt. % H_2O). In some cases, the synthesised silicate glasses exhibited nano-crystallisation, potentially caused by the intrinsic melt structure properties (*i.e.*, diffusion of elements and solubility), variations in oxygen fugacity and water content. The melt viscosity measurements will be derived using conventional and flash differential scanning calorimetry (C- and F-DSC), enabling the development of comprehensive viscosity models combined with the literature data. Preliminary

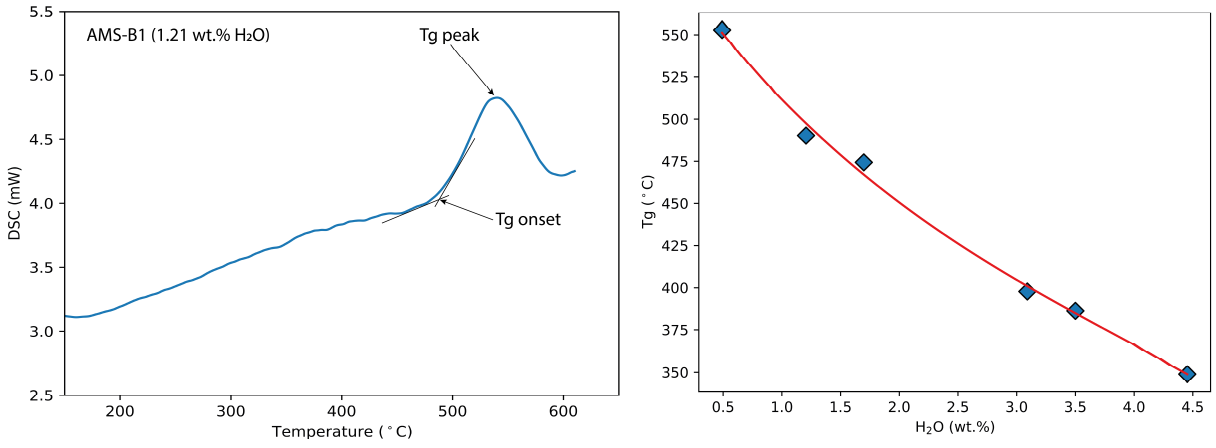

Fig. 3.5-12: Left: Measured DSC curve for hydrous AMS-B1 sample (1.21 wt. % H_2O) following a cooling and heating at 10 K/min. Glass transition temperature: Tg = 490 °C, and Tg peak = 540 °C. Right: The onset of glass transition temperatures for AMS-B1 trachyte, showing a decrease in Tg with increasing water content.

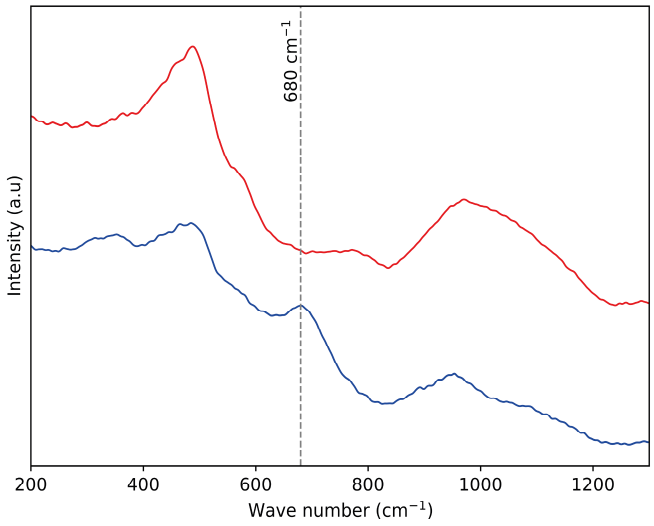

Fig. 3.5-13: Raman spectra of hydrous AMS-B1 trachyte glasses before C-DSC and F-DSC viscosity measurements. The blue spectrum, with a prominent peak at 680 cm^{-1}, suggests the presence of nanolite phases (Fe-Ti oxides) in the glass synthesised using the TZM apparatus. In contrast, the red spectrum corresponds to glass synthesised in the piston-cylinder experiment, which lacks this peak.

results (Fig. 3.5-12) from DSC analyses of Agnano-Monte Spina trachyte shows that the glass transition temperature (where the melt viscosity is equal to 10^{12} Pa s) decreases from 562 °C to 350 °C with increasing water content from 0.5 to 4.5 wt. %. Raman spectroscopy will be used to examine the structural changes in melts under hydrous conditions and also, assess changes induced by high-temperature DSC C-DSC and F-DSC measurements. Figure 3.5-13 shows the Raman spectra of hydrous Agnano-Monte Spina trachyte samples containing around 3 wt. % of water. The spectra indicate the crystallisation of nanolites in the glass synthesised using the TZM apparatus (blue spectra), compared to the glass synthesised with the piston-cylinder experiment (red spectra). This difference is likely attributed to variations in oxygen fugacity conditions during the synthesis.

Using viscosity measurements combined with Raman spectroscopy, this study will investigate how both melt structure properties and crystallisation tendency influence changes in magma viscosity over a range of high temperatures typical of volcanic eruptions. These findings will provide vital insights into the factors that control the explosivity and eruptive behaviour of the Campi Flegrei caldera and Mount Vesuvius.

i. *A new viscosity model for Colli Albani: Measurements and implications of nanolite formation in the melt (E. Fanesi/Camerino, D. Di Genova/Rome, P. Valdivia Munoz and D. Bondar, S. Dominijanni/Rome, A. Kurnosov, A. Vona and C. Romano/Rome, F. Arzilli/Camerino)*

In this study, we developed a new viscosity model for the tephri-phonolitic melts from the Pozzolane Nere eruption (407 ± 4 ka) in the Colli Albani volcanic district of central Italy. We investigated the tendency of the melt to nano-crystallise and the effect of nanolites on viscosity measurements. We used a furnace and a piston cylinder apparatus to synthesise both anhydrous and hydrous glasses, with water contents ranging from 0.43 wt. % to 5.29 wt. %, as assessed using FTIR spectroscopy. We measured the viscosity of the anhydrous composition using the

micropenetration technique (MP). Additionally, we performed indirect analyses using conventional differential scanning calorimetry (C-DSC). We characterised the structural features of the samples before and after viscometry and calorimetry using Raman spectroscopy. The post-experiment occurrence of a sharp peak at ~ 690 cm^{-1} confirmed the presence of Fe-Ti nanolites in both the samples analysed using MP and C-DSC. Nonetheless, we noticed that the sample subjected to C-DSC crystallised a minor amount of nanolites as compared to the ones subjected to MP, as inferred from the Raman spectra. This suggests that samples subjected to C-DSC were less altered, and therefore, more representative of a pristine melt. Furthermore, we observe that during MP measurements, at constant temperature, the measured viscosity increased from $10^{11.85}$ to $10^{12.27}$ Pa s at 691 °C, and from $10^{10.21}$ to $10^{10.58}$ Pa s at 780 °C, possibly due to nanolite precipitation.

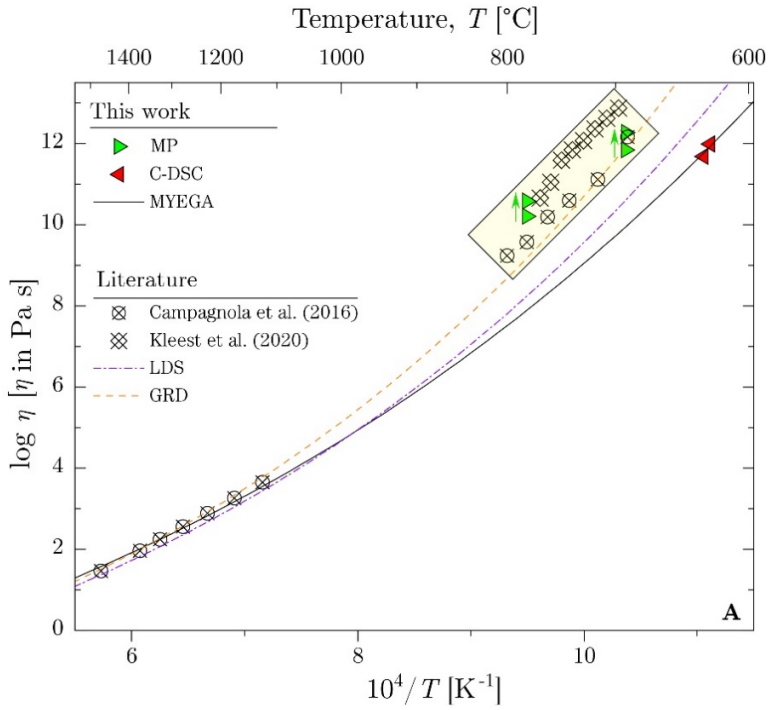

Fig. 3.5-14: Viscosity of the anhydrous Pozzolane Nere (PNR) sample as a function of temperature, as compared with previous studies. Red triangles show low-temperature viscosity data derived from DSC measurements of the reduced sample (PNR_0_RED). Green triangles indicate viscosity measured via micropenetration over 60 minutes. The solid black line represents the MYEGA model fit for PNR_0_RED, using high-temperature viscometry data (concentric cylinder) from Campagnola *et al.* (2016; Chem Geol 424:12). The fitting yielded a melt fragility index (m) of 31.32 ± 0.26 and T_g of 624.4 ± 2.0 °C. Crossed empty circles and diamonds represent low-temperature viscosity data from Campagnola *et al.* (2016) and Kleest *et al.* (2020; Contr Mineral Petrol 175: 82), where nanolites were detected before micropenetration measurements. The light-yellow rectangle highlights data influenced by nanolite formation before and/or during MP measurements. Dashed lines show viscosity predictions from the Giordano *et al.* (2008; EPSL 271: 123) (GRD) and Langhammer *et al.* (2021; Geochem Geophys Geosys 22: e2021GC009918) (LDS) models, with GRD predictions aligning with nanolite-bearing viscosity data.

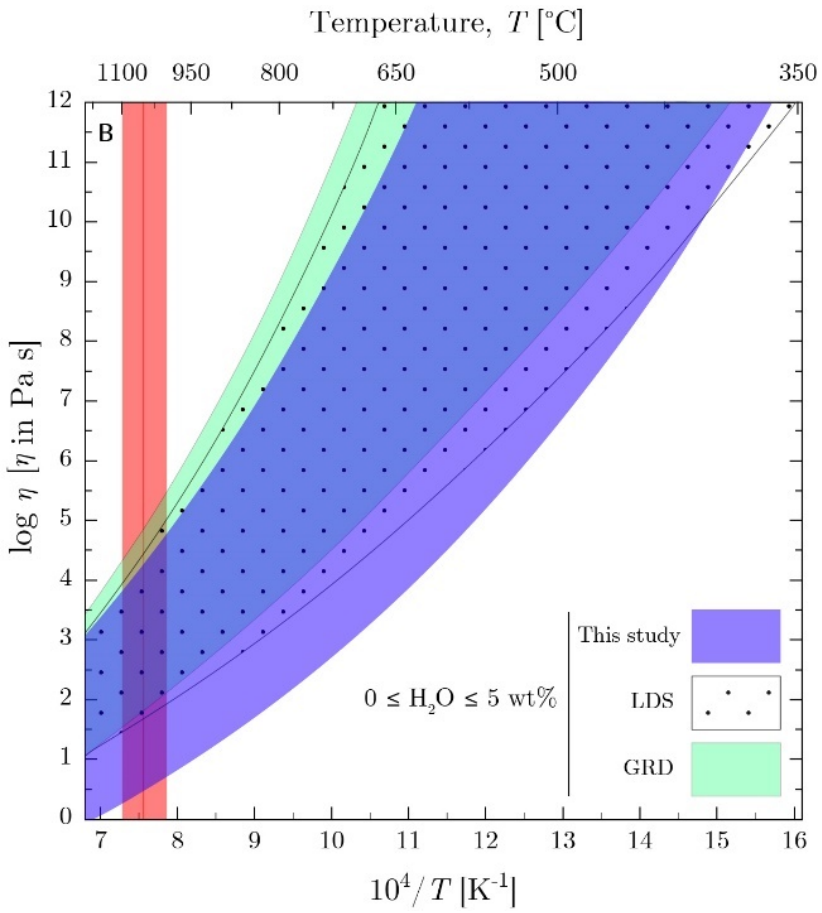

Fig. 3.5-15: Global viscosity model for Pozzolane Nere melt as a function of water content (0 to 5 wt. %) and temperature. The MYEGA model incorporates the T_g and m dependence on water content. The red-shaded vertical area marks the expected eruptive temperature interval (1000-1100 °C) for PNR magma. See Figure 3.5-15 for further explanations.

We employed the Mauro–Yue–Ellison–Gupta–Allan (MYEGA) parametrisation to develop a new viscosity model (Fig. 3.5-14) using our data together with the ones collected at high temperatures using a concentric cylinder from Campagnola *et al.* (2016; Chem Geol 424:12). Notably, the glass transition temperature (T_g) extrapolated by fitting our C-DSC data (T_g = 909.3 K) is lower than the one predicted by the global models of Giordano *et al.* (2008; EPSL 271: 123) (GRD) and Langhammer *et al.* (2021; Geochem Geophys Geosys 22: e2021GC009918) (LDS), by ~ 50 K and ~ 15 K respectively for the same composition.

Samples with a water content > 2.01 wt. % precipitated nanolites during synthesis, prior to thermal treatment, as shown by the presence of a sharp peak at ~ 690 cm^{-1} in the Raman spectra. The viscosity of hydrous samples was measured indirectly using the C-DSC method. The melt fragility index (m) of hydrous samples was estimated using the empirical relationship proposed by Cassetta *et al.* (2021; Sci Rep 11: 13072) that correlates m with acoustic wave velocities. The MYEGA parametrisation allowed us to develop hydrous viscosity models for the different

compositions. Finally, a new model accounting for both water content and temperature variation was built fitting together all the data.

To conclude, we compared our new model with the GRD and LDS models for eruptive conditions (*i.e.*, 1000 < T [°C] < 1100). Our model predicts a 5,000-fold increase in viscosity, from $10^{0.54}$ Pa·s to $10^{4.24}$ Pa·s, as the water content decreases from 5 wt. % to 0 wt. %. In contrast, the GRD and LDS empirical models predict a notably lower increase in viscosity. The GRD model shows a rise from $10^{1.82}$ Pa·s to $10^{4.86}$ Pa·s (a 1,090-fold increase), while the LDS model indicates an increase from $10^{1.65}$ Pa·s to $10^{4.44}$ Pa·s (a 610-fold increase, Fig. 3.5-15). In more general terms, this study illustrates nanolite precipitation in a tephri-phonolitic melt and its effect on viscosity. Furthermore, it demonstrates the limitations of the micropenetration technique, suggesting calorimetry as a more reliable approach.

j. *Nanolite crystallisation in volcanic glasses: Insights from high-temperature Raman spectroscopy (D. Bondar, A. Canizarès/Orléans, D. Bilardello/Minneapolis, P. Valdivia Munoz, A. Zandonà/Clausthal, C. Romano/Rome, M. Allix/Orléans and D. Di Genova/Rome)*

The *in situ* observation of nanolite formation in undercooled volcanic melts remains technically challenging and often relies on expensive large-scale infrastructures such as synchrotron facilities. This study aimed to overcome these limitations by utilising high- temperature Raman spectroscopy, a cost-effective and accessible method, to investigate nanolite formation in synthetic anhydrous andesite melts.

The experimental setup used Raman spectroscopy to examine nanolite crystallisation in an andesitic melt, representing a composition from Sakurajima volcano, Japan. Raman spectra were collected using a Renishaw InVia Qontor spectrometer, employing lasers of various wavelengths ranging from 355 to 514 nm. Laser power ranged from 20 to 50 mW with integration times of 60 seconds at high temperatures. Temperature control was achieved using a Linkam TS1500 heating stage, with heating and cooling rates adjusted between 5 and 20 °C/min, depending on the specific experimental conditions.

Nano-crystallisation in Fe-bearing volcanic melts was observed for the first time using *in situ* high-temperature Raman spectroscopy. Heating the glass above Tg induced crystallisation, forming Fe-Ti-oxide nanolites with distinct Raman spectral features at 310 and 670 cm^{-1}. The 310 cm^{-1} peak correlated solely with the degree of nanolite crystallisation, while the 670 cm^{-1} peak was temperature-dependent, becoming difficult to observe above 500 °C (Fig. 3.5-16). Low-temperature rock-magnetic analyses confirmed the formation of ~ 2.6 vol. % of nanolites with a mean size of ~ 20 nm after heating to 808 °C. Complementary high-temperature X-ray diffraction analyses supported these findings, emphasising the utility of high temperature Raman spectroscopy as a reliable technique for identifying nanocrystals and studying their development.

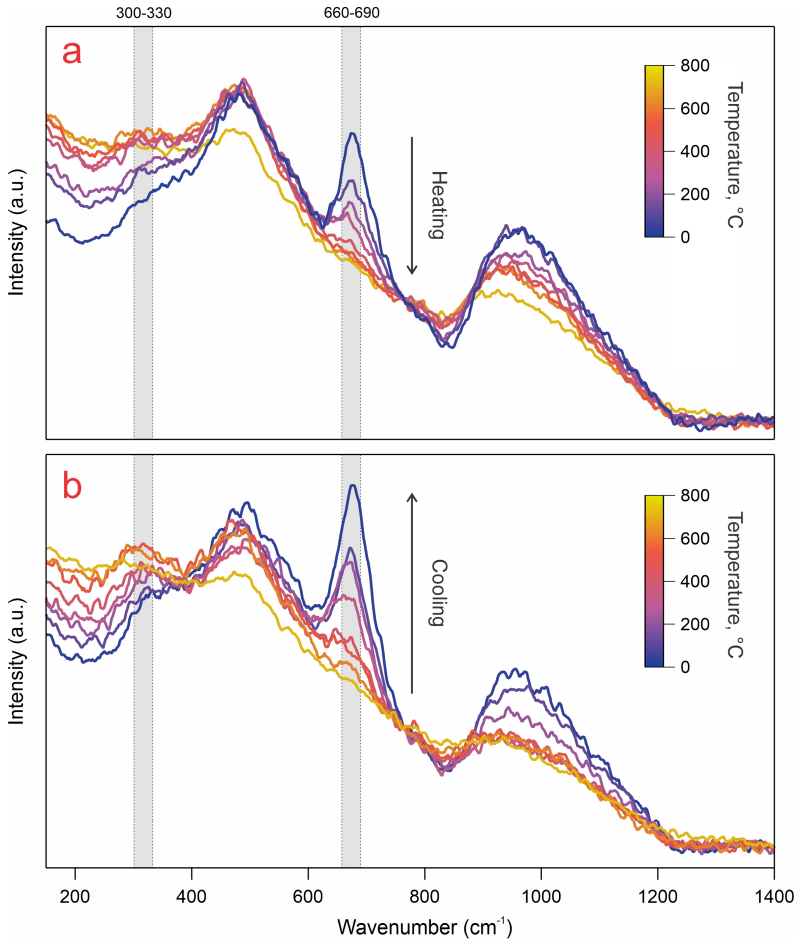

Fig. 3.5-16: Raman spectra of andesitic nanolite-bearing glass recorded upon heating to 723 °C (a) and subsequent cooling (b). This sequence demonstrates the vanishing/broadening and subsequent reappearance/sharpening of the 660-690 cm^{-1} spectral feature. The spectra were normalised at around 750 cm^{-1}. A linear baseline fit to the spectrum within the 1940-1430 cm^{-1} interval was subtracted.

Laser selection played a critical role in this research – the green laser was most effective for detecting changes in Raman features at room and high temperatures. However, above 720 °C, black body radiation became a significant limitation when using a non-confocal setup with poorly transparent samples. Alternative configurations, such as a confocal setup or lasers with shorter wavelengths, could potentially extend the temperature range of these measurements. The study also noted that blue and ultraviolet lasers were less sensitive to features associated with Fe-Ti oxides, with the former also being more destructive, underscoring the advantages of the green laser for high-temperature volcanic glass analyses.

This research provides a robust protocol for *in situ* Raman spectroscopic studies of volcanic glasses at high temperatures, offering a pathway for investigating nanolite formation and its implications for volcanic melt dynamics. It highlights the challenges of studying reactive volcanic melts, where rapid nano-crystallisation and iron oxidation can interfere with viscosity and DSC measurements.

k. *Nanoscale chemical heterogeneities in andesitic glass induced by nanolite formation: A STEM-EDS observation (P. Valdivia Munoz and N. Miyajima, in collaboration with D. Di Genova/Rome)*

While previous studies have established the role of nanolites in contributing to more explosive volcanic behaviour, the relationship between nanolite formation and nanoscale chemical variations in volcanic melts – particularly at elevated temperatures – remains underexplored. In this study, we use STEM-EDS analysis to investigate chemical heterogeneities in an andesitic composition at the nanoscale, with a focus on the formation and distribution of nanolites at high temperatures. We examined a sample of andesitic glass (Fig. 3.5-17) that was reheated to

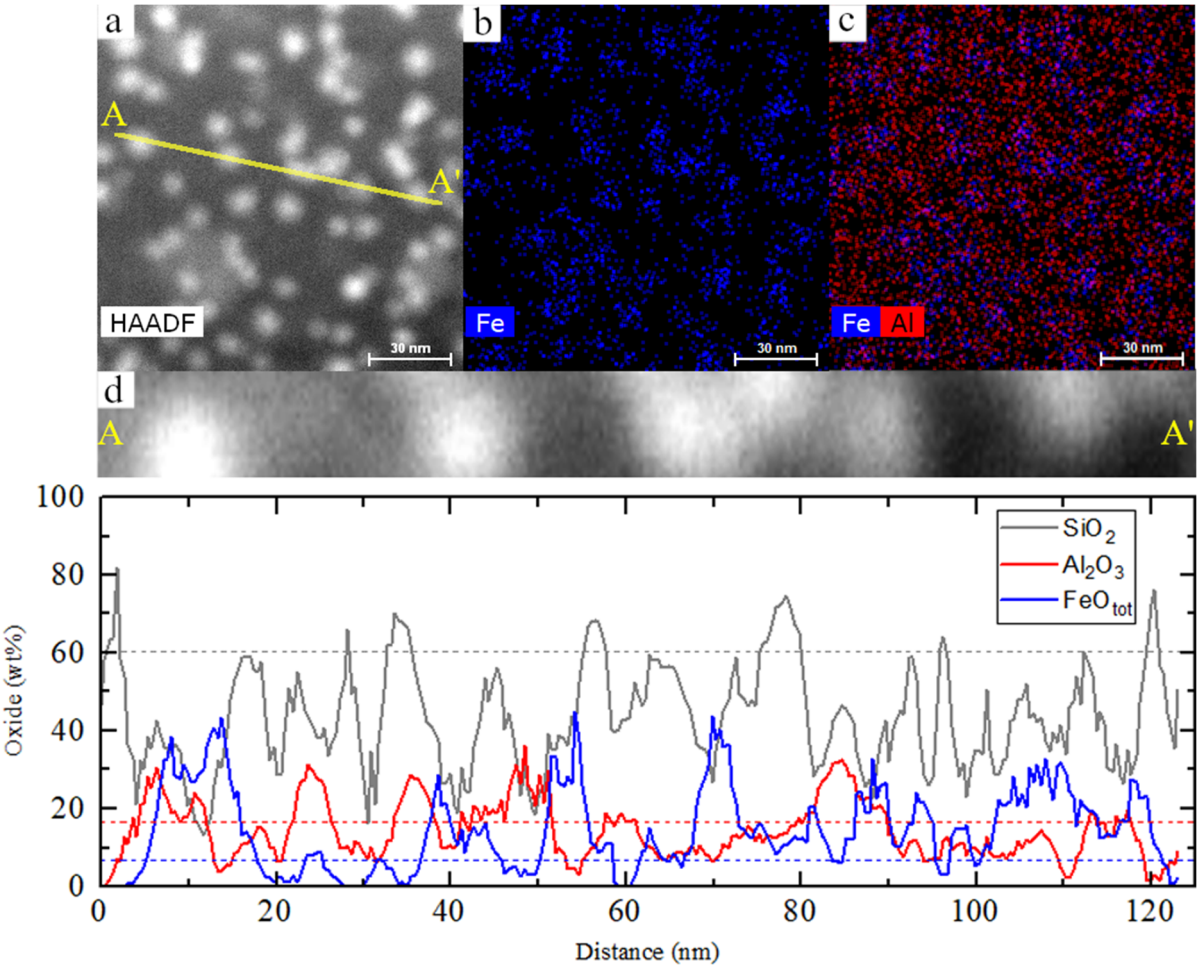

Fig. 3.5-17: Nanoscale local variations in chemistry of an andesitic glass containing nanolites. a) STEM-HAADF image of the sample. The bright pixels represent the crystalline phase. b) EDS elemental distribution map of Fe. c) EDS elemental distribution map of Fe+Al showing a preferential distribution of Al around Fe-rich nanolites. d) Magnification of A-A' EDS-line-scan. e) EDS line profile (A-A') results, with SiO_2, Al_2O_3 and FeO_{tot} concentrations in wt. %. Values in the x-axis represent the distance between the line profile (A-A'). Values in the y-axis represent the average composition of sevren neighboring pixels along the y-axis in d.

808 °C, more than 150 °C above its glass transition temperature (T_g = 654 °C), to investigate temperature-driven nanolite formation and its influence on nanoscale chemical variations within the glass. STEM-HAADF imaging (Fig. 3.5-17a) reveals Fe-rich nanolites, which correspond to the denser (brighter) crystalline phase. Elemental maps (Fig. 3.5-17b-c) show that aluminium (Al) preferentially surrounds these Fe-rich nanolites, forming Al-enriched regions around them, while Al-depleted zones are present between the nanolites. A more detailed EDS line-scan (Fig. 3.5-17d) further refines these observations, highlighting the clear distribution of Al around the nanolites within a SiO_2-enriched matrix. These findings provide new insights into how temperature-induced nanoscale chemical variations, driven by nanolite formation, can substantially impact magma viscosity at a nanoscale level, offering important implications for understanding eruption dynamics.

l. *Temperature-dependent evolution of nanolite formation in andesitic glass: Insights from SAXS and WAXS analysis (P. Valdivia Munoz and D. Bondar, in collaboration with E.C. Bamber and S. Dominijanni/Rome, A. Longo/Grenoble and D. Di Genova/Rome)*

In this study, we utilised Small-Angle X-ray Scattering (SAXS) and Wide-Angle X-ray Scattering (WAXS) techniques to explore the temperature-dependent changes in nanoparticle characteristics within andesitic glass (AND100) samples reheated above the glass transition temperature (T_g = 654 °C) at 660 °C, 723 °C, and 808 °C. SAXS, which is sensitive to electron density variations at the nanoscale, revealed significant temperature-induced shifts in nanoparticle size and distribution. At 660 °C (AND100_MP_{660}; Fig. 3.5-18a), SAXS data showed a peak at approximately 0.9 nm^{-1}, suggesting small, uniformly distributed particles. At 723 °C (AND100_MP_{723}; Fig. 3.5-18a), this peak shifted to 0.5 nm^{-1}, indicating larger particles with reduced density. At 808 °C (AND100_MP_{808}; Fig. 3.5-18a), the SAXS data exhibited a more complex scattering signal, with two particle populations centred at 0.5 nm^{-1} and 0.1 nm^{-1}, consistent with larger, aggregated particles. Modelling of the SAXS data demonstrated a progressive increase in nanoparticle radius, from 1.7 ± 0.02 nm at 660 °C to 3.8 ± 0.5 nm at 808 °C.

WAXS analysis (Fig. 3.5-18b) provided complementary insights into crystallinity and phase composition over a larger sample volume. For AND100_MP_{660}, the WAXS pattern (Fig. 3.5-18b) lacked distinct diffraction features, consistent with amorphous phase separation observed in SAXS data, indicating minimal particle aggregation. At 723 °C, WAXS patterns (Fig. 3.5-18b) showed peaks corresponding to titanomagnetite crystallographic orientations, suggesting the onset of crystalline phase development. At 808 °C, the WAXS data (Fig. 3.5-18b) revealed a more complex phase composition, including both titanomagnetite and pyroxene phases. Rietveld refinement of these data indicated an average crystallite size of 6.7 ± 0.5 nm for titanomagnetite and approximately 19.2 ± 0.5 nm for pyroxene, aligning with previous findings for similar volcanic material.

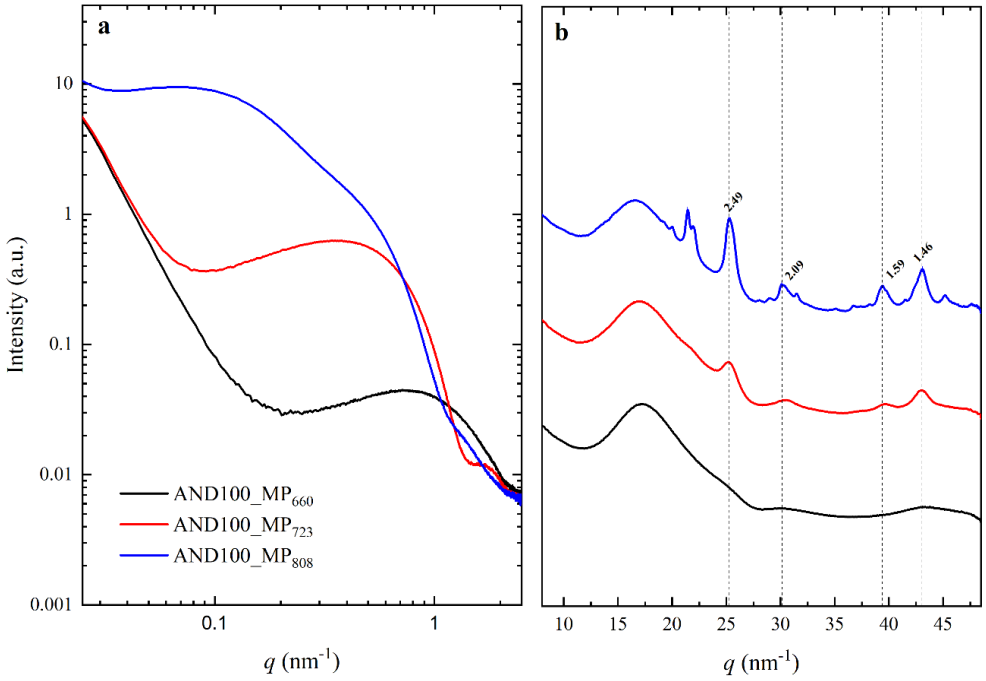

Fig. 3.5-18: SAXS-WAXS analyses of andesitic glass samples after viscosity measurements by micropenetration (AND100_MP). a) SAXS results. Sub-indices correspond to the experimental temperature. b) WAXS results. Numbers above peaks correspond to the calculated *d*-spacing (Å), where dashed lines correspond to peaks assignable to titanomagnetite. AND100_MP$_{660}$ was X-ray amorphous, while AND100_MP$_{723}$ exhibited diffraction peaks assignable to titanomagnetite and AND100_MP$_{808}$ contained titanomagnetite and pyroxene.

These results indicate distinct temperature-dependent changes in nanoparticle size, distribution, and crystallinity that directly influence magma viscosity and physical behaviour. The observed shift from small, uniform nanoparticles to larger aggregates with increasing temperature provides critical insights into the relationship between nanolite formation and temperature dependence, enhancing our understanding of eruption processes.

m. *SAXS and WAXS characterisation of volcanic glasses (S. Dominijanni/Rome, P. Valdivia Munoz, D. Bondar, E.C. Bamber/Rome, F. Arzilli/Camerino, L. Calabrò/Rome, A. Longo/ Grenoble and D. Di Genova/Rome)*

Nanostructured volcanic products are frequently associated with explosive eruptions. It has been proposed that nanoscale processes within magma may influence fragmentation, triggering explosive activity. This is due to the significant increase in magma viscosity observed when melts undergo nano-structuring. However, understanding this viscosity increase is a complex challenge. It requires both the precise measurement of the "pure" melt viscosity alongside nanodomains, and the comprehensive characterisation of nanodomains, including their size, volume, agglomeration, and atomic structure.

Traditional methods, such as Raman spectroscopy and scanning transmission electron microscopy, have been essential in unveiling this nano-structuring. For instance, the Raman peak at 670 cm^{-1} reliably indicates the presence of nanostructured regions in materials appearing structurally homogeneous under a scanning electron microscope. Yet, these methods have limitations. Raman spectroscopy provides no data on nanodomain dimensions or arrangement, while scanning transmission electron microscopy is time-consuming, costly, and restricted to small sample areas.

To overcome these challenges, we employed high-brilliance small-angle and wide-angle X-ray scattering (SAXS and WAXS) at the ESRF synchrotron in Grenoble. This approach offers a powerful tool for complementing electron microscopic observations and enables *in situ* tracking of the transient evolution of nanodomains – size, volume, degree of agglomeration, and timescales of nano-structuring – in volcanic melts. Our study focused on H_2O-bearing volcanic glasses synthesised from material that erupted during one of the largest explosive events of the Colli Albani volcano in central Italy. Samples were prepared using a Piston-Cylinder apparatus at BGI, polished, and analysed through SAXS and WAXS. SAXS data were processed using a Weibull function model, assuming spherical particle distribution, and revealed key parameters like particle radius, inter-particle distance and degree of agglomeration.

SAXS patterns showed that particle radius increases with water content, while WAXS analysis confirmed the absence of crystallisation (Fig. 3.5-19). These findings corroborate previous electron microscopic observations and support the interpretation of viscosity measurements, advancing our understanding of magma behaviour. In addition, our study sheds light on Fe-Ti solubility in volcanic melts, contributing to a broader understanding of their dynamics. This work paves the way for refining numerical models of magma viscosity in nanostructured systems. These models are essential for probabilistic eruption forecasts and for understanding the transition from effusive to explosive volcanic activity.

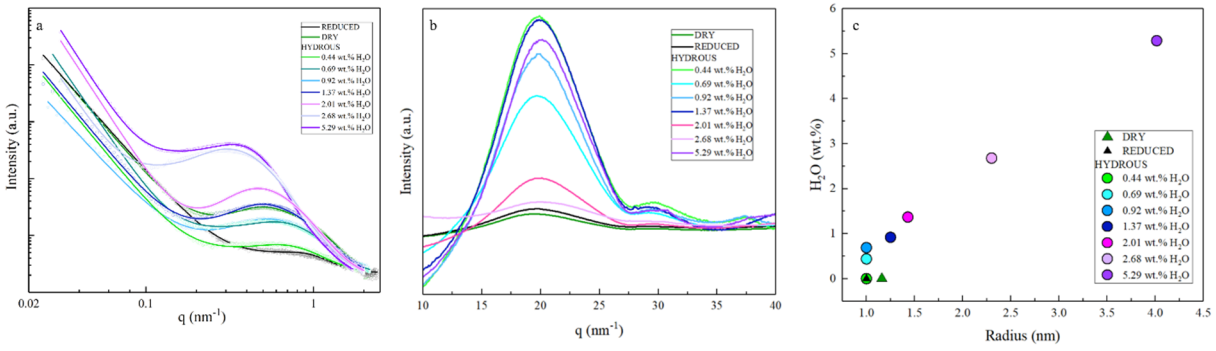

Fig. 3.5-19: SAXS (a) and WAXS (b) spectra of synthetic H_2O bearing glasses resembling the composition of the Pozzolane Nere eruption of the Colli Albani district. Panel (c) shows a positive correlation between glasses water content and the particle radius from the SAXS fit.

n. *Investigation of liquid-liquid phase transitions of sulphur under high pressures and temperatures using* in situ *ultrasonic interferometry (G. Niu/Beijing, L. Man, P. Mu/Beijing, R. Farla/Hamburg and D.J. Frost)*

A complete understanding of the melting relations in important systems, such as Fe-S, requires information on the behaviour of the S end member. Despite being a single component, elemental sulphur exhibits complex chemical behaviour under high pressure and high-temperature conditions, spanning both its solid and liquid states. More intriguingly, in contrast to many disordered systems that exhibit continuous transitions in response to variations with pressure and temperature, liquid sulphur displays abrupt changes in thermodynamic properties at elevated pressures, which are sometimes interpreted as first-order liquid-liquid phase transitions (LLPT).

During beamtime at the large volume press beamline P61B at DESY, Hamburg, we investigated the sound velocity in sulphur liquids. Melting temperatures were measured both by determining the disappearance of powder diffraction peaks and ultrasonic shear wave echoes. These measurements were in good agreement with previous studies, confirming the effectiveness of the method. A major challenge in ultrasonic measurements on liquids is maintaining parallel interfaces between the buffer rod, liquid and backing plate. In the radiographic X-ray image, shown in Figure 3.5-20a, these interfaces can be clearly seen to be undeformed and parallel at 7.1 GPa and 1023 K due to the successful use of Y_2O_3-stabilised ZrO_2 in this assembly.

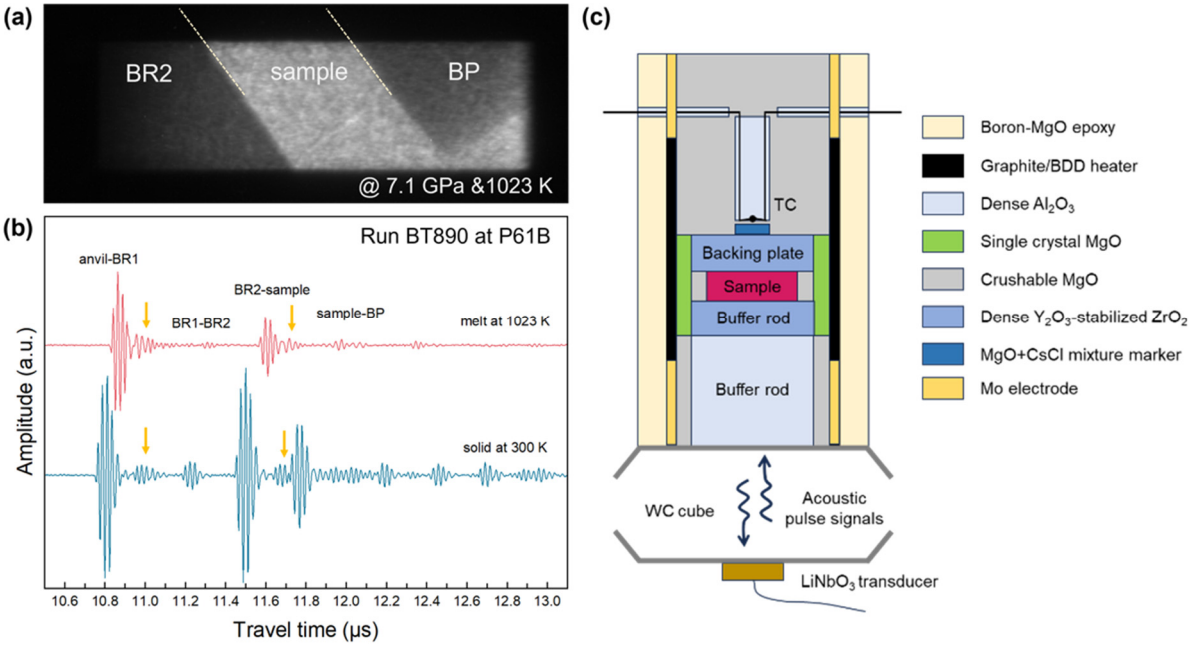

Fig. 3.5-20: (a) X-ray image of the sample and backing plates at 7.1 GPa and 1023 K. (b) Acoustic echo signals of solid and liquid sulphur. BR1 denotes the buffer rod, made of Al_2O_3, BR2 and BP denote the buffer rod and backing plate made of ZrO_2. (c) A schematic diagram of the multianvil assembly used.

Figure 3.5-20b shows the acoustic echo signals before and upon melting of sulphur. An obvious decrease in the travel time, by more than 20 %, is observed when the sample melts. The sample length, on the other hand, shows no significant decrease, indicating that the acoustic velocity drops abruptly on melting. A decrease in the amplitude of the sample signal also implies significant attenuation of longitudinal waves in liquid sulphur. Overall, the measured V_p of sulphur melt increases with pressure and decreases with temperature but the V_p relation with pressure is non-linear over the investigated conditions. It undergoes a continuous increase at 1-8 GPa with a slope that reaches a plateau at 8-10.5 GPa, but then becomes steeper again at 10.5-12 GPa. These changes in slope with pressure appear to correlate with previous proposals of LLPTs, that may be related to depolymerisation of the melt. However, definitive conclusions on the existence and mechanisms of LLPTs cannot be currently made based only on sound velocity measurements. Further direct evidence needs to be obtained through the examination of density and liquid structure variations, supported by computer simulations.

3.6 Rheology

The rheological behaviour of rocks and minerals is determined by their response to applied mechanical stresses, *i.e.*, their deformation under load. Depending on the physical and chemical conditions (pressure, temperature, fH_2O, fO_2, *etc.*) inside the Earth, the active deformation mechanisms may produce brittle or ductile macroscopic behaviour, resulting either in fast rupture processes such as earthquakes or slow creep behaviour such as plate tectonic movements or mountain building processes or a combination of both. Deformation experiments at BGI can be used to charatacterise the deformation mechanisms and ultimately the rheological flow laws. These data are underpinned by modelling work that allows extrapolation in parameter space (*e.g.*, deformation rate) which is limited in experiments. Lastly, also the investigation of naturally deformed rocks yields important constraints.

The first three contributions focus on the possible mechanisms for deep earthquakes. In the experimental project of Silva Souza *et al.* first results are presented of an attempt to reproduce the mechanism of earthquake nucleation in samples of serpentinite at high pressure and temperature. They can show that the dehydration of serpentine under stress leads to the formation of olivine on aligned fault planes, indicating a combination of dehydration embrittlement and transformation as a mechanism of deep earthquakes. In the contribution of Spang *et al.*, the possible roles of thermal runaway and ductile rupture as mechanisms for deep earthquakes are modelled for a rock consisting of olivine. They show that ductile deformation processes may lead to a very high local stress concentration and rupture of the material. This mechanism is a possible explanation for the occurrence of earthquakes in regions of the Earth where ductile deformation processes are prevalent. Hamadi *et al.* investigated the role of ductile deformation during the postseismic relaxation following earthquakes on the subduction surface. With their modelling approach, they can show that thermal weakening leads to a transition from brittle to ductile deformation, which is enhanced by a higher background temperature and strength contrast.

The fourth contribution by Heidelbach *et al.* presents an experimental deformation study where a series of plagioclase-clinopyroxene mixtures was deformed in axial compression in the ductile field in order to investigate the influence on texture development and seismic properties. Whereas the crystallographic textures remained rather similar throughout the series the seismic properties changed their characteristics with changing phase proportions, which will improve the interpretation of seismic anisotropies in lower crust or upper mantle material. The project of Zhou *et al.* presents experimental data about the rate of grain growth of bridgmanite in basaltic rocks under lower mantle conditions which is an important factor for the deformation behaviour of subducted slabs. Their results show that the growth rate of bridgmanite in a basaltic lithology is slightly lower than in comparable peridotitic material. In a microstructural study of naturally deformed rocks from the southern Alps, Jemal and Miyajima show that the reaction from albite to jadeite, which is a classical indicator of high-pressure conditions, may vary significantly on a local scale due to the influence of chemistry as well as the possible preservation of prograde or retrograde reaction textures.

a. *Dehydration embrittlement of serpentinite at high pressure and temperature with implications for intermediate focus earthquakes (D.S. Souza, M. Thielmann, F. Heidelbach and D.J. Frost)*

Deep earthquakes occur at 70 to 700 kilometres depth, primarily in subduction zones where tectonic plates descend into the mantle. These events are vital for understanding Earth's mantle structure and offer strong evidence for plate tectonics through the subduction of tectonic slabs. These earthquakes, which make up 25 % of all recorded events, differ from shallow ones which can be explained by brittle-frictional mechanisms. At depths larger than 70 km, fracture and sliding are hindered due to increased pressure, while ductile flow is induced at higher temperatures. The mechanisms that operate at intermediate focus earthquakes may differ from those of deep focus because their frequency and source properties differ at depth intervals of 100-350 km, 350-550 km and below 550 km.

There are three proposed mechanisms for deep earthquakes: dehydration embrittlement, transformational faulting, and thermal runaway. At intermediate focus depth (100-350 km) dehydration embrittlement might be the dominant mechanism. Dehydration embrittlement is defined as the brittle failure of rocks due to high fluid pore pressures, which counteract the high normal stresses caused by significant overburden pressures. Dehydration of serpentine is the most studied dehydration embrittlement system with experimental deformation. Even though previous studies observe serpentine failure at high pressures and temperatures, it does not always produce acoustic emissions (AE's). The mechanism of dehydration embrittlement at the microscopic level remains poorly understood. This hypothesis is based on increased pore pressure, however, the phase transformation caused by serpentine dehydration has a net decrease in pressure. To generate fluid pressure build-up and seismic failure, permeability and fluid drainage must be hindered by a less permeable layer around the dehydrating phase.

To better understand the micro-mechanisms involved in the dehydration of serpentinite, we have performed dehydration experiments under isostatic and non-isostatic conditions. The starting material was natural serpentinite consisting of an antigorite matrix with xenoblasts of diopside, iron oxides and sulphides (Fig. 3.6-1a). It displays a foliation marked by layers of diopside xenoblasts and its deformation tails. Cores with minimal amounts of xenoblasts were drilled parallel to the foliation and mounted in 12 mm cubic assemblies. Dehydration and deformation experiments were carried out with the 6-Ram multianvil press at a pressure of 5 GPa and temperatures between 550-784 °C, to a maximum strain of 15 % at strain rates between 1.67×10^{-4} s^{-1} to 2.91×10^{-6} s^{-1}.

Isostatic dehydration of antigorite at 5 GPa starts at ~ 550 °C and is completed at ~ 800 °C. At these conditions, no failure microstructure is observed. Between 550-650 °C, olivine starts to form at antigorite grain boundaries (Fig. 3.6-1b). At 784 °C, the former antigorite matrix transforms to olivine and enstatite, with poikilitic garnet being also present (Fig. 3.6-1c).

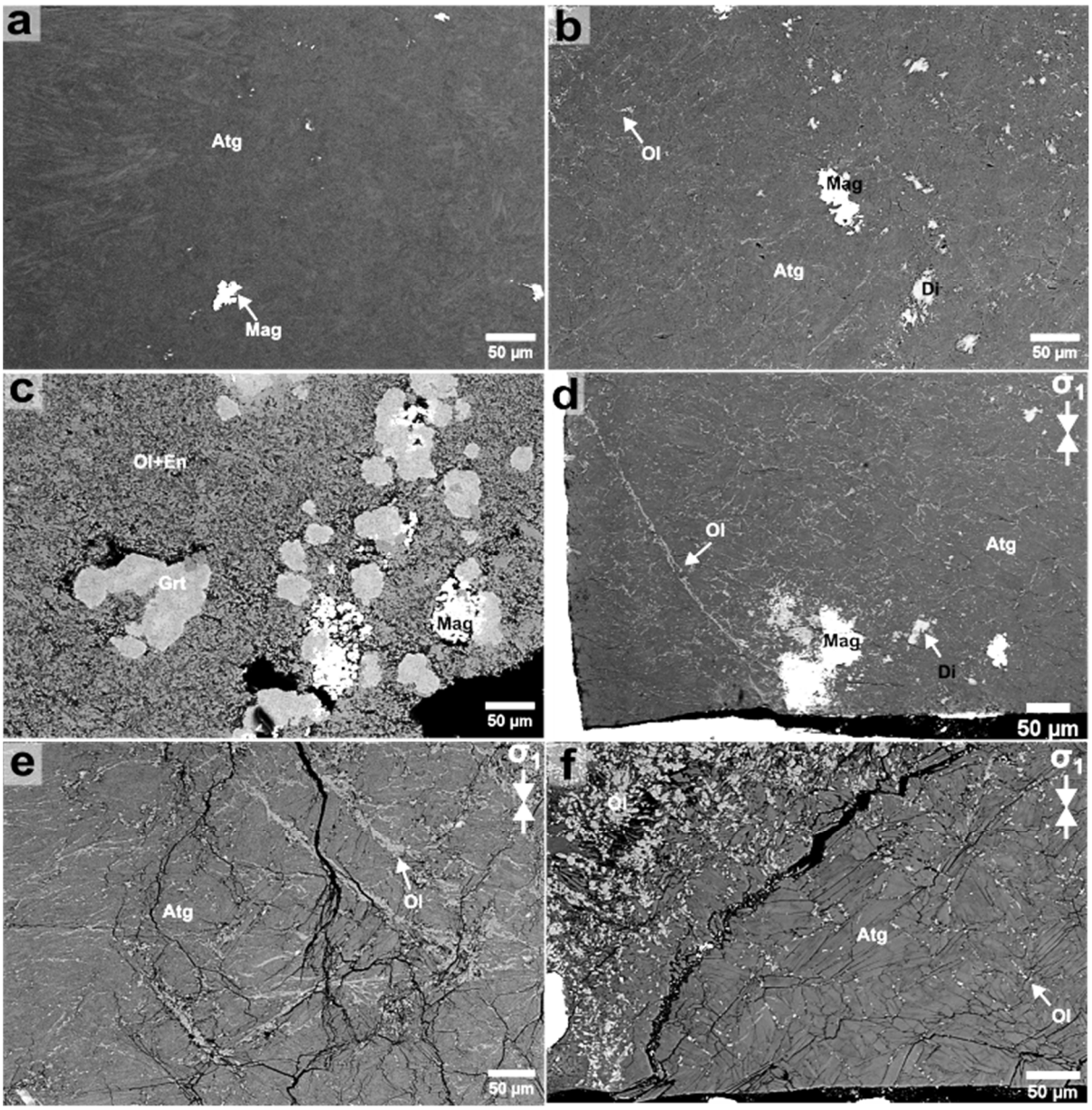

Fig. 3.6-1: SEM-BSE images of serpentinite, before and after experiments. a) Undeformed serpentinite sample. Antigorite (dark grey) makes up most of the matrix containing magnetite (white). b) Serpentinite sample after isostatic compression (5 GPa, 607 °C). Small olivine grains (light grey) start to grow at antigorite boundaries. c) Fully dehydrated undeformed serpentine, matrix containing olivine and enstatite (fiber-like phase), garnet is also present in round poikilitic aggregates that overprint the olivine/enstatite matrix. d) Serpentinite deformed in pure shear (1×10^{-5} s^{-1}), olivine grains grow around antigorite and connect to form shear bands. e) Deformed serpentinite at faster strain rates ($1.67x10^{-4}$ s^{-1}), olivine forms lenses at high angles to the main stress prior to brittle failure, displacement along the lens plane does not occur. f) Serpentinite deformed at the slowest strain rate ($2.91x10^{-6}$ s^{-1}), olivine grows along antigorite boundaries oriented obliquely to the main stress. Mineral abbreviations: Atg – antigorite; Di – diopside; En- enstatite; Grt – garnet; Mag - magnetite Ol- olivine.

In one deformation experiment at strain rates of $1x10^{-5}$ s^{-1} and ~ 600 °C, olivine grains link up in between antigorite grains and form a shear band with an apparent displacement of ~ 11 µm (Fig. 3.6-1d). At faster strain rates ($1.67x10^{-4}$ s^{-1}), the sample deforms in a brittle manner, indicated by fractures parallel to the primary stress direction. Olivine grains are linked but show no signs of displacement (Fig. 3.6-1e). At slower strain rates ($2.91x10^{-6}$ s^{-1}), fractures develop oblique and parallel to the main stress and around Ca-pyroxene xenoblasts, with dehydration concentrated in the sample centre. Antigorite is present at the top and bottom of the core. At the top, olivine grains grow along antigorite grain boundaries without linking, while at the bottom, they align obliquely to the main stress but do not connect or form displacement planes (Fig. 3.6-1f).

These results demonstrate that at a microscopic level, dehydration and failure of serpentine are complex. Pore overpressure may not be the only mechanism involved in its failure. The formation of olivine layers is related to the deformation geometry. On the other hand, the presence of the pre-existing foliation with xenoblasts and previous fractures may influence the formation of macroscopic fractures during laboratory deformation. Thus, future experiments will be carried out in pure undeformed antigorite. Additionally, experiments at similar conditions will be carried out with monitoring of acoustic emissions at beamline Petra-III P61B at DESY.

b. *Transient propagation of ductile ruptures by thermal runaway (A. Spang, M. Thielmann, A. de Montserrat/Zürich and L. Räss/Lausanne)*

Thermal runaway describes a positive feedback loop between localisation, shear heating and temperature-dependent viscosity which can lead to dramatic weakening of rocks and strong localisation of ductile deformation. One-dimensional (1D) numerical models have demonstrated that this mechanism can nucleate on weak inclusions in olivine, self-localise and produce temperatures above the melting point as well as slip velocities on the order of m/s.

Two-dimensional (2D) models that show thermal runaway exist but can usually not resolve the propagation front of thermal runaway spatially or temporally. Here, we present 2D numerical models, written in the Julia programming language and compatible with graphics processing units (GPU) that can capture nucleation and propagation of ductile ruptures driven by thermal runaway. We employ a compressible, temperature- and stress-dependent visco-elastic olivine rheology, including elasticity, diffusion creep, dislocation creep and low-temperature plasticity.

Our simple shear models show the transient behaviour of the ductile rupture that nucleates at a small heterogeneity and extends initially as a broad shear zone dominated by low-temperature plasticity before self-localising into a thin rupture driven by diffusion or dislocation creep (Fig. 3.6-2). In the rupture tip, temperatures increase by about 1000 K while elastically stored stresses of more than one GPa are released within seconds. Depending on material parameters and initial conditions (temperature, far-field deformation, lithostatic pressure), slip velocities range from µm/s which is in line with slow slip events to m/s which is comparable to earthquakes.

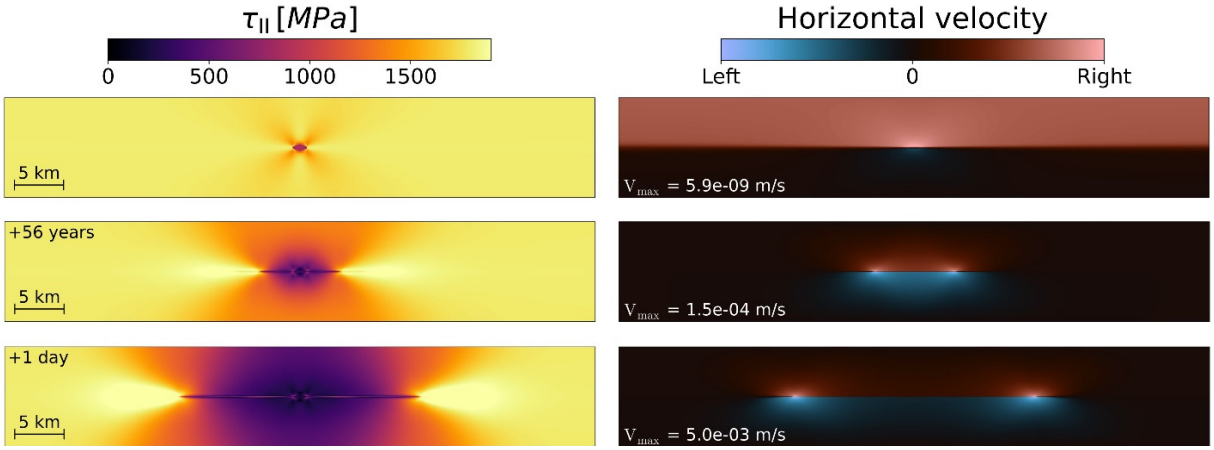

Fig. 3.6-2: Temporal evolution (from top to bottom) of ductile rupture propagation due to thermal runaway in a visco-elastic medium under simple shear boundary conditions. Time changes in the upper left corner show a difference from the previous row. The left side shows a deviatoric stress field in MPa and the right side shows a horizontal velocity field and maximum value. First Row: Broad shear zone dominated by low-temperature plasticity has divided upper and lower parts of the domain. Deformation starts to localise in the centre. Middle Row: Thermal runaway has started and propagates outwards as stress is released. Bottom Row: Rupture continues to propagate and slip velocities have reached a steady-state value.

This has important implications for deep seismicity. About 25 % of all detected earthquakes occur at depths greater than 60 km, some as deep as 700 km below the surface. Such events cannot be explained by brittle failure as brittle strength of rocks increases with pressure and several GPa of deviatoric stress would be necessary to break rocks at upper mantle conditions. Our models show that thermal runaway can cause "earthquake-like" slip velocities and rupture propagation without brittle failure and with less than 2 GPa of deviatoric stress.

Another feature of the ductile ruptures in our models is that their tips are flanked by zones of decreased (to the right in propagation direction) and increased (to the left) pressure. These perturbations are also typical for brittle fractures and reach magnitudes of more than one GPa, depending on slip velocity. In depths of 50 to 100 km, just below the brittle-ductile transition zone, these pressure anomalies can be strong enough to locally decrease the brittle strength of the rocks enough to trigger swarms of brittle slip events in an otherwise ductile region.

We also investigated the interaction of multiple weak inclusions. In Figure 3.6-3a, we show the case of 2 inclusions that are vertically offset. Initially, two sets of ductile ruptures develop, each parallel to the far-field deformation. As they propagate, they bend due to the stress field disturbance caused by the other ruptures and link up to create one continuous, curved rupture that connects both nucleation sites. Figure 3.6-3b shows another case where we randomly distributed 30 weak inclusions. Here, there is a branched link-up of the initial low-temperature plasticity dominated shear zones. Thermal runaway does, however, only initiate in one location

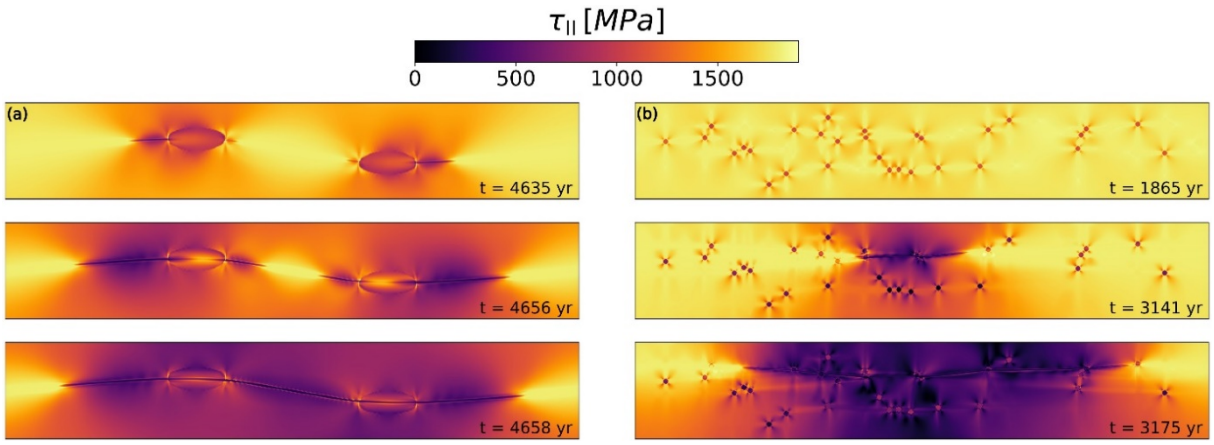

Fig. 3.6-3: Thermal runaway in visco-elastic medium under simple shear boundary conditions with multiple weak inclusions. Colormap indicates a deviatoric stress field. (a) Two large inclusions. (b) 30 small inclusions.

and then follows one of the initial shear zones. This rupture quickly unloads the entire model domain before any other location can initiate a thermal runaway.

c. *Postseismic relaxation of the subduction interface due to thermally activated ductile deformation (M.I. Hamadi, A. Spang and M. Thielmann)*

Megathrust earthquakes are large ($M_W \geq 8.5$), shallow earthquakes that occur at 0-70 km depths within the seismogenic zone, primarily along thrust faults in subduction zones. Following such earthquakes, transient surface deformation is usually observed as part of the postseismic phase. It is driven by mechanisms such as viscoelastic relaxation, poroelastic rebound, and afterslip. Afterslip, a gradual transient slip that decays over time, often occurs around the coseismic fault surface and may extend to depths below the seismogenic zone, within the brittle-ductile transition zone. This region is part of a complex subduction interface characterised by variations in lithology, pressure-temperature conditions, and dynamic processes like shear heating.

In this study, we explore how shear heating affects the stress and temperature state in the brittle-ductile transition zone and the afterslip process using simplified two-dimensional numerical models representing the subduction interface. The model employs a visco-elasto-brittle olivine rheology, including elastic deformation, brittle failure, diffusion creep, dislocation creep, and low-temperature plasticity, with brittle deformation approximated as an additional viscous mechanism. A viscous weakening factor ω_{vis} is introduced in the central part of the model to simulate the weak subduction interface. The simple-shear boundary conditions mimic subduction at a constant velocity. To simulate the effects of an earthquake, a sudden 10m slip event based on the 2011 Tohoku-Oki earthquake (M_W 9.0) is applied through the boundary conditions over 300 s. Using this model, we investigated how background temperature variations and viscous weakening factor (ω_{vis}) influence the long-term deformation and the afterslip process within the brittle-ductile transition zone.

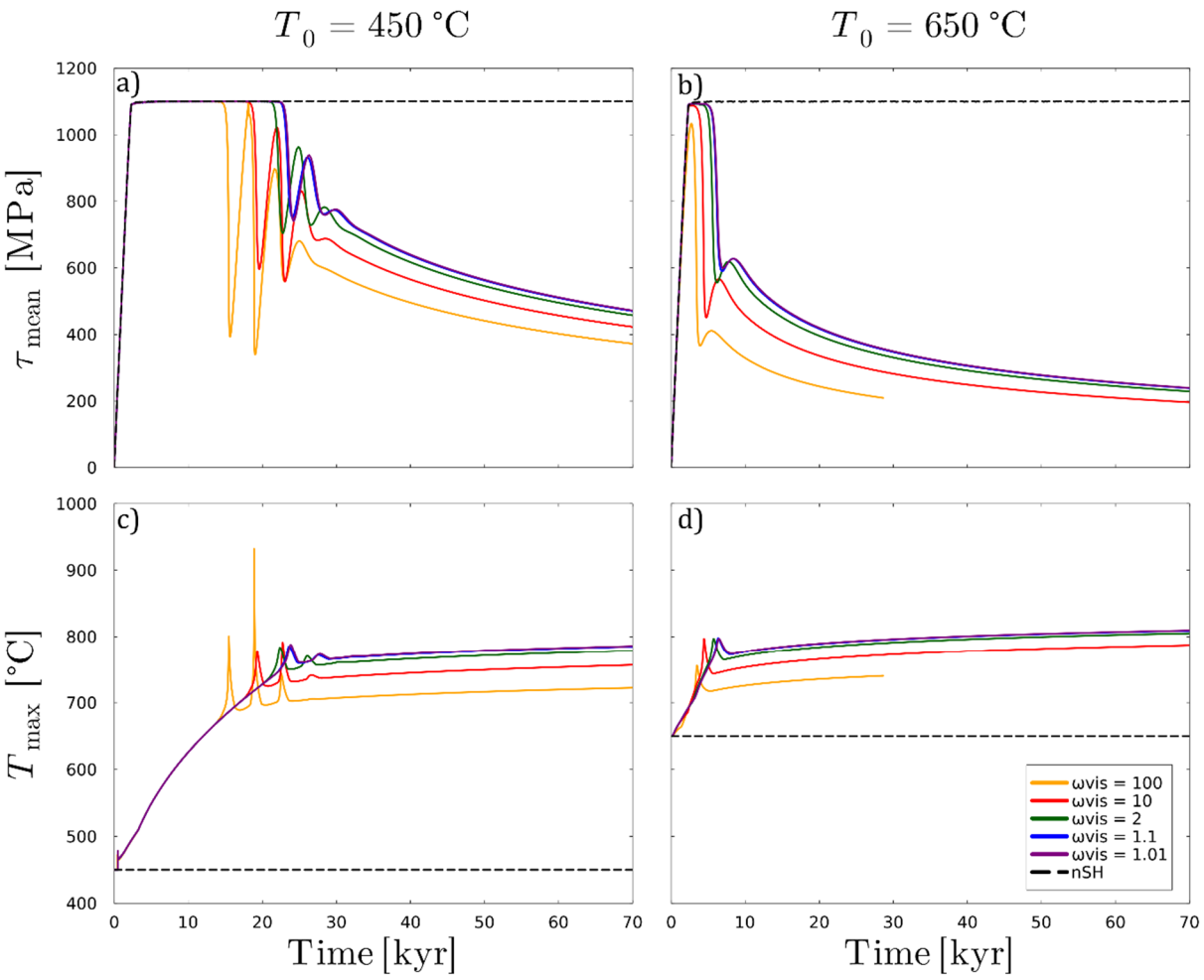

Fig. 3.6-4: Evolution of average deviatoric stress (τ_{mean}) and maximum temperature (T_{max}) in models with varying background temperatures (T_0) and viscous weakening factors (ω_{vis}), categorised by T_0. a) - b) Evolution of τ_{mean}. c) - d) T_{max} evolution. The black dashed line represents the reference model without shear heating for each T_0. Different line colours represent models with different ω_{vis} values.

We found that shear heating plays a crucial role in facilitating the transition from brittle to viscous deformation through thermal weakening, characterised by a significant decrease in average deviatoric stress and a temperature increase in the model (Fig. 3.6-4). Higher background temperature (T_0) and strength contrast (ω_{vis}) further accelerate this transition (Fig. 3.6-4). In contrast, models without shear heating remain predominantly in the brittle regime.

An earthquake's impact on deformation is found to be temporary, with an increase in average deviatoric stress (~ 80 MPa) and a modest temperature rise (max. 5 °C), followed by the postseismic relaxation phase (Fig. 3.6-4). Shear heating enhances the total afterslip and stress relaxation compared to models without it. However, variations in background temperature have a more pronounced effect than shear heating alone. Higher temperatures result in longer relaxation phases, greater total afterslip, and higher average afterslip velocities (Fig. 3.6-5).

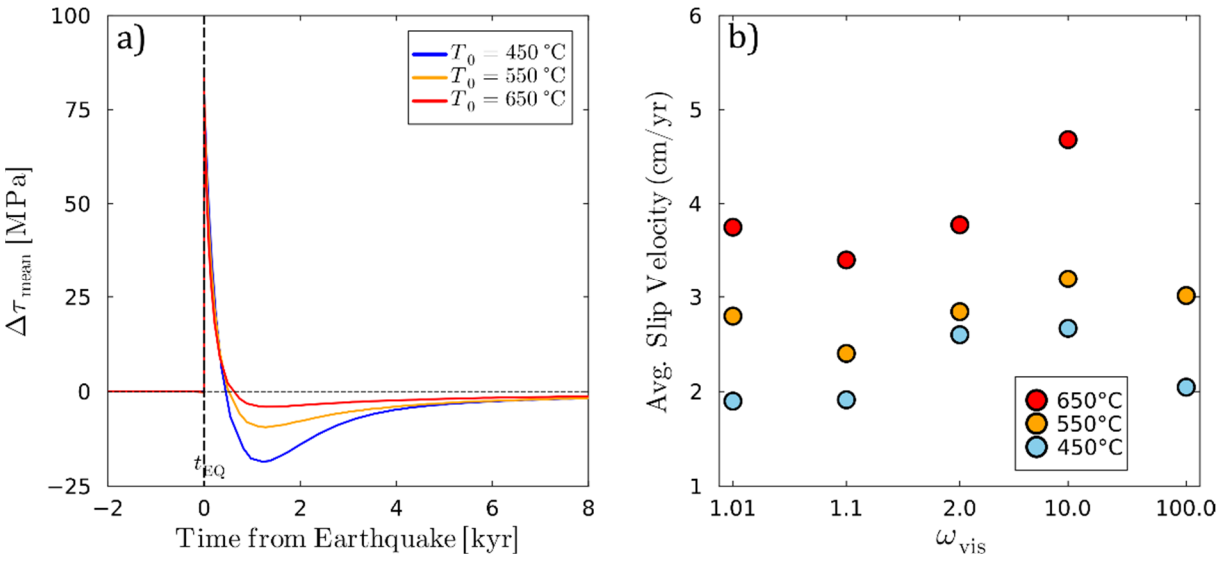

Fig. 3.6-5: a) Evolution of the difference in average deviatoric stress ($\Delta\tau_{\mathrm{mean}}$) between models with and without an earthquake, for $\omega_{vis} = 10$ and varying background temperatures (T_0). The horizontal black dashed line represents the reference model without earthquake for each model. The vertical black dashed line represents the time of the earthquake (t_{EQ}). b) Average slip velocity of the upper part of the model (cm/yr) as a function of T_0 and ω_{vis}. The x-axis (ω_{vis}) is shown on a logarithmic scale.

These findings align with previous studies, which suggest that higher slab surface temperatures are associated with faster average afterslip velocities. The afterslip rates are found to decrease significantly within a day after the earthquake, then remain constant for 100 years, and eventually drop to zero. These findings highlight the critical roles of temperature and shear heating in influencing afterslip behaviour and long-term deformation processes within the brittle-ductile transition zone.

d. *Textures and seismic properties of experimentally deformed plagioclase-diopside aggregates (M. Bystricky/Toulouse, S. Mackwell/College Park and F. Heidelbach)*

The plastic rheology of rocks may produce significant seismically detectable elastic anisotropies which can be used to trace deformation processes in the deeper parts of the Earth. The basis for interpretations of seismically observed anisotropy patterns is the characterisation of microstructures and textures in naturally or experimentally deformed rocks. As a case study, we deformed synthetic rocks with a basaltic composition consisting of plagioclase and clinopyroxene in different proportions. Basaltic compositions play a significant role both in the deformation of the oceanic crust (*e.g.*, during subduction) or in the lower crust (*e.g.*, during plate collision and mountain building).

Samples were prepared as mixtures of labradorite ($Ca_{0.54}Na_{0.42}K_{0.03}Al_{1.48}Si_{2.47}O_8$) and diopside ($Ca_{0.94}Mg_{0.76}Fe_{0.19}Si_{1.97}O_6$) from natural rocks collected from Adirondack anorthosite and Sleaford Bay clinopyroxenite respectively. After separating grain sizes, the two phases were mixed and compacted thoroughly in different proportions (100 % Pl, 75 % Pl – 25 % Cpx, 50 % Pl – 50 % Cpx and 25 % Pl – 75 % Cpx) and finally hot-pressed together in an internally heated gas-medium pressure vessel for up to 10 h at 1100 to 1180 °C and 300 MPa confining pressure. Additional annealing at room pressure and 1000 °C at oxygen fugacity conditions near Ni/NiO ($10^{-5.5}$ atm) produced an equigrained microstructure with a grain size of about 5-10 µm for both phases and less than 2 % porosity. Axial-compression creep experiments were performed at constant load using an internally heated Paterson gas-medium deformation apparatus at 1050-1180 °C, 300 MPa confining pressure and fO_2 buffered at Ni/NiO. Strain rates ranged from 1.2×10^{-6} to $3.0\text{x}10^{-4}$ s^{-1} and axial strains of up to 33 % were achieved in strain rate stepping tests. Deformed samples were then sectioned and polished in the plane containing the compression and extension directions for microstructural analysis with SEM-EBSD allowing to determine the fabrics of the two phases and to calculate their seismic properties.

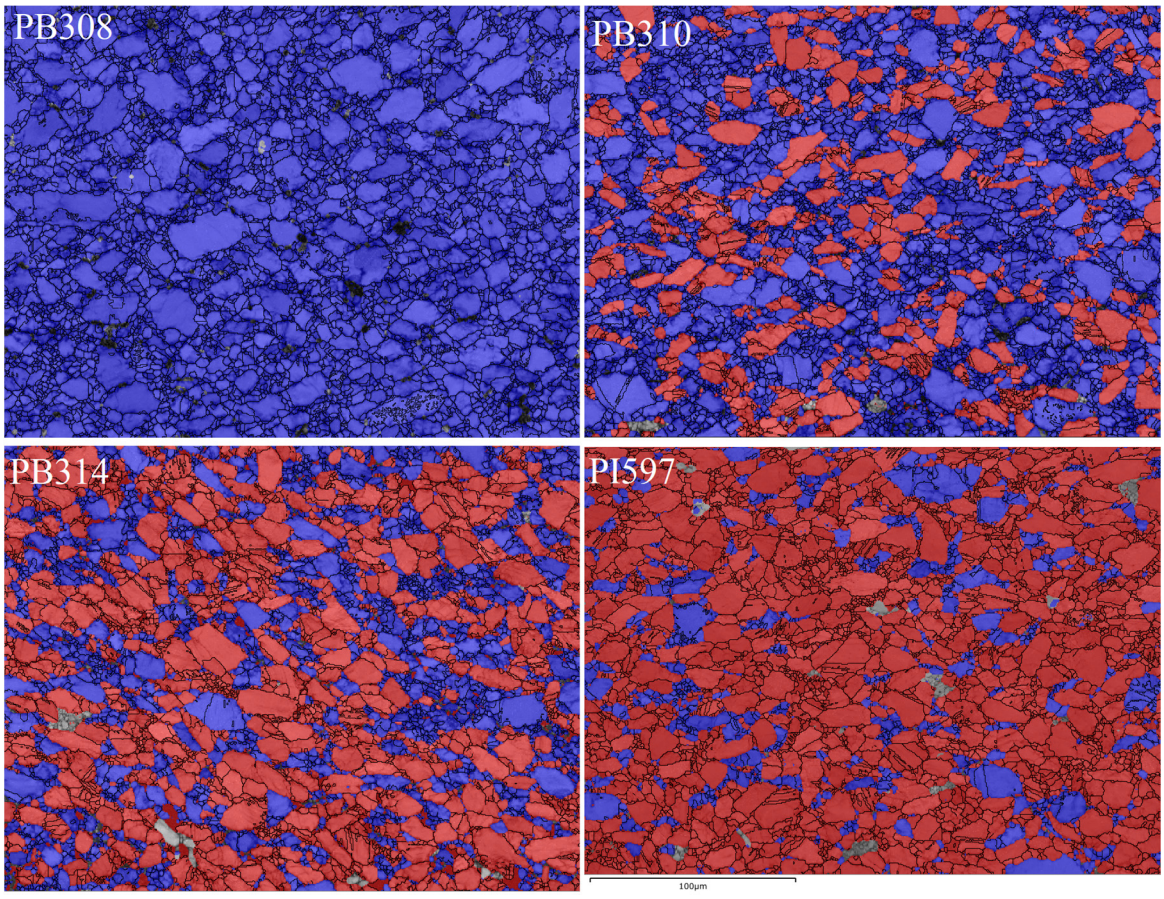

Fig. 3.6-6: SEM-EBSD phase maps (labradorite-blue, diopside-red, grain/phase boundaries black) of four deformed samples with 100 % (PB308), 75 % (PB310), 50 % (PB314) and 25 % (PI597) labradorite, respectively. The step size is 0.5 µm, and the axial compression axis is vertical.

The mechanical data are best approximated by a combined diffusion/dislocation creep flow law with the dislocation component being dominant at high stresses and strain rates. Microstructural analysis shows that the labradorite-diopside aggregates deform rather homogeneously with no obvious strength contrast between the two phases as shown here for four samples deformed (Fig. 3.6-6). Both phases also show weak but distinct crystallographic preferred orientations (Fig. 3.6-7) which are independent of their phase proportion. For diopside the direction <001> shows a girdle distribution in the compression plane and the {100}, {110} and {010} planes are subparallel to the compression plane consistent c-slip on these planes. For labradorite <100> forms a girdle in the compression plane whereas {001}, {011} and {111} are aligned with the compression direction consistent with a-slip on these planes.

The texture information was used in combination with the single crystal elastic tensors of labradorite and diopside to calculate the resulting elastic anisotropy of the sample (Fig. 3.6-8). For pure deformed labradorite the p-wave anisotropy is about 1.3 % with the lowest and highest velocities parallel and perpendicular to the compression plane, respectively. Shear wave splitting is strongest (2.8 %) in the compression plane with the polarisation of the fast shear wave perpendicular to the compression plane. Almost zero shear wave splitting is indicated in the compression direction. With increasing phase proportions of diopside, the p-wave anisotropy (1.2 %) flips, with the fast direction moving into the compression plane and the slow direction into the compression direction. Shear wave anisotropy patterns remain similar except for the polarisation of the fast shear wave which is parallel to the compression plane. Overall anisotropies are relatively low which is partly due to the low strain and weak texturing in the investigated samples. However even stronger textures may not necessarily enhance anisotropies since the labradorite and diopside counteract each other in p-wave anisotropy and partly in shear wave splitting. Plastically deformed basalts or gabbros therefore are expected to show a weak seismic anisotropy which changes distinctively with composition.

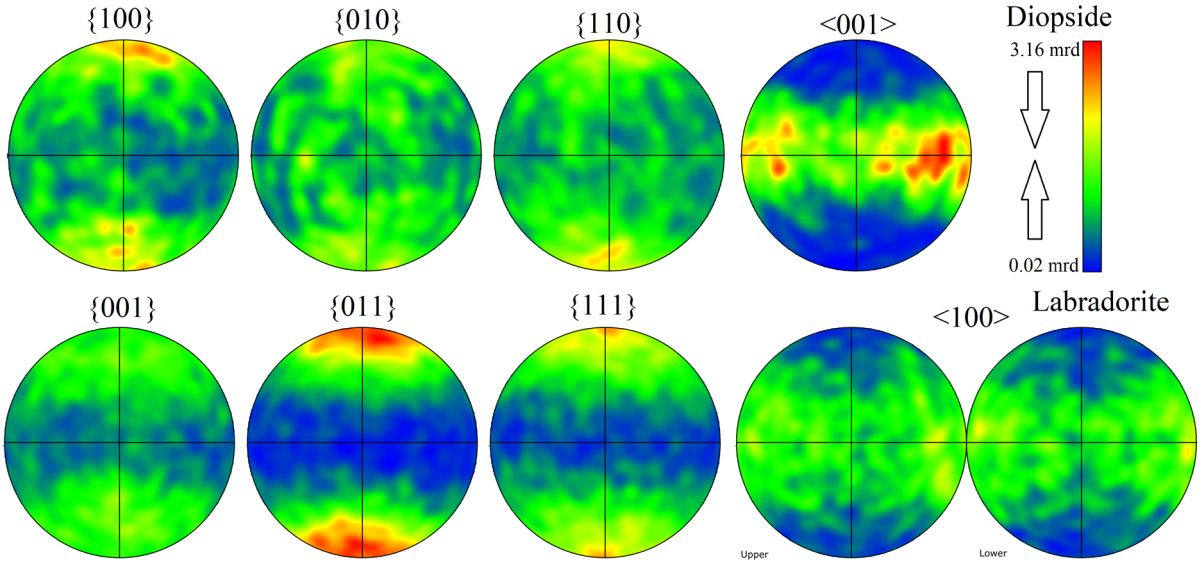

Fig. 3.6-7: Pole figures for diopside (top row) and labradorite (bottom row) of sample PB314; compression direction is vertical; equal-area projections, lower hemisphere, mrd = multiples of random distribution.

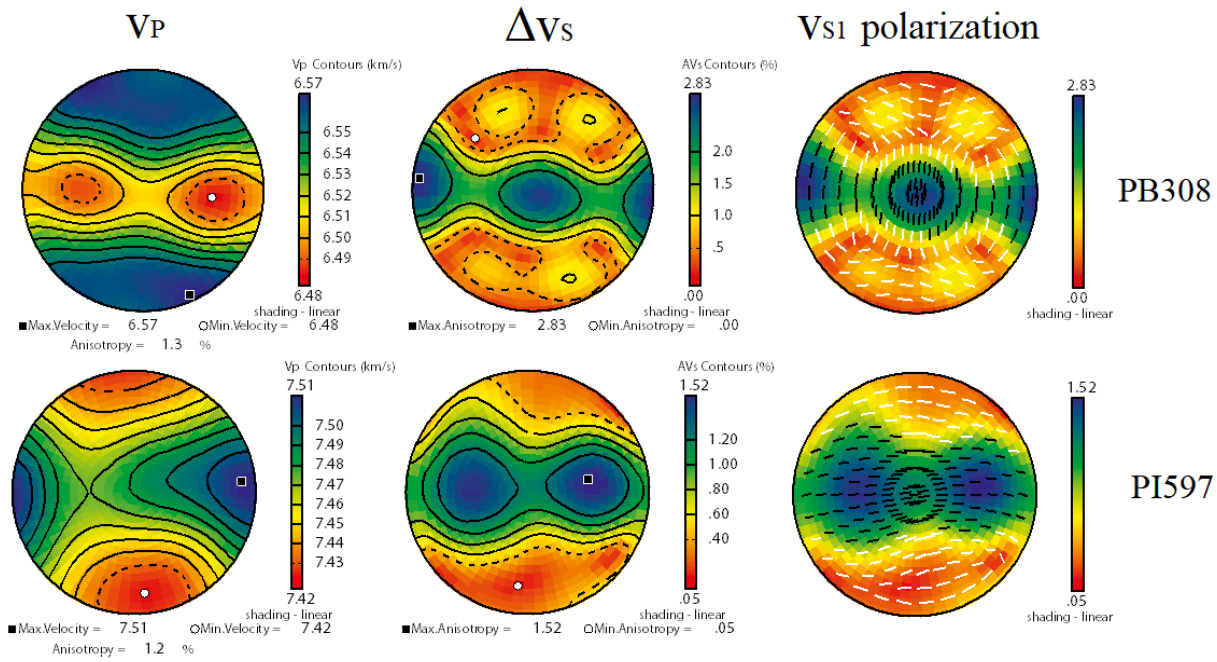

Fig. 3.6-8: Calculated seismic anisotropies for samples PB308 (100 % labradorite) and PI597 (25 % labradorite, 75 % diopside) combining the single crystal elastic tensors of diopside and labradorite and the CPOs of both phases. Compression direction is vertical; equal-area projections, lower hemisphere.

e. *Grain growth kinetics in basaltic rock under lower mantle conditions (S. Zhou, H. Fei, F. Xu and B. Zhang/Hangzhou, A. Chakraborti and T. Katsura)*

Determining the grain growth kinetics of basaltic rocks under lower mantle conditions is crucial for understanding the dynamics of the Earth. This research field has a significant impact on the processes of material and heat transport and mantle convection in the Earth's interior. The study of grain growth kinetics in the lower mantle is particularly important for the following reasons.

1. Viscosity effects: Grain size is one of the main factors determining the viscosity of mantle materials.
   Changes in grain size directly affect the fluidity and convection patterns of the mantle.
2. Slab behaviour: The density and viscosity contrast of subducting slabs determine the persistence of convective mixing and chemical heterogeneity in the lower mantle.
3. Phase transition effects: Slabs crossing the upper-lower mantle boundary experience significant grain size reduction through the post-spinel and post-garnet transitions.
4. Deformation mechanisms: Grain-size-sensitive creep may be the dominant deformation mechanism, and grain growth processes are an important factor controlling the viscosity of slab materials.

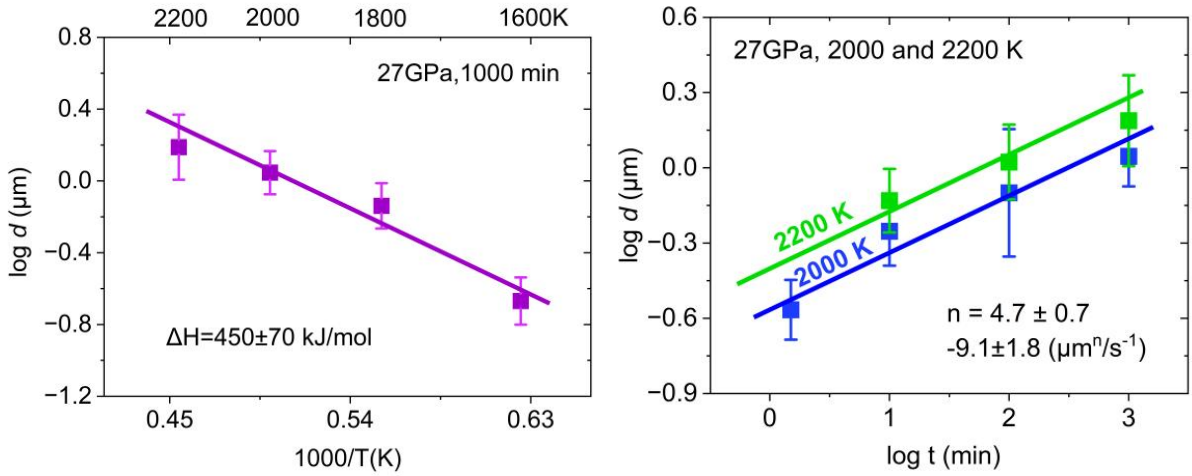

Fig. 3.6-9: Grain growth kinetics of bridgmanite in basaltic rock. (left) Log grain size as a function of the reciprocal temperature at a pressure of 27 GPa and for an annealing time of 1000 min. (right) Log grain size as a function of annealing time at 2000 K (blue) and 2200 K (green) and 27 GPa.

Considering these factors, an accurate understanding of the grain growth kinetics of basaltic rocks under lower mantle conditions is essential for modelling the dynamics of the Earth's interior and understanding mantle convection and the evolution of the Earth.

For this purpose, we performed annealing experiments on a lower-mantle basaltic rock with MORB composition pre-synthesised at 1700 K and 27 GPa for 5 min using a multianvil press. This sample contains bridgmanite, stishovite, davemaoite, and calcium-ferrite type $MgAl_2O_4$ with a grain size of <<0.1 µm. It was cut into approximately 100 µm pieces, each piece was embedded in gold powder within a Pt capsule, and annealed at 27 GPa for grain growth.
We performed the following three series of experiments: (1) as a function of temperature from 1600 to 2200 K for 1000 min, (2) as a function of time from 10 to 1000 min at 2000 K, and (3) also as a function of time from 10 to 1000 min at 2200 K. Cross-section of the annealed samples were made and examined with a scanning electron microscope. The grain size of bridgmanite was measured using ImageJ, an image processing software.

The results of series 1 are shown as an Arrhenius plot in Figure 3.6-9 (left). The log grain size increases linearly as a function of reciprocal temperature, indicating an activation enthalpy of 450±70 kJ/mol for the bridgmanite grain growth kinetics. The results of series 2 and 3 are shown in Figure 3.6-9 (right). The log grain size increases linearly as a function of log annealing time at both temperatures. These data have been fitted to an empirical equation of $d^n - d_0^n = k_0 \exp[-H_a/RT]\ t$, where d_0 and d are the initial and final grain sizes, n is the grain growth exponent, k_0 is the grain growth rate constant, H_a is the activation enthalpy, R is the gas constant, T is the temperature and t is the time. The grain growth exponents are 4.7±0.7, and the logarithmic grain growth rate constants are 2.1 ± 10^{-4} log[µm^n s^{-1}]. The grain growth rate constant of bridgmanite in basaltic rocks is slightly smaller than that of a simple system composed of 80 % bridgmanite and 20 % ferropericlase, which is 2.4 ± 10^{-4} log[µm^n s^{-1}].

f. *A TEM study of a retrograde overprint on the eclogite facies quartz diorite in the Sesia zone, western Alps, Italy (I. Jemal and N. Miyajima)*

The Sesia zone is part of the western Alps in Italy. The zone experienced emplacement to a depth of ≥ 50 km during the early Alpine orogenic event (100-130 Ma), during which a large part of the unit underwent eclogite-facies metamorphism (P > 15 kbar, T ~ 500-560 °C), followed by an uplift back to the surface.

Two meta-quartz-diorite rocks, labelled DKS-02 and R81/186, were previously collected from one of the several plutons which occur throughout the zone, known as the Monte Mucrone metagranitoid. Scanning electron microscopy (SEM) analysis of these rocks revealed that both contain jadeite and albite, unlike rocks from this region which have been discussed in the literature. The DKS-02 rock has a much higher modal composition of albite. In addition to jadeite and albite, both samples also contain phengite and zoisite (Fig. 3.6-10).

In this study, techniques in transmission electron microscopy (TEM), known as bright field (BF) and dark-field (DF) imaging, selected area electron diffraction (SAED), as well as energy-dispersive X-ray spectroscopy (EDS), were used to investigate the mechanism which resulted in the coexistence of albite and jadeite in these rocks. Due to the small amount and grain size of albite in R81/186, analyses were performed mainly on DKS-02, specifically on a pseudo-plagioclase domain within the sample that contained both albite and jadeite. These two minerals were distinguished from each other based on their silicon contents (20 at. % for jadeite and 23 at. % for albite) from obtained TEM-EDS results. Their textural relationships were examined through SAED patterns and BF and DF images. These results were combined with the tectonic history of the Sesia zone reported in literature to propose a possible formation mechanism of the mineral assemblage of the rocks.

At the peak pressure and temperature of the metamorphism that the Sesia zone experienced high-pressure and intermediate temperature conditions (> 15 kbar, ~ 500-560 °C), where plagioclase has been shown to undergo breakdown to jadeite, zoisite, kyanite and quartz in the presence of water according to the reaction:

$$\text{Na, Ca-plagioclase} + H_2O \rightarrow \text{zoisite} + \text{jadeite} + \text{kyanite} + \text{quartz} \quad (1)$$

The formation of jadeite is attributed to this stage. The coexistence of jadeite and albite in the rocks could then be explained by a small extent of reaction (1). However, a more likely explanation that is consistent with the tectonic history of the Sesia zone and the phase stability of albite and jadeite is fluid-assisted retrogression, whereby jadeite reacts with silica and water during uplift to yield albite and phengite, as described by the reaction:

$$\text{Jadeite} + SiO_2 \text{ (+ K-bearing } H_2O \text{ fluid)} \rightarrow \text{albite (+ Phengite/White mica)} \quad (2)$$

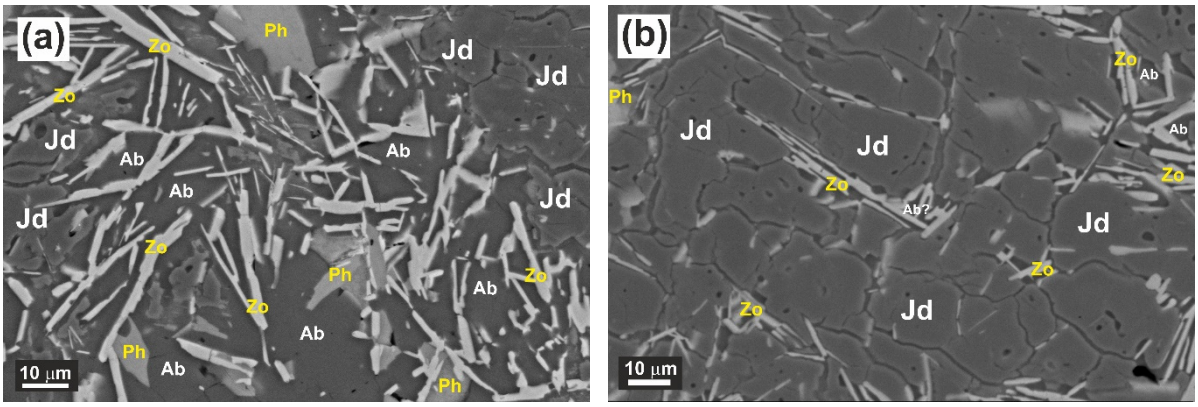

Fig. 3.6-10: Back-scattered electron SEM images of a pseudo-plagioclase domain in (a) DKS-02 (b) R81/186. Abbreviations: Ab: albite, Jd: jadeite, Ph: phengite, Zo: zoisite.

The irregular boundaries of a precursor jadeite (Fig. 3.6-11a,b) and the presence of phengite in the rocks serve as evidence for water activity in the system. Importantly, the presence of albite and phengite at the reaction interface between jadeite and zoisite (Fig. 3.6-11c), with zoisite likely acting as a silica source, provides evidence for the formation of albite and phengite from reaction (2).

This fluid-assisted retrogression model also helps explain the difference in the modal compositions of albite and phengite between the two rocks. It has been previously reported that water acts in reaction (2) both as a catalyst and a reactant. Based on this, higher water activity and/or longer duration of fluid flow parallel to the shear zone during uplift in DKS-02 explain its higher modal composition of albite (and phengite).

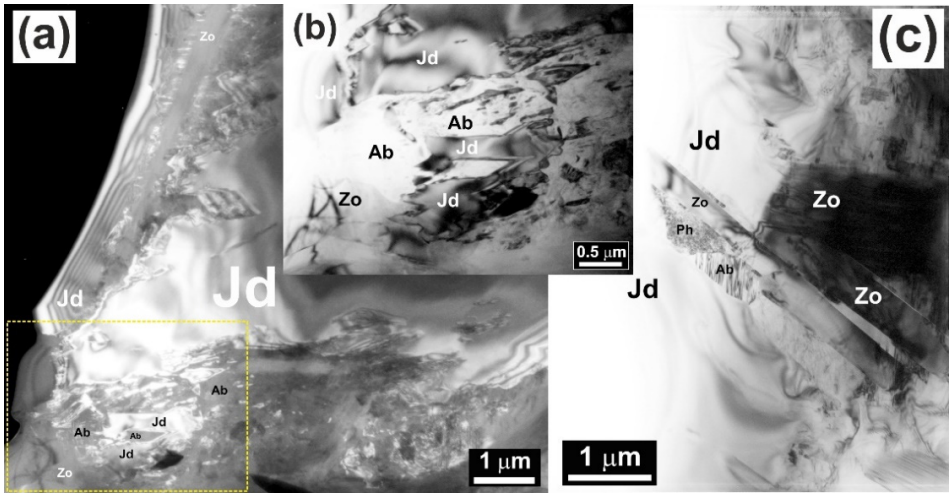

Fig. 3.6-11: Representative TEM images of a pseudo-plagioclase domain in DKS-02. (a) Precursor jadeite with an irregular boundary, and the product albite, magnified the lower left part in (b), and (c) albite and phengite coexisting in the reaction interfaces between jadeite and zoisite.

3.7 Material Sciences

Exposing materials to high pressure can yield novel and interesting behaviour via the compression energy input that easily exceeds any temperature effects. At the same time, the amount of material created by high-pressure synthesis is typically small, and the question of whether a newly formed material can be brought to room conditions – quenched – is critical in the assessment of whether there is even the remote potential of it being of technological significance. As in previous years, the contributions in this section of the annual report are dominated by various high-pressure reaction products in the diamond anvil cell characterised by X-ray diffraction performed at a synchrotron source. However, the installation of the new Rigaku-Synergy diffractometer at the BGI has led to two projects that are outside the typical range of material research projects presented in previous years.

With the large energy difference between the triple-bonded nitrogen molecule and nitrogen units with double- or even single-bonds, nitrides with high nitrogen contents are promising as high-energy-density materials. Following the stabilisation of CN_3^{5-} anions in lanthanide-based materials reported in 2023, the first contribution in this chapter expands this line of inquiry for scandium nitrides, and succeeds in creating N_6^{6-} and N_8^{6-} as well as a two-dimensional poly-nitrogen layer at successively higher pressure in the diamond anvil cell.

Similarly, the second contribution in this section expands a project on dysprosium carbides presented in the 2023 annual report. It considers a wide range of carbides that form with the reaction with rare-earth metals at high pressure, and an astonishing variety of shared structure types with varying carbon content are synthesised and characterised at the synchrotron. The third contribution presents the synthesis of rhenium carbide Re_3C in the diamond anvil cell. This phase has been predicted previously based on *ab initio* simulations, and is expected to exhibit high hardness. The fourth contribution in this section also deals with carbides: Rather than presenting experiments in the megabar range, it considers possible synthesis routes at approximately 10 GPa in the multianvil press for doping boron carbide with Si to further harden this already superhard material.

In geology, carbonates, like $CaCO_3$ calcite, are mostly present in sedimentary rocks, and are remarkably stable under high pressure with planar CO_3^{2-} units. In the fifth contribution, by contrast, a carbonate with CO_4^{4-} tetrahedra as building blocks is synthesised in the diamond anvil cell, and a similarly structured borate, both with Yttrium as the cation.

The sixth contribution in the section explores the behaviour of complex organic compounds built from two or more benzene rings under compression. In the study, benzopyrene shows a series of phase transitions at high pressure, in which the basic units of five fused benzene rings are rearranged. As mentioned above, the installation of the Rigaku-Synergy diffractometer at the BGI made the two final studies in this section possible. In the first, it is used to explore the structures of a hybrid organic-inorganic perovskite with excellent optoelectric properties with two enantiomers, placed in the diamond anvil cell. This opens the possibility to study these

materials also at high pressure, which is planned for the future. Similarly, in the final contribution to this section, the bright X-ray beam of the source allowed the structure determination of two organic thermally activated delayed fluorescence materials at room conditions, with a potential use as organic light-emitting diodes.

a. *Stabilisation of N_6 and N_8 anionic units and 2-D polynitrogen layers in high-pressure scandium polynitrides (A. Aslandukov, A. Aslandukova, S. Khandarkhaeva, F.I. Akbar, N.A. Dubrovinskaia and L.S. Dubrovinsky, in collaboration with Y. Yin/Linköping, D. Laniel/Edinburgh, S. Chariton and V. Prakapenka/Chicago, E. Lawrence Bright, C. Giacobbe, J. Wright, D. Comboni and M. Hanfland/Grenoble)*

Nitrogen catenation under high pressure (*P*) leads to the formation of polynitrogen compounds with potentially unique properties. The exploration of the entire spectrum of poly- and oligo-nitrogen moieties is still in its earliest stages. Polynitrides with a high nitrogen content are especially promising as high-energy-density materials (HEDM), because their decomposition results in the formation of molecular nitrogen, accompanied by a large energy release. The latter is due to the difference between the energy of the triple intramolecular bond in N_2 and the energy of double and single bonds in polynitrogen units. For HEDMs, the molecular weight of the compound also matters, with other properties being similar, the lighter the elements in the solid, the higher the gravimetric energy density of the compound. Since scandium is the lightest transition metal, its polynitrides may be especially promising as HEDM.

In this work, chemical reactions between scandium and nitrogen at high *P* (50-125 GPa) and high temperature (2500 K) in laser-heated diamond cells were studied. The crystal structures of synthesised compounds were determined using synchrotron high-*P* single-crystal X-ray diffraction data collected at APS (beamline 13IDD) and at ESRF (beamlines ID11 and ID15b).

At 50 GPa, the previously known ScN was synthesised, while, at 78-125 GPa, four novel scandium nitrides — Sc_2N_6, Sc_2N_8, ScN_5, and Sc_4N_3 — were synthesised (Fig. 3.7-1). High-*P* synchrotron single-crystal X-ray diffraction revealed that in the crystal structures of the nitrogen-rich Sc_2N_6, Sc_2N_8, and ScN_5 phases nitrogen is catenated, forming previously unknown N_6^{6-} and N_8^{6-} units and $^{2}_{\infty}(N_5^{3-})$ anionic corrugated 2D-polynitrogen layers consisting of fused N_{12} rings (Fig. 3.7-1). The two novel catenated nitrogen N_6^{6-} and N_8^{6-} units are intermediate non-cyclic species between dinitride and 1D-polynitrogen anions. The anionic corrugated polymeric $^{2}_{\infty}(N_5^{3-})$ layers in the crystal structure of ScN_5 present a unique example when nitrogen prefers to form layers instead of 1D-polymeric chains. These discoveries significantly expand the list of oligo- and poly-nitrogen anions, and contribute to the fundamental understanding of nitrogen chemistry under high *P*.

Density functional theory calculations corroborate experimental discoveries and confirm the dynamical stability of the synthesised compounds both at synthesis and ambient *P*. The key metrics of HEDM performance, such as volumetric and gravimetric energy densities,

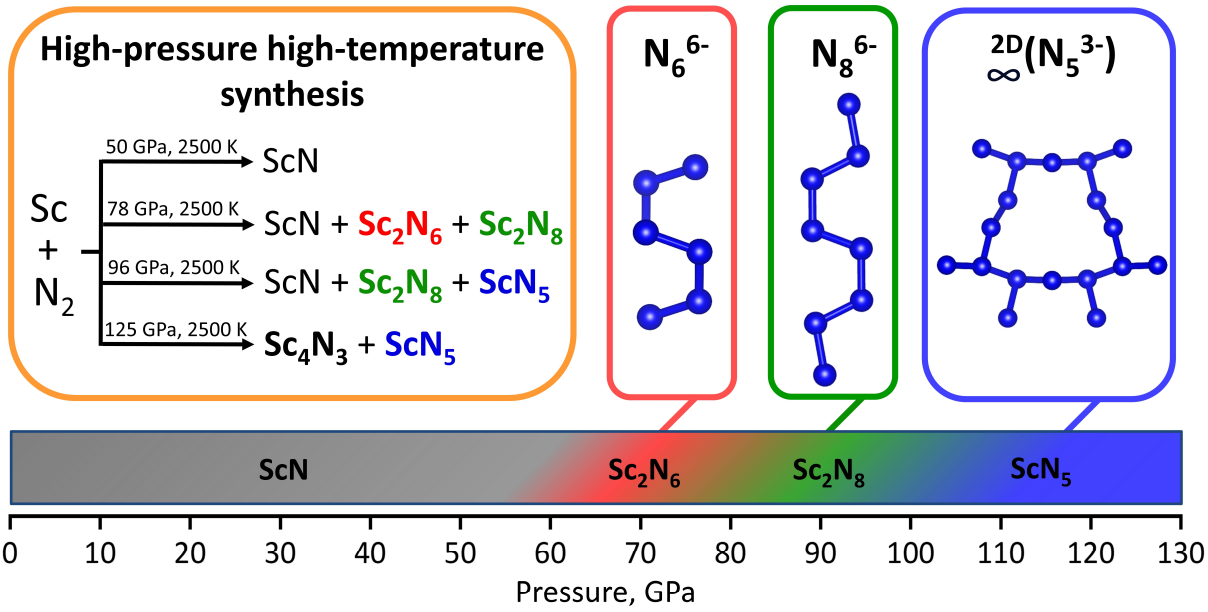

Fig. 3.7-1: Synthesis of exotic scandium polynitrides and their characteristic oligo- and poly-nitrogen structural units, accountable for the high-energy-density property of the compounds. The color pressure scale at the bottom indicates the synthesis of corresponding polynitrides.

detonation velocity, and detonation *P*, were estimated for Sc_2N_6, Sc_2N_8, and ScN_5 considering their decomposition to ScN and molecular nitrogen at 1 bar. The energy densities and explosive performance increase from Sc_2N_6 to ScN_5 along with the increase in nitrogen content. Sc_2N_6, Sc_2N_8, and ScN_5 possess volumetric energy densities, detonation velocities, and detonation *P* higher than those of trinitrotoluene (TNT).

One can expect that the N_6 and N_8 units will be stabilised at ambient conditions in the future, considering the example of CsN_5 that was initially synthesised at high *P* and subsequently the N_5 anion was stabilised at atmospheric *P*. This may not only open access to novel high-energy-density materials but also to analogues of Li- and Mg- metalorganic compounds that are currently widely used in organic synthesis. N_6 and N_8 units, if used as building blocks in organic chemistry, may provide new routes for the targeted synthesis of novel N-heteroatomic organic, metalorganic, and coordination compounds.

b. *High-pressure synthesis and structural characterisation of novel rare-earth metals carbides (F.I. Akbar, A. Aslandukova, A. Aslandukov, N.A. Dubrovinskaia and L.S. Dubrovinsky, in collaboration with Y. Yin/Linköping, E. Bykova and M. Bykov/Frankfurt a. M.)*

Metal-carbon compounds show a diverse range of chemical bonding and structural variations: The unique ability of carbon to form complex structures – chains, rings, clusters, and more – provides the basis for the vast richness of organic and inorganic chemistry. However, at ambient

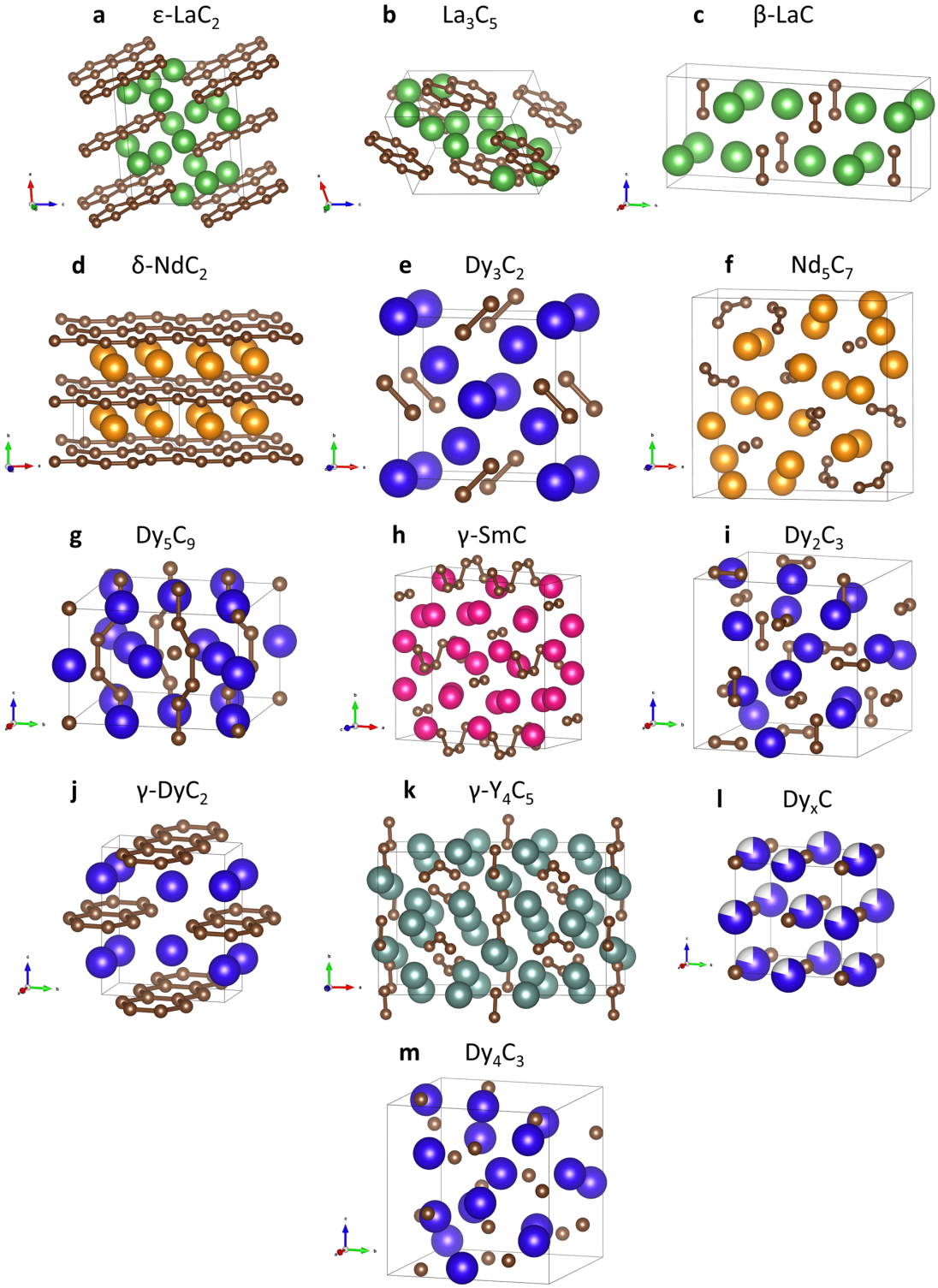

Fig. 3-7-2: Crystal structures of rare-earth metals carbides synthesised under extreme conditions: (a) ε-LaC_2, (b) La_3C_5, (c) β-LaC (β-NdC, β-SmC), (d) δ-NdC_2 (δ-SmC_2), (e) Dy_3C_2 (Nd_3C_2, Sm_3C_2, Gd_3C_2), (f) Nd_5C_7 (Sm_5C_7, Gd_5C_7, Yb_5C_7), (g) Dy_5C_9 (Y_5C_9, Nd_5C_9, Sm_5C_9, Gd_5C_9, Yb_5C_9), (h) γ-SmC, (i) Dy_2C_3 (Y_2C_3, Sm_2C_3, Gd_2C_3), (j) γ-DyC_2 (γ-YC_2, γ-SmC_2), (k) γ-Y_4C_5 (γ-Sm_4C_5, γ-Gd_4C_5, γ-Dy_4C_5), (l) Dy_xC (Y_xC, Gd_xC, Yb_xC), (m) Dy_4C_3 (Sc_4C_3, Gd_4C_3, Yb_4C_3). Yttrium carbides Y_2C_3 and γ-Y_4C_5 and dysprosium carbides γ-DyC_2, Dy_5C_9, γ-Dy_4C_5, Dy_4C_3, and Dy_3C_2 were synthesised and characterised earlier.

conditions, carbides showing structural motifs similar to those in organic compounds are limited to configurations with discrete carbon atoms, carbon dimers and trimers. Despite advances in theoretical predictions, experiments still reveal numerous unexpected phases and structures. This highlights the essential role of high-pressure (*P*) experiments in advancing our understanding of these compounds, enabling the discovery of unexpected structures that expand knowledge in crystal chemistry.

This work compiles outcomes of various experiments performed for different rare-earth metal-carbon systems relevant to materials science, which resulted in a number of significant findings, such as the discovery of previously unknown compounds and structural types, as well as in revealing the complex crystallochemistry and regularities in the structural organisation of rare-earth metals carbides. The primary tools employed in these studies include the laser-heated diamond anvil cell (DAC) technique for generating high *P* and high temperatures (*T*), and *in situ* powder and single-crystal X-ray diffraction (XRD) for phase identification and structure solution and refinement. We used the BX90 type DAC equipped with Boehler-Almax type anvils and a rhenium gasket. Flakes of pure rare-earth metals (REE) were loaded into the pressure chamber together with dried NaCl (used as thermoinsulator). After compression of the sample to ~ 20-125 GPa, REE flakes were laser heated from both sides (NIR laser, 1070 nm wavelength) to *T* ~ 2200-2800 K. The DACs with the samples were transferred to the extreme conditions beamline at PETRA III and beamlines ID11, ID15b and ID27 at ESRF for *in situ* X-ray diffraction structural studies of products of chemical reactions.

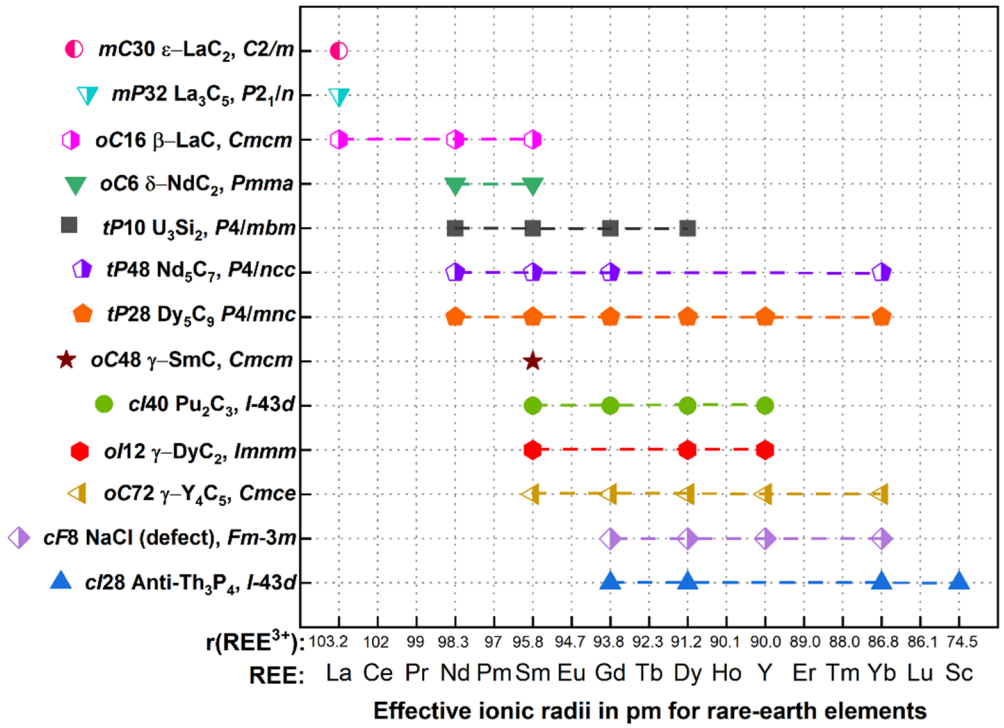

Fig. 3.7-3: Summary of rare-earth carbides formed in the high-pressure high-temperature experiments.

Experiments carried out on a series of rare-earth elements (REE = Sc, Y, La, Nd, Sm, Gd, Dy, and Yb) resulted in the observation of novel structure types: β-LaC, γ-SmC, γ-Y_4C_5, Nd_5C_7, La_3C_5, Dy_5C_9, γ-DyC_2, δ-NdC_2, and ε-LaC_2 (Fig. 3.7-2). The β-LaC structure type is common for LaC, NdC, and SmC (Fig. 3.7-3); the γ-SmC structure type for SmC; the γ-Y_4C_5 structure type for Sm_4C_5, Gd_4C_5, Dy_4C_5, and Yb_4C_5; the Nd_5C_7 structure type for Nd_5C_7, Sm_5C_7, Gd_5C_7, and Yb_5C_7; the La_3C_5 structure type for La_3C_5; the Dy_5C_9 structure type for Y_5C_9, Nd_5C_9, Sm_5C_9, Gd_5C_9, Dy_5C_9, and Yb_5C_9; the γ-DyC_2 structure type for YC_2, SmC_2, and DyC_2; the δ-NdC_2 structure type for NdC_2 and SmC_2; the ε-LaC_2 structure type for LaC_2. Of these, Nd_5C_7 and γ-Sm_4C_5 were found to be recoverable at ambient conditions. The structural characterisation revealed 32 novel compounds, which belong to 13 structural types, among which nine were previously unknown (Fig. 3.7-3). The fact that certain structure types are common for several metals provides evidence of the regularities in the chemistry of rare-earth carbides under high *P*. The compounds demonstrate a rich diversity of possible carbon entities encompassing carbon dumbbells [C_2], non-linear trimers [C_3], naphthalene-decalin-like carbon fragments, carbon chains, and polyacene-like ribbons. Several of the novel dysprosium carbides presented here were already discussed in the Annual Report 2023.

c. *High-pressure synthesis of rhenium carbide Re_3C under megabar compression (Y. Yin and I.A. Abrikosov/Linköping, L.S. Dubrovinsky, A. Aslandukov, A. Aslandukova and N. Dubrovinskaia, T. Fedotenko and K. Glazyrin/Hamburg, G. Garbarino/Grenoble)*

The rhenium-carbon system has long attracted attention and has been extensively studied both theoretically and experimentally at ambient and high pressure (*P*). Experimentally, at $P < 70$ GPa, only the anti-MoS_2 type structured Re_2C phase has been identified in the Re-C system. At significantly higher *P* of approximately 200 GPa, several rhenium carbides with compositions Re_2C, ReC_2, ReC, and $ReC_{0.2}$, were synthesised and characterised using single-crystal X-ray diffraction (SCXRD). Experimental studies of the rhenium-carbon system in the megabar *P*-range have not been performed, but computations have predicted the existence of several phases of a rhenium carbide with stoichiometry Re_3C. These are suggested to have high hardness and ultra-low compressibility, as well as the potential to be quenchable to ambient conditions. This makes Re_3C an intriguing subject for experimental investigation. Here, we report the successful synthesis of one of the predicted rhenium carbide Re_3C at 105(3) and 140(5) GPa.

The Re_3C compound was synthesised by direct reactions of the rhenium gasket with the diamond anvils. Two BX90-type screw-driven diamond anvil cells (DACs) equipped with 120 μm culet anvils were used. The sample chambers were formed by pre-indenting rhenium gaskets to ~ 20 μm thickness and laser-drilling a hole of 60 μm. Two DACs were loaded with a piece of CBr_4, and $Ca(OH)_2$ and boron-doped diamond, respectively, for other research purposes. As *P* was increased above 100 GPa, the chamber diameters shrank to less than ~ 40 μm, causing the laser beam to irradiate the edge of the Re gasket during double-sided sample laser-heating. Synchrotron SCXRD measurements on these samples were conducted at the

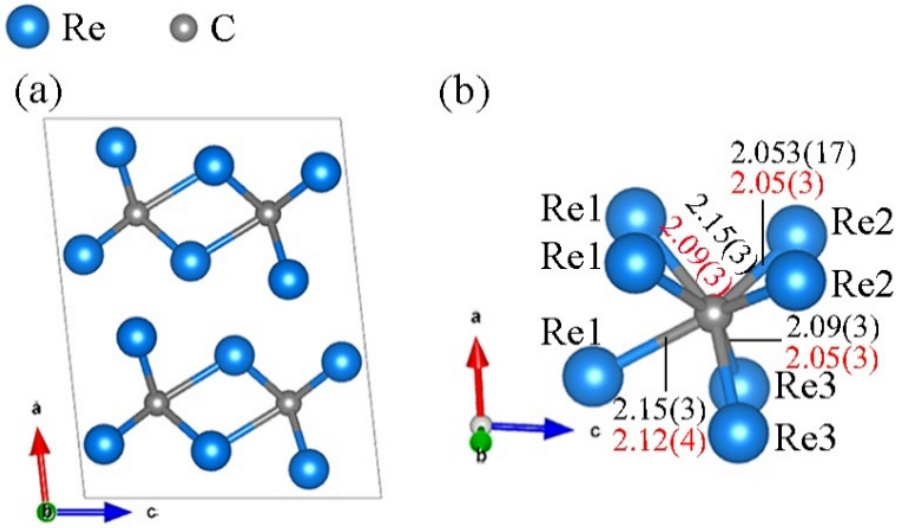

Fig. 3.7-4: The structure of *mC*16-Re_3C. (a) A unit cell viewed along the *b* direction. (b) A carbon atom is surrounded by seven Re atoms, forming a polyhedron with the shape of a capped trigonal prism. Two Re1-C distances in the polyhedron are equal, while the third is different, as imposed by symmetry. Two Re2-C distances are equal, as well as the two Re3-C distances. The numbers in panel (b) are interatomic distances (in Å) for *mC*16-Re_3C at 105(3) GPa (black) and 140(5) GPa (red). Rhenium atoms are shown in blue, carbon atoms in grey.

ESRF and PETRA III, and the data were analysed using our methodology for processing XRD patterns from multi-grain multi-phase samples with the DAFi program. We found that Re_3C has the monoclinic space group *C*2/*m* (#12; Pearson symbol *mC*16) at 105(3) and 140(5) GPa (Fig. 3.7-4). One C atom is surrounded by seven Re atoms, forming a CRe_7 capped trigonal prism with eight faces (Fig. 3.7-4). Our accompanying *ab initio* calculations support the experimental structural data.

d. *Synthesis of Si-doped boron carbide at high pressures and temperatures (M. Demoucron and Y. Le Godec/Paris, A. Chakraborti)*

Boron carbide (B_4C) is a superhard ceramic of interest in industrial applications ranging from engineering tools, the nuclear industry, to safety armours. However, it exhibits a gradual loss of strength when impacted beyond its Hugoniot elastic limit, and we have recently shown that this behaviour can be explained by the formation of boron vacancies under mechanical stress inside the C-B-C chain. In order to extend the plastic regime to more extreme conditions, we proposed to strengthen the triatomic C-B-C chains which connect the icosahedra of boron carbide. The aim is to replace the boron atom of the chain by silicon using high pressure (*P*) and high temperature (*T*). Therefore, we propose to investigate the high *P* – high *T* synthesis of Si-doped B_4C phase – without any trace of parasitic Si-C or Si-B compounds – from the direct reaction between molten Si and solid boron carbide.

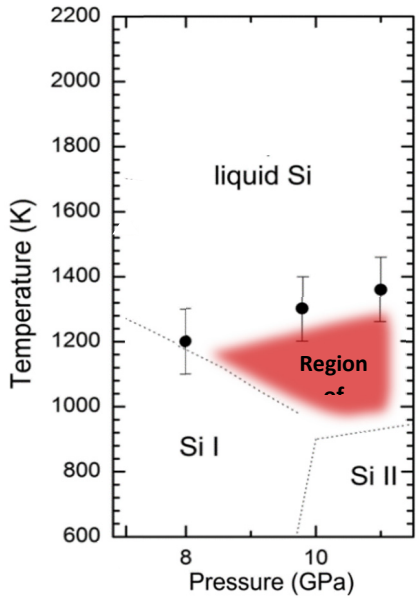

Fig. 3.7-5: Minimum temperature for the formation of SiC (solid symbols) as a function of pressure, with the phase diagram of Si (dotted lines).

Although Si-doping of B_4C occurs in very small amounts at room pressure, it generally leads to the amorphisation of boron carbide. Recently, density functional theory calculations and our *ex situ* experiments have shown that high *P* and *T* makes it much easier to incorporate more silicon into B_4C, thereby strengthening the triatomic C-B-C chains between the boron carbide icosahedra. In a preliminary experiment at ESRF we observed clearly the formation of a ternary Si-doped B_4C phase at 2000 °C and 4 GPa from a mix containing SiB_6 and B_4C. Nevertheless, the kinetics were very slow since this synthesis route is a solid-solid reaction which has the disadvantage of producing numerous unwanted Si-B phases. Therefore, we want to explore an alternative synthesis route involving molten silicon. The use of metallic silicon as a reactant with B_4C is not feasible at low *P* because of the formation of SiC prior to the reaction. Actually, at *P*-range below ~ 10 GPa, SiC formation occurs at a lower *T* than the synthesis of Si-doped B_4C. According to the silicon phase diagram and the conditions of SiC formation, a small *P-T* domain where silicon is liquid and *T* is not high enough to form SiC (around 1200 K/10 GPa, Fig. 3.7-5). The direct liquid-phase synthesis at high *P* between molten Si and B_4C will accelerate the reaction kinetics, also avoiding unwanted Si-B products. Exploratory *ex situ* experiments allowed us to confirm that with the use of single-crystal MgO as a capsule and graphite as a furnace, liquid silicon can be contained in multianvil experiments for several hours. This insight encourages us to attempt *in situ* synthesis for Si-doped B_4C at *P* above 10 GPa.

e. *Yttrium borate* oC*20-*YBO_3 *and yttrium orthocarbonate* hR*39-*$Y_3(CO_4)_2$ *synthesised at megabar pressures (A. Aslandukova, A. Aslandukov, L.S. Dubrovinsky and N.A. Dubrovinskaia, in collaboration with Y. Yin/Linköping, M. Bykov/Frankfurt a. M., V. Cerantola/Milano and A. Pakhomova/Grenoble)*

Metal borates and carbonates are important solids for inorganic chemistry, geoscience and materials science. High-pressure (*P*) phases expand borate and carbonate chemistry and reveal

novel properties of such materials, but high *P* studies on rare-earth borates and carbonates are still limited. There are a few known high-*P* rare-earth borates that are used for luminescent applications, while high-*P* rare-earth carbonates are yet unknown.

In this work, two novel ternary compounds, yttrium borate o*C*20-YBO_3 and yttrium orthocarbonate *hR*39-$Y_3(CO_4)_2$, were synthesised at *P* of ~ 90 and 120 GPa and temperature of ~ 3500 K in a laser-heated diamond anvil cell (DAC). Both compounds were obtained as minor byproducts during the high-*P* synthesis of yttrium hydrides, where the DAC was loaded with yttrium (Y) pieces placed between two layers of ammonia borane (NH_3BH_3), which was used as both a hydrogen-rich precursor and a *P* transmitting medium. The presence of oxygen in these reaction products is apparently related to the oxidation of yttrium upon DAC loading in air. Carbon originates from the diamond anvils, a well-known source of carbon, which often participates in chemical reactions.

In situ high-*P* synchrotron single-crystal X-ray diffraction reveals unprecedented structural motifs of YBO_3 and $Y_3(CO_4)_2$ (Fig. 3.7-6). The YBO_3 compound features infinite zig-zag chains of BO_4 tetrahedra, a previously unknown quasi-1D network in borates, while $Y_3(CO_4)_2$ represents the first rare-earth orthocarbonate, consisting of isolated $[CO_4]$ tetrahedra. Density functional theory calculations support experimental results and provide further insight into the stability and physical properties of the synthesised compound. Our results not only significantly expand the knowledge on structural diversity of borates and carbonate, but also provide a deeper understanding of how extreme conditions drive complex bonding configurations. These discoveries enhance our fundamental knowledge of high-*P* chemistry and open avenues for new materials with potential applications in optics and electronics.

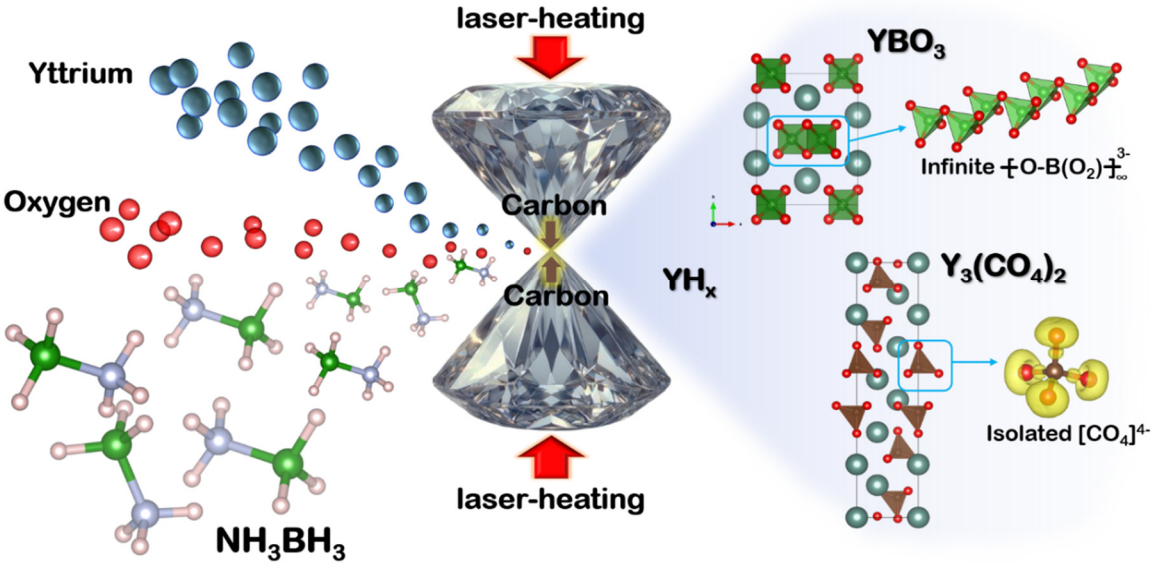

Fig. 3.7-6: Illustration of the formation of two novel ternary compounds, yttrium borate (YBO_3) and yttrium orthocarbonate ($Y_3(CO_4)_2$) formed in the laser-heated DAC. YBO_3 features unique, unbranched zig-zag chains of BO_4 tetrahedra, while $Y_3(CO_4)_2$ includes isolated $[CO_4]^{4-}$ orthocarbonate anions, marking the first instance of a rare-earth orthocarbonate.

f. *Structural transformations and stability of benzo[a]pyrene under high pressure (W. Zhou, A. Aslandukov, A. Minchenkova, L.S. Dubrovinsky and N.A. Dubrovinskaia, in collaboration with M. Hanfland/Grenoble)*

Polycyclic aromatic hydrocarbons (PAHs) are complex organic compounds consisting of two or more condensed benzene rings. Due to their exceptional properties and widespread applications, these compounds have attracted significant attention from geoscientists, chemists and physicists. It is thought that research into the evolution of PAHs under pressure (*P*) may help to understand the origins of our universe, and high-*P* single-crystal X-ray diffraction (SCXRD) is the best method to study it.

Benzo[*a*]pyrene (B*a*P) is one of the two isomeric species of benzopyrene ($C_{20}H_{12}$), a representative of PAHs, formed by a benzene rings fused to pyrene. In order to analyze the crystal structure of B*a*P at high *P*, we loaded single crystals of B*a*P into a diamond anvil cell (DAC) equipped with the culets size of 250 μm and a rhenium gasket with a hole of ~ 120 μm. As a *P*-transmitting medium, helium (He) was used. The DAC was gradually pressurised to 35 GPa. The samples were characterised using synchrotron SCXRD at the European Synchrotron Radiation Facility (ESRF) at beamline ID15B (λ= 0.410 Å). Upon compression of B*a*P-I ($P2_1/c$) to 4.8 GPa, we observed a phase transition to a previously unknown monoclinic polymorph B*a*P-II ($P2_1/c$). The next phase transition occurred at 7.1 GPa to B*a*P-III with a

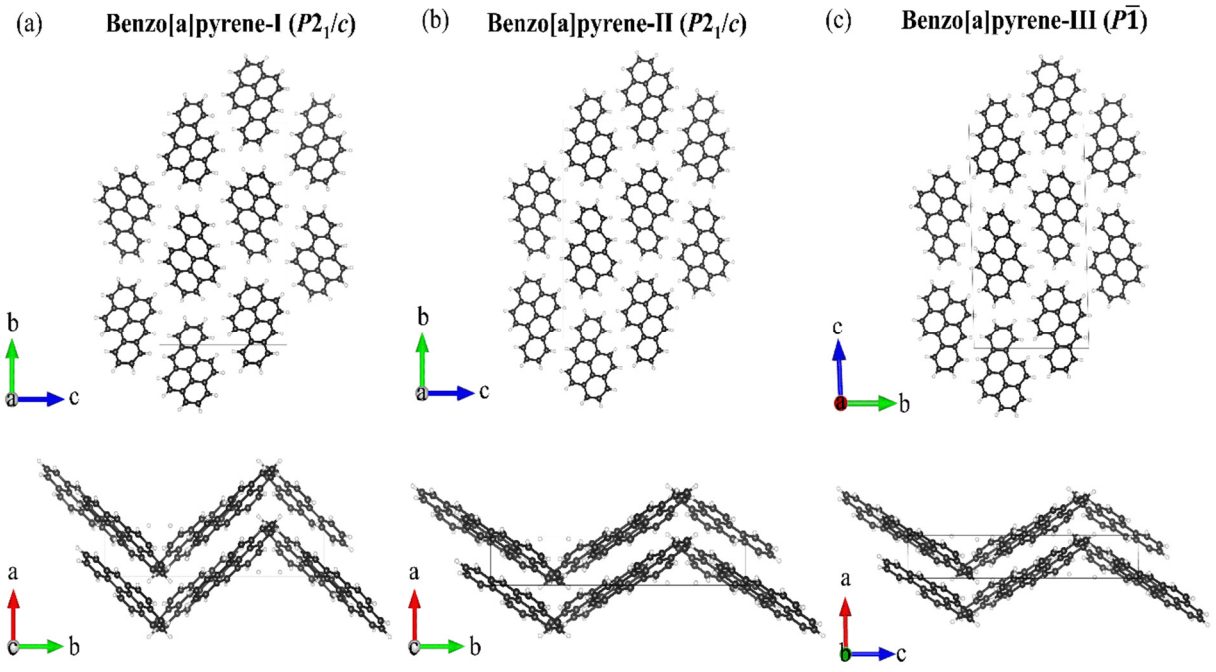

Fig. 3.7-7: Crystal structures of B*a*P polymorphs. (a) B*a*P-I at ambient conditions, as viewed along the *a*- (top figure) and *c*-axis (bottom figure); (b) B*a*P-II at 4.8 GPa, viewed along the *a*- (top) and *c*-axes (bottom); (c) B*a*P-III at 7.1 GPa, as viewed along the *a*- (top) and *b*-axis (bottom); C atoms are black. H atoms are white.

triclinic structure (*P*-1), stable to about 28 GPa. At the next *P* step of 35 GPa, the X-ray diffraction pattern disappeared. According to the DFT calculations, above 3.5 GPa, B*a*P-III is the most stable phase. The arrangement of molecules in B*a*P-II is similar to that in B*a*P-I (Fig. 3.7-7). In both structures, the molecules are arranged in a herringbone pattern in projection along the *a*-direction, but the intermolecular angles in B*a*P-I and B*a*P-II are noticeably different. The transformation manifests as an abrupt change in the intermolecular angle and unit cell parameters. Further compression of B*a*P-II resulted in the formation of B*a*P-III at 7.1 GPa, with a triclinic structure (*P*-1).

The analysis of Hirshfeld surfaces for the three B*a*P polymorphs, constructed using the CrystalExplorer program, showed that in all three polymorphs, the molecules are involved in similar contacts with neighboring molecules, participating in a planar stacking arrangement. A general trend is observed with an increase in the percentage contribution of C···C intermolecular contacts and a decrease in H···H contacts upon compression. The results of high-*P* studies of B*a*P up to about 28 GPa provide insights into the structural transformations in a representative of a broad class of organic materials - polycyclic aromatic hydrocarbons.

g. *Chiral perovskites at high pressure (A. Dibenedetto, M. Moroni and L. Malavasi/Pavia, T. Boffa Ballaran)*

Chiral perovskites are hybrid organic-inorganic perovskites with excellent optoelectronic properties important for several technological applications, for example in quantum computing and optical spintronics. Such properties are closely related to the packing of the organic molecules in the perovkiste structure. The primary goal of this research, therefore, is to investigate the structural and functional properties of chiral perovskites at high pressure (P). The materials studied, with the formula (3-APD)$PbBr_4$ (3-APD = 3-aminopiperidine), included single crystals of the R and S enantiomers synthesised specifically for single-crystal X-ray diffraction experiments in diamond anvil cells (DACs).

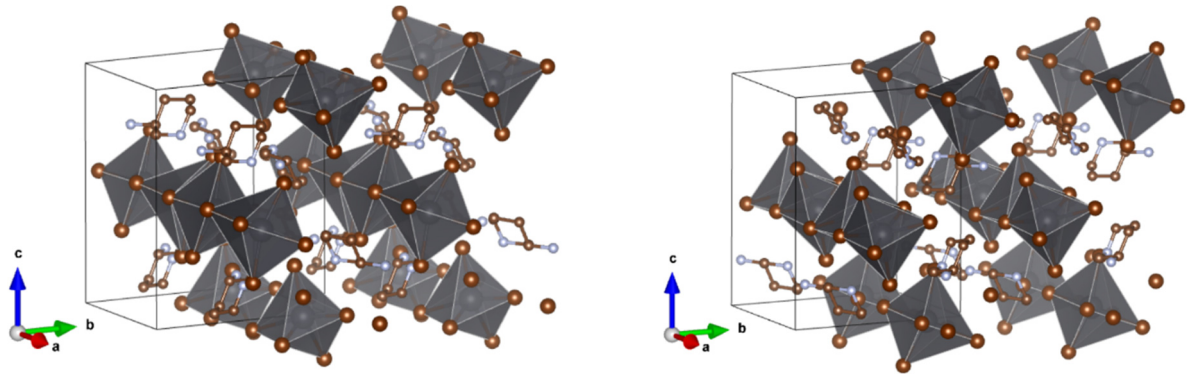

Fig. 3.7-8: Crystalline structures of S-3- APDPbBr$_4$ (left) and R-3- APDPbBr$_4$ (right) determined at room pressure within the DACs.

For the synthesis of *R*-3-APDPbBr$_4$ single crystals, Pb(CH$_3$COO)$_2$ (lead acetate) was dissolved in excess HBr and heated in an oil bath to 90 °C. The amine R-3APD·2HCl was then dissolved, and heating was stopped. The solution was cooled at a controlled rate of 1 K/h. The resulting white crystals were filtered, washed, and vacuum-dried at 65 °C overnight. The same methodology was applied for the synthesis of *S*-3- APDPbBr$_4$ single crystals, substituting the starting amine with the S enantiomer.

Two DACs were prepared, one for each enantiomere with culet sizes of 600 µm for the *R*-3-APDPbBr$_4$ sample and 500 µm for the *S*-3- APDPbBr$_4$ sample. The rhenium gaskets were indented to ~ 80 µm thickness and holes with dimensions of 300 µm and 250 µm, respectively were drilled using a laser. A ruby chip was placed adjacent to the sample to monitor the pressure inside the cell. After loading the crystals into the cells with helium as the pressure-transmitting medium, X-ray data were collected using the newly installed Rigaku single-crystal diffractometer. The high-resolution data collections allowed to solve the enantiomer structure (Fig. 3.7-8). Experiments at small pressure steps will be performed in the near future with the goal of better understanding the stability limits of the chiral structures under compression and potential changes in their optical and structural properties. These findings could have significant implications for the development of novel optoelectronic materials capable of operating under extreme pressure conditions.

h. *Solvent dependence of thermally-activated delayed fluorescence in DMAC-TRZ single crystals (A. Kuimov, S. Bagnich, A. Köhler, C. Greve and E.M. Herzig/Bayreuth, T. Boffa Ballaran)*

In recent years, organic thermally activated delayed fluorescence (TADF) materials, which are characterised by small energy differences (ΔEST) between their singlet and triplet states, have attracted growing attention from industry and science for applications in organic light-emitting diodes (OLEDs). TADF materials allow to simultaneously harvest singlet and triplet excitons through reverse intersystem crossing, enabling highly efficient light emission with potentially significantly higher efficiencies than classic OLEDs. However, the exact fluorescence properties of TADF materials strongly depend on their structure, as it determines the energy difference between singlet and triplet states.

In this study two single crystals of the donor-acceptor (D-A) type TADF-emitter DMAC-TRZ, an aromatic molecular compound containing a triazine ring, one grown from the solvent toluene and the other from the solvent ethyl acetate, were selected and intensity data were collected using the new Rigaku Synergy custom diffractometer installed at the BGI. The bright X-ray beam produced by a Mo-rotating anode and the Hybrid-Photon-Counting detector with a very large active area allowed to collect high-resolution data in less than 3 hours. The integrated intensities were used to solve and refine the structure of the two compounds (Fig. 3.7-9) which have both monoclinic symmetry. However, the DMAC-TRZ molecules are arranged differently

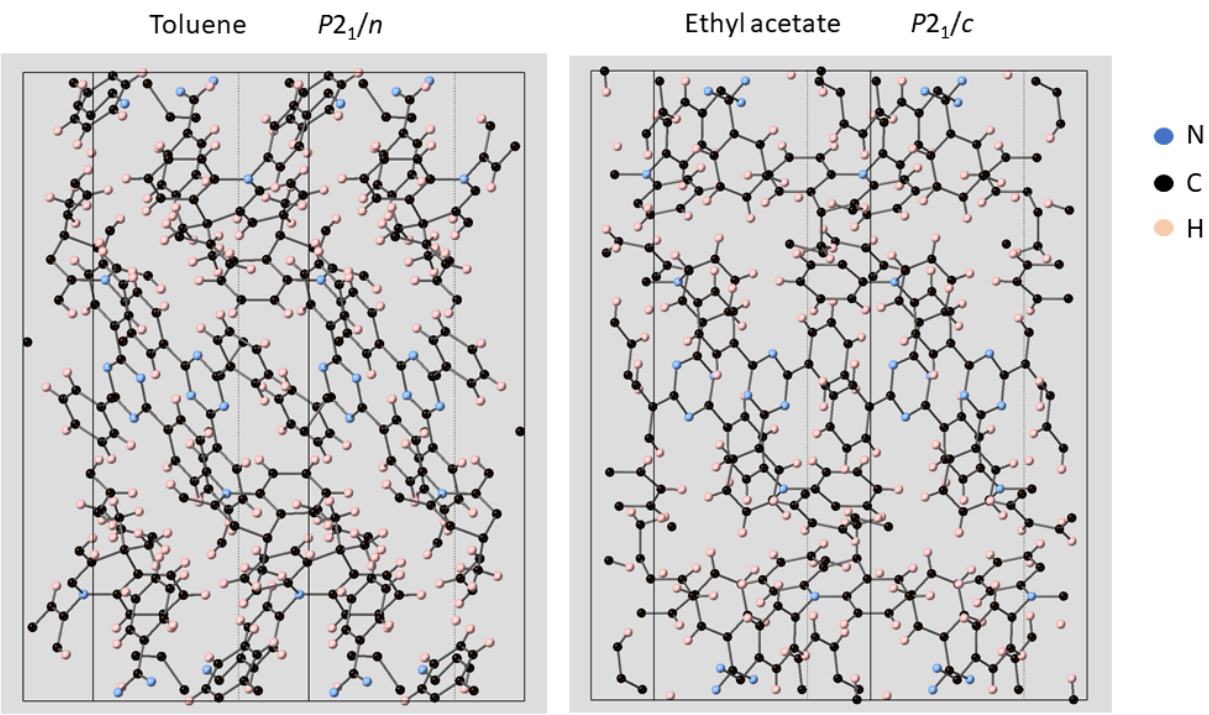

Fig. 3.7-9: Crystal structure of the two DMAC-TRZ compounds viewed down the reciprocal *c*-axis. The different arrangement of the DMAC-TRZ molecules is clearly visible.

in the two compounds, likely due to the different solvent molecules incorporated in the crystal structure. By connecting the earlier measured TADF properties, such as photoluminescence quantum yield and the spectral profile, with its molecular structure and the dihedral angle between the donor and acceptor moieties of DMAC-TRZ, the photophysical processes taking place can be understood. In particular, the influence of the solvent polarity on the single crystal structure could be quantified, opening a pathway to enhance DMAC-TRZ performance for its application in OLEDs by fine-tuning its molecular order during sample preparation.

3.8 Methodological development

The development of advanced research technologies is essential for progress in natural sciences across disciplines. Since its establishment in 1986, the Bayerisches Geoinstitut (BGI) has been at the forefront of innovation in experimental methodologies. Over the years, BGI's focus has expanded beyond experimental geoscience to include computational geodynamics and analytical geochemistry, reflecting the dynamic nature of Earth sciences. These advancements are crucial for maintaining its position as a leader in geoscientific research.

This year, the geochemistry laboratory, led by Prof. A. Bouvier, has made substantial strides in isotopic and elemental analysis. By employing the Neoma MC-ICPMS/MS system, they have pioneered methods such as ^{176}Lu-^{180}Hf and ^{149}Sm-^{150}Nd double-mix spikes calibration, enabling BGI to perform high-precision Sm-Nd and Lu-Hf geochronology. Additionally, Prof. Bouvier's team developed a high-precision method for tin isotope analysis, overcoming challenges in isotope fractionation during sample preparation. They also synthesised a cassiterite standard for *in situ* laser ablation analysis. Complementing these efforts, Zhang *et al.* introduced a refined approach to measuring highly siderophile elements (HSEs) in meteorites, surpassing the accuracy of existing neutron activation methods. Furthermore, Zhao *et al.* established an *in situ* ^{87}Rb-^{87}Sr dating technique that minimises sample destruction, a method particularly advantageous for planetary and Martian mineral studies.

In experimental geoscience, five notable innovations stand out. First, Kurnosov *et al.* installed the MAR345 image plate detector in the X-ray-Brillouin coupling system, enhancing data acquisition for mineral properties under mantle conditions. Second, Pöppelbaum *et al.* devised a novel method to measure fluid overpressure and permeability *in situ* under high-temperature, high-pressure conditions using X-ray tomography and diffraction. Third, Pierru *et al.* employed ultrafast 3D microtomography to precisely map the liquidus of complex Fe-Ni-Si-S systems, dramatically improving efficiency. Fourth, Keppler and Di Genova engineered a new apparatus for studying magma fragmentation at previously unattainable temperatures and pressures. Lastly, Minchenkova and Audétat tested the reliability of synthetic fluid inclusions in different host minerals to quantify friction corrections in piston cylinder experiments, and they developed a new method to map temperature gradients within the sample capsules during such experiments.

In geodynamics, members of the institute have been part of the development of GeophysicalModelGenerator.jl, an open-source software package that facilitates the integration and visualisation of diverse geoscientific datasets. This tool supports the creation of input geometries for numerical modelling, ensuring compatibility with multiple data formats and fostering collaboration across disciplines in order to become a standard tool in the field.

a. *Calibration of ^{176}Lu-^{180}Hf and ^{149}Sm-^{150}Nd double mixed spikes: Advancement in Sm-Nd and Lu-Hf geochronology (A. Bouvier and X.-J. Hu, in collaboration with J.D. Vervoort/Pullman)*

A critical requirement for isotope work on meteorites as well as early Earth samples is to use isotopic dilution methods for determining precise and accurate ^{147,146}Sm-^{143,142}Nd and ^{176}Lu-^{176}Hf ages for geochronology, and precise and accurate initial Nd and Hf isotope ratios. There are only a small number of isotope laboratories with fully calibrated, mixed radiogenic spikes. It is imperative to understand that these spikes are characterised by their enrichment in a specific isotope (97-98 % for ^{149}Sm, ^{150}Nd, ^{176}Lu, ^{180}Hf). These enriched spikes are produced at the Oak Ridge National Laboratory in the USA through a process of electromagnetic separation. The incorporation of these spikes into rock/sample solutions enables the precise determination of elemental concentrations, and therefore facilitating obtaining radioactive/radiogenic isotope ratios. To enable their use in radiogenic isotope research at BGI, new mixed ^{149}Sm-^{150}Nd and ^{176}Lu-^{180}Hf enriched isotope spikes were calibrated.

To calibrate the spikes, we used the Thermo Neoma MC-ICPMS/MS, which was commissioned at BGI in March 2024. Calibrating these isotope spikes involves accurately characterising the isotope abundance of the enriched isotopes as well as the mixtures of standards and spikes used in the calibrations. These measurements are challenging because the isotopes and mixtures do not have natural isotope ratios to correct for instrumental mass bias - something that is used in natural samples for their accurate analysis. To compensate for the non-natural isotope ratios, a highly stable MC-ICPMS is required, which we ensured for each analytical session.

Elemental standard mixtures of one ^{149}Sm-^{150}Nd and three ^{176}Lu-^{180}Hf spikes were previously prepared by Bouvier and Vervoort at Washington State University (WSU). The mixed spike solutions consist of a single Sm/Nd spike (due to the lack of large Sm/Nd variations in rocks and minerals) that can be diluted for analysis of compositions from low-abundance mafic to high-abundance-REE felsic rocks and a set of three Lu/Hf spikes with a range of Lu/Hf ratios to allow analysis of compositions from very low Lu/Hf crustal rocks, low Lu/Hf mafic rocks, to very high Lu/Hf for garnet and apatite samples. The spikes were mixed with NIST elemental standards in known ratios and processed through column chemistry to separate each element. During the course of the collaboration in Bayreuth, we calibrated all the spikes and successfully characterised the enriched isotope spikes. The results of the calibration of the mixed isotope spikes for measurements of USGS reference material standards (BCR-2 and BHVO-2 basalts) with the new Sm-Nd-5 and Lu-Hf-10 spikes are shown in Table 3.8-1. An additional Lu-Hf-4 spike for zircon and Archean granitic rocks is also available.

With these fully calibrated spikes, the BGI laboratory is one of the few laboratories in the world capable of accurately analysing the full range of terrestrial and meteoritic materials for high-precision Sm-Nd and Lu-Hf geochemistry and geochronology. We will also be able to measure high-precision concentrations of chondrites and samples returned from space missions to better constrain the abundance of these elements in the Solar System.

Table 3.8-1: Calculated compositions of mixed enriched spikes and ^{147}Sm-^{143}Nd and ^{176}Lu-^{176}Hf isotopic compositions of USGS reference materials obtained using the new spikes that are compared with the range of reported reference values also obtained using the isotope dilution method.

Spike name	**Type**	**^{176}Lu (nmole/g)**	**^{180}Hf (nmole/g)**	**$^{176}Lu/^{180}Hf$**
Lu-Hf-10	mafic rocks	2.8048	3.22819	0.8688
Lu-Hf-11	felsic rocks	1.5928	4.77375	0.3337
Lu-Hf-12	high-Lu minerals	13.8607	1.37841	10.056
		^{149}Sm (nmole/g)	**^{150}Nd (nmole/g)**	**$^{149}Sm/^{150}Nd$**
Sm-Nd-5	all	12.8949	12.4449	1.0361
Standards	**$^{147}Sm/^{144}Nd$**	**$^{143}Nd/^{144}Nd$**	**$^{176}Lu/^{177}Hf$**	**$^{176}Hf/^{177}Hf$**
BCR-2 (n=1)	0.1386±0.0003	0.512636±0.000007	0.01430±0.00003	0.282862±0.000004
Reference values by ID (range)	0.1377-0.1396	0.512630-0.512640	0.01427-0.01435	0.282862-0.282875
BHVO-2	0.1504±0.0003	0.512988±0.000021	0.00871±0.00002	0.282112±0.000004
Reference values by ID (range)	0.1492-0.1505	0.512979-0.512989	0.00872	0.282105-0.282118

ID = isotopic dilution, $^{143}Nd/^{144}Nd$ normalised to the JNd_i standard value of 0.512115 and $^{176}Hf/^{177}Hf$ normalised to JMC 475 standard value of 0.282160.

b. *Advancing Sn isotope analysis: Double spike ^{117}Sn-^{122}Sn technique and cassiterite standard development (D. Zhu, E. Kubik and A. Bouvier)*

Tin (Sn) has ten naturally occurring stable isotopes, the largest number of any element, formed by various nucleosynthetic processes. This abundance provides significant advantages for the study of cosmochemical (such as the origin of volatiles in planetary materials) and geological processes (including magmatic-hydrothermal transitions, petrology, and ore deposit formation), as well as for studies of the provenance and transactions of archaeological artefacts. Although Sn isotope measurements have been reported over the last decade due to advances in multi-collector inductively coupled plasma mass spectrometry (MC-ICP-MS), several challenges remain. These include isotope fractionation caused by Sn loss during sample preparation and the need for greater precision and accuracy to detect subtle variations in Sn isotopic ratios. Additionally, the difficulty of digesting cassiterite (SnO_2) in acids and chemical heterogeneity within individual cassiterite grains motivate the development of *in situ* analysis of Sn isotopic ratios.

In this study, we present the ongoing development of analytical methods to measure Sn isotopic ratios using a Thermo Neoma MC-ICP-MS/MS either in solution mode using a double spike for rock and fluid analyses or with a laser ablation solid source for cassiterite analysis in natural

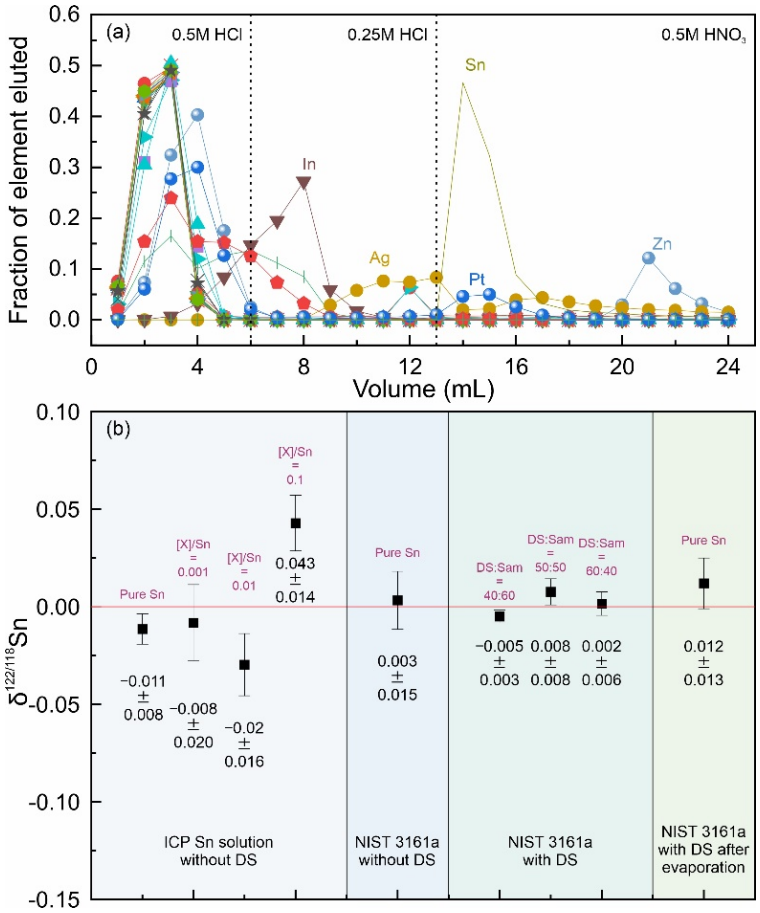

Fig. 3.8-1: a) Elution curves of the Sn purification procedure using different reagents using TRU resin. b) $\delta^{122/118}$Sn values measured from pure Sn solution, mixed with matrix, double spike correction (^{122}Sn-^{117}Sn), and NIST 3161a solution after evaporation.

samples and experimental charges. After the dissolution of bulk rock basalt standards, Eichrom® TRU ion exchange resin is used for Sn purification to eliminate the matrix effect (Fig. 3.8-1a), effectively reducing most elements to < 0.1 % in Sn fraction. To assess matrix effects, an ICP Sn standard solution was doped with varying concentrations of matrix elements commonly found in natural cassiterite. The results show that when the [X]/Sn ratio is below 0.001, the $\delta^{122/118}$Sn value remains at -0.008 ± 0.020 ‰ (Fig. 3.8-1b), confirming that the matrix has a minimal effect on Sn isotope analysis of unprocessed cassiterite samples (*i.e.*, those that will eventually be analysed using laser ablation). The double spike (^{117}Sn-^{122}Sn) technique was introduced to correct for isotope fractionation of Sn during sample preparation and measurement. With sample/spike ratios ranging from 40:60 to 60:40, the NIST 3161a Sn standard solution gave $\delta^{122/118}$Sn values of 0.001 ± 0.008 ‰ (Fig. 3.8-1b). Considering the potential isotopic fractionation due to Sn loss during evaporation, our results demonstrate that even at low Sn recovery rates, the double spike technique remains effective in correcting NIST 3161a values to 0 ($\delta^{122/118}$Sn = 0.012 ± 0.013 ‰). Next, we will analyse Sn isotope values in bulk rock standards (such as BCR-2 and BHVO-2) to further confirm that measurements of rock samples are accurate and reproducible compared to literature values.

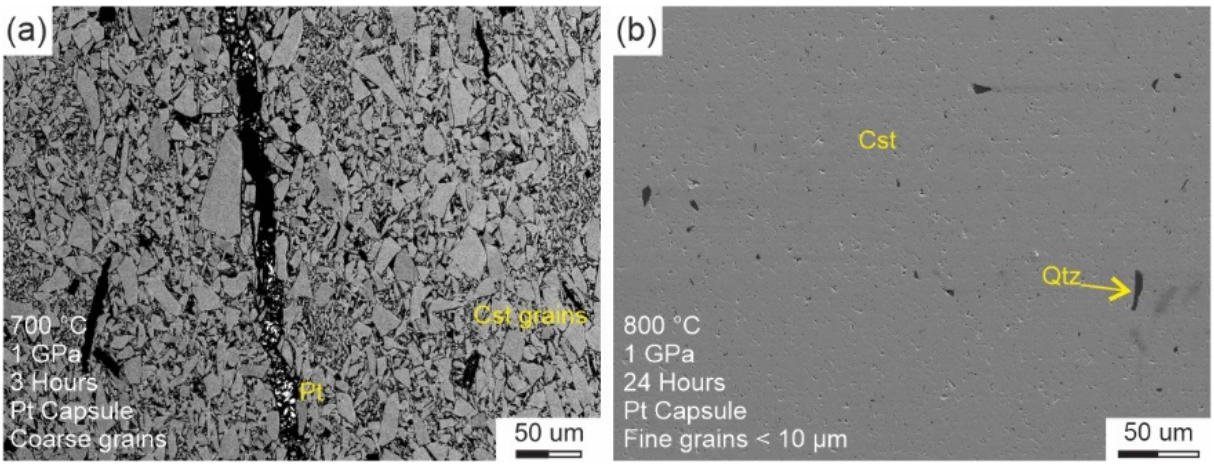

Fig. 3.8-2: SEM images of experimentally synthesised cassiterite under different conditions. a) Unaltered coarse cassiterite grains at a temperature of 700 °C, with a heating time of 3 hours, derived from coarse starting material. Pt entered the sample along the crack. b) Homogenised cassiterite at a temperature of 800 °C, with a heating time of 24 hours, derived from fine-grained starting cassiterite, showing a few quartz grains within the cassiterite.

The laser ablation analysis approach requires an isotopically homogeneous standard that closely matches the cassiterite matrix. At present, only a Sn metal is available as a standard for inter-laboratory comparison of LA-MC-ICPMS Sn isotopic data. A piston-cylinder apparatus was employed to synthesise cassiterite under high-temperature (700-800 °C) and high-pressure (1 GPa) conditions. The synthesised cassiterite has a homogeneous surface without recrystallisation after increased temperature, extended heating time, and using finer starting cassiterite grains (Fig. 3.8-2). The synthesised cassiterite was subsequently sectioned into two halves: one half was cast in an epoxy mount for *in situ* analysis, and the other half was ground for bulk solution analysis. We now plan to measure the composition of the standard and test the homogeneity of the Sn isotopes from edge to centre, with the aim of establishing this material as a standard for *in situ* Sn isotope analysis of cassiterite.

c. In situ *^{87}Rb-^{87}Sr chronology by the Neoma MC-ICPMS/MS coupled with laser ablation (B. Zhang/Houston, C. Timoner, R. Zhao, D. Zhu and A. Bouvier)*

A Thermo Neoma MS/MS multi-collector mass spectrometer (MC-ICPMS/MS) equipped with a pre-filtering system consisting of a double-Wien filter and collision cell technology (CCT) has been installed at BGI. The MS/MS technology allows the separation of isobaric ions using a combination of reactive gases and mass filtration. Applications using MC-ICPMS/MS combined with a laser ablation source have recently been developed for *in situ* ^{87}Rb-^{87}Sr geochronology of individual K-bearing minerals in terrestrial granites, a Martian polymict breccia and a chondrite meteorite. Although the method may be less precise than traditional

methods involving mechanical separation of mineral phases and purification chemistry prior to mass spectrometry, it allows the analysis of individual mineral phases in their petrological context and minimises sample mass destruction (which is particularly important for planetary samples returned from space missions).

Table 3.8-2: Comparison of Rb-Sr isochron parameters for the Shap and Dartmoor granites.

Sample*	Instrument	Number of analyses	Date (Ma)	Err (Ma)	Slope Err (%)	MSWD	$(^{87}Sr/^{86}Sr)_0$
Shap	TIMS	4	405	2	N/A	0.36	0.7072
Shap (section)‡	Proteus	120	398.6	2.5	N/A	1.7	0.70755 ± 4
	Neoma (BGI)	**30**	**405.5**	**4.5**	**N/A**	**1.0**	**0.7084 ± 2**
Dartmoor	TIMS	17	285	1	N/A	1.9	0.7094 ± 4
Dartmoor (section)‡	Proteus	118	N/A	N/A	1.1	1.7	0.70944 ± 8
	Neoma (BGI)	**94**	**N/A**	**N/A**	**0.77**	**1.0**	**0.70917 ± 24**

*Dartmoor is used as a standard to calibrate Rb-Sr fractionations in feldspar analyses. The slope is compared to the value obtained by TIMS. We find a correction factor of 0.750687 to correct the Rb-Sr fractionation of Shap.

The BGI Neoma was coupled to a new ESL NWR GEO (1-500 Hz) 193nm excimer laser ablation system for a solid sampling source. The laser was operated at 5 J/cm^2 and a pulse frequency of 20 Hz with an area size of 20 μm. We employed a matrix-matched standard (AMNH-107160 labradorite) to calibrate the Sr isotopic ratios of feldspar and plagioclase, while NIST 610 and 612 glass standards were used for such calibrations in the previous studies. All Ar^+ and other interferences in the SrF^+ mass range were removed by the double Wien mass filter. After the pre-filter, SF_6 mixed with He was injected into the CCT at 0.5 mL/min to react with Sr to form SrF^+, leaving Rb as Rb^+. After the ions passed through an electrostatic analyser and a magnetic sector to be separated based on their mass/charge ratios, $^{87}Rb^+$, $^{84}Sr^{19}F^+$, $^{85}Rb^{19}F^+$, and $^{88}Sr^{19}F^+$ were collected simultaneously on Faraday cups equipped with 10^{11} Ω amplifiers and $^{86}Sr^{19}F^+$, and $^{87}Sr^{19}F^+$ by Faraday cups equipped with 10^{13} Ω amplifiers. The 11 Faraday collectors (10 of which are movable) provide an improved mass dispersion of ~ 22 %, allowing the measurement of $^{85,87}Rb^+$ and $^{105,106,107}SrF^+$ ions in a single-line static measurement. The instrument was operated at 2100 mass resolution. NIST 610 glass and AMNH-107160 labradorite standards were used to bracket the unknowns to correct $^{87}Rb/^{86}Sr$ and internally normalised $^{87}Sr/^{86}Sr$ ratios, respectively. We used the Rb-Sr data reduction scheme (DRS) developed for Neoma in the data reduction software Iolite.

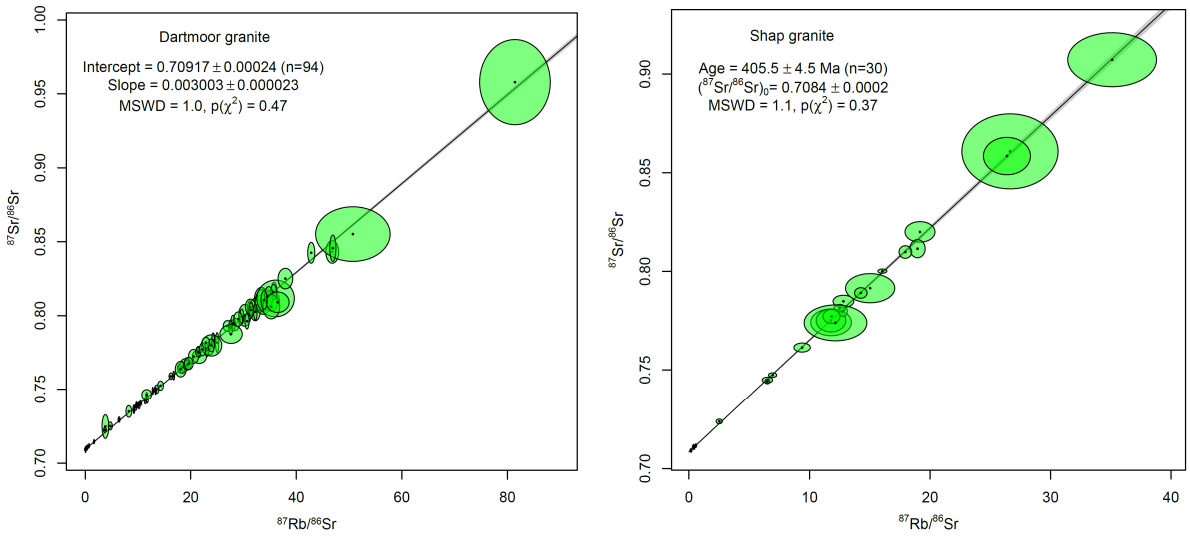

Fig. 3.8-3: (left) Rb-Sr isochron linear fit for the Dartmoor granite with an accepted age of 285 ± 1 Ma obtained from mineral isochron and Rb-Sr analyses by TIMS, and (right) Rb-Sr isochron diagram for the Shap granite. Data plotted using Isoplot R.

We analysed the same sections of the Dartmoor granite and the Shap granite as previously published studies using prototype instruments. The Dartmoor granite and AMNH-107160 labradorite, respectively, were used as standards to calibrate the Rb/Sr and Sr isotopic ratios of the Shap granite. Overall, we obtained better linearity and lower slope and intercept uncertainties for the Dartmoor granite than those obtained in previous studies (Table 3.8-2). Furthermore, our Rb-Sr isochron date for the Shap granite (405.5 ± 4.5 Ma) (Fig. 3.8-3) is identical to those obtained by mineral separation and thermal ionisation mass spectrometry (TIMS) analysis at 405 ± 2 Ma. Our results also show a significant improvement in accuracy compared to the previous date of 398.6 ± 2.5 Ma for the same section from previous LA-MC-ICPMS/MS analyses (Table 1). However, the initial $^{87}Sr/^{86}Sr$ for the Shap granite isochron (Fig. 3.8-3 right; 0.7084) is slightly higher than the TIMS value (0.7072). This difference could be explained by the fact that we did not analyse as many plagioclase grains and no biotite. We will measure mineral phases with lower and higher Rb/Sr than feldspars (*e.g.*, Ca-phosphate, biotite) and calibrate additional matrix-matched standards to improve the methodology for future measurements of feldspars (a relatively common mineral phase) in planetary materials.

d. *Precise and accurate measurement of highly siderophile element (HSE) abundances in planetary metals using laser ablation ICP-MS (R. Zhao, D. Zhu and A. Bouvier, in collaboration with B. Zhang/Houston)*

Metallic iron-rich alloys are abundant phases in chondrite and achondrite meteorites. The elemental composition of the metal present in meteorites is a powerful tracer of the redox conditions during condensation in the differentiation processes of the protoplanetary disk. Iron

meteorites sample the metallic cores of early-formed and differentiated bodies. The elemental compositions of iron meteorites constrain 13 major chemical groups (and possibly 50 other parent bodies of ungrouped irons), based mainly on bulk composition in siderophile elements such as Ga, Ge, Ni, Co, W, Ir and Au. Traditionally, compositional analysis of bulk iron meteorites has relied on *in situ* neutron activation analysis (INAA), which is time-consuming and limited by laboratory capabilities. *In situ* analysis of HSE abundance using laser ablation ICP-MS offers higher efficiency than INAA but has analytical limitations due to matrix mismatch between standard materials (NIST SRM 610-617 glass) and Fe-Ni metal, and analysing individual phases rather than bulk. Additionally, at least 1 g of an iron meteorite sample is generally required to obtain a representative sample of most iron meteorite subgroups, while additional mass may be required for medium and coarse octahedrites. In this study, we developed a method for precise and accurate measurement of chemical composition in planetary Fe-Ni metal by laser ablation ICP-MS at BGI. We optimised the laser ablation ICP-MS data reduction scheme by testing line scan and spot analysis modes, a variety of glass standards and matrix-matched metal samples as secondary standards.

The elemental glass reference material NIST SRM 610 glass, combined with the Hoba (IVB) and North Chile (IIAB) meteorites was used before and after measurements of unknown samples for measurement corrections. Additionally, the chemical compositions of Seymchan (Pallasite), Coahuila (IIAB) and Chinga (IVB) were determined to evaluate the accuracy and precision of the methodology of this study against literature data. The ESL NWR 193 nm laser ablation coupled with a Thermo iCap TQ ICPMS system at BGI was used for all measurements in this study. ^{31}P, ^{52}Cr, ^{57}Fe, ^{59}Co, ^{61}Ni, ^{63}Cu, ^{71}Ga, ^{72}Ge, ^{75}As, ^{95}Mo, ^{99}Ru, ^{103}Rh, ^{105}Pd, ^{120}Sn, ^{121}Sb, ^{182}W, ^{185}Re, ^{189}Os, ^{193}Ir, ^{195}Pt and ^{197}Au were analysed. The laser energy, frequency, spot size of spot analysis, and the frequency and scan speed of line scan were sequentially tested and optimised. The optimised laser ablation experimental conditions of spot analysis consisted of 20s of blank measurement, followed by 1000 burst count of sample ablation at 15 Hz, 150 μm spot size, and fluence of 5 J cm^{-2}. The laser ablation experimental conditions of the line scan analysis consisted of 20s of blank measurement, followed by 6 μm/s scan speed sample ablation at 20 Hz, 100 μm width, and fluence of 5 J cm^{-2}. Line scan of laser ablation avoids downhole fractionation of multiple elements with a total of 8 mm long laser ablation tracks. The analytical sequence started and ended with repeated measurements in NIST SRM 610 glass, North Chile and Hoba. The Co concentration obtained using EPMA was used for internal normalisation. For external normalisation, NIST SRM 610 glass was used for Cr, Ga, Ge, As, Sn and Sb and Hoba for the other elements.

The measurement precision of each analysed element, expressed by the RSD, is better than 10 % for most elements using line scan, while the RSD of spot analysis is better than 20 % in North Chile. Cr and Ni concentrations can be strongly influenced by chromite or phosphide inclusions in the metal (Table 3.8-3). A Line scan of an 8 mm total length averages heterogeneities found for highly siderophile elements present at the sub-millimeter scale in iron meteorites with the

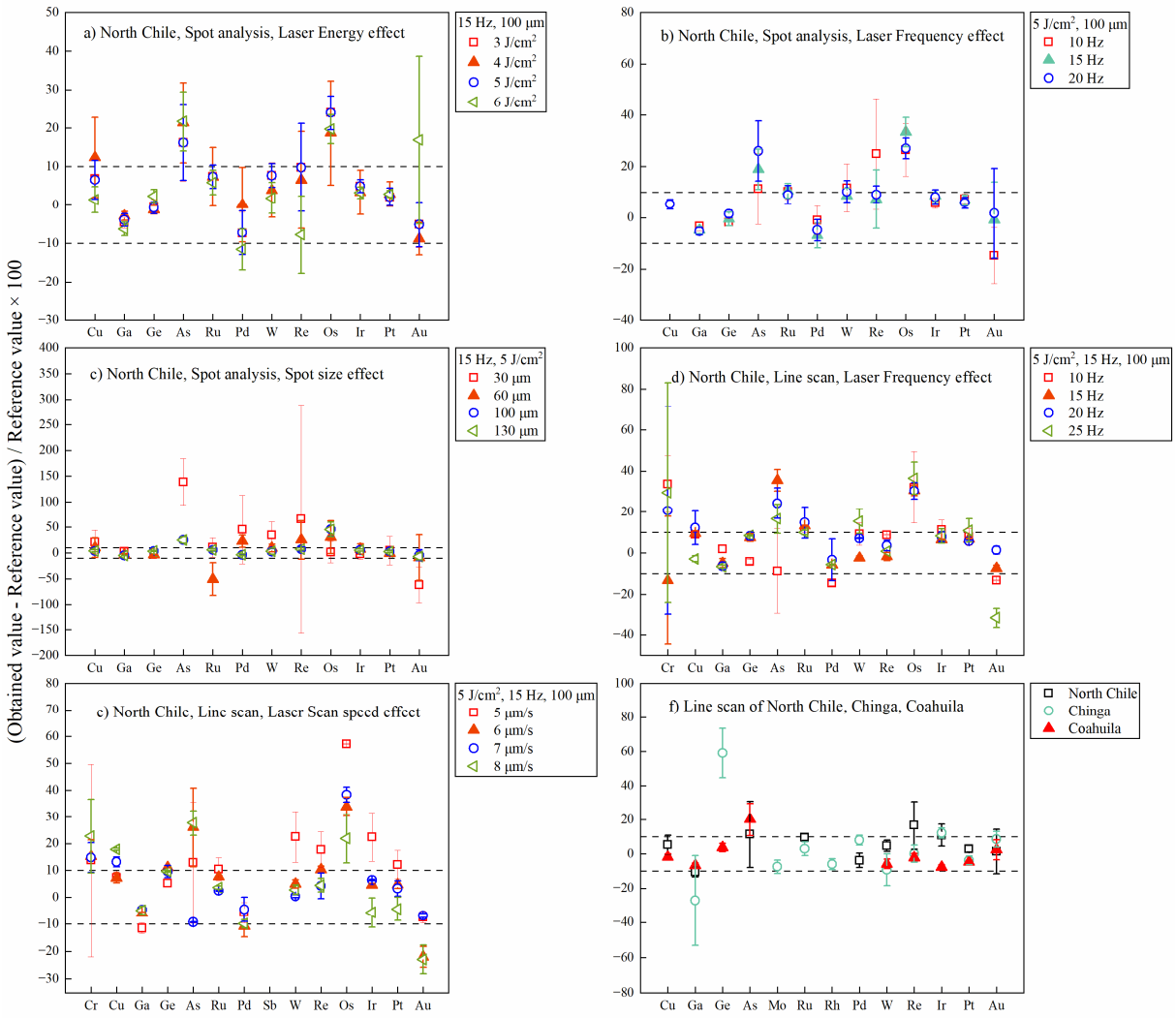

Fig. 3.8-4: Accuracy and precision of chemical analysis represented by the differences in mean composition and one standard deviation of elements with reported bulk compositions obtained by INAA. a.-e. The effects of laser energy, frequency, spot size and scan speed of spot analysis and line scan on the chemical analysis of North Chile were tested sequentially. f. The accuracy and precision of chemical analysis in North Chile, Chinga, Coahuila were determined using the line scan of LA-ICP-MS with 100 µm width, 6 µm/s scan speed, 5 J/cm^2 energy fluence, 20 Hz frequency.

homogeneous Co concentration (1 SD < 5 %) determined using EPMA in the bulk sample. The modal abundances of minerals (kamacite, taenite, phosphides) and their corresponding elemental compositions can be used to calculate an average bulk composition by mass balance.

Overall, the LA-ICP-MS measurements of known iron meteorites show that metal composition for siderophile elements can be accurately determined by laser ablation ICP-MS analysis and that classification of unknown samples is possible when combined with mineralogy and multi-phase analysis.

Table 3.8-3. Mean composition of the North Chile meteorite was analysed using a line scan and spot analysis of LA-ICP-MS compared with the values reported by INAA in a previous study. Sb content in North Chile using line scan is lower than the measured D.L. of 0.05 μg/g in NIST610, thus no RSD of Sb is given here.

North Chile	Cr	Cu	Ga	Ge	As	Ru	Pd	W	Re	Os	Ir	Pt	Au
INAA	46	130	59	176	4.7	18	1.85	2.6	0.22	1.00	3.4	22	0.62
LA-ICP-MS Spot analysis													
Average (μg/g)	52	473	66	184	5.8	17	1.5	2.7	0.23	1.3	3.5	23	0.63
RSD (%)	53	67	71	28	16	36	38	5	11	8	3	4	5
D.L. (μg/g)	0.25	1.4	0.03	0.25	0.21	0.06	0.03	0.03	0.08	0.01	0.01	0.01	0.03
LA-ICP-MS Line scan													
Average (μg/g)	63	137	53	189	5.3	19	1.8	2.7	0.26	1.7	3.7	22	0.63
RSD (%)	31	5	3	3	17	2	4	3	12	26	6	2	13
D.L. (μg/g)	0.13	0.12	0.02	0.1	0.58	0.07	0.04	0.02	0.25	0.03	0.01	0.04	0.01

e. *Installation of a MAR345 detector in the coupled X-ray – Brillouin system for density measurements at simultaneous high pressures and temperatures (A. Kurnosov and T. Boffa Ballaran)*

In recent years, significant efforts have been made to install a CO_2 laser heating system to perform high-pressure/-temperature Brillouin scattering measurements to constrain the acoustic wave velocities of minerals under mantle conditions (see Annual Reports 2021-2023). However, in order to obtain self-consistent data, it is important to be able to measure the density of the material under investigation under the same conditions where acoustic wave velocities are obtained. At room temperature, density is typically measured by X-ray diffraction under the same pressure conditions as for Brillouin scattering by centering multiple single crystal reflections at eight different positions with a point detector. Due to the limitation of the CO_2 laser system, whose light path needs to be enclosed either in a flexible hollow silica waveguide or in an articulated arm containing junctions in which mirrors are mounted to direct the laser to the exit point close to the diamond anvil cell containing the sample, this eight-position centring is not possible because the sample would not be homogeneously heated during all the necessary movements around the four circles of the diffractometer. The use of a 2D detector instead of the point detector would allow several sample reflections to be measured at a given position, reducing the need for large movement of the diamond anvil cell to cover sufficient *d*-spacing for accurate (albeit less precise) density determination.

A MAR345 image plate detector was chosen for its large active area and high resolution. Thanks to the large active area, the detector was installed at a distance of 410 mm from the centre of the diffractometer (Fig. 3.8-5), leaving enough space around the sample for the incident lens of the Brillouin scattering system and the power meter of the CO_2 laser system. In this way, a

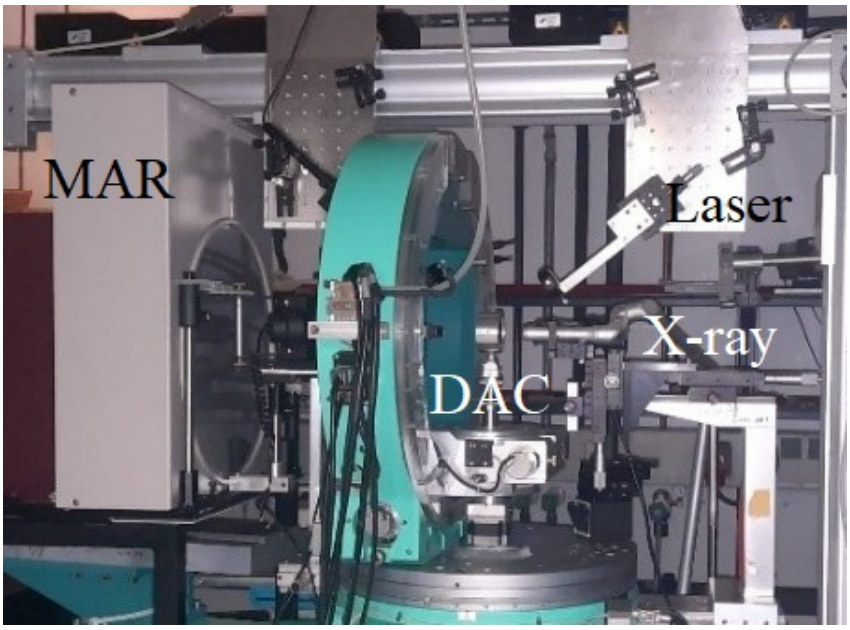

Fig. 3.8-5: MAR345 detector mounted on the 2Θ arm of the four-circle diffractometer behind the incident lens of the Brillouin system. The photo also shows the diamond anvil cell (DAC) mounted on the diffractometer and the final junction of the articulated arm of the CO_2 laser system.

resolution of about 1.6 Å can be achieved without moving the detector. The MAR345 software is used to acquire XRD images and control the shutter, whereas the rotation of the sample (φ circle) is controlled by the SPEC software installed on the same Linux-based PC. We have written a SPEC script that synchronises both devices. In this way, the images can be acquired and saved at any pre-defined φ angle range and step size according to the experimental strategy. A calibration procedure similar to those developed at synchrotron beam lines has been used to calibrate the detector distance and tilt. First, a few mg of a powdered LaB_6 standard have been placed in a 250 µm hole of a 40 µm thick metallic glass gasket, and a wide scan image has been collected by rotating the φ circle between -10° and +10°. The standard powder diffraction pattern has then been used to determine the sample-to-detector distance and detector tilt. Second, the diffraction (Fig. 3.8-6) of a YLID (2-dimethylsufuranylidene-l,3-indanedione) single-crystal standard with orthorhombic symmetry has been used to refine the detector and goniometer parameters in the CrysalisPro programme, which will be used to integrate the intensity data and calculate the unit-cell lattice parameters of the materials under investigation at high pressure and high temperature. The calibration obtained in this way has been tested on a pyrope single crystal placed in a diamond anvil cell without a pressure medium. The unit-cell parameters and volume of this pyrope crystal, determined using 30 reflections collected in a φ rotation between -30° and +30°, are in excellent agreement with those collected for the same sample using the eight-position centring method, although the uncertainties are one order of magnitude larger. Further work is being carried out to test the MAR345 detector with a sample heated at high pressure using a CO_2 laser.

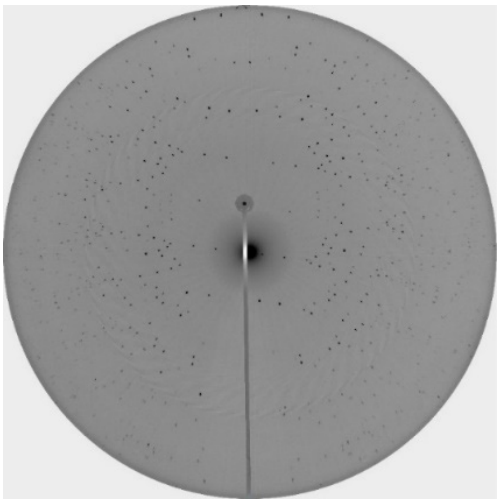

Fig. 3.8-6: Wide scan construction of the step scans (0.5° rotation of the phi circle) collected for the Ylid standard single crystals. More than 700 reflections could be integrated and have been used to calibrate the detector and goniometer parameters in CrysalisPro.

f. *A method for high-pressure fluid-rock permeability measurements using* in situ *X-ray determinations of fluid overpressures (M. Pöppelbaum, D.J. Frost, T. Boffa Ballaran, L. Man and D.S. Souza, in collaboration with R. Farla/Hamburg)*

Subduction-related fluids released into the overlying mantle wedge are responsible for the metasomatic signature and large degrees of partial melting attributed to arc magmas. However, the fluid flow mechanisms and timescales from the subducting slab through the mantle wedge to the arc magma source region are poorly understood. An important question is whether fluid flow is likely to be per or channelled or whether fluid flow is so slow that it is trapped in the subducted slab. This uncertainty is due to the difficulty in measuring the permeability of key rock types under high-pressure conditions. Permeability measurements require not only a method to measure the fluid flux but also to constrain the pressure difference that drives the flow. We have developed a method to measure fluid flux by examining the extent of the transformation of MgO to brucite as H_2O passes through a layer of hot-pressed mineral. However, in order to constrain the pressure difference between the source and sink of H_2O we have conducted high-pressure, high-temperature experiments at the large-volume press beamline P61B of the Petra III Synchrotron (DESY) in Hamburg.

The experiments were conducted using 12/9 (cube edge length/anvil truncation length) cubic assemblies with the 'Aster-15' six-ram press at P61B. In the experiment, a fluid source (serpentine) is dehydrated, which produces an overpressure due to the volume change of the reaction. The resulting fluid passes through a sample core of hot-pressed olivine with a known grain size. When the fluid emerges on the other side of the olivine it passes into a layer of MgO, which then transforms to brucite. The sample layers are placed in a cylindrical capsule made from a single crystal of olivine (Fig. 3.8-7) with a lid. The serpentinite and MgO were mixed with 5 % of Au and Pt as pressure markers, respectively. Experimental conditions were ~ 2.5 GPa and 700 °C. During the experiment, the pressures in all layers were monitored by collecting X-ray powder diffraction from Au, Pt, olivine and MgO. Pressures outside of the capsule were also monitored using diffraction from MgO.

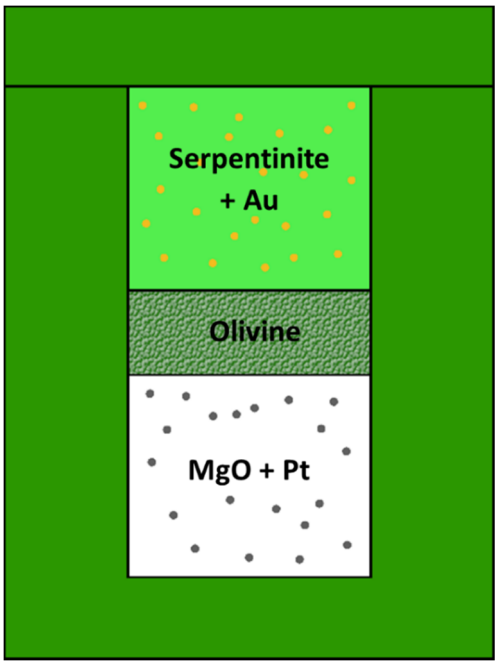

Fig 3.8-7: Schematic of a cylindrical single crystal olivine capsule with an outer diameter of 3 mm, showing the fluid source and sink layers on either side of a hot-pressed olivine core. The serpentine fluid source is mixed with fine Au powder. As the serpentine decomposes, fluid is released and passes through the olivine core near the centre of the capsule. When it reaches the other side of the olivine sample, it reacts with MgO to form brucite. The thickness of the brucite layer is measured after the experiment. The MgO is mixed with Pt so that the pressure difference can be determined from *in situ* X-ray diffraction measurements of the Au and Pt unit cells.

During the initial compression of the experiments at room temperature, no pressure was transmitted through the capsule to the sample layers. While the pressure measured using the MgO outside the capsule reached approximately 1.7 GPa, the pressure inside the capsule was closer to ambient pressure (Fig. 3.8-8).

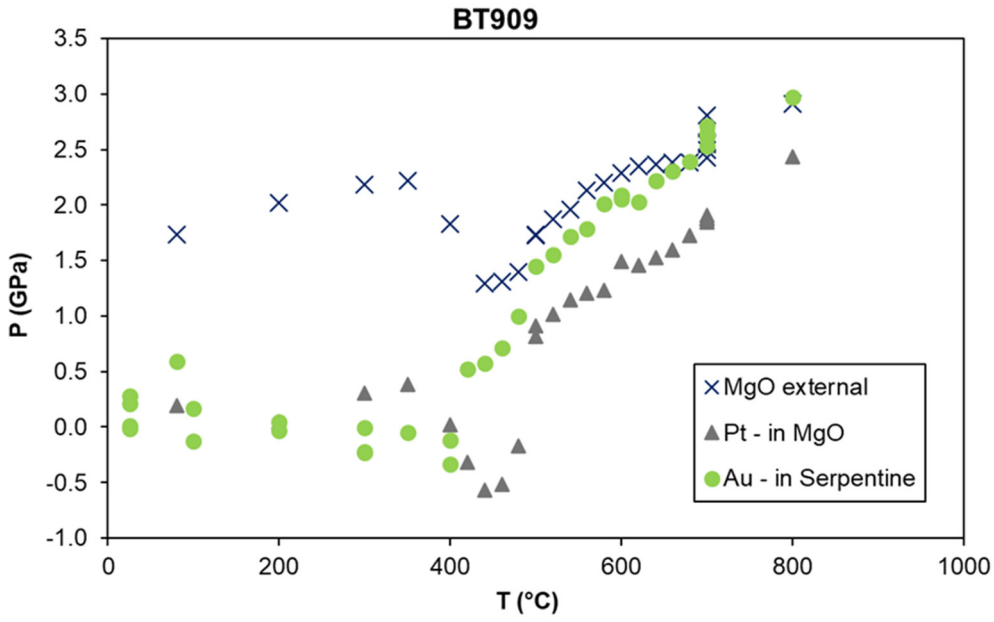

Fig. 3.8-8: Pressures measured in different layers of the experiment as a function of temperature during heating to 800 °C. The crosses indicate the pressure outside (external) of the capsule. Pt – in MgO indicates pressures measured using the Pt equation of state in the MgO fluid sink layer and Au- in serpentinite are pressures in the serpentine fluid source layer measured using Au.

The clearly very strong olivine single crystal capsule blocked the samples from the applied force. As the experiment was heated, the pressure in the layers did not increase initially. In fact, it appeared to become negative up to 400 °C. This might result from the anisotropic thermal expansion of olivine or from differences in thermal expansion between the capsule and the MgO layer inside. On the other hand, it cannot be explained by uncertainties in either temperature or the equations of state employed. The low pressures inside the capsule resulted in the serpentine starting to dehydrate above 400 °C. This caused the pressure in the serpentinite layer, measured using Au, to increase with increasing temperature. The pressure in the MgO layer below the polycrystalline olivine also started to increase but always lagged behind that in the serpentinite layer. This is consistent with an overpressure being maintained in the serpentinite layer due to the volume change of the dehydration reaction. The same behaviour was observed in three experiments, including one "blank" experiment where the serpentinite was replaced by another MgO layer. In the "blank" experiment, the pressure inside the capsule only started to increase above 600 °C, possibly due to the yielding of the olivine capsule.

The pressure difference between the serpentinite and MgO layers was the largest, ~ 1.23 GPa, at 440-480 °C, which is in good agreement with the theoretical fluid overpressure value of ~ 1.1 GPa, which can be calculated based on the volume change. The pressure difference decreased slightly at higher temperatures but was still maintained at the final temperature of 700 °C, where the experiments were paused for periods of up to an hour to allow water to pass through the polycrystalline olivine sample. Imaging of the recovered samples showed that a thin brucite layer was formed between the olivine sample and the MgO layer (Fig. 3.8-9a,b), indicating that fluid flow occurred through the olivine core. However, there are also cracks around the olivine sample that channelled fluid during the experiment and allowed it to reach the base of the MgO sink layer (Fig. 3.8-9a,c). The amount of brucite formed as a result of this channelled flow is 6 times that formed by pervasive flow through the hot-pressed olivine sample.

Using Darcy's law with the *in situ* determined pressure difference between the source and sink and the fluid flux estimated from the brucite layer thickness, a time-averaged permeability of 5.3×10^{-21} m² can be calculated for the polycrystalline olivine sample. This is in the range where fluid flow is dominated by grain boundary diffusion, but it is also in agreement with some extrapolated estimates of permeability under high-pressure conditions.

In conclusion, it is possible to use *in situ* X-ray diffraction to measure an overpressure created by a dehydration reaction. This overpressure is maintained in the multianvil apparatus for sufficient time to allow a fluid flow through a hot-pressed rock sample. However, the use of an outer single-crystal capsule created unexpected complications in the current experiments, which demonstrate the very high strength of olivine at low temperatures. Both channelled and permeable fluid flow were observed in the experiments. The permeability calculated for permeable flow through the olivine sample would effectively isolate fluids in the subducting lithosphere. Much faster-channelled flow might be promoted in the Earth, as observed in these experiments, by differences in strength between olivine and other mineral phases.

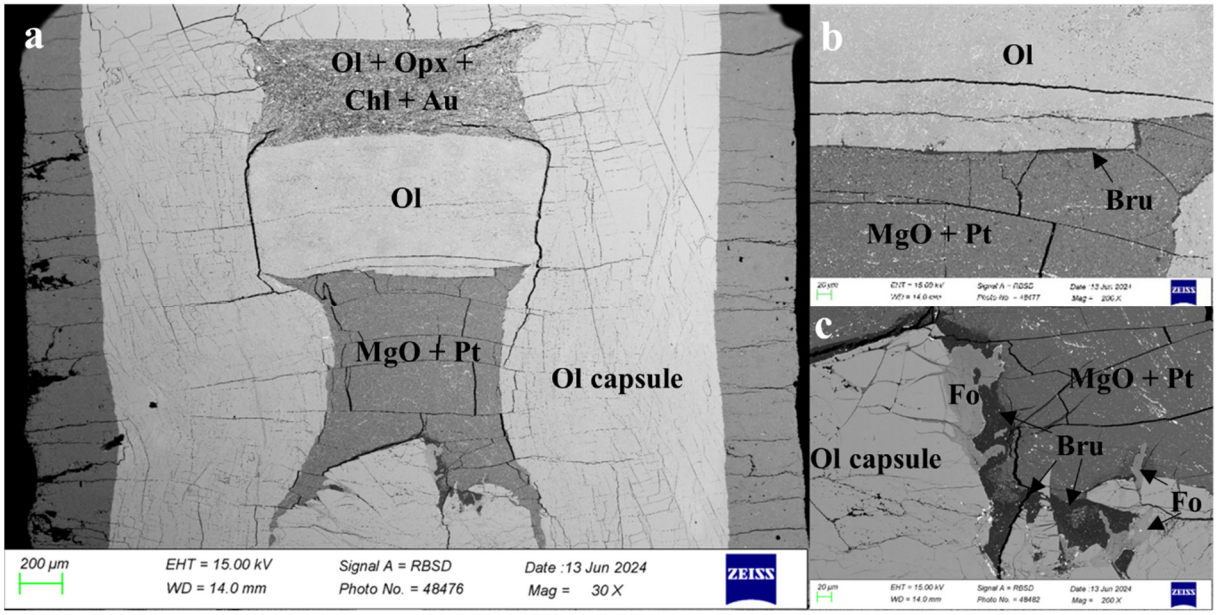

Fig. 3.8-9: Scanning electron microscope images of a polished recovered sample. a) The outer deformed olivine capsule contains a dehydrated olivine layer at the top, followed by a hot-pressed olivine cylinder and a MgO sink layer below. A small brucite layer below the olivine cylinder can be seen in the enlargement shown in b). Cracks on either side of the olivine cylinder were formed during the experiment, allowed water to be transferred to the bottom of the MgO layer, forming a brucite layer shown in c).

g. *Accurate liquidus determination in complex Fe-Ni-Si-S system using ultrafast 3D microtomography in the UToPEC (R. Pierru, in collaboration with L. Henry, S. Pandolfi, I. Blanchard, N. Guignot, D. Antonangeli and G. Morard/Paris)*

The cores of terrestrial planets are mainly composed of iron alloy with nickel and lighter elements such as S, C, O, Si and H. Although the core could remain in a liquid state for billions of years after the initial planetary differentiation, crystallisation inevitably takes place (or will take place) over time as a direct consequence of secular cooling. Crystallisation releases light elements that are incompatible with the solid, and this is generally thought to be one of the main driving forces behind the dynamo effect and, hence, the magnetic field. Understanding the solid-liquid element partitioning during core crystallisation as a function of composition, pressure (P) and temperature (T) is fundamental to constraining the dynamics taking place in planetary cores. For instance, the shape of the liquidus in the binary Fe-S system has been extensively studied, and its non-ideal shape is at the origin of proposed models of planetary cores, arguing for either stratification (*e.g.*, Mars) or extremely complex dynamics (*e.g.*, Ganymede), depending on the size and composition of the planet. Building on the established Fe-S system, we aim to add Ni and Si to determine how the inclusion of other elements changes this non-ideal shape. For example, recent cook-and-look studies have shown that Ni can strongly influence the liquidus temperature. As planetary cores are complex chemical systems, it is essential to characterise the effect of light elements such as C or S in addition to Ni. The

conventional approach to determining the liquidus shape in iron alloy phase diagrams relies on post-analysis of quench products. However, this approach is expensive and time-consuming but has limitations in accurate *P-T* measurement.

The *in situ* experiment in a Paris-Edinburgh press has become feasible at the Psiché beamline of the SOLEIL synchrotron. Fe-Ni-Si-S samples were compressed to target pressures between 1.5 and 5 GPa and heated to 2000 K. Tomography and XRD were recorded every 30 K around the initial melting, giving us several points to determine the liquidus shape for a few hours. This would take several days using a conventional quenching method. The eutectic melting can be clearly observed by both XRD based on the appearance of diffuse scattering and 3D tomography. When the sample is completely molten, measurements of density and liquid structure can be made using X-ray absorption (Beer-Lambert law) and combined angle and energy dispersive X-ray diffraction (CAESAR). We compared the analyses of the recovered sample using 3D volume reconstruction and in-house scanning electron microscopy (SEM) on a polished cross section. This comparison confirmed similar shapes observed by these methods. By knowing the starting chemistry, the proportion of liquid can be confirmed by mass balance using quantitative chemical measurement. In addition, backscattered electron images can also give us an estimate by pixel analysis.

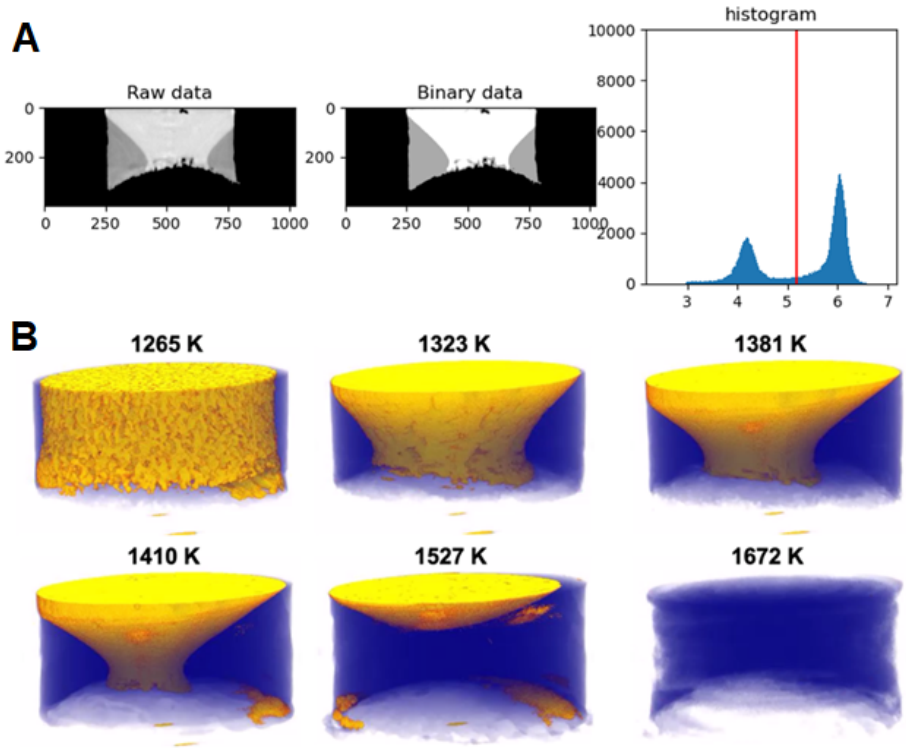

Fig 3.8-10: A) Example of a processed 3D volume. (Left) vertical slice before quenching, (middle) binary data from multi-Otsu thresholding and (right) histogram of the total volume after the first thresholding of the environment. B) Change of the solid/liquid fractions during heating after thresholding. Blue and yellow represent the liquid and solid portions, respectively.

In conclusion, we established a benchmark of the technique of 3D reconstruction of the liquid/solid fraction at high pressures and temperatures. This highlights the feasibility of the experimental approach for quantitative measurements of liquidus shape using 3D tomography under high pressure. The methodological approach for *in situ* quantitative determination of liquidus shape for Fe alloys under high pressure has been successfully established.

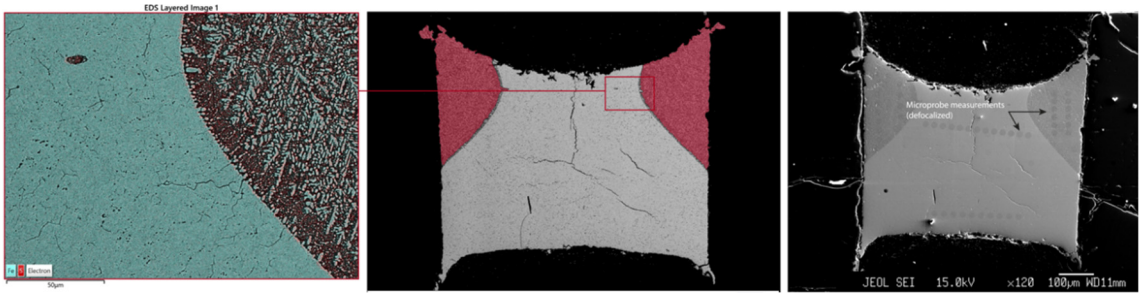

Fig. 3.8-11: SEM analysis of a recovered sample. (Left) Chemical mapping of the sample at the solid-liquid interface; (middle) BSE image of the sample, the red part represents the liquid; (right) BSE image of the sample showing the different zones measured by the microprobe.

h. *Quantifying friction corrections and temperature gradients in piston-cylinder experiments by means of synthetic fluid inclusions and mineral solubility maps (A. Minchenkova and A. Audétat)*

In piston-cylinder experiments, precise pressure and temperature control are essential for understanding phase stability and reaction kinetics in geological materials. In this project, we assessed the use of synthetic fluid inclusions as a method for quantifying friction corrections, alongside calibrating a pure MgO assembly at pressures from 6 to 20 kbar and temperatures from 700 to 1400 °C. Additionally, a novel temperature-mapping approach was developed, extending a previous approach whose application was limited to temperatures above 1100 °C.

To assess the suitability of synthetic fluid inclusions as recorders of pressure and temperature conditions, we first conducted a series of tests in NaCl assemblages, which exhibit zero friction and thus provide a baseline. These tests addressed two potential problems: (1) the risk of changes in the density of the trapped fluid due to precipitation of host material dissolved at high *P-T*, and (2) the bias towards the early stages of the experiments if the fluid inclusions form early and are not able to adapt to changes in pressure due to decreasing friction.

To assess whether density changes occur in synthetic fluid inclusions due to precipitation of host minerals dissolved at high *P-T*, we synthesised a series of aqueous fluid inclusions quartz at P-T conditions where the SiO_2 solubility in H_2O ranged from 3.1 to 12.4 wt. %. Surprisingly, in all three cases, the H_2O densities determined in the fluid inclusions agreed within 1-3 % of the theoretical values, suggesting that dissolution of up to 12.4 wt. % SiO_2 in the fluid does not significantly affect the fluid density in synthetic fluid inclusions produced under these conditions.

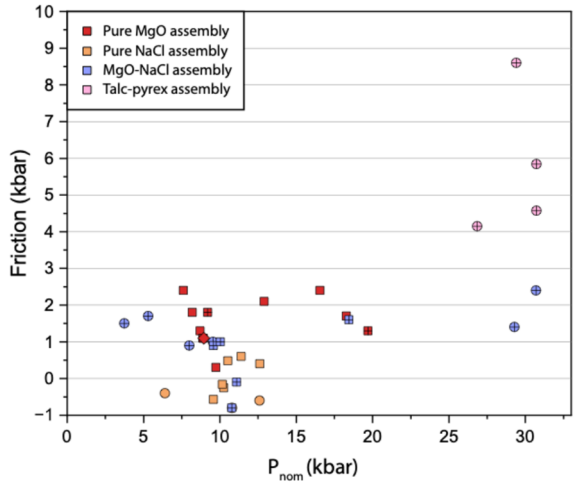

Fig. 3.8-12: Friction correction as a function of nominal pressure. The colour scheme represents different types of assemblies, while the marker shapes indicate the minerals used in the experiments: squares for corundum, circles for quartz, and diamonds for garnet. Open markers correspond to results obtained in this study, while markers with a cross represent previous results from other students at BGI.

To test the adaptability of the fluid inclusions to pressure changes during the experiment, two-step pressure experiments were conducted: one involving a 2 kbar pressure increase, and the other involving a 2 kbar pressure decrease. The results revealed significant differences between corundum and quartz as host minerals. Fluid inclusions hosted in corundum showed a lower ability to adapt to pressure changes than fluid inclusions hosted in quartz. However, in neither mineral, they adapted fully to the final pressure, with 0.5-1.0 kbar discrepancy remaining in both cases. This suggests that synthetic fluid inclusions may not record the final *P*-*T* conditions if the friction considerably changes during the experiment.

The pressure calibration of the pure MgO assembly was conducted in 10 experiments over a *P*-*T* range of 6-20 kbar and 700-1400 °C (Fig. 3.8-12), with corundum and quartz as the primary host minerals for the synthetic fluid inclusions. The use of a graphite foil surrounding the assembly resulted in significantly reduced friction compared to previous experiments conducted using MoS_2 paste. The results revealed surprisingly constant absolute frictions of 1.9±0.6 kbar over the entire range of investigated *P*-*T* conditions (Fig. 3.8-12; excluding one outlier), suggesting that the pure MgO assembly is highly suitable for high-precision piston-cylinder experiments up to very high temperatures.

Temperature gradients within sample capsules have previously been mapped by measuring the solubility of titanite in small pools of synthetic sodium–aluminium–silicate melt. Since this approach is limited to temperatures above ~ 1100 °C, we developed an alternative approach based on the solubility of rhodonite in hydrous rhyolite. This approach is more cost-effective and can be applied over a broader temperature range. It can be used with any perfectly glassy obsidian, and when H_2O is added, it avoids the crystallisation problem faced in other systems when working at relatively low temperatures.

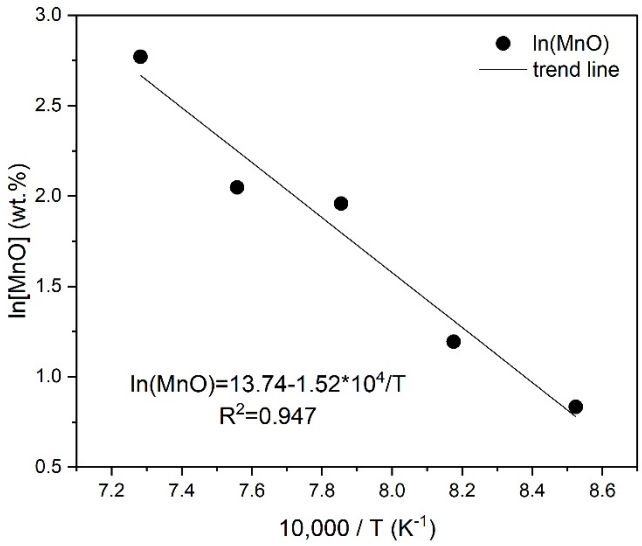

Fig. 3.8-13: Rhodonite solubility (wt. % MnO) in hydrous rhyolite melt as a function of temperature.

We performed five experiments from 900 to 1100 °C at 50 °C intervals to calibrate the temperature dependence of rhodonite solubility in a natural rhyolite melt with 8 wt. % H_2O added (Fig. 3.8-13). In the same experiments, we mapped the temperature gradients within sample capsules contained in two MgO-NaCl assemblies, two pure MgO assemblies, and one talc-pyrex assembly. The results reveal relatively small and reproducible temperature gradients

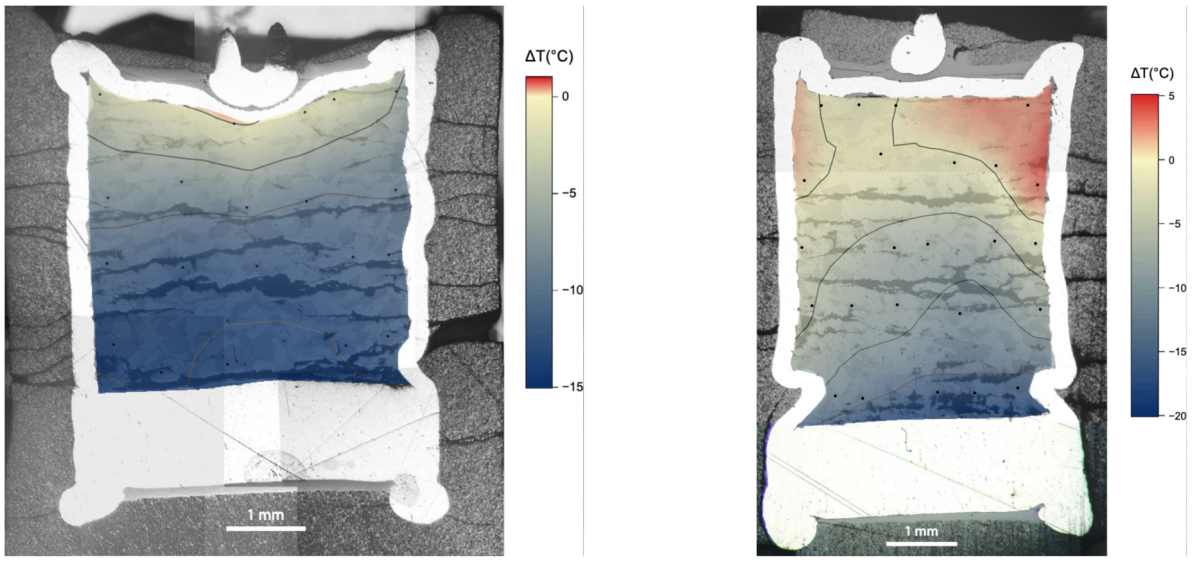

Fig. 3.8-14: Reflected-light images of two sample capsules taken from (left) a pure MgO assembly at 900 °C and 10 kbar, and (right) from a MgO-NaCl assembly at 950 °C and 10 kbar, with the measurement points and corresponding temperature distribution superimposed in a semi-transparent layer. The very dark features are cracks, the medium grey areas within the sample capsules are melt pools, and the lighter grey rest is rhodonite.

in all cases, ranging from 16 °C to 24 °C along the length of the capsules (Fig. 3.8-14). The reproducibility of the results suggests that the approach is robust and adaptable, suitable for both high- and low-temperature piston-cylinder assemblies.

i. *A new fragmentation apparatus for andesitic and basaltic magmas (H. Keppler and D. Di Genova)*

Magma fragmentation – the brittle failure of magma in response to high stress and strain rates – is an important process behind explosive volcanic eruptions. Whether fragmentation occurs depends on the properties of the silicate melt phase, the oversaturation with volatiles, and possibly also on the formation of nanolites during cooling and decompression. Due to technical limitations, these processes can only be studied at relatively low temperatures, which may be realistic for very silicic magmas. The more common eruptions of andesitic and basaltic magmas occur at temperatures beyond the capabilities of current experimental facilities.

To study magma fragmentation in andesitic and basaltic magmas, a new apparatus has been developed and built at the Bayerisches Geoinstitut (Fig. 3.8-15). The core of the apparatus is an autoclave made of titanium-zirconium-molybdenum alloy (TZM), surrounded with a tightly fitting steel jacket to protect it from contact with air. The autoclave allows experiments at 1100 °C and 1200 °C at 1 kbar and 500 bar, respectively, which is sufficient to cover typical

Fig. 3.8-15: A new apparatus for studying magma fragmentation in andesitic and basaltic systems. A TZM alloy autoclave is located inside the furnace (red). Both ends of the autoclave are water-cooled. At the top of the autoclave (above the furnace) is a ruptured disc that will fail at a pre-determined pressure. Material erupted from the autoclave is collected in the large tank at the top of the apparatus.

pre-fracturing conditions in andesitic and basaltic systems. Both ends of the autoclave are water-cooled. A device containing a ruptured disc is mounted at the top end. The rupture disc is designed to fail at a pre-determined pressure, causing a small-scale eruption of magma held in the hot part of the vessel. The fragmentation products are collected in the large alumina tank at the top of the apparatus.

j. *GeophysicalModelGenerator.jl: A Julia package to visualise geoscience visualisation and Model generation (B. Kaus/Mainz, M. Thielmann, P. Aellig/Mainz, A. de Montserrat/Zürich, L. de Siena/Bologna, J. Frasunkiewicz/Mainz, L. Fuchs/Frankfurt a. M., A. Piccolo, H. Ranocha/Mainz, N. Riel/Mainz, C. Schuler/Mainz, A. Spang and T. Weiler)*

Geoscience data come in many different formats. However, to achieve a consistent interpretation of a region, it is helpful to visualise different data sets together in the same coordinate system to understand their relationship. Such datasets include seismic tomography, surface geology, topography, Moho depth, earthquake locations, gravity anomalies, GPS surface velocities and others. The lack of a standard format for geoscience data makes this task challenging. Seismic tomography, for example, may be in the form of ASCII data with lon/lat/depth axes or as NetCDF files, with the order of the data typically varying from one dataset to another.

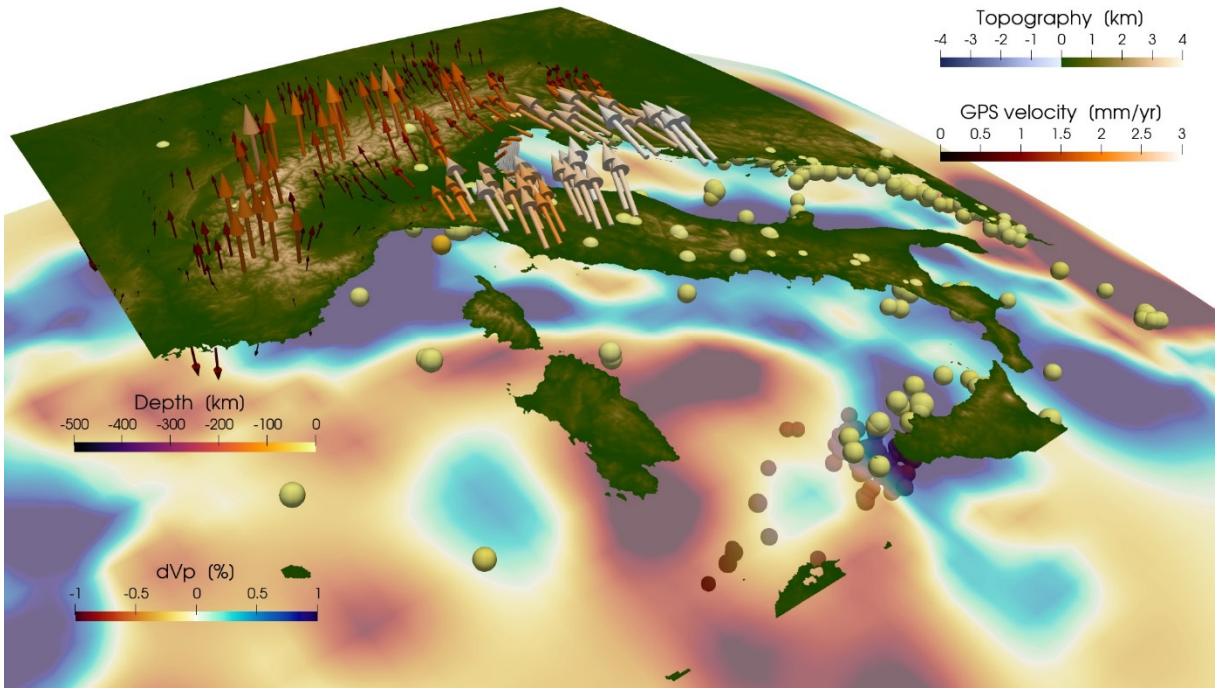

Fig. 3.8-16: Integration of various geoscience datasets. Visualisation of topography, GPS velocity, Vp tomography, Moho depth and earthquake locations within a unified coordinate system.

If one wishes to create mechanical or thermo-mechanical numerical models of the region, it is essential to create an input setup that respects these constraints. And since most numerical codes operate in Cartesian boxes, it is helpful to have tools to project the data from geographic to Cartesian coordinates. Even after combining a variety of data sets into one coordinate system and projecting them into Cartesian coordinates, it is usually not possible to use the same software to create 2D and 3D input models for geodynamic codes.

This project was a collaborative effort to create a single software package that can simplify the collection, conversion, projection and joint visualisation of different geoscientific data sets and the creation of input geometries for geodynamic models. The GeophysicalModelGenerator.jl package is written in the Julia programming language, open source and compatible with Windows, Mac and Linux systems. Output files can be visualised in Paraview and used by the geodynamics code LaMEM, both of which are also open source. Examples are shown in Figure 3.8-16.

4. Publications, Conference Presentations, Seminars

4.1 Publications (published)

Supplement to **2023** (papers published at the end of 2023):

LANIEL, D.; TRYBEL, F.; ASLANDUKOV, A.; KHANDARKHAEVA, S.; FEDOTENKO, T.; YIN, Y.Q.; et al. (2023): Synthesis of ultra-incompressible and recoverable carbon nitrides featuring CN_4 tetrahedra. Adv. Mat. 36(3), 2308030, https://doi.org/10.1002/adma.202308030

NAKANISHI, N., *et al.* with the Hayabusa2 Initial Analysis Chemistry Team (including BOUVIER, A.) (2023): Nucleosynthetic s-process depletion in Mo from Ryugu samples returned by Hayabusa2. Geochem. Persp. Lett. 20, 31-36, https://doi.org/10.7185/geochemlet.2341

2024

a) Refereed international journals

AKBAR, F.I.; ASLANDUKOVA, A.; YIN, Y.; ASLANDUKOV, A.; LANIEL, D.; BYKOVA, E.; BYKOV, M.; LAWRENCE BRIGHT, E.; WRIGHT, J.; COMBONI, D.; HANFLAND, M.; DUBROVINSKAIA, N.; DUBROVINSKY, L. (2024): High-pressure dysprosium carbides containing carbon dimers, trimers, chains, and ribbons. Carbon 228, 119374, https://doi.org/10.1016/j.carbon.2024.119374

ALÉON, J., *et al.* with the Hayabusa2 Initial Analysis Chemistry Team (including BOUVIER, A.) (2024): Hydrogen in magnetite from asteroid Ryugu. Meteorit. Planet. Sci. 59, 2058-2072, https://doi.org/10.1111/maps.14139

ARENAS, R.; FUENLABRADA, J.M.; TIMONER, C.; FERNÁNDEZ, R.D.; ROJO-PÉREZ, E. (2024): Frontier of the Paleo-Tethys Ocean in the western Mediterranean: Isotopic (Sm-Nd) constraints on sources of Devonian units from Menorca Island. Geoscience Frontiers 15(5), 101865, https://doi.org/10.1016/j.gsf.2024.101865

ASLANDUKOV, A.; LIANG, A.; EHN, A.; TRYBEL, F.; YIN, Y.; ASLANDUKOVA, A.; AKBAR, F.I.; RANIERI, U.; SPENDER, J.; HOWIE, R.T.; LAWRENCE BRIGHT, E.; WRIGHT, J.; HANFLAND, M.; GARBARINO, G.; MEZOUAR, M.; FEDOTENKO, T.; ABRIKOSOV, I.A.; DUBROVINSKAIA, N.; DUBROVINSKY, L.; LANIEL, D. (2024): Synthesis of $LaCN_3$, $TbCN_3$, $CeCN_5$, and $TbCN_5$ polycarbonitrides at megabar pressures. J. Am. Chem. Soc. 146(26), 17531-18186, https://doi.org/10.1021/jacs.4c06068

ASLANDUKOV, A.; ASLANDUKOVA, A.; LANIEL, D.; KHANDARKHAEVA, S.; YIN, Y.; AKBAR, F.I.; CHARITON, S.; PRAKAPENKA, V.; LAWRENCE BRIGHT, E.; GIACOBBE, C.; WRIGHT, J.; COMBONI, D.; HANFLAND, M.; DUBROVINSKAIA, N.; DUBROVINSKY, L. (2024): Stabilization of N_6 and N_8 anionic units and 2D polynitrogen layers in high-pressure scandium polynitrides. Nat. Commun. 15, 2244, https://doi.org/10.1038/s41467-024-46313-9

ASLANDUKOVA, A.; ASLANDUKOV, A.; AKBAR, F.I.; YIN, Y.; TRYBEL, F.; HANFLAND, M.; PAKHOMOVA, A.; CHARITON, S.; PRAKAPENKA, V.; DUBROVINSKAIA, N.; DUBROVINSKY, L. (2024): High-pressure *oC*16-YBr_3 polymorph recoverable to ambient conditions: From 3D framework to layered material. Solids, 63(34), 15611-15618, https://doi.org/10.1021/acs.inorgchem.4c00813

ASLANDUKOVA, A.; ASLANDUKOV, A.; LANIEL, D.; YIN, Y.; AKBAR, F.I.; BYKOV, M.; FEDOTENKO, T.; GLAZYRIN, K.; PAKHOMOVA, A.; GARBARINO, G.; LAWRENCE BRIGHT, E.; WRIGHT, J.; HANFLAND, M.; CHARITON, S.; PRAKAPENKA, V.; DUBROVINSKAIA, N.; DUBROVINSKY, L. (2024): Diverse high-pressure chemistry in Y-NH_3BH_3 and Y–paraffin oil systems. Sci. Adv. 10(11), eadl5416, https://doi.org/10.1126/sciadv.adl5416

ATKINSON, A.J.; BOFFA BALLARAN, T.; CARPENTER, M.A. (2024): Local strain heterogeneity associated with Al/Si ordering in anorthite, $CaAl_2Si_2O_8$, with implications for thermodynamic mixing behavior and trace element partitioning in plagioclase feldspars. Am. Mineral. 109, 1292-1302, https://doi.org/10.2138/am-2023-9197

BYSTRICKY, M.; LAWLIS, J.; MACKWELL, S.; HEIDELBACH, F. (2024): High-temperature deformation of enstatite-olivine aggregates. J. Geophys. Res. Solid Earth 129(3), e2023JB027699, https://doi.org/10.1029/2023JB027699

CHANG, J.; AUDÉTAT, A.; PETTKE, T. (2024): The gold content of mafic to felsic potassic magmas. Nat. Commun. 15, 6988, https://doi.org/10.1038/s41467-024-51405-7

CHANYSHEV, A.; MARTIROSYAN, N.; WANG, L.; CHAKRABORTI, A.; PUREVJAV, N.; WANG, F.; KIM, E.J.; TANG, H.; FEDOTENKO, T.; BHAT, S.; FARLA, R.; KATSURA, T. (2024): Thermal equation of state of cubic silicon carbide at high pressures. ChemPhysChem 25(9), e202300604, https://doi.org/10.1002/cphc.202300604

CHENG, K.W.; BALLANTYNE, H.A.; GOLABEK, G.J.; JUTZI, M.; ROZEL, A.B.; TACKLEY, P.J. (2024): Combined impact and interior evolution models in three dimensions indicate a southern impact origin of the Martian Dichotomy. Icarus 420, 116137, https://doi.org/10.1016/j.icarus.2024.116137

CHENG, K.W.; ROZEL, A.B.; GOLABEK, G.J.; BALLANTYNE, H.A.; JUTZI, M.; TACKLEY, P.J. (2024): Mars's crustal and volcanic structure explained by southern giant impact and resulting mantle depletion. Geophys. Res. Lett. 51(6), e2023GL105910, https://doi.org/10.1029/2023GL105910

CHRAPPAN SOLDAVINI, B.; MERLINI, M.; GEMMI, M.; PARLANTI, P.; JOSEPH, B.; MILANI, S.; KURNOSOV, A. (2024): New ring-structured high pressure and temperature $CaSiO_3$ polymorph and its stability field. Acta Cryst. A80, e 260, https://doi.org/10.1107/S2053273324097390

CRINITI, G.; BOFFA BALLARAN, T.; KURNOSOV, A.; LIU, Z.; GLAZYRIN, K.; MERLINI, M.; HANFLAND, M.; FROST, D.J. (2024): Thermal equation of state and structural evolution of Al-bearing bridgmanite. J. Geophys. Res. Solid Earth 129(1), e2023JB026879, https://doi.org/10.1029/2023JB026879

FANG, J.; CHOU, I.M.; AUDÉTAT, A.; ZHANG, L. (2024): Quantitative redox measurements for hydrothermal experiments conducted in cold-seal pressure vessels. Chem. Geol. 663, https://doi.org/10.1016/j.chemgeo.2024.122286

FEI, H.; LYU, Y.; WANG, F.; MCCAMMON, C.; KATSURA, T. (2024): The effects of trivalent cations (Al and Fe) on the grain growth rates of bridgmanite. Earth Planet. Sci. Lett. 646, 118983, https://doi.org/10.1016/j.epsl.2024.118983

FEI, H. (2024): Stability of H_2O-rich fluid in the deep mantle indicated by the MgO-SiO_2-H_2O phase relations at 23 GPa and 2000 K. J. Geophys. Res. Solid Earth 129(7), 2024JB029446, https://doi.org/10.1029/2024JB029446

FROSSARD, P.; BONNAND, P.; BOYET, M.; BOUVIER, A. (2024): Role of redox conditions and thermal metamorphism in the preservation of Cr isotopic anomalies in components of non-carbonaceous chondrites. Geochim. Cosmochim. Acta 367, 165-178, https://doi.org/10.1016/j.gca.2023.12.022

FUJITA, W.; NAKAMURA, M.; UESUGI, K.; EICHHEIMER, P.; THIELMANN, M.; GOLABEK, G.J. (2024): Imaging flow focusing and isolation of aqueous fluids in synthetic quartzite: Implications for permeability and retained fluid fraction in deep-seated rocks. Prog. Earth Planet Sci. 11, 40, https://doi.org/10.1186/s40645-024-00632-z

FUKUSHIMA, R.; TSUJIMORI, T.; MIYAJIMA, N. (2024): Simulation of microtextural evolution in omphacite: Ordering transformation kinetics as an archive of convergent margin dynamics. Phys. Earth Planet. Inter. 354, 107227, https://doi.org/10.1016/j.pepi.2024.107227

GIULIANI, G.; DI GENOVA, D.; DI FIORE, F.; VALDIVIA, P.; MOLLO, S.; ROMANO, C.; BOFFA BALLARAN, T.; KURNOSOV, A.; VONA, A. (2024): The effect of carbonate assimilation and nanoheterogeneities on the viscosity of phonotephritic melt from Vesuvius. Chem. Geol. 670, 122408, https://doi.org/10.1016/j.chemgeo.2024.122408

GÖTZE, J.; MACRAY, C.; PAN, Y.; WILSON, N.C.; TORPY, A.; AUDÉTAT, A. (2024): The 450 nm (2.8 eV) cathodoluminescence emission in quartz and its relation to structural defects and Ti contents. Am. Mineral. 109, 122-134, https://doi.org/10.2138/am-2022-8884

HAMMOUDA, T.; FROSSARD, P.; BOYET, M.; BOUVIER, A.; NEWVILLE, M.; LANZIROTTI, A. (2024): Mapping the redox state of the young solar system using ytterbium valence state. Geochim. Cosmochim. Acta 372, 124-133, https://doi.org/10.1016/j.gca.2024.03.018

HU, X.; LI, H.; ZHU, D.; BOUVIER, A.; WU, J.-H.; MENG, Y. (2024): Differentiating Jurassic Cu-, W-, and Sn (–W)-bearing plutons in the Nanling Range (South China): An integrated apatite study. Ore Geol. Rev. 170, 106137, https://doi.org/10.1016/j.oregeorev.2024.106137

HU, Y., *et al.* with the Hayabusa2 Initial Analysis Chemistry Team (including BOUVIER, A.) (2024): Pervasive aqueous alteration in the early Solar System revealed by potassium isotopic variations in Ryugu samples and carbonaceous chondrites: Icarus 409, 115884, https://doi.org/10.1016/j.icarus.2023.115884

HUANG, W.; YANG, Y.; LI, Y.; XU, Z.; YANG, S.; GUO, S.; XIA, Q. (2024): Inefficient nitrogen transport to the lower mantle by sediment subduction. Nat. Commun. 15, 6998, https://doi.org/10.1038/s41467-024-51524-1

HUANG, Y.; OKUMURA, S.; MATSUMOTO, K.; TAKAHASHI, N.; TANG, H.; WU, G.; TSUJIMORI, T.; NAKAMURA, M.; OKAMOTO, A.; LI, Y. (2024): Experimental constraints on serpentinite carbonation in the presence of a H_2O–CO_2–NaCl fluid. Contrib. Mineral. Petrol. 179, 98, https://doi.org/10.1007/s00410-024-02175-4

ISHII, T.; CRINITI, G.; PUREVJAV, N.; KATSURA, T.; OHTANI, E. (2024): Hydrogen partitioning between stishovite and hydrous phase δ: implications for water cycle and distribution in the lower mantle. Prog. Earth Planet. Sci. 11, 10, https://doi.org/10.1186/s40645-024-00615-0

ISHII, T.; SINMYO, R.; KATSURA, T. (2024): Synthesis and crystal structure of ilmenite-type silicate with pyrope composition. Solids 5, 394-403, https://doi.org/10.3390/solids5030026

KATSURA, T. (2024): Preface to 'Lectures on Mineral Physics', Japanese Magazine of Mineralogical and Petrological Sciences 53(1), 230612a, https://doi.org/10.2465/gkk.230612a

KATSURA, T. (2024): Lectures on mineral physics part 1: thermodynamic properties. Japanese Magazine of Mineralogical and Petrological Sciences 53(1), 230612b, https://doi.org/10.2465/gkk.230612b

KATSURA, T. (2024): Lecture on mineral physics part 2: linear elasticity. Japanese Magazine of Mineralogical and Petrological Sciences, 53(1), 231009, https://doi.org/10.2465/gkk.231009

KAUS, B.J.P.; THIELMANN, M.; AELLIG, P.; DE MONTSERRAT, A.; DE SIENA, L.; FRASUKIEWICZ, J.; FUCHS, L.; PICCOLO, A.; RANOCHA, H.; RIEL, N.; SCHULER, C.; SPANG, A.; WEILER, T. (2024): GeophysicalModelGenerator.jl: A Julia package to visualise geoscientific data and create numerical model setups. J. Open Source Softw. 9(103), 6763, https://doi.org/10.21105/joss.06763

KEPPLER, H.; OHTANI, E.; YANG, X. (2024): The subduction of hydrogen: Deep water cycling, induced seismicity, and plate tectonics. Elements 20(4), 229-234, https://doi.org/10.2138/gselements.20.4.229

KHANDARKHAEVA, S.; FEDOTENKO, T.; ASLANDUKOVA, A.; AKBAR, F.I.; BYKOV, M.; LANIEL, D.; ASLANDUKOV, A.; RUSCHEWITZ, U.; TOBECK, C.; WINKLER, B.; CHARITON, S.; PRAKAPENKA, V.; GLAZYRIN, K.; GIACOBBE, C.; LAWRENCE BRIGHT, E.; BELOV, M.; DUBROVINSKAIA, N.; DUBROVINSKY, L. (2024): Extending carbon chemistry at high-pressure by synthesis of CaC_2 and Ca_3C_7 with deprotonated polyacene- and para-poly(indenoindene)-like nanoribbons. Nat. Commun. 15, 2855, https://doi.org/10.1038/s41467-024-47138-2

KITA, N., *et al.* with the Hayabusa2 Initial Analysis Chemistry Team (including BOUVIER, A.) (2024): Disequilibrium oxygen isotope distribution among aqueously altered minerals in Ryugu asteroid returned samples. Meteorit. Planet. Sci. 59, 2097-2116, https://doi.org/10.1111/maps.14163

KOLLER, T.J.; JIN, S.; KROL, V.; AMBACH, S.J.; RANIERI, U.; KHANDARKHAEVA, S.; SPENDER, J.; MCWILLIAMS, S.; TRYBEL, F.; GIORDANO, N.; POREBA, T.; MEZOUAR, M.; KUANG, X.; LU, C.; DUBROVINSKY, L.; DUBROVINSKAIA, N.; HERMANN, A.; SCHNICK, W.; LANIEL, D. (2024): Simple molecules under high-pressure and high-temperature conditions: Synthesis and characterization of α- and β-$C(NH)_2$ with fully sp^3-hybridized carbon. Angew. Chem. Int. Ed. 63(7), e202318214, https://doi.org/10.1002/anie.202318214

KURNOSOV, A.; CRINITI, G.; BOFFA BALLARAN, T.; MARQUARDT, H.; FROST, D.J. (2024): High pressure and high temperature Brillouin scattering measurements of pyrope single crystals using flexible CO_2 laser heating systems. Phys. Chem. Minerals 51, 38, https://doi.org/10.1007/s00269-024-01297-2

LANIEL, D.; TRYBEL, F.; ZHOU, W.; ASLANDUKOV, A.; SPENDER, J.; TASNÁDI, F.; FEDOTENKO, T.; RANIERI, U.; LIANG, A.; ASLANDUKOVA, A.; AKBAR, F.I.; YIN, Y.; CHARITON, S.; PAKHOMOVA, A.; GARBARINO, G.; MEZOUAR, M.; HANFLAND, M.; PRAKAPENKA, V.; ABRIKOSOV, I.A.; DUBROVINSKY, L.; DUBROVINSKAIA, N. (2024): High-pressure synthesis of *oP*28-C_3N_4 recoverable to ambient conditions. Adv. Funct. Mater. 2416892, https://doi.org/10.1002/adfm.202416892

LI, X.; BYKOVA, E.; VASIUKOV, D.; APRILIS, G.; CHARITON, S.; CERANTOLA, V.; BYKOV, M.; MÜLLER, S.; PAKHOMOVA, A.; AKBAR, F.I.; MUKHINA, E.; KANTOR, I.; GLAZYRIN, K.; COMBONI, D.; CHUMAKOV, A.I.; MCCAMMON, C.; DUBROVINSKY, L.; SANCHEZ-VALLE, C.; KUPENKO, I. (2024): Monoclinic distortion and magnetic transitions in FeO under pressure and temperature. Commun. Phys. 7, 305, https://doi.org/10.1038/s42005-024-01797-1

LI, Y. (2024): The origin and evolution of Earth's nitrogen. National Science Review 11(6), nwae201, https://doi.org/10.1093/nsr/nwae201

LIANG, A.; OSMOND, I.; KRACH, G.; SHI, L.-T.; BRÜNING, L.; RANIERI, U.; SPENDER, J.; TASNADI, F.; MASSANI, B.; STEVENS, C.R.; MCWILLIAMS, R.S.; LAWRENCE BRIGHT, E.; GIORDANO, N.; GALLEGO-PARRA, S.; YIN, Y.; ASLANDUKOV, A.; AKBAR, F.I.; GREGORYANZ, E.; HUXLEY, A.; PEÑA-ALVAREZ, M.; SI, J.-G.; SCHNICK, W.; BYKOV, M.; TRYBEL, F.; LANIEL, D. (2024): High-pressure synthesis of ultra-incompressible, hard and superconducting tungsten nitrides. Adv. Funct. Mater., 34(32), 2313819 https://doi.org/10.1002/adfm.202313819

LIBON, L.; SPIEKERMANN, G.; BLANCHARD, I.; KAA, J.M.; DOMINIJANNI, S.; FÖRSTER, M.; SIEBER, M.J.; ALBERS, C.; MORGENROTH, W.; APPEL, K.; MCCAMMON, C.; SCHREIBER, A.; RODDATIS, V.; GLAZYRIN, K.; HUSBAND, R.; HENNET, L.; WILKE, M. (2024): Reevaluating the fate of subducted magnesite in the Earth's lower mantle. Phys. Earth Planet. Inter. 355, 107238. https://doi.org/10.1016/j.pepi.2024.107238

LIN, Y.; ISHII, T.; VAN WESTRENEN, W.; KATSURA, T.; MAO, H.-K. (2024): Melting at the base of a terrestrial magma ocean controlled by oxygen fugacity. Nat. Geosci. 17, 803-808, https://doi.org/10.1038/s41561-024-01495-1

LIU, D.; PUREVJAV, N.; FEI, H.; WITHERS, A.C.; YE, Y.; KATSURA, T. (2024): Temperature and compositional dependences of H_2O solubility in majorite. Am. Mineral. 109, 1646-1652, https://doi.org/10.2138/am-2023-9130

LIU, S.; KEPPLER, H. (2024): The mobility of Cu, Zn, Mo, and W in subduction zone fluids. Geochim. Cosmochim. Acta 365, 174-185, https://doi.org/10.1016/j.gca.2023.11.009

MAN, L.; FEI, H.; KIM, E.J.; NÉRI, A.; XIE, L.; FROST, D.J. (2024): Alumina solubility in periclase determined to lower mantle conditions and implications for ferropericlase inclusions in diamonds. Geochim. Cosmochim. Acta 375, 36-49, https://doi.org/10.1016/j.gca.2024.05.002

MARRAS, G.; MIKHAILENKO, D.; MCCAMMON, C.A.; AGASHEVA, E.; STAGNO, V. (2024): Ferric iron in eclogitic garnet and clinopyroxene from the V. Grib kimberlite pipe (NW Russia): Evidence for a highly oxidized subducted slab. J. Petrol. 65(6), egae054, https://doi.org/10.1093/petrology/egae054

MIYAJIMA, N.; SILVA SOUZA, D.; HEIDELBACH, F. (2024): Dauphiné twin in a deformed quartz: Characterization by electron channelling contrast imaging and large-angle convergent-beam diffraction. Eur. J. Mineral. 36(5), 709-719, https://doi.org/10.5194/ejm-36-709-2024

MOROZOVA, N.V.; ZHEVSTOVSKIKH I.V.; KOROBEINIKOV, I.V.; SARYCHEV M.N.; SEMENOVA O.I.; OVSYANNIKOV, S.V. (2024): Manipulating the phase stability of a halide perovskite, $CH_3NH_3PbI_3$ by high-pressure cycling. J. Alloys Compd. 988, 174305, http://dx.doi.org/10.1016/j.jallcom.2024.174305

MOSENFELDER, J.L.; BUREAU, H.; WITHERS, A.C. (2024): Hydrogen in the deep Earth. Elements Magazine 20(4), 223-228, https://doi.org/10.2138/gselements.20.4.223

NEAVE, D.A.; STEWART, A.G.; HARTLEY, M.E.; MCCAMMON, C. (2024): Re-evaluating stoichiometric estimates of iron valence in magmatic clinopyroxene crystals. Contrib. Mineral. Petrol. 179, 5, https://doi.org/10.1007/s00410-023-02080-2

NÉRI, A.; MAN, L.; CHANTEL, J.; FARLA, R.; BAUER, G.,; LINHARDT, S.; BOFFA BALLARAN, T.; FROST, D.J. (2024): The development of internal pressure standards for in-house elastic wave velocity measurements in multi-anvil presses. Rev. Sci. Instrum. 95, 013902, https://doi.org/10.1063/5.0169260

NEUMANN, W.; MA, N.; BOUVIER, A.; TRIELOFF, M. (2024): Recurrent planetesimal formation in an outer part of the early solar system. Sci. Rep. 14, 14017, https://doi.org/10.1038/s41598-024-63768-4

PAUL, J.; GOLABEK, G.J.; ROZEL, A.B.; TACKLEY, P.J.; KATSURA, T.; FEI, H. (2024): Effect of bridgmanite-ferropericlase grain size evolution on Earth's average mantle viscosity: Implications for mantle convection in early and present-day Earth. Prog. Earth Planet Sci. 11, 64, https://doi.org/10.1186/s40645-024-00658-3

PAUSCH, T.; JOACHIM-MROSKO, B.; LUDWIG, T.; WITHERS A.C.; VAZHAKUTTIYAKAM, J.; KONZETT, J. (2024): The role of Ca-phosphates and silicates in the storage and transport of phosphorus at the upper-to-lower mantle transition: An experimental study to 25 GPa in a model peridotitic bulk composition. Geochim. Cosmochim. Acta 374, 200-216, https://doi.org/10.1016/j.gca.2024.04.026

PUREVJAV, N.; FEI, H.; ISHII, T.; CRINITI, G.; LIN, Y.; MAO, H.; KATSURA, T. (2024): Temperature dependence of H_2O solubility in Al-free stishovite. Geophys. Res. Lett. 51(3), e2023GL104029, https://doi.org/10.1029/2023GL104029

PUTAK JURICEK, M; AUDETAT, A; KEPPLER, H. (2024): Trace element partitioning between saline aqueous fluids and subducted metasediments and the origin of the "sediment fingerprint" in arc magmas. Geochem. Geophys. Geosyst. 25, e2023GC011342, https://doi.org/10.1029/2023GC011342

PUTAK JURICEK, M.; KEPPLER, H. (2024): Stability of hydrous basaltic melts at low water fugacity: Evidence for widespread melting at the lithosphere-asthenosphere boundary. Contrib. Mineral. Petrol. 179, 97, https://doi.org/10.1007/s00410-024-02177-2

RAORANE, A.; BRASSER, R.; MATSUMURA, S.; LAU, T.C.H.; LEE, M.H.; BOUVIER, A. (2024): Giant planet formation in the solar system. Icarus 421, 116231, https://doi.org/10.1016/j.icarus.2024.116231

RÖSCHE, C.; BOFFA BALLARAN, T.; MALCHEREK, T.; PAULMANN, C.; ANGEL, R.J.; GORFMAN, S.; MIHAILOVA, B. (2024): The high-pressure structure of (1-x)$Na_{0.5}Bi_{0.5}TiO_3$-x$BaTiO_3$ at the morphotropic phase boundary. Sci. Rep. 14, 18799, https://doi.org/10.1038/s41598-024-69313-7

ROGMANN, E.M.; JENNINGS, E.S.; ROSS, J.; MIYAJIMA, N.; WALTER, M.J.; KOHN, S.C.; LORD, O.T. (2024): The effect of potassium on aluminous phase stability in the lower mantle. Contrib. Mineral. Petrol. 179, 52, https://doi.org/10.1007/s00410-024-02129-w

RUSTIONI, G.; WIEDENBECK, M.; MIYAJIMA, N.; CHANYSHEV, A.; KEPPLER, H. (2024): Magnesiowüstite as a major nitrogen reservoir in Earth's lowermost mantle. Geochem. Persp. Lett. 28, 43-47, https://doi.org/10.7185/geochemlet.2401

SATTA, N.; CRINITI, G.; KURNOSOV, A.; BOFFA BALLARAN, T.; ISHII, T.; MARQUARDT, H. (2024): Elastic anomalies across the $P2_1nm \rightarrow Pnnm$ structural phase transition in δ-(Al,Fe)OOH. Am. Mineral. 109, 1934-1944, https://doi.org/10.2138/am-2023-9129

SPANG, A.; THIELMANN, M.; KISS, D. (2024): Rapid ductile strain localization due to thermal runaway. J. Geophys. Res. Solid Earth 129(10), e2024JB028846, https://doi.org/10.1029/2024JB028846

SPIELMANN, J.; BRAIG, D.; STRECK, A.; GUSTMANN, T.; KUHN, C.; REINAUER, F.; KURNOSOV, A.; LEUBNER, O.; POTAPKIN, V.; HASSE, C.; DEUTSCHMANN, O.; ETZOLD, B.J.M.; SCHOLTISSEK, A.; KRAMM, U.I. (2024): Exploring the oxidation behavior of undiluted and diluted iron particles for energy storage: Mössbauer spectroscopic analysis and kinetic modeling. Phys. Chem. Chem. Phys. 26(17), 13049-13060, https://doi.org/10.1039/D3CP03484D

SPITZER, F., *et al.* with the Hayabusa2 Initial Analysis Chemistry Team (including BOUVIER, A.) (2024): The Ni isotopic composition of Ryugu reveals a common accretion region for all carbonaceous chondrites. Sci. Adv. 10, eadp2426, https://doi.org/10.1126/sciadv.adp2426

STOPPONI, V.; D'ARCO, A.; KONO, Y.; PICCIRILLI, F.; POE, B.T.; LUPI, S.; NAZZARI, M.; PAPPALARDO, L.; MARRAS, G.; ZACCHIGNA, M.; MANNING, C.E.; ROMANO, C.; STAGNO, V. (2024): *In situ* investigation of the atomic structure of carbonate-silicate liquids at high pressure-temperature and spectroscopic characterization of the recovered quenched glasses. Chem. Geol. 659, 122152, https://doi.org/10.1016/j.chemgeo.2024.122152

TIMONER, C.; ARENAS, R.; FUENLABRADA, J.M.; MORENO, J.A.; ROJO-PÉREZ, E. (2024): Alkaline Devonian magmatism of the Menorca Island: Tracking the mantle isotopic sources in the realm of the western Paleo-Tethys Ocean. Chem. Geol. 669, 122362, https://doi.org/10.1016/j.chemgeo.2024.122362

TRAUTNER, V.E.; RIJAL, A.; PLUECKTHUN, C.; SATTA, N.; KOEMETS, E.; BUCHEN, J.; WANG, B.; GLAZYRIN, K.; COBDEN, L.; MARQUARDT, H. (2024): Iron content-dependence of ferropericlase elastic properties across the spin crossover from novel experiments and machine learning. Geophys. Res. Lett. 51(22), e2024GL111276, https://doi.org/10.1029/2024GL111276

TRUBOWITZ, C.; MURAKAMI, M.; PETITGIRARD, S.; LIEBSKE, C.; MCCAMMON, C. (2024): Structural evolution of basaltic melts in the deep Earth: Insights from sound velocity. J. Geophys. Res. Solid Earth 129(9), e2024JB028969, https://doi.org/10.1029/2024JB028969

UENVER-THIELE, L.; WOODLAND, A.B.; MIYAJIMA, N.; BOFFA BALLARAN, T.; ALIG, E.; FINK, L. (2024): High-*P*-*T* phase relations of Al-bearing magnetite: Post-spinel phases as indicators for *P*-*T* conditions of formation of natural samples. Am. Mineral. 109(6), 1062-1073, https://doi.org/10.2138/am-2023-8948

WANG, W.; LI, Y. (2024): Redox control of the partitioning of platinum and palladium into magmatic sulfide liquids. Commun. Earth Environ. 5, 190, https://doi.org/10.1038/s43247-024-01366-y

WIDMANN, I.; KINIK, G.; JÄHNIG, M.; GLAUM, R.; SCHWARZ, M.; WÜSTEFELD, C.; JOHRENDT, D.; TRIBUS, M.; HEJNY, C.; BAYARJARGAL, L.; DUBROVINSKY, L.; HEYMANN, G.; SUTA, M.; HUPPERTZ, H. (2024): Real competitors to ruby: The triel oxonitridoborates AlB_4O_6N, $Al_{0.97}Cr_{0.03}B_4O_6N$, and $Al_{0.83}Cr_{0.17}B_4O_6N$. Adv. Funct. Mater. 34(28), 2400054, https://doi.org/10.1002/adfm.202400054

WOODLAND, A.B.; SCHUMANN, K.; UENVER-THIELE, L.; ROSBACH, K.; BOFFA BALLARAN, T.; MELAI, C.; BYKOVA, E. (2024): Chrome incorporation in high-pressure Fe-Mg oxides. Eur. J. Mineral. 36, 845-862, https://doi.org/10.5194/ejm-36-845-2024

XIE, L.; WALTER, M.; KATSURA, T.; XU, F.; WANG, J.; FEI, Y. (2024): Crystallization of a hydrous magma ocean in the shallow lower mantle. Earth Planet. Sci. Lett. 633, 118651, https://doi.org/10.1016/j.epsl.2024.118651

YAO, J.; CIOBANU, C.L.; COOK, N.J.; EHRIG, K.; DIMA, G.I.; STEINLE-NEUMANN, G. (2024): *Ab initio* calculations and crystal structure simulations for mixed layer compounds from the tetradymite series. Am. Mineral. 109, 1375-1386, https://doi.org/10.2138/am-2023-9018

YIN, Y.; ASLANDUKOV, A.; BYKOV, M.; LANIEL, D.; ASLANDUKOVA, A.; PAKHOMOVA, A.; FEDOTENKO, T.; ZHOU, W.; AKBAR, F.I.; HANFLAND, M.; GLAZYRIN, K.; GIACOBBE, C.; LAWRENCE BRIGHT, E.; GARBARINO, G.; JIA, Z.; DUBROVINSKAIA, N.; DUBROVINSKY, L. (2024): Polytypism of incommensurately modulated structures of crystalline bromine upon molecular dissociation under high pressure. Phys. Rev. B, 110, 104111, https://doi.org/10.1103/PhysRevB.110.104111

YIN, Y.; DUBROVINSKY, L.; ASLANDUKOV, A.; ASLANDUKOVA, A.; AKBAR, F.I.; ZHOU, W.; HANFLAND, M.; ABRIKOSOV, I.A.; DUBROVINSKAIA, N. (2024): High-pressure synthesis of the iodide carbonate $Na_5(CO_3)_2I$. Solids, 5(2), 333-340, https://doi.org/10.3390/solids5020022

YIN, Y.; DUBROVINSKY, L.; ASLANDUKOV, A.; ASLANDUKOVA, A.; FEDOTENKO, T.; GLAZYRIN, K.; GARBARINO, G.; ABRIKOSOV, I.A.; DUBROVINSKAIA, N. (2024): High-pressure synthesis of rhenium carbide Re_3C under megabar compression. Phys. Chem. Minerals 51(4), 39, https://doi.org/0.1007/s00269-024-01300-w

YIN, Y.; WANG, L.; ZHAI, S.; LIU, Y. (2024): Lorenz number and transport properties of Fe: Implications to the thermal conductivity at Earth's core-mantle boundary. Am. Mineral. 109(11) 1850-1860, https://doi.org/10.2138/am-2023-9246

YUAN, L.; STEINLE-NEUMANN, G. (2024): Earth's "missing" chlorine may be in the core. J. Geophys. Res. 129, e2023JB027731, https://doi.org/10.1029/2023JB027731
ZHANG, L.; QI, N.; LI, Y.; WANG, X.; ZHANG, L. (2024): Immiscible metamorphic water and methane fluids preserved in carbonated eclogite. Commun. Chem. 7, 267, https://doi.org/10.1038/s42004-024-01355-4
ZHOU, W.; YIN, Y.; LANIEL, D.; ASLANDUKOV, A.; BYKOVA, E.; PAKHOMOVA, A.; HANFLAND, M.; POREBA, T.; MEZOUAR, M.; DUBROVINSKY, L.; DUBROVINSKAIA, N. (2024): Polymorphism of pyrene on compression to 35 GPa in a diamond anvil cell. Commun. Chem. 7(1), 209, https://doi.org/10.1038/s42004-024-01294-0
ZHU, D.-P.; KONG, H.; ALGEO, T.J.; BOUVIER, A.; LIU, B.; WU, J.-H.; HU, X.-J.; WU, Q.-H. (2024): Evolution of skarn to quartz-vein mineralization: Insights from the Tongshanling Cu–Pb–Zn deposit, South China. Ore Geol. Rev. 166, 105952, https://doi.org/10.1016/j.oregeorev.2024.105952

4.2 Publications (submitted, in press)

ASLANDUKOVA, A.; ASLANDUKOV A.; YIN, Y.; BYKOV, M.; CERANTOLA, V.; PAKHOMOVA, A.; DUBROVINSKAIA, N.; DUBROVINSKY, L.: High-pressure yttrium borate *oC*20-YBO_3 and orthocarbonate *hR*39-$Y_3(CO_4)_2$ synthesized at megabar pressures. Chem. Eur. J. (submitted)
AUDÉTAT, A.; CHANG, J.; GAYNOR, S.P.: Widespread occurrence of former anhydrite phenocrysts in Laramide-age magmas related to porphyry-skarn Cu mineralization at Santa Rita and Hanover-Fierro, New Mexico, USA. Econ. Geol. (submitted)
BAMBER, E.C.; ARZILLI, F.; CIPICCIA, S.; BATEY, D.J.; LA SPINA, G.; POLACCI, M.; GHOLINIA, A.; BAGSHAW, H.; DI GENOVA, D.; BROOKER, R.; GIORDANO, D.; VALDIVIA, P.; BURTON, M.R.: 3D visualisation of nanolite aggregation in basaltic magmas using X-ray ptychography: Implications for magma differentiation and rheology. Sci. Adv. (submitted)
BONDAR, D.; CANIZARÈS, A.; BILARDELLO, D.; VALDIVIA, P.; ZANDONÀ, A.; ROMANO, C.; ALLIX, M.; DI GENOVA, D.: Nanolite crystallization in volcanic glasses: insights from high-temperature Raman spectroscopy and low-temperature rock-magnetic analysis. Geochem. Geophys. Geosyst. (submitted)
BOUVIER, A.; BERMINGHAM, K.R.; FÜRI, E.: Planetary materials: A record of early solar system events to planetary processes. – In: Treatise on Geochemistry (Third Edition) 7, (Eds. Anbar, A.; Weis, D.), Elsevier (in press), https://doi.org/10.1016/B978-0-323-99762-1.00137-6
CHANG, J.; AUDÉTAT, A.; PETTKE, T.: Ten kilometers ascent of porphyry Cu (Au, Mo)-forming fluids in the Sanjiang region, China. Nat. Commun. (submitted)
CHRAPPAN SOLDAVINI, B.; MERLINI, M.; GEMMI, M.; PARLANTI, P.; FUMAGALLI, P.; MILANI, S.; JOSEPH, B.; BAIS, G.; POLENTARUTTI, M.; KURNOSOV, A.; POLI, S. (2024): Crystal structure and elastic properties of parabreyite: a new high-pressure ring silicate in the $CaSiO^3$ system. Eur. J. Mineral. (in press), https://doi.org/10.5194/ejm-37-13-2025

DALE, K.; MORBIDELLI, A.; RUBIE, D.C.; NESVORNÝ, D.: Compositional outcomes of Earth formation from a narrow ring. Earth Planet. Sci. Lett. (submitted)

DORN, C.; GOLABEK, G.J.; BOWER, D.J.: Interior-atmosphere interactions for terrestrial Solar System objects, Super-Earths and Sub-Neptunes. Handbook of Exoplanets (in press)

FANESI, E.; DI GENOVA, D.; VALDIVIA, P.; BONDAR, D.; DOMINIJANNI, S.; ABEYKOON, S.; GIULIANI, G.; KURNOSOV, A.; GIORDANO, G.; CASSETTA, M.; VONA, A.; ROMANO, C.; ARZILLI, F.: A review of the differential scanning calorimetry shift–factor approach: application to Colli Albani melt viscosity and implications for mafic Plinian eruptions. J. Volcanol. Geotherm. Res. (submitted)

FANG, J.; AUDÉTAT, A.; DOLEJŠ, D.: Molybdenum speciation in magmatic-hydrothermal fluids: Constraints from molybdenite solubility experiments and thermodynamic modeling. Geochim. Cosmochim. Acta. (submitted)

FARLA, R.; NÉRI, A.; PÖPPELBAUM, M.; GLAZYRIN, K.: Thermal equations of state of B2-structured rubidium halides RbCl, RbBr and RbI. J. Appl. Phys. (submitted)

GAUTIER, A.; BOLFAN-CASANOVA, N.; MOINE, B.; BUREAU, H.; KHODJA, H.; WITHERS, A.C.; PIANI, L.: H and D/H analysis in olivine and wadsleyite with a multianalytical approach combining Raman spectroscopy, ion and nuclear probes. Eur. J. Mineral. (submitted)

GILLMANN, C.; ARNEY, G.N.; AVICE, G.; DYAR, M.D.; GOLABEK, G.J.; GÜLCHER, A.J.P.; JOHNSON, N.M.; LEFÈVRE, M.; WIDEMANN, T.: Venus. – In: Treatise on Geochemistry (Third Edition) 7, (Eds. Anbar, A.D.; Weis, D.), Elsevier (in press), https://doi.org/10.1016/B978-0-323-99762-1.00099-1

HAMANO, K.; GILLMANN, C.; GOLABEK, G.J.; LOURENÇO, D.; WESTALL, F.: The evolutionary divergence of Mars, Venus and Earth. – In: Treatise on Geochemistry (Third Edition) 7, (Eds. Anbar, A.D.; Weis, D.), Elsevier (in press), https://doi.org/10.1016/B978-0-323-99762-1.00104-2

HU, X.; LI, H.; LIU, B.; BOUVIER, A.; KANG, F.; ZHU, D.: Integrated apatite analyses unveil post-Jurassic metallogenic peak associated with persistent magmatism in the Dengfuxian Ore Field, South China. Chem. Geol. (submitted)

HU, S.; ANAND, M.; FRANCHI, I.A.; ZHAO, X.; ZHANG, B.; BOUVIER, A.; LIU, Y.; TANG, G.; LI, Q.; AGEE, C.; LIN, Y.: Discovery of OH-bearing whitlockite in an extraterrestrial sample. Sci. Rep. (submitted)

IIZUKA, T. *et al.* with the Hayabusa2 Initial Analysis Chemistry Team (including BOUVIER, A.): The fate of water on carbonaceous asteroids inferred from hafnium isotopes in Ryugu samples, Nature (submitted)

KATSURA, T.: Phase relations of bridgmanite, the most abundant mineral in the Earth's lower mantle. Commun. Chem. (in press), https://doi.org/10.1038/s42004-024-01389-8

KEPPLER, H.; AUDETAT, A.: The redox dependence of the fluid/melt partitioning of tin. Geochim. Cosmochim. Acta (submitted)

MAN, L.; LI, X.; BOFFA BALLARAN, T.; ZHOU, W.; CHANTEL, J.; NÉRI, A.; KUPENKO, I.; APRILIS, G.; KURNOSOV, A.; NAMUR, O.; HANFLAND, M.; GUIGNOT, N.; HENRY, L.; DUBROVINSKY, L.; FROST, D.J.: The structure and stability of $Fe_{4+x}S_3$ and its potential to form a Martian inner core. Nat. Commun. (submitted), http://dx.doi.org/10.21203/rs.3.rs-5070782/v1

MARRAS, G.; MIKHAILENKO, D.; MCCAMMON, C.; LOGVINOVA, A.; HĂNZEL, D.; DALLAI, L.; STAGNO, V.: Oxy-thermobarometry of grospydite and high-Ca eclogite xenoliths from Zagadochnaya kimberlite pipe (Yakutia, Siberian craton). Mineral. Petrol. (submitted)

MCGREGOR, N.J.; NIMMO, F.; GILLMANN, C.; GOLABEK, G.J.; PLATTNER, A.M.; CONRAD, J.W.: Probing the viscosity of Venus's mantle from dynamic topography at Baltis Vallis. J. Geophys. Res. (submitted)

O'CONNELL, D.; MCCAMMON, C.; BYRNE, J.; JAKOBSEN, R.; JENSEN, M.M.; THAMDRUP, B.; BRUUN HANSEN, H.C.; POSTMA, D.: Isotopic exchange between aqueous Fe(II) and solid Fe(III) in lake sediment – a kinetic assemblage approach. Environ. Sci. Technol. (submitted)

OHASHI, T.; SAKAMAKI, T.; FUNAKOSHI, K.-i.; STEINLE-NEUMANN, G.; HATTORI, T.; YUAN, L.; SUZUKI, A.: Pressure-induced elongation of hydrogen-oxygen bond in sodium silicate melts. J. Mineral. Petrol. Sci. (submitted)

PIERRU, R.; BONNET-GIBET, V.; FRANÇOISE, M.; DOMINIJANNI, S.; PARISIADES, P.; ANDRIAMBARIARIJAONA, L.; ZHAO, B.; PANDOLFI, S.; BOCCATO, S.; BLANCHARD, I.; WEHR, N.; GUIGNOT, N.; HENRY, L.; KING, A.; BADRO, J.; MICHAUT, C.; ANTONANGELI, D.: Melting properties and melting phase relations of the Martian mantle from in situ measurements on iron-rich mineralogical assemblages. Phys. Earth Planet. Inter. (submitted)

RUBIE, D.C.; NATHAN, G.; DALE, K.I.; NAKAJIMA, M.; JENNINGS, E.S.; GOLABEK, G.J.; JACOBSON; S.A.; MORBIDELLI, A.: Tungsten isotope evolution during Earth's formation and new constraints on the viability of accretion simulations. Earth Planet. Sci. Lett. (in press), https://doi.org/10.1016/j.epsl.2024.119139

SAHA, P.; MURAKAMI, M.; MIYAJIMA, N.: Earth's lower mantle predominated by ferric iron-rich bridgmanite. Nat. Geosci. (submitted)

SCHÖNBÄCHLER, M., *et al.* with the Hayabusa2 Initial Analysis Chemistry Team (including BOUVIER, A.): Zirconium isotope composition indicate s-process depletion in samples returned from asteroid Ryugu. Meteorit. Planet. Sci. (in press)

STROZEWSKI, B.; RAUTELA, O.; BUCHEN, J.; STURHAHN, W.; ISHII, T.; OHIRA, I.; PARDO, O.S.; LAVINA, B.; ZHAO, J.; TOELLNER, T.S.; JACKSON, J.M.: Sound velocities of (Al,Fe)-phase H and the seismic visibility of dense oxyhydroxides in Earth's lower mantle. Phys. Earth Planet. Inter. (submitted)

VALDIVIA, P.; ZANDONÀ, A.; LÖSCHMANN, J.; BONDAR, D.; GENEVOIS, C.; CANIZARÈS, A.; ALLIX, M.; MIYAJIMA, N.; KURNOSOV, A.; BOFFA BALLARAN, T.; DI FIORE, F.; VONA, A.; ROMANO, C.; DEUBENER, J.; BAMBER, E.C., DI GENOVA, D.: Nanoscale chemical heterogeneities control magma viscosity. Commun. Earth Environ. (submitted)

WANG, F.; BAUSCH, H.J.; GARDNER, L.L.; ZHANG, D.; ARMSTRONG, K.; BELL, A.S.; ZHAO, J.; ALP, E.E.; JACOBSEN, S.D.: Thermoelastic properties of iron-rich ringwoodite and the deep mantle aerotherm of Mars. Geophys. Res. Lett. 51, e2024GL109666 (in press), https://doi.org/10.1029/2024GL109666

WANG, F.; WANG, L.; FEI, H.; MIYAJIMA, N.; MCCAMMON, C.; FROST, D.J.; KATSURA, T.: Bridgmanite's ferric iron content determined Earth's redox state. Nat. Geosci. (submitted)

WANG, L.; MIYAJIMA, N.; WANG, F.; KATSURA, T.: Persistence of davemaoite at lower mantle conditions. Nat. Geosci. (submitted)

WEGNER, L.; BURTON, E.D.; MCCAMMON, C.; SCHEINOST, A.C.; PLANER-FRIEDRICH, B.; PEIFFER, S.; HOCKMANNN, K.: Ferrous iron oxidation in the presence of antimonate: Mutual effects on iron mineral products and antimony sequestration. J. Hazard. Mater. (submitted)

WHITNEY, D.L.; WILKE, M.; HANEL, S.; HEIDELBACH, F.; ROSA, A.: $Fe^{3+}/\Sigma Fe$ variation in lawsonite and epidote in subducted oceanic crust. European Journal of Mineralogy (accepted)

ZHOU, C.; BUCHEN, J.; DOBROSAVLJEVIC, V.V.; STROZEWSKI, B.; PARDO, O.S.; STURHAHN, W.; ISHII, T.; TOELLNER, T.; WILDING, J.D.; CHARITON, S.; KALKAN, B.; KUNZ, M.; JACKSON, J.M.: Elasticity and density of a sulfur-poor iron-nickel alloy: Earth's sulfur-depleted inner core. Geophys. Res. Lett. (submitted)

ZHOU, W.; ASLANDUKOV, A.; MINCHENKOVA, A.; HANFLAND, M.; DUBROVINSKY, L.; DUBROVINSKAIA, N.: Structural transformations and stability of benzo[*a*]pyrene under high pressure. IUCrJ (accepted), https://doi.org/10.1107/S2052252524010455

4.3 Presentations at scientific institutions and at congresses

AKBAR, F.I.: 18.-21.03.2024, 32nd Annual Meeting of the Crystallographic society (DGK) Bayreuth, Germany: "Novel high-pressure rare-earth carbides with diverse carbon atoms arrangements"

ASLANDUKOV, A.: 18.-21.03.2024, 32nd Annual Meeting of the Crystallographic society (DGK) Bayreuth, Germany: "Stabilization of the CN_3^{5-} anion in recoverable high-pressure $Ln_3O_2(CN_3)$ (Ln = La, Eu, Gd, Tb, Ho, Yb) oxoguanidinates"

ASLANDUKOVA, A.: 18.-21.03.2024, 32nd Annual Meeting of the Crystallographic society (DGK) Bayreuth, Germany: "High-pressure *oC*16-YBr_3 polymorph recoverable to ambient conditions: from 3D framework to layered material"

AUDÉTAT, A.: 25.-28.11.2024, DOME Research School, GFZ Potsdam, Germany: "Synthetic fluid inclusions"

BELTRAME, M.; ZIBERNA, L.; MCCAMMON, C.; MASOTTA, M.; VENIER, M.; DE FELICE, A.; MAJGSUREN, Y.; DE MIN, A.: 30.09.-04.10.2024, 7th Orogenic Lherzolite Meeting, Oviedo, Spain: "The lithospheric mantle beneath central Mongolia: constraints from spinel-bearing peridotite xenoliths and high-pressure experiments"

BLANCHARD, I.; SIEBERT, J.; WILKE, M.; LOBANOV, S.S.; KUBIK, E.; SCHREIBER, A.; BONINO, V.; CALVO, L.; PETITGIRARD, S.; PARISIADIS, P.; GUIGNOT, N.: 13.-17.05.2024, Earth and Planets Origin and Evolution Meeting, Paris, France: "New constraints on Earth's late veneer from metal–silicate partitioning of gold and rhenium"

BOFFA BALLARAN, T.; CRINITI, G.; KURNOSOV, A.; GLAZYRIN, K.: 18.-23.08.2024, 4th European Mineralogical Conference, Dublin, Ireland (*invited*): "Single crystals at high-pressures and high-temperatures: constraining planetary interiors"

BONDAR, D.; CANIZARÈS, A.; VALDIVIA, P.; ZANDONÀ, A.; ROMANO, C.; ALLIX, M.; DI GENOVA, D.: 18.-20.09.2024, 6th Alfred Rittmann Conference, Catania, Italy: "High-temperature Raman spectroscopy investigation of volcanic glasses"

BOUVIER, A.: 04.-09.02.2024, Winter School 'Small Bodies of the Solar System and their link with Extraterrestrial Samples', Les Houches, France (*invited*): "Timescales of early solar system processes"

BOUVIER, A.: 13.03.2024, Chinese Academy of Sciences, Beijing, P.R. China (*invited*): "Constraints on the formation and impact history of the Moon from micro-zircon studies"

BOUVIER, A.: 11.04.2024, Universität Münster, Germany (*invited*): "Meteorite records of planetary crust formation"

BOUVIER, A.: 29.04.2024, Ed Scott Lecture Series, The Meteoritical Society, online (*invited*): "Achondrite meteorites: Messengers of early planetary accretion and evolution"

BOUVIER, A.; OBENGO, E.; REGER, P.M.; NEUMANN, W.; SCHWARZ, W.H.; LUDWIG, T.; TRIELOFF, M.: 28.07.-02.08.2024, 86th Annual Meeting of the Meteoritical Society, Brussels, Belgium: "Accretion and thermal history of the angrite parent body", LPI Contrib. No. 3036, Abstract 6210

BUCHEN, J.: 31.01.2024, Universität Bayreuth (Antrittsvorlesung), Bayreuth, Germany: "Minerals under pressure: Fragments of a deep-earth mosaic"

BUCHEN, J.; WANG, B.; SATTA, N.; TRAUTNER, V.; CRINITI, G.; MÉNDEZ, A.S.J.; LIERMANN, H.-P.; MARQUARDT, H.: 22.01.2024, Status and research highlights of the ECB (P02.2) at PETRA III, Hamburg, Germany: "Seismic waves in the dynamic DAC: Stress and strain in polycrystalline materials"

BUCHEN, J.; KURNOSOV, A.; CRINITI, G.; MARQUARDT, H.; BOFFA BALLARAN, T.: 18.-21.03.2024, 32nd Annual Meeting of the Crystallographic society (DGK) Bayreuth, Germany: "Single-crystal elastic properties from high-pressure experiments: a comparison of inversion strategies"

BUCHEN, J.; PARDO, O.S.; DOBROSAVLJEVIC, V.V.; STURHAHN, W.; ISHII, T.; CHARITON, S.; GREENBERG, E.; TOELLNER, T.S.; JACKSON, J.M.: 27.05.2024, Deutsches GeoForschungsZentrum, Potsdam, Germany: "Linking water and ferric iron in Earth's lower mantle"

BUCHEN, J.; PARDO, O.S.; DOBROSAVLJEVIC, V.V.; STURHAHN, W.; ISHII, T.; CHARITON, S.; GREENBERG, E.; TOELLNER, T.S.; JACKSON, J.M.: 18.-23.08.2024, 4th European Mineralogical Conference, Dublin, Ireland: "Spin transition links water and ferric iron in Earth's lower mantle"

CALVO, L.; LABIDI, J.; KUBIK, E.; SIEBERT, J.: 13.-17.05.2024, Earth and Planets Origin and Evolution Meeting, Paris, France: "Experimental tracing of volatile elements origin on Earth through S isotopes"

CHANYSHEV, A.; ISHII, T.; WANG, F.; MARTIROSYAN, N.; HAN, K.; FARLA, R.; KATSURA, T.: 26.-31.05.2024, JpGU 2024, Chiba, Japan: "Post-spinel phase transition in Mg_2SiO_4-Fe_2SiO_4 system as an interpretation of the 660-km discontinuity elevation"

CHANYSHEV, A.; MARTIROSYAN, N.; WANG, L.; CHAKRABORTI, A.; PUREVJAV, N.; WANG, F.; KIM, E.J.; TANG, H.; FEDOTENKO, T.; BHAT, S.; FARLA, R.; KATSURA, T.: 26.-31.05.2024, JpGU 2024, Chiba, Japan: "Thermal equation of state of B3-SiC at high pressures"

CRINITI, G.; BOFFA BALLARAN, T.; ISHII, T.; CHANYSHEV, A.; KURNOSOV, A.; APRILIS, G.; PAKHOMOVA, A.; FEDOTENKO, T.; WALTER, M.J.; FROST, D.J.: 18.-23.08.2024, Goldschmidt 2024, Chicago, USA: "Does pressure promote Fe^{3+}-Al disordering in lower mantle bridgmanite?"

DUBROVINSKY, L.S.: 05.2024, German Chemical Society, Frankfurt a. M., Germany: "The alchemy of pressure and heat: Crystallography's uncharted territory"

FEI, H.; WANG, F.; MCCAMMON, C.; KATSURA, T.: 14.-19.04.2024, EGU General Assembly 2024, Vienna, Austria: "The effect of Fe^{3+} on the grain growth kinetics of bridgmanite and implications for the lower mantle seismic velocity anomalies", Abstract EGU24-5736

FROST, D.J.: 24.02.2024, University of Delhi, Department of Geology, Delhi, India: "Diamond formation and the Earth's deep cycle of volatiles"

FROST, D.J.: 26.-28.02.2024, Workshop on 'Deformation Mechanisms, Processes and Fabric Analysis in Earth Materials from the Global to the Nano Scale – Methods and Applications', Indian Institute of Technology, Kharagpur, India: "The experimental study of the rheology of mantle rocks"

FROST, D.J.: 28.02.2024, Jadavpur University, Department of Geological Sciences, Kolkata, India: "Diamond formation and the Earth's deep cycle of volatiles"

FROST, D.J.: 01.03.2024, Indian Institute of Sciences, Center for Earth Science, Bangalore, India: "Diamonds and the Earth's deep carbon cycle"

FROST, D.J.: 08.04.2024, Center for High Pressure Science and Technology Advanced Research (HPSTAR), Beijing, P.R. China: "The redox state of Earth's mantle and its development"

FROST, D.J.; MAN, L.; CHANTEL, J.; BOFFA BALLARAN, T.; DOLINSCHI, J.; GUIGNOT, N.; HENRY, L.; FARLA, R.; WANG, Y.: 18.-23.08.2024, Goldschmidt 2024, Chicago, USA: "Experimental constraints on the composition of the Martian core"

FROST, D.J.: 02.12.2024, University Clermont Auvergne, Laboratoire Magmas et Volcans, Aubière, France: "Diamonds and the Earth's deep carbon cycle"

FUKUSHIMA, R.; TSUJIMORI, T.; MIYAJIMA, N.: 26.-31.05.2024, JpGU 2024, Chiba, Japan: "Dehydration melting of lawsonite eclogite xenolith in Colorado Plateau: Microtextural analyses for the fluid migration history"

GOLABEK, G.J.: 13.02.2024, ETH Zurich, Switzerland: "Outgassing and atmosphere formation on terrestrial bodies"

GOLABEK, G.J.; ZIPPOLI, M.; RADUCAN, S.; JUTZI, M.: 08.-12.04.2024, Impact Workshop, Rochester, USA: "Post-impact thermal evolution of iron-rich planetesimals"

GOLABEK, G.J.; LICHTENBERG, T.; BARTELS, L.M.; TACKLEY, P.J.; MEIER, T.; BOWER, D.: 14.-19.04.2024, EGU General Assembly 2024, Vienna, Austria: "Magma oceanography of the dense, ultrashort-period sub-Earth GJ 367 b", Abstract EGU24-5832

GOLABEK, G.J.: 06.09.2024, University of Alabama, Tuscaloosa, USA: "Outgassing and atmosphere formation on terrestrial bodies"

HECKEL, C.; WOODLAND, A.B.; GIBSON, S.A.; LINCKENS, J.; WITHERS, A.C.; SEITZ, H.-M.; LUDWIG, T.: 08.-12.07.2024, 12^{th} International Kimberlite Conference, Yellowknife, Canada: "Sheared peridotites: linking deformation and H_2O metasomatism to the onset of craton destabilization"

HECKEL, C.; WOODLAND, A.B.; GIBSON, S.A.; LINCKENS, J.; WITHERS, A.C.; SEITZ, H.-M.; LUDWIG, T.: 18.-23.08.2024, 4th European Mineralogical Conference, Dublin, Ireland: "Sheared peridotites: linking deformation and hydrous metasomatism to the onset of craton destabilization"

JOURNAUX, B.; PAKHOMOVA, A.; POWELL-PALM, M.; COLLINGS, I.E.; PETITGIRARD, S.; BROWN, J.M.; VANCE, S.; BOFFA BALLARAN, T.: 05.-10.05.2024, Astrobiology Science Conference (AbSciCon), Providence, USA: "Salty ices for exotic oceanic cocktails: Icy worlds petrological diversity and what it can tell us about their ocean and habitability"

KATSURA, T.: 19.01.2024, Tokyo Institute of Technology, Tokyo, Japan: "A new hypothesis about the structure and origin of the lowermost mantle and the hotspot-feeding process"

KATSURA, T.: 19.- 20.03.2024, Review of Beamlines P61A (HEREON) und P61B (DESY), Hamburg, Germany: "Precise determination of geophysically important phase relations and reactions using a large-volume multi-anvil press"

KATSURA, T.: 14.-19.04.2024, EGU General Assembly 2024, Vienna, Austria: "Large Low-Velocity Provinces (LLVPs): a new model for their structure, origin, and evolution", Abstract EGU24-8054

KATSURA, T.; WANG, L.; WANG, F.; MIYAJIMA, N.: 26.-31.05.2024, JpGU 2024, Chiba, Japan: "Investigation of bridgmanite chemistry using an ultrahigh-pressure multi-anvil press"

KATSURA, T.; FEI, H.; BALLMER, M.; FAUL, U.; WALTE, N.; CAO, W.: 26.-31.05.2024, JpGU 2024, Chiba, Japan: "Grain growth kinetics of bridgmanite as a function of the fraction of coexisting ferropericlase: A new interpretation for the mid-mantle viscosity jump"

KATSURA, T.; WANG, L.; MIYAJIMA, N.; WANG, F.: 11.09.2024, Center for High Pressure Science and Technology Advanced Research (HPSTAR), Beijing, P.R. China: "Davemaoite does exist in the lower mantle"

KATSURA, T.; WANG, L.; MIYAJIMA, N.; WANG, F.: 13.09.2024, Guiyang Institute of Geochemistry, Guiyang, P.R. China: "Davemaoite does exist in the lower mantle"

KATSURA, T.; WANG, L.; MIYAJIMA, N.; WANG, F.: 23.09.2024, Guangzhou Institute of Geochemistry, Guangzhou, P.R. China: "Davemaoite does exist in the lower mantle"

KATSURA, T.; WANG, L.; MIYAJIMA, N.; WANG, F.: 25.09.2024, Jilin University, Changchun, P.R. China: "Davemaoite does exist in the lower mantle"

KEPPLER, H.: 29.02.-01.03.2024, Fourth general assembly of DOME: Dynamics of Ore Metal Enrichment, Bad Kissingen: "The surprising redox dependence of tin partitioning"

KUBIK, E.; NERI, A.; MAN, L.; CHAKRABORTI, A.; HIN, R.: 13.-17.05.2024, Earth and Planets Origin and Evolution Meeting, Paris, France: "Thermal gradient measurements in box furnace multianvil assemblies designed for high-temperature experiments"

KUBIK, E.: 08.07.2024, CoMBINE Workshop, Bristol, U.K. (*invited*): "Core–mantle isotopic fractionation in large terrestrial planets"

KUBIK, E.: 26.09.2024, StarPlan, Copenhagen, Denmark (*invited*): "Core–mantle isotopic fractionation in large terrestrial planets"

KUBIK, E.: 26.12.2024, Laboratoire de Planétologie et Géosciences, Nantes Université, Nantes, France (*invited*): "Core–mantle isotopic fractionation in large terrestrial planets"

MARRAS, G.; MIKHAILENKO, D.; MCCAMMON, C.; AULBACH, S.; LOGVINOVA, A.; ZEDGENIZOV, D.; STAGNO, V.: 08.-12.07.2024, 12th International Kimberlite Conference, Yellowknife, Canada: "Mineral inclusions in E-type diamonds from the Siberian craton: witnesses of Archaean mantle redox heterogeneities and eclogite buffering capacity"

MARRAS, G.; MIKHAILENKO, D.; MCCAMMON, C.; HĂNZEL, D.; STAGNO, V.: 08.-12.07.2024, 12th International Kimberlite Conference, Yellowknife, Canada: "Ferric iron measurements of coexisting garnet and clinopyroxene in grospydite xenoliths from Zagadochnaya kimberlite pipe (Yakutia, Siberian craton)"

MCCAMMON, C.: 18.-23.08.2024, 4th European Mineralogical Conference, Dublin, Ireland: "What's so special about Mössbauer spectroscopy anyway?"

MCCAMMON, C.: 22.-23.07.2024, Iron Mössbauer Applied to Environmental Systems Workshop, Bristol, UK: "Monster spectrum: Iron in freshwater lake sediments"

MELAI, C.; WITHERS, A.C.; TOMLINSON, E.L.: 08.-12.07.2024, 12th International Kimberlite Conference, Yellowknife, Canada: "Experimental investigation of silica enrichment in Archean cratonic lithosphere"

MELAI, C.; WITHERS, A.C.; TOMLINSON, E.: 18.-23.08.2024, 4th European Mineralogical Conference, Dublin, Ireland: "Unveiling silica enrichment in archean peridotite: The role of komatiite melt"

MIYAJIMA, N.; PUREVJAV, N.; WITHERS, A.C.: 18.-23.08.2024, 4th European Mineralogical Conference, Dublin, Ireland: "High resolution transmission electron microscopy of a defect in hydrous forsterite"

NEAVE, D.A.; STEWART, A.G.; HARTLEY, M.E.; NAMUR, O.; MCCAMMON, C.: 03.-05.01.2024, Volcanic and Magmatic Studies Group 60th Anniversary Meeting, Bristol, UK: "Iron valence systematics in clinopyroxene from oceanic basalts: revisiting stoichiometric estimates of ferric iron content"

NERI, A.; KUBIK, E.; GOLABEK, G.J.; BOUVIER, A.; WALTE N.P.: 28.07.-02.08.2024, 86th Annual Meeting of the Meteoritical Society, Brussels, Belgium: "On the peculiar separation of metal and troilite in acapulcoites"

PIERRU, R.; BONNET-GIBET, V.; FRANÇOISE, M.; DOMINIJANNI, S.; PARISIADES, P.; ANDRIAMBARIARIJAONA, L.; ZHAO, B.; PANDOLFI, S.; BOCCATO, S.; BLANCHARD, I.; WEHR, N.; GUIGNOT, N.; HENRY, L.; KING, A.; BADRO, J.; MICHAUT, C.; ANTONANGELI, D.: 03.-07.06.2024, 14e Forum de technologie des hautes pressions, Argelès-sur-Mer, France: "Investigating Martian mantle melting: Insights into Shergottite origins, thermal evolution, and potential melting under the Tharsis region"

PIERRU, R.; BONNET-GIBET, V.; FRANÇOISE, M.; DOMINIJANNI, S.; PARISIADES, P.; ANDRIAMBARIARIJAONA, L.; ZHAO, B.; PANDOLFI, S.; BOCCATO, S.; BLANCHARD, I.; WEHR, N.; GUIGNOT, N.; HENRY, L.; KING, A.; BADRO, J.; MICHAUT, C.; ANTONANGELI, D.: 08.-13.09.2024, Europlanet Science Congress 2024, Freie Universität Berlin, Germany: "Investigating Martian mantle melting: Insights into Shergottite origins, thermal evolution, and potential melting under the Tharsis region"

RUBIE, D.C.; DALE, K.; NATHAN, G.; NAKAJIMA, M.; JENNINGS, E.S.; GOLABEK, G.J.; JACOBSON, S.A.; MORBIDELLI, A.: 13.-17.05.2024, Earth and Planets Origin and Evolution Meeting, Paris, France: "Tungsten isotope evolution during Earth's formation and new constraints on the viability of accretion simulations"

SAHA, P.; MURAKAMI, M.; MCCAMMON, C.; LIEBSKE, C.; KRYMARYS, E.: 18.-23.08.2024, Goldschmidt 2024, Chicago, USA: "Pressure induced structural transition in Deep Terrestrial Magma Ocean"

SPANG, A.; THIELMANN, M.; KISS, D.: 14.-19.04.2024, EGU General Assembly 2024, Vienna, Austria: "Thermal runaway as driving mechanism of deep earthquakes – Constraints from numerical modeling", Abstract EGU24-10403

SPANG, A.; THIELMANN, M.; KISS, D.; PRANGER, C.: 14.-19.04.2024, EGU General Assembly 2024, Vienna, Austria: "Thermal runaway and the challenges of rapid localization", Abstract EGU24-18807

SPANG, A.; THIELMANN, M.; KISS, D.: 01.-06.09.2024, 2024 Ada Lovelace Workshop on Modelling Mantle and Lithosphere Dynamics, Sète, France: "Thermal runaway as driving mechanism of deep earthquakes – Constraints from numerical modeling"

STAGNO, V.; MCCAMMON, C.; KAMINSKY, F.; MARRAS, G.: 14.-19.04.2024, EGU General Assembly 2024, Vienna, Austria: "The redox state of the Earth's lower mantle: combined evidence from natural mineral inclusions in superdeep diamonds and experimental predictions", Abstract EGU24-19097

THIELMANN, M.: 18.01.2024, Geokolloquium, University of Jena, Germany: "Processes and repercussions of slab detachment"

THIELMANN, M.; KAUS, B.J.P.; MEIER, T.: 15.03.2024, Adria Array Meeting, Sofia, Bulgaria: "The Geophysical Model Generator: a tool to unify and interpret geophysical datasets"

THIELMANN, M.: 24.06.2024, Geophysical Kolloquium, University of Hamburg, Germany: "The multiscale quest for deep earthquake processes"

THIELMANN, M.: 12.11.2024, UMET seminar, University of Lille, France: "Strain localization across the scales"

THIELMANN, M.: 02.12.2024, Geophysical Kolloquium, University of Münster, Germany: "Strain localization across the scales"

TIMONER, C.; ZHU, D.; ZHAO, R.; ZHANG, B.; BOUVIER, A.: 28.07.-02.08.2024, 86th Annual Meeting of the Meteoritical Society, Brussels, Belgium: "Asteroidal anorthosites: Tracking protoplanetary crust formation in the early solar system", LPI Contrib. No. 3036, Abstract 6133

VALDIVIA, P.; ZANDONÀ, A.; LÖSCHMANN, J.; BONDAR, D.; GENEVOIS, C.; CANIZARÈS, A.; MIYAJIMA, N.; KURNOSOV, A.; BOFFA BALLARAN, T.; DI FIORE, F.; VONA, A.; ROMANO, C.; ALLIX, M.; DEUBENER, J.; DI GENOVA, D.: 14.-19.04.2024, EGU General Assembly 2024, Vienna, Austria: "*In situ* nanoscale insights on magma viscosity and explosive", Abstract EGU24-7627

VALDIVIA, P.; ZANDONÀ, A.; LÖSCHMANN, J.; KURNOSOV, A.; BOFFA BALLARAN, T.; DEUBENER, J.; DI GENOVA, D.: 18.-20.09.2024, 6th Alfred Rittmann Conference, Catania, Italy: "A new viscosity model for hydrous andesitic magmas: insights from Sakurajima volcano"

WANG, F.; WANG, L.; FEI, H.; MIYAJIMA, N.; MCCAMMON, C.; FROST, D.; KATSURA, T.: 09.-13.12.2024, AGU Fall Meeting 2024, Washington D.C., USA: "Bridgmanite induced ferrous iron charge disproportionation and the redox state of the Earth"

WEILER, T.; PICCOLO, A.; SPANG, A.; THIELMANN, M.: 01.-06.09.2024, 2024 Ada Lovelace Workshop on Modelling Mantle and Lithosphere Dynamics, Sète, France: "What's beneath the Hindu Kush? On the road to data-driven modelling of the terminal stage of subduction"

ZHANG, B.; TIMONER, C.; ZHAO, R.; ZHU, D.; BOUVIER, A.: 18.-23.08.2024, Goldschmidt 2024, Chicago, USA: ""*In situ* Rb-Sr geochronology using MC-ICP-MS/MS"

ZIBERNA, L.; BELTRAME, M.; DE MIN, A.; MCCAMMON, C.; MASOTTA, M.; DEL RIO, M.; NARDUZZI, F.; ČERNOK, A.; TERRANOVA, K.; VENIER, M.: 03.-05.09.2024, SGI-SIMP Joint Congress: Geology for a sustainable management of our Planet, Bari, Italy: "The continental Moho from a geobarometric perspective"

ZUCCHINI, A.; BOFFA BALLARAN, T.; MASOTTA, M.; PENNACCHIONI, L.; MCCAMMON, C.; FASTELLI, M.; COMBONI, D.; HANFLAND, M.; FRONDINI, F.; COMODI, P.: 18.-23.08.2024, 4th European Mineralogical Conference, Dublin, Ireland: "Cation disorder and Fe-content in ankerite: their effect on its mineral physics"

4.4 Lectures and seminars at Bayerisches Geoinstitut

AUDÉTAT, Andreas: Bayerisches Geoinstitut, Bayreuth, Germany: "Combining natural samples and experiments to unravel the genesis of porphyry copper deposits", *Academy Commission Business Meeting*, 02.05.2024

ANTONANGELI, Daniele, Sorbonne Université, IMPMC, Paris, France: "Phase diagram and thermo-elastic properties of iron alloys under planetary core conditions", 11.07.2024

CASELLI, Paola, Max-Planck-Institut für extraterrestrische Physik, Garching, Germany: "Our astrochemical origins", 25.01.2024

CHAKRABORTY, Amrita, Bayerisches Geoinstitut, Bayreuth, Germany: "Ferropericlase morphology in Earth's lower mantle", *Academy Commission Business Meeting*, 02.05.2024

CHARNOZ, Sébastien, Institut de Physique du Globe (IPGP), Paris, France: "Origin of the first solids in the Solar System by non-equilibrium condensation", 05.12.2024

CONCONI, Roberto, Università degli Studi di Milano-Bicocca, Dipartimento di Scienze dell'Ambiente e della Terra, Milano, Italy: "There's plenty of room at the bottom: Micro- to nano-scale investigation of minerals and implications", 10.06.2024

COOPER, Frances, University College London, Department of Earth Sciences, London, U.K.: "How crustal exhumation rates determine the fate of porphyry copper deposits", 28.11.2024

DEMOUCHY, Sylvie, Université Clermont Auvergne, Laboratoire Magmas et Volcans, Aubière, France: "Everything flows, but how? Inferring the role of novel agents of ductile deformation in olivine", 16.05.2024

DOLINSCHI, Jonathan, Bayerisches Geoinstitut, Bayreuth, Germany: "Development of a novel method to measure deformation stresses", 29.04.2024

FUJIYA, Wataru, Ibaraki University, Faculty of Science, Mito, Japan: "Mn-Cr dating of carbonates: Applications to Ryugu and carbonaceous chondrites", 27.06.2024

GASC, Julien, Ecole Normale Supérieure de Paris, Département de Géosciences, Paris, France: "Labquakes caused by metamorphic reactions during high-pressure experiments and their scaling laws", 17.10.2024

HOARE, Liam, Ruhr-Universität Bochum, Institut für Geologie, Mineralogie und Geophysik, Bochum, Germany: "Isotopic and experimental constraints on continental crust formation in the early Earth", 18.01.2024

KHAN, Siddarth, Université Clermont Auvergne, Laboratoire Magmas et Volcans, Aubière, France: "Water storage and incipient melting in the shallow lower mantle", 12.12.2024

KRAWCZYK, Charlotte, GFZ Potsdam, Section 2.2: Geophysical Imaging, Potsdam, Germany: "Seismic imaging of geodynamic processes – how fibre-optic sensing changes the game", 24.10.2024

MAN, Lianjie, Bayerisches Geoinstitut, Bayreuth, Germany: "Integrating high-pressure experiments on iron-rich liquids: Unveiling the evolution and composition of the Martian core", *Academy Commission Business Meeting*, 02.05.2024

MARKS, Michael, Universität Tübingen, Petrologie und Mineralische Rohstoffe, Tübingen, Germany: "What is so special about carbonatites? Some new concepts to explain carbonatite-silicate rock associations", 18.07.2024

MARROCCHI, Yves, Université de Lorraine, Centre de Recherches Pétrographiques et Géochimiques, Nancy, France: "Dust production and evolution in the inner solar system", 14.11.2024

MERKEL, Sébastien, Université de Lille, Unité Matériaux et Transformations, Lille, France: "Pyrolite microstructures and deep mantle anisotropy from multigrain XRD in the laser-heated diamond anvil cell", 13.06.2024

MERLINI, Marco, Università degli Studi di Milano, Dipartimento di Scienze della Terra Ardito Desio, Milano, Italy: "Structural complexities of high-pressure silicates and carbonates and their relevance for upper mantle processes", 21.11.2024

MOTTE, Mikaël, Laboratoire de Planétologie et Géosciences (LPG), Nantes, France: "The fO_2 of MORB glasses using a multi-proxy approach", 20.08.2024

RADUCAN, Sabina, Universität Bern, Physikalisches Institut, Bern, Switzerland: "Lessons learned from NASA's DART impact about deflecting rubble-pile asteroids", 04.07.2024

RIEL, Nicolas, Johannes-Gutenberg Universität, Institut für Geowissenschaften, Mainz, Germany: "Modeling stable phase equilibrium for petrological and geodynamic application, an overview using MAGEMin", 06.06.2024

SAKURAI, Moe, Okayama University, Department of Earth Sciences, Okayama, Japan: "In-situ IR high-pressure experiments on hydrous forsterite: An attempt to determine hydrogen positions in olivine", 07.11.2024

SAVRANSKAIA, Tatiana, GFZ Potsdam, Section 2.3: Geomagnetism, Potsdam, Germany: "What cosmogenic ^{10}Be archives tell us about the history of the geomagnetic field", 11.01.2024

SPIEKERMANN, Georg, ETH Zurich, Switzerland: "Aspirine, Olivine, Brillouine: How to determine anisotropy when there is no single-crystal", 01.02.2024

TSUJINO, Noriyoshi, Japan Synchrotron Radiation Research Institute (JASRI), Hyogo, Japan: "In-situ stress and strain measurements of bridgmanite and state of the art at press beamlines at SPring-8", 25.04.2024

VALDIVIA MUNOZ, Pedro, Bayerisches Geoinstitut, Bayreuth, Germany: "Are volcanic melts less viscous than we thought? The case of Stromboli basalt", 08.02.2024

VERVOORT, Jeffrey, Washington State University, School of the Environment, Pullman, USA: "The growth of Earth's earliest crust – unravelling the isotope record", 23.05.2024

WITTKOP, Chad, Minnesota State University, Department of Biochemistry, Chemistry, and Geology, Mankato, USA: "Inferring Pleistocene ice sheet behavior from the geochemistry of glacial tills", 20.06.2024

ZHOU, Wenyi, Texas A&M College of Arts and Sciences, Geology & Geophysics, College Station, USA: "Mantle convection and composition in the Earth's and Martian interiors", 13.05.2024

4.5 Conference organisation

18.-21.03.2024, 32nd Annual Meeting of the Crystallographic society (DGK) Bayreuth, Germany (L.S. DUBROVINSKY, co-organizer)

08.-12.04.2024, Impact Workshop, Rochester, USA (D. BREUER, G.J. GOLABEK, M. NAKAJIMA, K. WÜNNEMANN)

14.-19.04.2024, European Geosciences Union General Assembly 2024, Vienna, Austria: "Venus: models, observations, (ancient) Earth- and exoplanet analogue" (M. PERSSON, C. GILLMANN, A. GÜLCHER, M. LEFEVRE, G.J. GOLABEK)

14.-19.04.2024, European Geosciences Union General Assembly 2024, Vienna, Austria: "Dynamics, structure and evolution of Earth and rocky planets from formation to the present day (P. TACKLEY, G.J. GOLABEK, L. NOACK, P. SOSSI)

07.-08.06.2024, Co-convener, Section Meeting Petrology/Petrophysics & Geochemistry, Deutsche Mineralogische Gesellschaft, Karlsruhe, Germany (A. BOUVIER)

08.-11.10.2024, Short Course at the China University of Geosciences, Wuhan, P.R. China: "Practical application of fluid inclusions" (A. AUDÉTAT)

5. Visiting Scientists

5.1 Visiting scientists funded by the Bayerisches Geoinstitut

ANTONANGELI, Daniele, Sorbonne Université, IMPMC, Paris, France: 10.-12.07.2024

CASELLI, Paola, Max-Planck-Institut für extraterrestrische Physik, Garching, Germany: 24.-26.01.2024

CHARNOZ, Sébastien, Institut de Physique du Globe (IPGP), Paris, France: 04.-05.12.2024

CONCONI, Roberto, Università degli Studi di Milano-Bicocca, Dipartimento di Scienze dell'Ambiente e della Terra, Milano, Italy: 09.-13.06.2024

DEMOUCHY, Sylvie, Université Clermont Auvergne, Laboratoire Magmas et Volcans, Aubière, France: 13.-18.05.2024

DOLEJŠ, David, Universität Freiburg, Institut für Geo- und Umweltnaturwissenschaften, Freiburg, Germany: 18.-22.02.2024

FANESI, Emanuele, Università di Camerino, Scuola di Studi Superiori "Carlo Urbani", Camerino, Italy: 01.01.-26.04.2024

FUJIYA, Wataru, Ibaraki University, Faculty of Science, Mito, Japan: 27.-29.06.2024

GASC, Julien, Ecole Normale Supérieure de Paris, Département de Géosciences, Paris, France: 16.-18.10.2024

HOARE, Liam, Ruhr-Universität Bochum, Institut für Geologie, Mineralogie und Geophysik, Bochum, Germany: 17.-19.01.2024

KHAN, Siddarth, Université Clermont Auvergne, Laboratoire Magmas et Volcans, Aubière, France: 10.-13.12.2024

KRAWCZYK, Charlotte, GFZ Potsdam, Section 2.2: Geophysical Imaging, Potsdam, Germany: 23.-25.10.2024

LÜNENSCHLOSS, Laura, Universität Tübingen, Experimentelle Mineralogie, Tübingen, Germany: 08.-10.10.2024

MARKS, Michael, Universität Tübingen, Petrologie und Mineralische Rohstoffe, Tübingen, Germany: 18.-19.07.2024

MARROCCHI, Yves, CNRS, Université de Lorraine, Centre de Recherches Pétrographiques et Géochimiques, Nancy, France: 14.-15.11.2024

MASOTTA, Matteo, Università di Pisa, Dipartimento di Scienze della Terra, Pisa, Italy: 18.-22.02.2024

MERKEL, Sébastien, Université de Lille, Unité Matériaux et Transformations, Lille, France: 12.-14.06.2024

MERLINI, Marco, Università degli Studi di Milano, Dipartimento di Scienze della Terra Ardito Desio, Milano, Italy: 20.-23.11.2024

RADUCAN, Sabina, Universität Bern, Physikalisches Institut, Bern, Switzerland: 03.-05.07.2024

RIEL, Nicolas, Johannes-Gutenberg Universität, Institut für Geowissenschaften, Mainz, Germany: 05.-07.06.2024

SAVRANSKAIA, Tatiana, GFZ Potsdam, Section 2.3: Geomagnetism, Potsdam, Germany: 11.-12.01.2024

SPIEKERMANN, Georg, ETH Zurich, Switzerland: 31.01.-02.02.2024

VERVOORT, Jeffrey, Washington State University, School of the Environment, Pullman, USA: 01.-31.05.2024

WALTE, Nico, TU München, Forschungs-Neutronenquelle Heinz Maier-Leibnitz (FRM II), Garching, Germany: 19.-23.02.2024

ZHANG, Bidong, University of California, Department of Earth, Planetary, and Space Sciences, Los Angeles, USA: 06.-14.01.2024

5.2 Visiting scientists supported by other externally funded BGI projects

RÖSCHE, Constanze, Universität Hamburg, Mineralogisch-Petrographisches Institut, Hamburg, Germany: 18.-28.03.2024 (DFG)

DFG: Deutsche Forschungsgemeinschaft

5.3 Visitors (externally funded)

ABEYKOON, Sumith, Università di Camerino, Scuola di Scienze e Tecnologie, Camerino, Italy: 26.-31.08.2024

BAIN, Hero, University of Bristol, School of Earth Sciences, Bristol, U.K.: 13.11.-14.12.2024

BAMBER, Emily Charlotte, CNR-ISSMC, Istituto di Scienza, Tecnologia e Sostenibilitá per lo sviluppo dei Materiali Ceramici Faenza, Italy: 13.-27.11.2024

BELIKOV, Roman, Goethe-Universität Frankfurt a. M., Geozentrum, Frankfurt a. M., Germany: 06.-07.09.2024

BYKOV, Maxim, Goethe-Universität Frankfurt a. M., Geozentrum, Frankfurt a. M., Germany: 05.-06.02.2024, 12.-13.04.2024

BYKOVA, Elena, Goethe-Universität Frankfurt a. M., Geozentrum, Frankfurt a. M., Germany: 06.-07.09.2024

CHRAPPAN SOLDAVINI, Benedetta, Università delgi Studi di Milano, Dipartimento di Scienze della Terra, Milano, Italy: 10.10.-06.12.2024

COOPER, Frances, University College London, Department of Earth Sciences, London, U.K.: 26.-29.11.2024

CRINITI, Giacomo, Earth & Planets Laboratory, Washington D.C., USA: 02.-03.08.2024

DIBENEDETTO, Andrea, Università di Pavia, Dipartimento di Chimica, Pavia, Italy: 19.-28.02.2024, 08.-19.07.2024

FUKUSHIMA, Ryo, Tohoku University, Center for Northeast Asian Studies, Sendai, Japan: 23.-27.04.2024

HAUPT, Cordula, Universität Münster, Institut für Mineralogie, Münster, Germany: 13.-23.08.2024, 28.-31.10.2024

HUANG, Yongsheng, Guangzhou Institute of Geochemistry, Chinese Academy of Sciences, Guangzhou, P.R. China: 20.-29.04.2024

KULKA, Britany, University of Oxford, Department of Earth Sciences, Oxford, U.K.: 19.-26.02.2024

LEDOUX, Estelle, University of Oxford, Department of Earth Sciences, Oxford, U.K.: 26.08.-08.09.2024

LEINENWEBER, Kurt, Arizona State University, School of Molecular Sciences, Eyring Materials Center, Tempe, USA: 03.-04.06.2024

LIU, Dan, China University of Geosciences, Gemmological Institute, Wuhan, P.R. China: 15.06.-05.09.2024

LIU, Zhiwei, Guangzhou Institute of Geochemistry, Chinese Academy of Sciences, Guangzhou, P.R. China: 22.10.-31.12.2024

LYU, Yifu, Zhejiang University, Department of Information Science and Electronic Engineering, Hangzhou, P.R. China: 17.02.-05.03.2024

MA, Shuai, University College Cork, School of Biological, Earth & Environmental Sciences, Cork, Ireland: 16.09.-06.11.2024

MANDIC, Marijana, MDPI, Basel, Switzerland: 09.04.2024

MELAI, Caterina, Trinity College Dublin, Department of Geology, Dublin, Ireland: 31.05.-31.12.2024

MORONI, Marco, Università di Pavia, Dipartimento di Chimica, Pavia, Italy: 19.-28.02.2024, 08.-12.07.2024

MOTTE, Mikaël, Laboratoire de Planétologie et Géosciences (LPG), Nantes, France: 18.-31.08.2024

MU, Peiyang, Center for High Pressure Science & Technology Advanced Research (HPSTAR), Beijing, P.R. China: 20.-27.04.2024

NAVROTSKY, Alex, Arizona State University, School of Molecular Sciences, Eyring Materials Center, Tempe, USA: 03.-04.06.2024

NIU, Guoliang, Center for High Pressure Science & Technology Advanced Research (HPSTAR), Beijing, P.R. China: 17.-27.04.2024

NOVAIS RODRIGUES, Eduardo, Università degli Studi di Padova, Dipartimento di Scienze della Terra, Padova, Italy: 15.10.-08.12.2024

PANTOUSAS, Apostolos, ESRF Grenoble, France: 18.-28.02.2024

PAUSCH, Tristan, Universität Innsbruck, Institut für Mineralogie und Petrographie, Innsbruck, Austria: 26.02.-10.03.2024

SAKURAI, Moe, Okayama University, Department of Earth Sciences, Physics of the Earth and Planetary Interiors, Okayama, Japan: 24.08.-09.11.2024

SPAHR, Dominik, Goethe-Universität Frankfurt a. M., Geozentrum, Frankfurt a. M., Germany: 06.-07.09.2024

STOPPONI, Veronica, CNR-ISSMC, Istituto di Scienza, Tecnologia e Sostenibilitá per lo sviluppo dei Materiali Ceramici Faenza, Italy: 13.-27.11.2024

TOMLINSON, Emma, Trinity College, Dublin, Ireland: 03.-07.11.2024

TRIBUS, Martina, Universität Innsbruck, Institut für Mineralogie und Petrographie, Innsbruck, Austria: 08.-09.07.2024

TSUJINO, Noriyoshi, Japan Synchrotron Radiation Research Institute (JASRI), Hyogo, Japan: 24.-27.04.2024

WANG, Biao, University of Oxford, Department of Earth Sciences, Oxford, U.K.: 16.-30.06.2024

WEN, Guang, China University of Geosciences, State Key Laboratory of Geological Processes and Mineral Resources, Wuhan, P.R. China: 21.09.-20.10.2024

WITTKOP, Chad, Minnesota State University, Department of Biochemistry, Chemistry, and Geology, Mankato, USA: 13.-27.06.2024

WU, Francis, MDPI, Basel, Switzerland: 09.04.2024

YIN, Yuqing, Linköping University, Department of Physics, Chemistry and Biology, Linköping, Sweden: 24.06.-07.07.2024

YOKOYAMA**,** Hiroaki, Tohoku University, Department of Earth Sciences, Sendai, Japan: 08.-12.12.2024

6. Additional scientific activities

6.1 Theses

Ph.D. theses

AKBAR, Fariia Iasmin: High-pressure synthesis and structural characterisation of novel rare-earth metal carbides.
DOLINSCHI, Jonathan: Novel method to measure deformation stress at high pressure and temperature.
ZHOU, Wenju: High-pressure studies of naphthalene, anthracene, pyrene, and benzo[a]pyrene using single-crystal X-ray diffraction in a diamond anvil cell.

M.Sc. theses

ANDREIEVA, Daria: Carbon-nitrogen compounds at interiors of the giant planets.
HAMADI, Muhammad Ilham: Postseismic relaxation of the subduction interface due to thermally activated ductile relaxation.
HLEDE, Matej: The contributions of subducted sediments to the formation of magmatic-hydrothermal deposits.
OBENGO, Edna: Shock effects and microstructural investigations in angrite meteorites.
TIMONER BOSCH, Cristian: Petrogenesis of asteroidal anorthosites.

6.2 Honours and awards

ASLANDUKOV, Andrey	GRC Jamieson Award at High Pressure Research Gordon Conference, Holderness, USA
BUCHEN, Johannes	Victor Moritz Goldschmidt Prize of the German Mineralogical Society (Deutsche Mineralogische Gesellschaft, DMG)
DUBROVINSKY, Leonid	Invited Lecturer, Institute of Physics, Polish Academy of Sciences
MCCAMMON, Catherine	Neumann Medal of the Mineralogical Society of the United Kingdom and Ireland

6.3 Editorship of scientific journals

AUDÉTAT, Andreas	Associate Editor "Economic Geology"

BOFFA BALLARAN, Tiziana	Associate Editor "European Journal of Mineralogy"
BOUVIER, Audrey	Associate Editor "Geochimica et Cosmochimica Acta"
DUBROVINSKY, Leonid	Member, Editorial Board "High Pressure Research" Member, Advisory Board "Minerals" Editor-in-Chief, "Minerals"
FROST, Dan	Member, Executive Committee for "Elements"
KEPPLER, Hans	Editorial Board "Contributions to Mineralogy and Petrology" Editorial Board "ACS Earth and Space Chemistry"
LI, Yuan	Associate Editor "Geochimica et Comochimica Acta" Advisory Board "Earth and Planetary Science Letters" Advisory Board "Acta Geochimica"
MIYAJIMA, Nobuyoshi	Associate Editor "European Journal of Mineralogy"

6.4 Membership of scientific advisory bodies

AUDÉTAT, ANDREAS	Member, Review Board of the German Science Foundation (DFG)
BOUVIER, Audrey	Chair, Section Geochemistry, Deutsche Mineralogische Gesellschaft (DMG) Member, Leonard medal, Nier prize and Fellows committee, Meteoritical Society Member, Science Working Team for Early Solar System Evolution, Martian Moons eXploration (MMX) mission, Japanese Aerospace Exploration Agency Member, Mars Sample Return (MSR) Campaign Science Group, European Space Agency
DUBROVINSKY, Leonid	Member, Review Panel of Canadian Light Source Chair Member, Subcommission on Spectroscopy, Diffraction, and new Instrumentations in Mineral Physics of the International Mineralogical Association Member, Review Panel of PETRA III Lithuanian Research Council, Head of Evaluation Committee in Civil Engineering

	Lithuanian Research Council, Head of Evaluation Committee in Natural Sciences
FROST, Dan	Member, Royal Society Member, Bavarian Academy of Sciences Member, German National Academy of Sciences (Leopoldina) Member, Scientific Advisory Committee of the GeoForschungsZentrum Potsdam Member, Royal Society Fellows Sectional Committee SC5 Vice President of the European Association of Geochemistry
KATSURA, Tomoo	Japan Association of Mineralogical Sciences Award Committee Chair
KEPPLER, Hans	Member, German National Academy of Sciences (Leopoldina) Member, Bavarian Academy of Sciences Member, Leibniz Prize selection committee, DFG
MCCAMMON, Catherine	Member, Project Review Panel P01, PETRA III Member, Council, International Mineralogical Association Member, Mediation Committee, International Mineralogical Association Member, Award Committee of the International Board on the Applications of Mössbauer Spectroscopy

7. Scientific and Technical Personnel

Name		Position	Duration in 2024	Funding source
AKBAR, Fariia Iasmin	M.Sc.	Wiss. Mitarbeiterin	to 30.09.	DFG
ANDREIEVA, Daria	B.Sc.	Student. Hilfskraft	to 31.03.	DFG
ANTUNES, Anaelle Coralie	B.Sc.	Student. Hilfskraft	to 10.03.	BGI
			from 11.03.	DFG
ASLANDUKOV, Andrii	M.Sc.	Wiss. Mitarbeiter	01.10.-31.12.	DFG
ASLANDUKOVA, Alena	M.Sc.	Wiss. Mitarbeiterin	01.10.-31.12.	DFG
AUDÉTAT, Andreas	Dr.	Akad. Oberrat		BGI
BAUER, Gerald	Dipl.-Ing. (FH)	Techn. Angestellter		BGI
BOFFA BALLARAN, Tiziana	Dr.	Akad. Oberrätin		BGI
BONDAR, Dmitry	Dr.	Wiss. Mitarbeiter		EU
BOUVIER, Audrey	Prof. Dr.	Professorin		BGI
BUBMANN, Daniela		Techn. Angestellte		BGI
BUCHEN, Johannes	Dr.	Juniorprofessor		BGI
BUCHERT, Petra		Fremdsprachen-Sekretärin		BGI
CALOGERO, Meredith	Dr.	Wiss. Mitarbeiterin	to 14.08.	EU
CHAKRABORTI, Amrita	Dr.	Wiss. Mitarbeiterin	to 31.03.	EU
			01.04.-31.07.	DFG
			01.08.-31.10.	BGI/VP
CHANG, Jia	Dr.	Wiss. Mitarbeiter	to 14.07.	BGI/VP
CHANYSHEV, Artem	Dr.	Wiss. Mitarbeiter		DFG
CZEKAY, Laura	Dr.	Wiss. Mitarbeiterin		DFG
DELL, Serghius		Elektrotechniker		BGI
DOLINSCHI, Jonathan	M.Sc.	Wiss. Mitarbeiter	to 31.05.	Leibniz
DUBROVINSKAIA, Natalia	Prof. Dr.	Professorin	from 01.10.	BGI
DUBROVINSKY, Leonid	Apl. Prof. Dr.	Akad. Direktor		BGI
FISCHER, Heinz		Mechaniker		BGI
FROST, Daniel	Prof. Dr.	Stellvertr. Leiter		BGI
GASPERT, Olga		Verwaltungsreferentin		BGI
GOLABEK, Gregor	Prof. Dr.	Professor		BGI
HAMADI, Muhammad	B.Sc.	Student. Hilfskraft	to 31.05.	Leibniz
HAN, Kui	Dr.	Stipendiat		CSC
HEIDELBACH, Florian	Dr.	Wiss. Mitarbeiter		BGI
HLEDE, Matej	B.Sc.	Student. Hilfskraft	to 30.09.	DFG
			01.10.-31.12.	UBT

HU, Xiao-Jun	M.Sc.	Stipendiatin		CSC
JEMAL, Ibrahim Jibril	B.Sc.	Student. Hilfskraft		DFG
KATSURA, Tomoo	Prof. Dr.	Professor		BGI
KELK-HUTH, Denise		Sekretärin	from 01.10.	BGI
KEPPLER, Hans	Prof. Dr.	Leiter		BGI
KRAUßE, Detlef	Dipl.-Inform. (FH)	Techn. Angestellter		BGI
KONRAD, Erik		Präparator	from 01.04.	BGI
KRIEGL, Holger		Haustechniker		BGI
KUBIK, Edith	Dr.	Stipendiatin		AvH
KURNOSOV, Alexander	Dr.	Wiss. Mitarbeiter		DFG
LI, Yuan	Dr.	Akad. Rat auf Probe	from 06.03.	BGI
LINHARDT, Sven		Elektrotechniker		BGI
MAN, Lianjie	M.Sc.	Wiss. Mitarbeiter	to 31.05.	Leibniz
			from 01.06.	DFG
MARTIROSYAN, Naira	Dr.	Wiss. Mitarbeiterin	to 29.02.	DFG
MATTHÄUS, Rebecka		Chem.-Techn. Assistentin		BGI
MCCAMMON, Catherine	PD Dr.	Wiss. Mitarbeiterin		DFG
MIYAJIMA, Nobuyoshi	Dr.	Akad. Oberrat		BGI
MINCHENKOVA, Anastasiia	B.Sc.	Student. Hilfskraft		DFG
NJUL, Raphael		Präparator		BG
OBENGO, Edna	B.Sc.	Student. Hilfskraft	20.03.-30.09.	DFG
OVSYANNIKOV, Sergey	Dr.	Wiss. Mitarbeiter		DFG
PAUL, Jyotirmoy	Dr.	Wiss. Mitarbeiter	to 31.01.	BGI/VP
PICCOLO, Andrea	Dr.	Wiss. Mitarbeiter	to 31.05.	DFG
PIERRU, Rémy Alfred	Dr.	Wiss. Mitarbeiter	from 08.01.	BGI
PÖPPELBAUM, Melanie	M.Sc.	Wiss. Mitarbeiterin	to 31.05.	Leibniz
			from 01.06.	DFG
POTZEL, Anke		Chem.-Techn. Assistentin		BGI
QIAN, Cheng	M.Sc.	Stipendiatin	from 08.01.	CSC
QIAO, Yi-Bo	M.Sc.	Wiss. Mitarbeiter	from 12.06.	DFG
RAUSCH, Oliver		Mechaniker		BGI
SCHARNAGEL, Janina		Sekretärin	to 30.06.	BGI
SCHULZE, Maximilian	Dr.	Wiss. Mitarbeiter	from 01.06.	DFG
SIKDAR, Jinia	Dr.	Wiss. Mitarbeiterin		EU
SILVA SOUZA, Danielle	M.Sc.	Wiss. Mitarbeiterin		DFG
SONG, Yunke	M.Sc.	Stipendiat		CSC
SPANG, Arne	Dr.	Wiss. Mitarbeiter		DFG

STEINLE-NEUMANN, Gerd	Privatdozent Dr.	Akad. Oberrat		BGI
THIELMANN, Marcel	Dr.	Wiss. Mitarbeiter		DFG
TIMONER BOSCH, Cristian	B.Sc.	Student. Hilfskraft	to 30.09.	DFG
TRENZ, Ulrike		Biol.-Techn. Assistentin		BGI
ÜBELHACK, Stefan		Mechaniker		BGI
VALDIVIA MUNOZ, Pedro Antonio	M.Sc.	Wiss. Mitarbeiter	to 27.11.	DFG
			from 28.11.	EU
WANG, Fei	Dr.	Wiss. Mitarbeiter	to 31.03.	EU
			from 01.04.	DFG
WANG, Lin	Dr.	Wiss. Mitarbeiter		BGI
WEILER, Tatjana	M.Sc.	Wiss. Mitarbeiterin		DFG
WETZEL, Stephanie		Sekretärin	from 01.12.	BGI
WIESNER, Dorothea		Techn. Assistentin		BGI
WITHERS, Antony	Dr.	Wiss. Mitarbeiter		BGI
ZHAO, Ran	M.Sc.	Stipendiat		CSC
ZHOU, Shan	M.Sc.	Stipendiatin		CSC
ZHOU, Wenju	M.Sc.	Wiss. Mitarbeiter	01.10.-30.11.	DFG
ZHOU, Wenyi	Dr.	Wiss. Mitarbeiterin	from 01.11.	BGI/VP
ZHU, Da-Peng	M.Sc.	Stipendiat		CSC
ZIPPOLI, Matteo	B.Sc.	Student. Hilfskraft		DFG

Abbreviations/explanations:

AvH	Alexander von Humboldt Foundation
BGI	Staff Position of Bayerisches Geoinstitut
BGI/VP	Visiting Scientists' Program of Bayerisches Geoinstitut
CSC	China Scholarship Council
DFG	German Science Foundation
EU	European Union
Leibniz	Leibniz-Preis der Deutschen Forschungsgemeinschaft Prof. Frost
UBT	Universität Bayreuth

Index